THE UNIVERSITY of ADELAIDE

In-situ Micro and Nanomechanical Characterization and Ultrasonic Machining of Zirconia Ceramics

by

Afifah Zakiyyah Juri
(BEng 1st Class Honours)

Thesis submitted to The University of Adelaide for the degree of

DOCTOR OF PHILOSOPHY

School of Mechanical Engineering
Faculty of Sciences, Engineering and Technology
The University of Adelaide
Australia

October 2022

Abstract

Zirconia ceramics are popular load-bearing ceramics exhibiting superior mechanical, chemical, optical, and biocompatibility properties, suitable for dental applications. These ceramic properties are available in distinct microstructures under pre-sintered and sintered states, respectively. Their mechanical properties, behavior, and deformation are influenced by their distinct microstructures. Zirconia product failure rates are a concern and understanding of the material general properties associated with distinct microstructures at small-scale contact can provide insight into their load-bearing functions. Shaping of these ceramics structures are conducted using dental CAD/CAM diamond machining processes involving micro and nanoscale diamond tools and material contacts, resulting in severe machining-induced damage. Addressing these matters requires a fundamental understanding of the influence of the ceramics distinct microstructures on indentation mechanics, which lays the foundation of generic insight into indentation-induced deformation and material removal mechanisms. Further, a review of the literature has revealed that conventional machining induces severe machining damage; whereas ultrasonic machining is an emerging technology with the capability to reduce such damage, possessing superior machining responses. A comparison of the ceramics machining responses can provide an alternative to using ultrasonic technology for the improvement of product longevity. This thesis has pursued an understanding of the microstructure-property-processing relations of zirconia materials. Hence, a thorough investigation was made into the influence of distinct microstructures in zirconia materials in terms of their micro and nanomechanical responses at small scale length and conventional and ultrasonic machining processes.

The first objective of this thesis is an investigation of zirconia materials with distinct microstructures under external load at small-scale contact volume, providing the critical micromechanical properties and behaviors for load-bearing functions. *In-situ* micropillar compression tests were conducted on pre-sintered and sintered zirconia materials. The two zirconia materials revealed micropillar-induced plastic behaviors with severe buckling occurred more frequently in pre-sintered zirconia than in sintered zirconia. Pre-sintered zirconia showed lower Young's moduli, strength properties (yield, compression, and fracture) and energy absorption properties (toughness and resilience) but higher ductility, in comparison with sintered zirconia. In addition, different quasi-brittle failure

mechanisms were revealed including mushrooming buckling damage with microcracks and severe compaction for pre-sintered zirconia. Plastic crushing damage with microcracks and microfractures in sintered zirconia was also observed.

The second objective of this thesis is an examination of the microstructure responses associated with indentation mechanics and behavior of zirconia materials at small-scale contact using sharp diamond indenters simulating tool-sample contact mechanics in dental abrasive machining. *In-situ* nanoindentation tests combined with an in-situ technique were also conducted on pre-sintered and sintered zirconia materials. The nanoindentation revealed quasi-brittle behavior for both zirconia materials but at the microstructural level different quasi-plastic mechanisms were identified for the two materials. Weak pore interface boundaries in the pre-sintered zirconia resulted in compression, fragmentation, pulverization, and microcracking of zirconia crystals. Shear bands with localized microfractures were induced in sintered zirconia. Pre-sintered zirconia had a lower rank in quasi-plasticity than sintered zirconia, predicting that it is more susceptible to abrasive machining-induced damage than sintered zirconia. The higher indentation volume in pre-sintered zirconia compared with sintered zirconia indicates the pre-sintered state has higher machining efficiency than the sintered state.

The third objective of this thesis is the cyclic nanoindentation of the zirconia materials. To further understand diamond machining of zirconia materials, experiments to help with understanding of material responses under repetitive indentation mechanics, which more closely represents the machining process, were conducted. *In-situ* cyclic nanoindentation tests were performed with 10 repeated loading and unloading cycles. Cyclic nanoindentation induced quasi-plastic deformation for the two zirconia materials with distinct mechanisms of quasi-plasticity. Agglomeration of zirconia crystals, cracks, compresses, and pulverized crystals were revealed in pre-sintered zirconia cyclic indentation imprints. Shear band, edge pile-ups, and microfractures were revealed in sintered zirconia indentation imprints. Advanced analysis of the zirconia materials deformation mechanisms revealed zirconia microstructures determined their cyclic nanoindentation induced deformation, predicting the ease of machining for pre-sintered zirconia but also revealing they may potentially suffer more severe abrasive machining damage than sintered zirconia.

The fourth objective of this thesis is to investigate the zirconia materials responses to edge chipping damage induced in conventional and ultrasonic vibration-assisted diamond machining processes. The edge chipping damage observed in zirconia materials largely depends on microstructure and the applied vibration amplitude during machining. Edge chipping damage was more severe in pre-sintered zirconia with weak pore interface boundaries and a higher brittleness index than in dense zirconia with a tightly packed microstructure and a lower index. Ultrasonic machining at an optimum vibration amplitude led to different material removal mechanisms reducing the brittle fracture induced during machining, hence significantly decreasing edge chipping damage and fracture in both zirconia materials.

The fifth objective of this thesis is an examination of the microstructural influence of damage-induced surface asperities produced by conventional and ultrasonic vibration-assisted diamond machining processes. The machining-induced surface damage, removal mechanisms, and surface asperities in the processing of pre-sintered and sintered zirconia depend on microstructure and ultrasonic vibration amplitudes. Conventional and ultrasonic milling induced mixed ductile and brittle fracture modes in pre-sintered and sintered zirconia materials. Milled pre-sintered zirconia showed dominant brittle fracture removal mechanism whereas ductile deformation was the dominant mode for sintered zirconia. Milled pre-sintered zirconia surfaces had more fractures and cracks and higher surface asperities than milled sintered zirconia surfaces. At an optimized vibration amplitude in both zirconia materials, ultrasonic machining enabled the minimization of brittle fracture at the micro-scale to result in more ductile deformation, with reduced surface damage and asperities than conventional machining.

Declaration

I certify that this work contains no material that has been accepted for the award of any other degree or diploma in my name, in any university or other tertiary institution and, to the best of my knowledge and belief, contains no material previously published or written by another person, except where due reference has been made in the text. In addition, I certify that no part of this work will, in the future, be used in a submission in my name, for any other degree or diploma in any university or other tertiary institution without the prior approval of the University of Adelaide and where applicable, any partner institution responsible for the joint-award of this degree.

I acknowledge that the copyright of published works contained within this thesis resides with the copyright holder(s) of those works.

I also give permission for the digital version of my thesis to be made available on the web, via the University's digital research repository, the Library Search and also through web search engines, unless permission has been granted by the University to restrict access for a period of time.

I acknowledge the support I have received for my research through the provision of an Australian Government Research Training Program Scholarship.

……..

Afifah Zakiyyah Juri

Acknowledgments

My deepest gratitude goes to my principal supervisor Associate Professor Ling Yin, who has accepted me into this research project and has relentlessly and patiently supported and supervised me during the course of the project. I have gained tremendous knowledge and insights from her invaluable experience in dental materials, fabrication, and characterization.

Next, I am thankful to my co-supervisor Dr Animesh Basak for his great guidance and encouragement in experimental work throughout my research. I would like to thank my co-supervisor Professor Andrei Kotousov for his academic supervision, support, and encouragement during my candidature. I appreciate Professor Yoshitaka Nakanishi, Kumamoto University, Japan for his collaboration, support and guidance for surface analysis, and Professor Yu Zhang, University of Pennsylvania, USA for his guidance on dental ceramics.

A special thanks goes to Mr Evan Johnson and Mr Alson Ng, Institute for Photonics and Advanced Sensing, UoA for their experimental assistance; Yanzhong Zhang for experimental support; Dr Alison Jane Hunter, School of Mechanical Engineering, UoA for the academic writing training; Mrs. Paula Billington, School of Mechanical Engineering, UoA for administrative support; and Dr Lei Chen, School of Mechanical Engineering, UoA for postgraduate support.

I acknowledge Adelaide Graduate Research School, the Faculty of Sciences, Engineering and Technology and the School of Mechanical Engineering of UoA for providing me the prestigious Ph.D. scholarship and the financial support of my conference attendances. I am also grateful for funding support from the seed grant in manufacturing and bio-manufacturing from UoA; the Australian Research Council (Grant ID DP200102300); and the Grants-in-Aid for Scientific Research, Promotion of Joint International Research (Fostering Joint International Research B) from the Japan Society for the Promotion of Science, Japan (Grant ID 17401).

Finally, I would like to thank my parents Juri Saedon and Norasmah Ahmad; my brothers Azib Azamuddin and Ahmad Aiman; and my colleagues and friends for their support.

Table of Contents

List of Figures

List of Tables

Lists of Publications

Refereed Journal Papers	**Status**
Juri, A. Z., Basak, A. K., Yin, L., 2022. *In-situ* SEM micropillar compression of porous and dense zirconia materials. J. Mech. Behav. Biomed. Mater. 105268.	**Published**
Juri, A. Z., Basak, A. K., Yin, L., 2022. *In-situ* SEM cyclic nanoindentation of pre-sintered and sintered zirconia materials. J. Mech. Behav. Biomed. Mater. 126, 105068.	**Published**
Juri, A. Z., Basak, A. K., Yin, L., 2021. Microstructural responses of Zirconia materials to *in-situ* SEM nanoindentation. J. Mech. Behav. Biomed. Mater. 118, 104450.	**Published**
Juri, A. Z., Nakanishi, Y., Yin, L., 2021. Microstructural influence on damage-induced zirconia surface asperities produced by conventional and ultrasonic vibration-assisted diamond machining. Ceram. Int. 47, 25744–25754.	**Published**
Juri, A. Z., Zhang, Y., Kotousov, A., Yin, L., 2021. Zirconia responses to edge chipping damage induced in conventional and ultrasonic vibration-assisted diamond machining. J. Mater. Res. Technol. 13, 573–589.	**Published**

Refereed Conference Abstracts	
Juri, A. Z., Nakanishi, Y., Kotousov, A., Yin, L., 2022. Zirconia Fracture and Deformation Induced by Conventional and Ultrasonic Vibration-Assisted Diamond Machining. Proceedings of the 17th Asia-Pacific Conference on Fracture and Strength and the 13th Conference on Structural Integrity and Failure, Adelaide, Australia.	**Accepted**

Juri, A. Z., Basak, A. K., Yin, L., 2022. Quasi-Plastic Deformation Behavior of Porous Zirconia. Proceedings of the 7th Combined Australian Materials Societies (CAMS) Conference 2022, Melbourne, Australia.	**Presented**
Juri, A. Z., Nakanishi, Y., Kotousov, A., Yin, L., 2021. Conventional and ultrasonic diamond milling of pre-sintered zirconia. Proceedings of the 10th Australasian Congress on Applied Mechanics, Adelaide, Australia.	**Presented**
Juri, A. Z., Zhang, Y., Kotousov, A., Yin, L., 2021. Machining-induced edge chipping damage in zirconia materials. Proceedings of the 12th International Conference on Structural Integrity and Failure, Melbourne, Australia.	**Presented**

Chapter 1 Introduction

1.1 Background and Prospects

Dental ceramic materials are used extensively in restorative application as posterior and anterior crowns, implants, inlay, onlay and bridges because of their superior mechanical properties and their tooth-like color aesthetics (Denry and Kelly, 2008; Li et al., 2014). One of these dental ceramics is zirconia, which possesses high mechanical strength and high fracture toughness (Belli et al., 2017; Denry and Kelly, 2008; Miyazaki et al., 2013). Zirconia possess high fracture toughness and it is due to its phase transformations mechanisms producing high resistance to damage, which makes it attractive compared with other dental ceramics (Denry and Kelly, 2008; Garvie at al., 1975; Piconi and Maccauro, 1999). However, zirconia is vulnerable to aging and has poor translucency.

The performance of zirconia structures in load-bearing applications are influenced by their microstructure and mechanical properties (Camposilvan and Anglada, 2016; Peterson et al., 1998; Quinn et al., 2003). Understanding the role of microstructure in the mechanical behavior of zirconia at small-scale can reduce its failure rates. Currently, general bulk mechanical properties including hardness, Young's modulus, fracture toughness, and strength of sintered zirconia have been determined (Alao et al., 2014a; 2014b; Belli et al., 2017; 2018; Ritzberger et al., 2010; Wendler et al., 2017). However, limited research has been carried out to evaluate the other strength properties (yield, compressive, and fracture), ductility and, energy absorptions (resilience and toughness) of pre-sintered and sintered zirconia materials. Furthermore, the vital zirconia materials deformation and damage mechanisms and their brittle to ductile transition have not yet been fulfilled. Since zirconia ceramic is brittle, small-scale testings are the solution to understanding these key micro/nano mechanical properties of zirconia materials in achieving maximized structure performance.

Zirconia materials possess excellent mechanical properties enabling them to be fabricated using abrasive machining (Denry and Kelly, 2008; Miyazaki et al., 2009; 2013). Soft and hard abrasive machining processes are available for two-step zirconia materials, which are machined in the pre-sintered state using soft machining and subsequently heated to

the sintered form (Denry and Kelly, 2008). This procedure allows for fast machining but is time-consuming for the latter heat treatment process and suffers from severe machining damage (Alao et al., 2017; Lambert et al., 2017; Fraga et al., 2017). The fully sintered zirconia is ready to use and machined using hard machining but suffers from tool wear (Abduo et al., 2010; Miyazaki et al., 2013). The different microstructures of zirconia consisting of different mechanical properties lead to different machining processes. In both soft and hard machining processes, machining-induced surface and subsurface damage (Anand et al., 2018; Denkena et al., 2017; Luthardt et al., 2004) is inevitable, resulting in poor surface quality (Alao et al., 2017) and property degradation (Xu et al., 1997). Hence, there is a need to understand zirconia material behavior during the machining process. This is difficult to obtain due to machining process complications involving fast and dynamic tool to surface movement and heat transfer. Hence, the indentation technique using a diamond indenter at the nanoscale, which mimics abrasive machining, is well suited to the task due to its inducing similar microfracture and deformation events, in delivering the key scientific insights into zirconia materials (Lawn et al., 2021; Malkin and Hwang, 1996; Xu et al., 1996). The machining speeds, forces and abrasive shapes in abrasive machining can be represented by loading rates, peak loads applied, and indenter geometries, respectively (Xu et al., 1996; Yan et al., 2006). Furthermore, understanding of zirconia materials deformation and damage mechanisms and their partition deformation into elasticity, plasticity, resistance to plasticity, and resistance to machining-induced cracking can provide a fundamental understanding of zirconia microstructural influence. These insights are invaluable for evaluating and predicting zirconia material machinability.

Since conventional machining of zirconia materials inevitably produces machining-induced damage (Alao et al., 2017; Anand et al., 2018; Denkena et al., 2017), a post-polishing process may be added to remove such damage, making this process complex and expensive. Thus, to minimize machining-induced damage, the development of innovative manufacturing technologies is urgently required to improve the longevity of dental restorations. Ultrasonic vibration-assisted machining is one of the emerging machining techniques with superior machining responses over conventional machining (Xu and Zhang, 2015). It is a technique performed by applying an external vibration at a high frequency to create relative displacement between the tool and the material's surface, in addition to the original cutting motion (Xu and Zhang, 2015). Recent studies have

shown that ultrasonic machining can machine hard, brittle, and fragile materials effectively with better machining performance than conventional machining processes (Abdo et al., 2019; Jia et al., 2019; Song et al., 2018; Tesfay et al., 2016; Yang et al., 2019). Ultrasonic machining has been proven to produce beneficial responses, such as better surface quality (Abdo et al., 2019; Jia et al., 2019; Yang et al., 2019), minimize burr formation (Kim and Loh, 2011), and minimize edge chipping damage (Song et al., 2018; Tesfay et al., 2016).

The requirements for fabrication of dental restorations with low surface damage and excellent aesthetic appearance have become ever more demanding to meet the challenges of the competitive global market. Thus, the ultimate goal of this project is to address these challenges through investigations of *in-situ* micro and nanomechanical characterization and ultrasonic machining processes on zirconia materials.

1.2 Aim and Objectives

The overall aim of the project is to investigate the *in-situ* micro and nanomechanical characterization and ultrasonic machining of zirconia ceramic. The specific objectives necessary to achieve the project aim are:

Objective 1. To characterize zirconia materials brittle to ductile transitions deformation, strength properties (yield, compressive, and fracture), ductility and energy absorption (resilience and toughness) properties.

Objective 2. To investigate zirconia materials single indentation mechanics and deformation mechanisms to relate to their machinability.

Objective 3. To investigate zirconia materials cyclic loading indentation mechanics and characterize their elastic, plastic, resistance to plasticity, and resistance to machining-induced cracking behaviors.

Objective 4. To investigate the responses of zirconia materials to machining-induced edge chipping damage produced in conventional and ultrasonic vibration-assisted diamond machining.

Objective 5. To investigate zirconia materials responses to conventional and ultrasonic vibration-assisted diamond machining processes to investigate the influence of zirconia microstructures on machining-induced surface asperities.

1.3 Thesis Organization

This thesis is formatted as a collection of manuscripts that have been published in high-quality journals or are ready to be published, except for Chapters 1, 2 and 8.

Chapter 1 introduces the thesis with a general background on dental computer-aided design/manufacturing materials in restorative applications and rational for the selection of pre-sintered and sintered zirconia materials as the research motivation of this study. The thesis aim and objectives are numbered.

Chapter 2 presents a literature review of the existing types of dental zirconia ceramics, microstructure mechanical properties, and CAD/CAM systems. The microstructure-property-processing relations of zirconia materials are also specified. A critical review of literature specific to the research gaps discovered contributing to significant scientific findings presented in this thesis is expanded in Chapters 3–7.

Chapter 3 investigates the micromechanical properties and behavior of pre-sintered and sintered zirconia using *in-situ* micropillar compression performed inside scanning electron microscopy. In the introduction, the chapter provides a critical literature review of *in-situ* micropillar compression studies performed on brittle materials and highlights the research gaps as the focus for studying their micromechanical properties, deformation, and damage mechanisms. The experimental procedure and the extraction of their mechanical properties from the stress-strain curves are then discussed in further detail. The chapter also presents a thorough analysis of their micropillar compression-induced deformation mechanisms and failure modes investigated from the micropillars deformations both throughout the compression process and after the compression tests. Furthermore, it also discusses the links between zirconia microstructures, mechanical properties, and micropillar compression deformation and damage mechanisms relations. This chapter was published in the journal listed below:

Juri, A. Z., Basak, A. K., Yin, L., 2022. In-situ SEM micropillar compression of porous and dense zirconia materials. J. Mech. Behav. Biomed. Mater. 105268. https://doi.org/10.1016/j.jmbbm.2022.105268.

Chapter 4 investigates the single loading indentation mechanics of pre-sintered and sintered zirconia materials using *in-situ* SEM nanoindentation conducted inside scanning electron microscopy. In the introduction section of this chapter, a thorough literature review is presented on nanoindentation studies of zirconia materials using ex-situ and *in-situ* approaches. It also highlights the research gap for studying their indentation mechanics and deformation. A thorough experimental procedures of the nanoindentation testings is presented. It presents the single loading nanoindentation induced deformation mechanisms studied throughout the nanoindentation process and their indentation imprints. Finally, it discusses the influence of zirconia microstructures on nanoindentation-induced deformations, mechanical properties, and also the significance contribution of this chapter findings to prediction of their machining responses in the abrasive machining process. This chapter was published in the journal listed below:

Juri, A. Z., Basak, A. K., Yin, L., 2021. Microstructural responses of Zirconia materials to in-situ SEM nanoindentation. J. Mech. Behav. Biomed. Mater. 118, 104450. https://doi.org/10.1016/j.jmbbm.2021.104450.

Chapter 5 investigates *in situ* SEM cyclic loading indentation mechanics of the mechanical behavior of pre-sintered and sintered zirconia. In the introduction, a thorough literature review was presented highlighting the research gaps for studying their cyclic loading indentation mechanics and the relations between cyclic nanoindentation processes and abrasive machining. A thorough experimental procedures of the cyclic nanoindentation testings and the extraction of their mechanical properties are also provided. It characterizes their deformation into elasticity, plasticity, resistance to plasticity, and resistance to machining-induced cracking. It also presents the cyclic loading nanoindentation induced deformation studied through the cyclic nanoindentation process and their cyclic nanoindentation imprints. Furthermore, it also discusses the relations between zirconia microstructures, advanced mechanical behavior and nanoindentation-induced deformation, alongside presenting the scientific contribution of this chapter. This chapter was published in the journal listed below:

Juri, A. Z., Basak, A. K., Yin, L., 2022. In-situ SEM cyclic nanoindentation of pre-sintered and sintered zirconia materials. J. Mech. Behav. Biomed. Mater. 126, 105068. https://doi.org/10.1016/j.jmbbm.2021.105068.

Chapter 6 studies the zirconia responses to edge chipping damage induced in conventional and ultrasonic machining processes with respect to edge chipping damage depths, areas, morphology, and material removal mechanisms. In the introduction section, a detailed literature review on conventional and ultrasonic machining processes and the research gaps for the motivation of the study are carried out. A thorough experimental procedures of the machining processes, edge chipping quantification and statistical analysis are presented. It also discusses the microstructure-mechanical behaviour-processing of zirconia materials and the beneficial influence of ultrasonic vibration assistance technology on machining-induced edge chipping damage. This chapter was published in the journal listed below:

Juri, A. Z., Zhang, Y., Kotousov, A., Yin, L., 2021. Zirconia responses to edge chipping damage induced in conventional and ultrasonic vibration-assisted diamond machining. J. Mater. Res. Technol. 13, 573–589. https://doi.org/10.1016/j.jmrt.2021.05.005.

Chapter 7 studies the damage-induced zirconia surface asperities produced by conventional and ultrasonic machining processes with respect to 3D surface texture parameters, damage morphology, and material removal mechanisms. A thorough experimental procedures of the machining processes, 3D surface roughness quantification and statistical analysis are also presented. It also discusses the effects of microstructure and ultrasonic vibration amplitude on the zirconia materials surface quality produced by conventional and ultrasonic machining. This chapter was published in the following journal:

Juri, A. Z., Nakanishi, Y., Yin, L., 2021. Microstructural influence on damage-induced zirconia surface asperities produced by conventional and ultrasonic vibration-assisted diamond machining. Ceram. Int. 47, 25744–25754. https://doi.org/10.1016/j.ceramint.2021.05.301.

Chapter 8 presents the concluding remarks and highlights a list of the original contributions to knowledge to be found throughout this thesis, along with recommendations for future works.

References

Abduo, J., Lyons, K., Swain, M., 2010. Fit of zirconia fixed partial denture: a systematic review. J. Oral Rehabil. 37, 866–876. https://doi.org/10.1111/j.13652842.2010.02113.x.

Abdo, B., Anwar, S., El-Tamimi, A. M., Abouel Nasr, E., 2019. Experimental analysis on the influence and optimization of μ-RUM parameters in machining alumina bioceramic. Mater. 12, 616. https://doi.org/10.3390/ma12040616.

Alao, A. R., Yin, L., 2014a. Nano-scale mechanical properties and behavior of pre-sintered zirconia. J. Mech. Behav. Biomed. Mater. 36, 21–31. https://doi.org/10.1016/j.jmbbm.2014.03.019.

Alao, A. R., Yin, L., 2014b. Loading rate effect on the mechanical behavior of zirconia in nanoindentation. Mater. Sci. Eng. A 619, 247–255. https://doi.org/10.1016/j.msea.2014.09.101.

Alao, A. R., Stoll, R., Song, X. F., Miyazaki, T., Hotta, Y., Shibata, Y., Yin, L., 2017. Surface quality of yttria-stabilized tetragonal zirconia polycrystal in CAD/CAM milling, sintering, polishing and sandblasting processes. J. Mech. Behav. Biomed. Mater. 65, 102–116. https://doi.org/10.1016/j.jmbbm.2016.08.021.

Anand, P. S. P., Arunachalam, N., Vijayaraghavan, L., 2018. Effect of grinding on subsurface modifications of pre-sintered zirconia under different cooling and lubrication conditions. J. Mech. Behav. Biomed. Mater. 86, 122–130. https://doi.org/10.1016/j.jmbbm.2018.06.026.

Belli, R., Wendler, M., de Ligny, D., Cicconi, M. R., Petschelt, A., Peterlik, H., Lohbauer, U., 2017. Chairside CAD/CAM materials. Part 1: Measurement of elastic constants and microstructural characterization. Dent. Mater. 33, 84–98. https://doi.org/10.1016/j.dental.2016.10.009.

Belli, R., Wendler, M., Petschelt, A., Lube, T., Lohbauer, U., 2018. Fracture toughness testing of biomedical ceramic-based materials using beams, plates and discs. J. Eur. Ceram. Soc. 38, 5533–5544. https://doi.org/10.1016/j.jeurceramsoc.2018.08.012.

Camposilvan, E., Anglada, M., 2016. Size and plasticity effects in zirconia micropillars compression. Acta Mater. 103, 882–892. https://doi.org/10.1016/j.actamat.2015.10.047.

Denry, I., Kelly, J. R., 2008. State of the art of zirconia for dental applications. Dent. Mater. 24, 299–307. https://doi.org/10.1016/j.dental.2007.05.007.

Denkena, B., Breidenstein, B., Busemann, S., Lehr, C. M., 2017. Impact of hard machining on zirconia based ceramics for dental applications. Procedia CIRP 65, 248–252. https://doi.org/10.1016/j.procir.2017.04.055.

Fraga, S., Amaral, M., Bottino, M. A., Valandro, L. F., Kleverlaan, C. J., May, L. G., 2017. Impact of machining on the flexural fatigue strength of glass and polycrystalline CAD/CAM ceramics. Dent. Mater. 33, 1286–1297. https://doi.org/10.1016/j.dental.2017.07.019.

Garvie, R. C., Hannink, R. H., Pascoe, R. T., 1975. Ceramic steel?. Nature 258, 703–704. https://doi.org/10.1038/258703a0.

Jia, D., Li, C., Zhang, Y., Yang, M., Zhang, X., Li, R., Ji, H., 2019. Experimental evaluation of surface topographies of NMQL grinding ZrO_2 ceramics combining multiangle ultrasonic vibration. Int. J. Adv. Manuf. Technol. 100, 457–473. https://doi.org/10.1007/s00170-018-2718-y.

Kim, G. D., Loh, B. G., 2011. Direct machining of micro patterns on nickel alloy and mold steel by vibration assisted cutting. Int. J. Precis. Eng. Manuf. 12, 583–588. https://doi.org/10.1007/s12541-011-0075-y.

Lambert, H., Durand, J. C., Jacquot, B., Fages, M., 2017. Dental biomaterials for chairside CAD/CAM: State of the art. J Adv. Prosthodont. 9, 486–495. https://doi.org/10.4047/jap.2017.9.6.486.

Lawn, B. R., Borrero, O., Huang, H., Zhang, Y., 2021. Micromechanics of machining and wear in hard and brittle materials. J. Am. Ceram. Soc. 104, 5–22. https://doi.org/10.1111/jace.17502.

Li, R. W. K., Chow, T. W., Matinlinna, J. P., 2014. Ceramic dental biomaterials and CAD/CAM technology: state of the art. J. Prosthodont. Res. 58, 208–216. https://doi.org/10.1016/j.jpor.2014.07.003.

Luthardt, R. G., Holzhüter, M. S., Rudolph, H., Herold, V., Walter, M. H., 2004. CAD/CAM-machining effects on Y-TZP zirconia. Dent. Mater. 20, 655–662. https://doi.org/10.1016/j.dental.2003.08.007.

Malkin, S., Hwang, T. W., 1996. Grinding mechanisms for ceramics. CIRP Ann. 45, 569–580. https://doi.org/10.1016/S0007-8506(07)60511-3.

Miyazaki, T., Hotta, Y., Kunii, J., Kuriyama, S., Tamaki, Y., 2009. A review of dental CAD/CAM: current status and future perspectives from 20 years of experience. Dent. Mater. J. 28, 44–56. https://doi.org/10.4012/dmj.28.44.

Miyazaki, T., Nakamura, T., Matsumura, H., Ban, S., Kobayashi, T., 2013. Current status of zirconia restoration. J. Prosthodont. Res. 57, 236–261. https://doi.org/10.1016/j.jpor.2013.09.001.

Peterson, I. M., Pajares, A., Lawn, B. R., Thompson, V. P., Rekow, E. D., 1998. Mechanical characterization of dental ceramics by Hertzian contacts. J. Dent. Res. 77, 589–602. https://doi.org/10.1177%2F00220345980770041201.

Piconi, C., Maccauro, G., 1999. Zirconia as a ceramic biomaterial. Biomaterials 20, 1–25. https://doi.org/10.1016/S0142-9612(98)00010-6.

Quinn, J. B., Sundar, V., Lloyd, I. K., 2003. Influence of microstructure and chemistry on the fracture toughness of dental ceramics. Dent. Mater. 19, 603–611. https://doi.org/10.1016/S0109-5641(03)00002-2.

Ritzberger, C., Apel, E., Höland, W., Peschke, A., Rheinberger, V. M., 2010. Properties and clinical application of three types of dental glass-ceramics and ceramics for CAD-CAM technologies. Mater. 3, 3700–3713. https://doi.org/10.3390/ma3063700.

Song, X.F., Yang, J.J., Ren, H.T., Lin, B., Nakanishi, Y., Yin, L., 2018. Ultrasonic assisted high rotational speed diamond machining of dental glass ceramics. Int. J. Adv. Manuf. Tech. 96, 387–399. https://doi.org/10.1007/s00170-017-1571-8.

Tesfay, H.D., Xu, Z., Li, Z.C., 2016. Ultrasonic vibration assisted grinding of bio-ceramic materials: an experimental study on edge chippings with Hertzian indentation tests. Int. J. Adv. Manuf. Tech. 86, 3483–3494. https://doi.org/10.1007/s00170-015-8326-1.

Wendler, M., Belli, R., Petschelt, A., Mevec, D., Harrer, W., Lube, T., Danzer, R., Lohbauer, U., 2017. Chairside CAD/CAM materials. Part 2: Flexural strength testing. Dent. Mater. 33, 99–109. https://doi.org/10.1016/j.dental.2016.10.008.

Xu, H. H., Jahanmir, S., Ives, L. K., 1997. Effect of grinding on strength of tetragonal zirconia and zirconia-toughened alumina. Mach. Sci. Technol. 1, 49–66. https://doi.org/10.1080/10940349708945637.

Xu, H. H., Smith, D. T., Jahanmir, S., 1996. Influence of microstructure on indentation and machining of dental glass-ceramics. J. Mater. Res. 11, 2325–2337. https://doi.org/10.1557/JMR.1996.0296.

Xu, W. X., Zhang, L. C., 2015. Ultrasonic vibration-assisted machining: principle, design and application. Adv. Manuf. 3, 173–192. https://doi.org/10.1007/s40436-015-0115-4.

Yan, J., Takahashi, H., Gai, X., Harada, H., Tamaki, J. I., Kuriyagawa, T., 2006. Load effects on the phase transformation of single-crystal silicon during nanoindentation tests. Mater. Sci. Eng. A 423, 19–23. https://doi.org/10.1016/j.msea.2005.09.120.

Yang, Z., Zhu, L., Ni, C., Ning, J., 2019. Investigation of surface topography formation mechanism based on abrasive-workpiece contact rate model in tangential ultrasonic vibration-assisted CBN grinding of ZrO2 ceramics. Int. J. Mech. Sci. 155, 66–82. https://doi.org/10.1016/j.ijmecsci.2019.02.031.

Zhang, Y., Lawn, B. R., 2019. Evaluating dental zirconia. Dent. Mater. 35, 15–23. https://doi.org/10.1016/j.dental.2018.08.291.

Chapter 2 Literature Review

This chapter reviews the microstructural-property-process relations of zirconia materials in digital dentistry. Firstly, the microstructures of zirconia materials are discussed. Then, the mechanical properties of these materials, such as hardness, Young's modulus, strength, and fracture toughness are summarized and, their microstructure-property relations are explained. Next, current dental computer-aided design/ manufacturing (CAD/CAM) and emerging processes applied in the manufacturing of zirconia materials are reviewed with respect to subsurface damage and surface quality. The machinability and brittleness indexes associated with the mechanical properties are also explored to reflect their property-processing relations. Finally, the challenges in digital dental manufacturing processes for zirconia materials are highlighted to guide the microstructural design of dental zirconia ceramics and optimization of the processing of zirconia restorations.

2.1 Introduction

Zirconia possesses high mechanical strength of 900–1200 MPa, fracture toughness of approximately 6 MPa $m^{1/2}$ and hardness of approximately 15 GPa, tooth-like color aesthetics and promising qualities of low affinity against bacterial plaque and good biocompatibility (ArRejaie et al. 2018; Denry and Kelly, 2008; Li et al., 2014; Schünemann et al. 2019; Zhang and Lawn; 2019). These properties are crucial in its applications in the biomedical industry, particularly make it suitable for dental restorative applications, such as implants, bridges, posterior and anterior crowns (Denry and Kelly, 2008; Li et al., 2014).

The history of zirconia materials from the first discovery to the evolution of the current usage in the dental industry (Hanawa, 2020) is described in Fig. 2.1. Zirconia was first discovered in 1789 (Hisbergues et al., 2009) and commenced its application as a refractory material in 1892 (Audley, 1917). In 1929 and 1937, stabilized and cubic zirconia materials were respectively developed (Hanawa, 2020). In 1952, magnesia-partially-stabilized zirconia was developed (Duwez et al., 1952). The application of zirconia as surgical implants in medicine commenced in 1969 (Helmer and Driskell,

1969). In 1975, partially-stabilised zirconia (PSZ) was developed, which revealed attractive fracture toughness and was considered as ceramic steel (Garvie et al., 1975). In 1977, yttria-stabilized tetragonal zirconia polycrystal (Y-TZP) was introduced, which contained yttria and 98% tetragonal zirconia phase and yielded superior mechanical strength of 690 MPa (Gupta et al., 1977). In 1985, Y-TZP was clinically used as a ball head of an artificial hip joint (Clarke et al., 2003). In 1989, glass-infiltrated zirconia-toughened alumina (ZTA) ceramic was developed (Wang and Stevens, 1989). In 2001, Y-TZP containing 3 mol% of yttria was clinically marketed as a dental restorative material, which had the advantage of superior aesthetic white color similar to human teeth. Since then, Y-TZP has become a major ceramic widely used in dentistry. Since 2006, Y-ZTP has also been used as dental implants and abutments (Hanawa 2020). Since 2016, novel translucent yttria partially stabilized zirconia (4Y-PSZ) has been developed, and has been further evolved in the forms of 5Y-PSZ and 6Y-PSZ as highly translucent materials for restorative dentistry (Zhang et al., 2016; Zhang and Lawn, 2018).

Zirconia has three main polymorph forms and it is influenced by surrounding temperature and pressure applied. Zirconia is monoclinic (m-ZrO_2) at the temperature below 1170 °C. Tetragonal zirconia (t-ZrO_2) is formed at the temperature of 1200–2370 °C and cubic zirconia (c-ZrO_2) is generated at the temperature above 2370°C (Hannink et al., 2000). Since zirconia must be used at room temperature, its fully cubic or partially tetragonal phase must be stabilized by alloying it with some metal oxides, such as yttria and magnesia (Denry and Kelly, 2008; Hannink et al., 2000). Therefore, stabilized zirconia materials applied in restorative dentistry include Y-TZP, which is commonly designated as zirconia; translucent (4Y-PSZ) and highly translucent (5Y-PSZ and 6Y-PSZ) zirconias; glass-infiltrated zirconia-toughened alumina (ZTA); and magnesia-partially-stabilized zirconia (Mg-PSZ).

In dental applications, zirconia restorations are expected to have high reliability and long longevity (Miura et al., 2021). However, they are subjected to load-bearing conditions in oral environments, which result in wear and fatigue damage in the restorations (Rekow at al., 2011). The complexity of small-scale contacts of zirconia restorations in their services requires a deep understanding of the microstructure-property relations of zirconia materials. Meanwhile, digital processing of zirconia restorations using dental computer-aided design/manufacturing (CAD/CAM) units involves abrasive machining processes

(Denry and Kelly, 2008; Miyazaki et al., 2009; 2013). These machining processes with sharp diamond or tungsten carbides tools inevitably induce surface and subsurface damage and produce poor surface integrity of zirconia restorations, leading to catastrophic fracture failures of the restorations in services (Alao et al., 2017; Anand et al., 2018; Denkena et al., 2017; Liu et al., 2022a). From the machining science perspective, the mechanical properties of a material determine its machining responses (e.g., a material with high hardness is deemed to be difficult to machine (Yin et al., 2006)). As zirconia mechanical properties are controlled by their microstructures, the success of zirconia restorations depends not only on the microstructures and mechanical properties but also on the processing-induced damage (Alao et al., 2017; Peterson et al., 1998; Quinn et al., 2003).

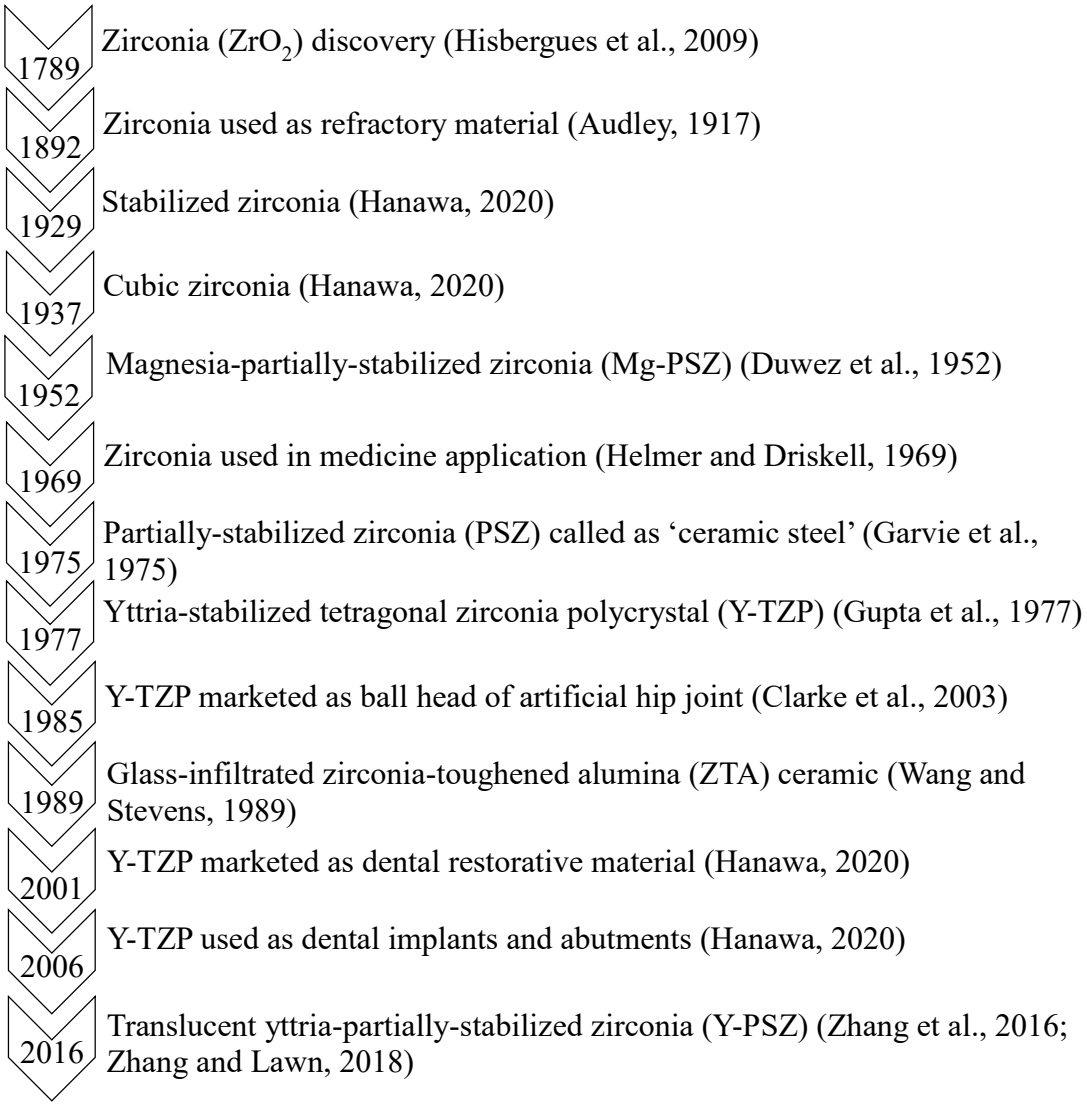

Fig. 2.1 History of zirconia materials.

However, the microstructure-property-processing relations for dental CAD/CAM zirconia materials have not yet been established. Therefore, this chapter aims to conduct a comprehensive review of zirconia materials to understand their microstructure-property-processing relations for dental restorations. The review is commenced with this introduction. Following is the description of the microstructures of dental CAD/CAM zirconia materials. Next, the mechanical properties of these zirconia materials are summarized, including their hardness, Young's moduli, mechanical strength, and fracture toughness. The zirconia materials microstructure-property relations are discussed. Then, digital CAD/CAM processing and emerging manufacturing processes, such as ultrasonic vibration-assisted machining, for zirconia materials are highlighted, particularly focusing on surface/subsurface damage and quality. The property-processing relations for zirconia materials are attempted using the brittleness and machinability indices associated with their mechanical properties. Finally, an outlook is provided to underline the critical challenges in zirconia restorations.

2.2 Microstructures of Zirconia Materials

Dental CAD/CAM zirconia materials include pre-sintered and sintered zirconias (Y-TZPs), translucent (4Y-PSZ) and highly translucent (5Y-PSZ and 6Y-PSZ) zirconias, and ZTA and Mg-PSZ (Denry and Kelly, 2008; Zhang and Lawn, 2018). Fig. 2.2 shows SEM micrographs of these zirconia microstructures. Table 2.1 summarizes the microstructural features of these materials based on zirconia crystal types, commercial names and manufacturers.

2.2.1 Pre-Sintered and Sintered Zirconias: Y-TZPs

Y-TZP comprises of a fully metastable tetragonal zirconia phase and yttria of approximately 2–5 mol.% (Elias et al., 2019). It has pre-sintered (Fig. 2.2(a)) and sintered (Fig. 2.2(b)) states, which pre-sintered state reveals porous microstructure with grain sizes of 0.15–0.3 μm and sintered states reveals dense microstructure with grain sizes of 0.2–1 μm, respectively. Y-TZP is most popular amongst zirconia materials and is the only zirconia system qualified for the ISO standards for surgical applications (Lughi and Sergo, 2010). This is due to its well-known transformation toughening mechanism through volumetric expansion of around 3–5% (Piconi and Maccauro, 1999). This mechanism operates as an opposite of a stress field that favours crack propagation, as

seen in Fig. 2.3 (Vagkopoulou et al., 2009). As a result, compressive stresses acting on a fracture tip hinder crack propagation, leading to an increased fracture toughness.

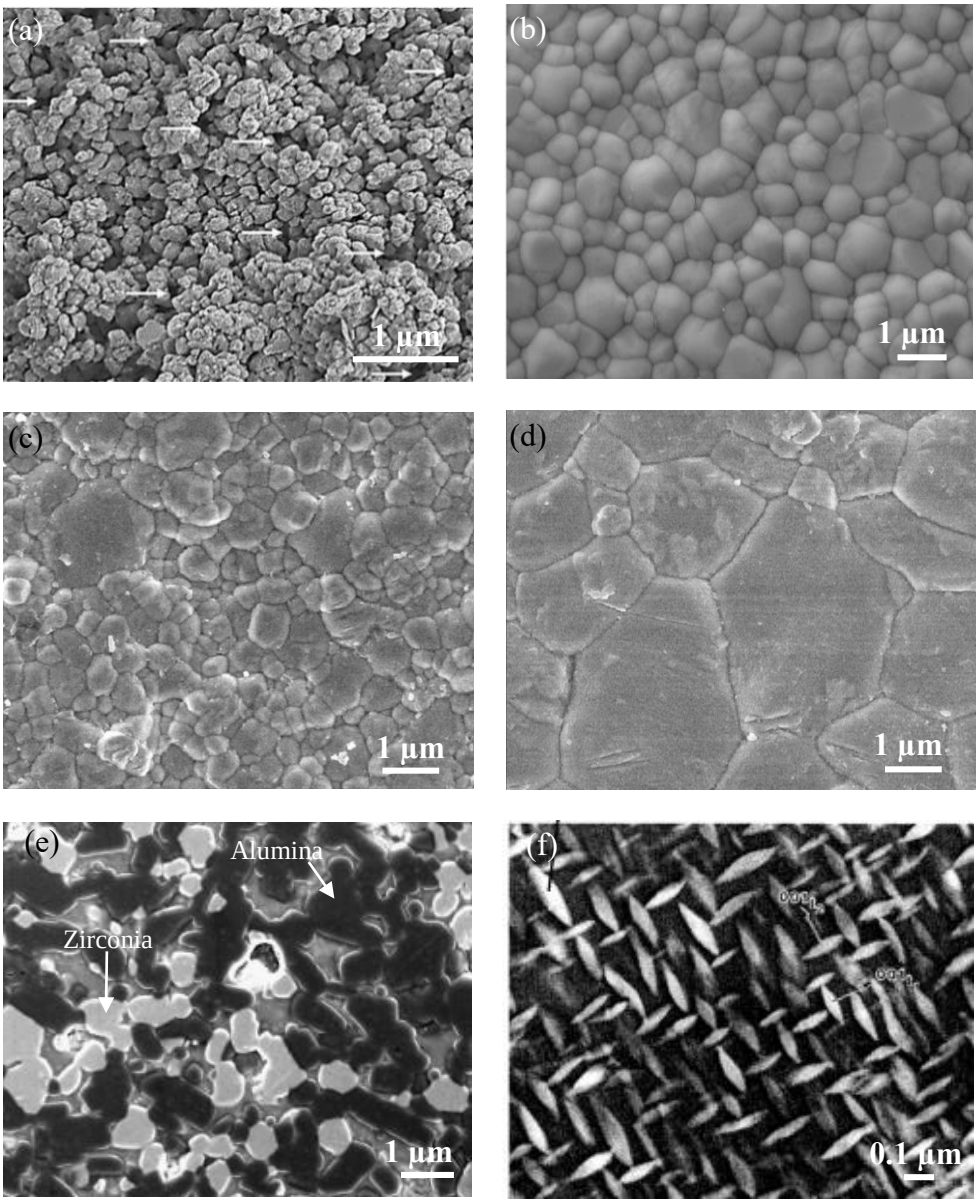

Fig. 2.2. SEM micrographs of microstructures of zirconia materials: (a) pre-sintered zirconia (Y-TZP) with pores indicated by white arrows (Anand et al., 2018), (b) sintered zirconia (Y-TZP) (Belli et al., 2017), (c) translucent zirconia (4Y-PSZ) (Inokoshi et al., 2018), (d) highly translucent zirconia (6Y-PSZ) (Inokoshi et al., 2018), (e) ZTA (Denry and Kelly, 2008) and (f) Mg-PSZ (Kelly and Denry, 2008).

Table 2.1. Microstructures of zirconia ceramic materials.

Material	Commercial Name	Manufacturer	Type	Microstructure
Pre-Sintered Zirconias: Yttria-Stabilized Tetragonal Zirconia Polycrystals (Y-TZP)	Inframat	Advanced Materials	3Y-TZP	Yttria-stabilized tetragonal zirconia polycrystalline with grain size of 0.1–0.2 μm, pre-sintered at 900°C[a].
	IPS e.max ZirCAD	Ivoclar-Vivadent	3Y-TZP	Yttria-stabilized tetragonal zirconia polycrystalline with grain size of 0.15–0.3 μm, pre-sintered at 850°C[b,c].
Sintered Zirconias: Yttria-Stabilized Tetragonal Zirconia Polycrystals (Y-TZP)	IPS e.max ZirCAD	Ivoclar-Vivadent	3Y-TZP	Yttria-stabilized tetragonal zirconia polycrystalline with grain size of 0.20–1.00 μm, sintered at 1550 °C[d].
	Zpex	Tosoh	3Y-TZP	Yttria-stabilized tetragonal zirconia polycrystalline with grain size of 0.17–0.40 μm, sintered at 1500°C[e].
	Lava Frame	3M ESPE	3Y-TZP	Yttria-stabilized tetragonal zirconia polycrystalline with grain size of 0.14–0.38 μm, sintered at 1400°C[f].
	Zenostar	Wieland Dental	3Y-TZP	Yttria-stabilized tetragonal zirconia polycrystalline with grain size of 0.20–0.62 μm, sintered at 1530°C[g].
Translucent Zirconias: Yttria-Partially-Stabilized Zirconia (4Y-PSZ)	Katana HT	Kuraray Noritake	4Y-PSZ	Yttria-partially-stabilized zirconia with grain size of 0.25–0.95 μm sintered at 1500°C[h].
	Zpex4	Tosoh	4Y-PSZ	Yttria-partially-stabilized zirconia with grain size of 0.6–0.74 μm sintered at 1450°C[i].
	Katana ML	Kuraray Noritake	4Y-PSZ	Yttria-partially-stabilized zirconia with grain size of 0.53–0.63 μm, sintered at 1500 °C[j].
Highly Translucent Zirconias: Yttria-Partially-Stabilized Zirconias (5Y-PSZ and 6Y-PSZ)	Zpex Smile	Tosoh	5Y-PSZ	Yttria-partially-stabilized zirconia with grain size of 0.55–1.2 μm, sintered at 1450 °C[h].
	Katana STML	Kuraray Noritake	5Y-PSZ	Yttria-partially-stabilized zirconia with grain size of 0.77–1.45 μm sintered at 1550 °C[h].
	Katana UTML	Kuraray Noritake	6Y-PSZ	Yttria-partially-stabilized zirconia with grain size of 1.35–2.07 μm sintered at 1550 °C[h].
Glass-Infiltrated Zirconia-Toughened Alumina (ZTA)	In-Ceram Zirconia	Vita Zahnfabrick	ZTA	Glass-infiltrated zirconia ceramic with large alumina grains of 6 μm long and 2 μm wide, small zirconia grains of less than 1 μm in diameter[k].
Magnesia-Partially-Stabilized Zirconia (Mg-PSZ)	Denzir M	Decim AB, Skellefteå, Sweden	Mg-PSZ	Magnesia-partially-stabilized zirconia with cubic grain sizes of 200 nm diameter and 75 nm thick, sintered at 1800 °C[l].

[a] Data from Amat et al., 2020
[b] Data from Alao and Yin, 2014a
[c] Data from Anand et al., 2018
[d] Data Belli et al., 2017
[e] Data from Zhang et al., 2016
[f] Data from Presenda et al., 2015
[g] Data from Elsaka, 2019
[h] Data from Inokoshi et al., 2018
[i] Data Liu et al., 2022b
[j] Data from Kolakarnprasert et al., 2019
[k] Data from Denry and Kelly, 2008
[l] Data from Kelly and Denry, 2008

Pre-sintered zirconia has 3% monoclinic and 97% tetragonal zirconia phases whereas sintered state has 100% tetragonal phase (Ritzberger et al., 2010). Pre-sintered and sintered zirconias are commercially produced by Advanced Materials, Ivoclar-Vivadent, Tosoh, 3M ESPE, and Wieland Dental. Pre-sintered zirconia is used in soft machining, in which the tool wear can be minimized. In general, pre-sintered zirconia was reported to have porosities of 47.3–49.3% (Ritzberger et al., 2010) and densities of 3.03–3.21 g/cm^3 (Ritzberger et al., 2010). Sintered zirconia after heat treatment at 1500–1550 ºC was reported to have porosities of < 0.5% (Ritzberger et al., 2010), and densities of 6.00–6.02 g/cm^3 (Ritzberger et al., 2010).

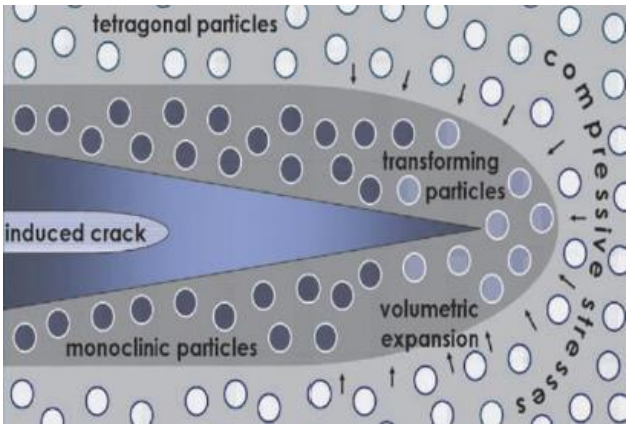

Fig. 2.3 Schematic representation of zirconia phase transformation toughening mechanism (Vagkopoulou et al., 2009).

2.2.2 Translucent 4Y-PSZ, and Highly Translucent 5Y-PSZ and 6Y-PSZ

For better aesthetics, zirconia materials with higher translucency were developed by increasing the yttria content in PSZs, leading to an increase in the volume fraction of the optically isotropic cubic phase in the material (Zhang and Lawn, 2018). The yttria addition ultimately augments the translucency of zirconias (Yan et al. 2018). Translucent (4Y-PSZ) zirconias containing roughly 6.6–7.1 wt% or 4 mol% of yttria (Inokoshi et al., 2021; Too et al., 2021) are commercially available as Katana HT (Kuraray Noritake) and Zpex (Tosoh). They have 41.7–50.0% tetragonal, 50.0–57.3% cubic, and 0.8% monoclinic zirconias (Inokoshi et al., 2021). 4Y-PSZ materials are generally sintered at temperatures of 1450 °C and 1500 °C, yielding compact zirconia structures with grain sizes of less than 1 μm as shown in Fig. 2.2(c) (Inokoshi et al., 2018).

Highly translucent (5Y-PSZ and 6Y-PSZ) materials contain approximately 8.9–10.8 wt% yttria or 5–6 mol% of yttria (Inokoshi et al., 2021; Too et al., 2021). They are generally used in monolithic, multi-layered (ML), super translucent multi-layered (STML), and ultra-translucent multi-layered (UTML) zirconia systems (Kuraray Noritake). These materials (e.g., Zpex Smile, Tosoh) have 30.0–39.5% tetragonal, 59.9–70.0% cubic and 0.4% monoclinic zirconias in STML and 25.0–28.9% tetragonal, 70.6–75.0% cubic and 0.2% monoclinic zirconias in UTML (Inokoshi et al., 2021). As highly translucent zirconias consist of substantial quantities of cubic zirconia and reduced alumina content, these materials are hydrothermally stable due to the insufficient c-m phase transformation (Inokoshi et al. 2018). 5Y-PSZ and 6Y-PSZ materials are sintered at temperatures of 1450 °C and 1550 °C, producing coarse zirconia structures with zirconia grain sizes of larger than 2 μm, as shown in Fig. 2.2(d) (Inokoshi et al., 2018).

2.3 ZTA and Mg-PSZ

ZTA consuming the excellent properties of alumina and zirconia, has been extensively investigated in dental and orthopaedic applications (Denry and Kelly, 2008; Guazzato et al., 2002; 2004; Ponnilavan et al. 2019). The toughening mechanism possessed by tetragonal zirconia in ZTA helps to lessen crack propagations, which usually occur as a result of the brittleness of alumina (Ponnilavan et al. 2019). This t-m phase transition in ZTA is commonly present in surrounding areas of zirconia grains at crack regions (Ponnilavan et al. 2019). Therefore, the fracture transformation toughening in ZTA is due to the existence of surplus tetragonal zirconia at room temperature (Ponnilavan et al. 2019). Commercially available ZTA for dental restoration is In-Ceram Zirconia (Vita Zahnfabrik), which is an interpenetrating composite of 30% glass and 70% polycrystalline alumina-zirconia with 70/30 vol.% ratio (Kelly and Denry, 2008). Further, sintered ZTA has high porosities of 8–11% (Guazzato et al., 2003). The microstructure of the ZTA (Fig. 2.2(e)) has larger alumina grains of approximately 2.5 μm and smaller zirconia grains of approximately 1.3 μm (Borba et al., 2011).

Mg-PSZ was created using 8–10 mol% magnesia as a stabilizing ingredient in zirconia (Hannik et al., 2000), which causes tetragonal precipitates to develop a cubic zirconia matrix, resulting in partially stabilized zirconia (Piconi et al., 2014). There may be monoclinic and tetragonal phases in Mg-PSZ. The materials are more resistant to low-temperature aging than Y-TZP (Masaki, 1986; Roy et al., 2007), which is unique in the

zirconia family. However, Mg-PSZ materials have not been successfully used in biomedical applications due to their residual porosities and large grain sizes that lead to wear (Piconi and Maccauro, 1999). Fig. 2.2(f) shows the Mg-PSZ microstructure, consisting of lensed grain shapes of 200 nm diameter and 75 nm thickness (Kelly and Denry, 2008). In addition, Mg-PSZ materials must be sintered at a high temperature of 1800°C using specific furnaces (Piconi and Maccauro, 1999). Further, the formation of metastable tetragonal precipitates during cooling, particularly during the aging stage, necessitates a strict control of the cooling cycle in terms of the temperatures and durations (Piconi and Maccauro, 1999). An example of Mg-PSZ currently available for dental restoration is Denzir M (Denry and Kelly, 2008).

In comparison of all zirconia materials in Fig. 2.2, ZTA (Fig. 2.2(e)) and Mg-PSZ (Fig. 2.2(f)) have entirely different microstructures from Y-TZP (Figs. 2.2(a) and 2.2(b)), 4Y-PSZ (Fig. 2.2(c)) and 6Y-PSZ (Fig. 2.2(d)) with round grains. Pre-sintered Y-TZP (Fig. 2.2(a)) has the finest grains and highest porosity. Sintered Y-TZP (Fig. 2.2(b)) and translucent 4Y-PSZ (Fig. 2.2(c)) have similar grain shapes and sizes whereas highly translucent 6Y-PSZ (Fig. 2.2(d)) has relatively larger grain sizes.

2.3 Mechanical Properties of Zirconia Materials

The mechanical properties of zirconia materials are largely influenced by their microstructures (Alao et al., 2017; Peterson et al., 1998; Quinn et al., 2003). They control the materials' machinability and surface quality in processing (Alao et al., 2017; Yin et al., 2003), which determine the functionality of zirconia materials, such as wear (Nagarajan and Jahanmir, 1996), and fatigue performance (Zhang and Lawn, 2019). Therefore, it is important to understand their mechanical properties influenced by their microstructures, including hardness, Young's modulus, fracture toughness, and strength. Table 2.2 summarizes the mechanical properties of zirconia materials based on their microstructures outlined in Table 2.1.

Table 2.2. Mechanical properties of zirconia materials.

Material	Commercial Name	Manufacturer	Hardness (GPa)	Young's modulus (GPa)	Flexural Strength (MPa)	Fracture Toughness (MPa $m^{1/2}$)
Pre-Sintered Zirconias: Yttria-Stabilized Tetragonal Zirconia Polycrystals (Y-TZP)	Inframat	Advanced Materials	0.7–1.3[a]			2.4–2.8[a]
	IPS e.max ZirCAD	Ivoclar-Vivadent	0.8–1.5[b]	24–34[b]	50–90[c]	0.7–0.8[d]
Sintered Zirconias: Yttria-Stabilized Tetragonal Zirconia Polycrystals (Y-TZP)	IPS e.max ZirCAD	Ivoclar-Vivadent	11.0–14.3[e,f]	202–210[g]	900–1300[c,h]	5.5–5.7[c,i]
	Zpex	Tosoh	12.7–13.6[j]	200–210[k]	924–1051[j]	3.7–7.9[j,l]
	Lava Frame	3M ESPE	9.7–15.0[m,n]	200–210[k]	920[m]	4.3–7.5[n,o]
	Zenostar	Wieland Dental	11.0[m]	200–210[k]	800–1133[m]	4.4–5.0[p]
Translucent Zirconias: Yttria-Partially-Stabilized Zirconia (4Y-PSZ)	Katana HT	Kuraray Noritake	12.3–13.9[q]	200–210[k]	1194–1207[r,s]	3.5–4.5[k]
	Zpex4	Tosoh		200–210[k]	725–833[t]	3.5–4.5[k]
	Katana ML	Kuraray Noritake		200–210[k]	866–1130[r]	3.5–4.5[k]
Highly Translucent Zirconias: Yttria-Partially-Stabilized Zirconias (5Y-PSZ and 6Y-PSZ)	Zpex Smile	Tosoh	13.6–14.2[j]	200–210[k]	400–660[j,k]	2.2–3.5[k]
	Katana STML	Kuraray Noritake	12.9–13.1[u]	200–210[k]	486–829[k,u]	2.5–2.7[k,u]
	Katana UTML	Kuraray Noritake	12.8–13.5[v,w]	200–210[k]	465–600[v,w]	2.2–2.7[k]
Glass-Infiltrated Zirconia-Toughened Alumina (ZTA)	In-Ceram Zirconia	Vita Zahnfabrick	10.2–11.9[x,y]	236–252[x,y]	476–688[x,y,z]	3.6–5.3[x,y,z]
Magnesia-Partially-Stabilized Zirconia (Mg-PSZ)	Denzir M	Decim AB, Skellefteå, Sweden	11.0–12.5[ii,iii]	210[iii]	400–650[iii]	8.0–11.0[ii,iii]

[a] Data from Amat et al., 2020
[b] Data from Alao and Yin, 2014a
[c] Data from Ritzberger et al., 2010
[d] Data from Alao and Yin, 2016; Anand et al., 2018
[e] Data from Inokoshi et al., 2014; Alao and Yin, 2014b
[f] Data from Shi et al., 1998
[g] Data from Belli et al., 2017
[h] Data from Wendler et al., 2017
[i] Data from Belli et al., 2018
[j] Data from De Araújo-Júnior et al., 2020
[k] Data from Zhang and Lawn, 2018
[l] Data from Zhang et al., 2016
[m] Data from Zhuang et al., 2019
[n] Data from Presenda et al., 2015
[o] Data from Marinis et al., 2013
[p] Data from Elsaka, 2019
[q] Data from Eldafrawy et al., 2018
[r] Data from Choi et al., 2020
[s] Data from Kwon et al., 2018
[t] Data from Liu et al., 2022b
[u] Data from Cokic et al., 2020
[v] Data from Nakamura et al., 2022
[w] Data from Camposilvan et al., 2018
[x] Data from Guazzato et al., 2002
[y] Data from Guazzato et al., 2004
[z] Data from Yilmaz et al., 2007
[ii] Data from Sundh and Sjögren, 2006
[iii] Data from Piconi et al., 2014

2.3.1 Hardness

Hardness is a measure of a material's resistance to localized deformation (Quinn and Quinn, 1997). Indentation testing is commonly used to measure hardness properties, which involves the application of a certain force to an indenter on a material surface. The hardness is assessed through microscopic measurement of the indented area or indentation width (Mukhopadhyay and Paufler, 2006). Various types of indentation testing have been conducted on zirconia materials at different length scales using spheres or sharp-tip indenters under different load conditions (Mukhopadhyay and Paufler, 2006).

Fig. 2.4 shows the hardness of zirconia materials based on the values shown in Table 2.2. Pre-sintered Y-TZP has the lowest hardness of 0.7–1.5 GPa (Alao and Yin, 2014a; Amat et al., 2020) while sintered Y-TZP materials have the hardness in the range of 9.7–15.0 GPa (Alao and Yin, 2014b; Inokoshi et al., 2014; Presenda et al., 2015; Shi et al., 1998; Zhuang et al., 2019), depending on the manufactures and sintering conditions. The hardness values for translucent 4Y-PSZ and highly translucent 5Y-PSZ and 6Y-PSZ are very close, in the range of 12.3–14.2 GPa (De Araújo-Júnior et al., 2020; Camposilvan et al., 2018; Cokic et al., 2020; Eldafrawy et al., 2018; Nakamura et al., 2022). ZTA and Mg-PSZ have the similar hardness, in the range of 10.2–12.5 GPa (Guazzato et al., 2002; 2004; Piconi et al., 2014; Sundh and Sjögren, 2006; Yilmaz et al., 2007), softer than translucent and highly translucent materials.

The lowest hardness for pre-sintered Y-TZP is associated with its weak bonding between zirconia crystals due to its high porosity (47.3–49.3%) and low density (Anand et al., 2018; Monaco et al., 2013; Ritzberger et al., 2010). The low pre-sintering temperature of approximately 900–1100 ^{o}C for the material (Amat et al., 2020) produces an interconnected microstructure (Fig. 2.2(a)), which can be easily broken under loading. The high hardness values for sintered Y-TZP, translucent and highly translucent materials are attributed to their low porosities (< 0.5) and high densities (Monaco et al., 2013; Ritzberger et al., 2010). This is because sintering at high temperatures of approximately 1500 ^{o}C significantly densify zirconia microstructures (Inokoshi et al., 2014). This also indicates that the higher densification of zirconia microstructures lead to higher resistances to deformation. The lower hardness for ZTA may be attributed to its higher porosity of approximately 8–11% compared with sintered Y-TZP (Guazzato et al., 2004).

Further, ZTA contains roughly 30% glass, which contributes to the lower hardness value (Guazzato et al., 2004).

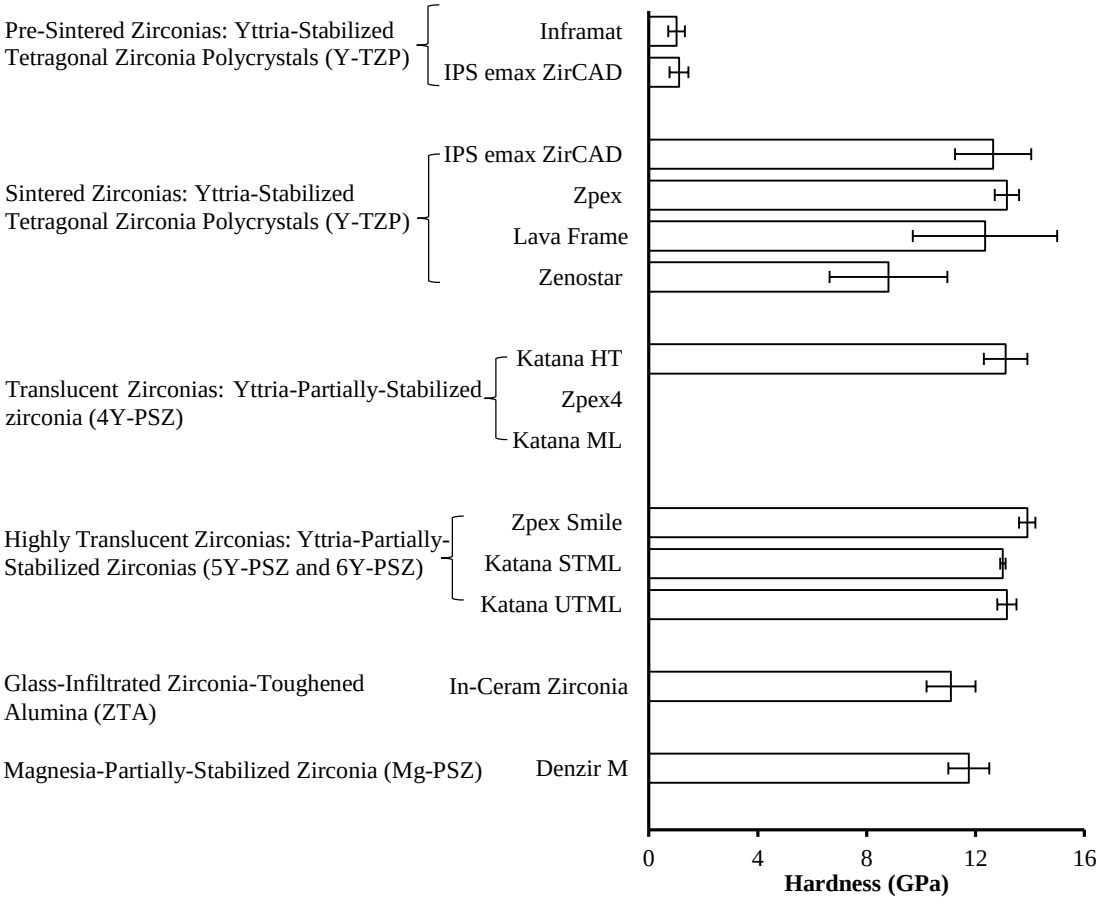

Fig. 2.4 Hardness of zirconia materials based on the values in Table 2.2.

2.3.2 Young's Modulus

Young's modulus is a measure of a material's linear elasticity, which can be obtained from either stress-strain diagrams in tensions or compressions, or force-displacement curves in indentation. Fig. 2.5 shows the Young's moduli of zirconia materials based on the values shown in Table 2.2. Pre-sintered Y-TZP materials have the lowest Young's moduli of 24–34 GPa (Alao and Yin, 2014a). Sintered Y-TZP materials have much higher moduli of 200–210 GPa, depending on the sintering conditions (Belli et al., 2017; Zhang and Lawn, 2018). The moduli for translucent 4Y-PSZ and highly translucent 5Y-PSZ and 6Y-PSZ have the same range of 200–210 GPa (Zhang and Lawn, 2018). ZTA has the highest moduli of 236–252 GPa (Guazzato et al., 2002; 2004) among the zirconia

materials. Mg-PSZ shared the high end of moduli of translucent and highly translucent zirconia materials, with 210 GPa (Piconi et al., 2014).

In comparison of all zirconia moduli in Fig. 2.5, the lowest Young's modulus of pre-sintered Y-TZP is attributed to its porous microstructure, which can be easily deformed under loading. All sintered Y-TZP, translucent 4Y-PSZ and highly translucent 5Y-PSZ and 6Y-PSZ, and Mg-PSZ share the same scales of modulus values, which indicate yttria and magnesia additions in zirconia microstructures do not alter the elastic behaviour of the materials. In contrast, glass infiltration in ZTA has resulted in the highest Young's modulus for ZTA.

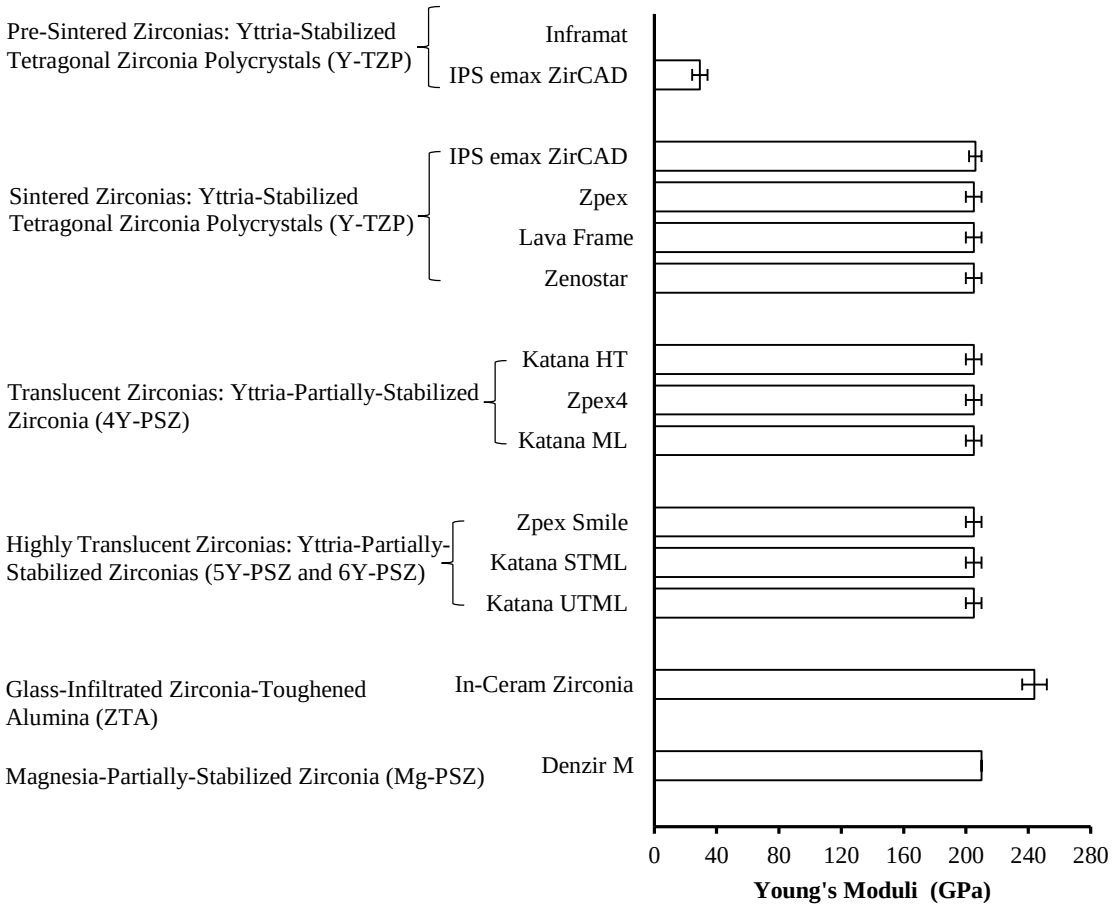

Fig. 2.5 Young's moduli of zirconia materials based on the values in Table 2.2.

2.3.3 Flexural Strength

Ceramic strength is generally defined as flexural strength measured in three-point or four-point bending, representing the maximum surface stress in the bent at the instant of failure

(Callister, 2007). Fig. 2.6 shows the flexural strength of zirconia materials based on the values in Table 2.2. As expected, pre-sintered Y-TZP has the lowest strength of 50–90 MPa (Ritzberger et al., 2010). Sintered Y-TZP materials have significantly higher strength than pre-sintered state (ANOVA, $p < 0.05$), in the range of 800–1300 GPa (De Araújo-Júnior et al., 2020; Ritzberger et al., 2010; Wendler et al., 2017; Zhuang et al., 2019), depending on the manufacturer, sintering conditions and measuring techniques. Translucent 4Y-PSZ materials have slightly less strong than sintered Y-TZP, with the strength of 725–1207 MPa (Choi et al., 2020; Liu et al., 2022b; Kwon et al., 2018). Highly translucent 5Y-PSZ and 6Y-PSZ materials are much weaker than translucent 4Y-PSZ, with the strength of 400–829 MPa (Camposilvan et al., 2018; Cokic et al., 2020; De Araújo-Júnior et al., 2020; Nakamura et al., 2022; Zhang and Lawn, 2018). ZTA with the strength of 476–688 MPa (Guazzato et al., 2002; 2004; Yilmaz et al., 2007), slightly stronger than Mg-PSZ with 400–650 MPa (Piconi et al., 2014), both of which are quite similar to the strength for highly translucent zirconia materials.

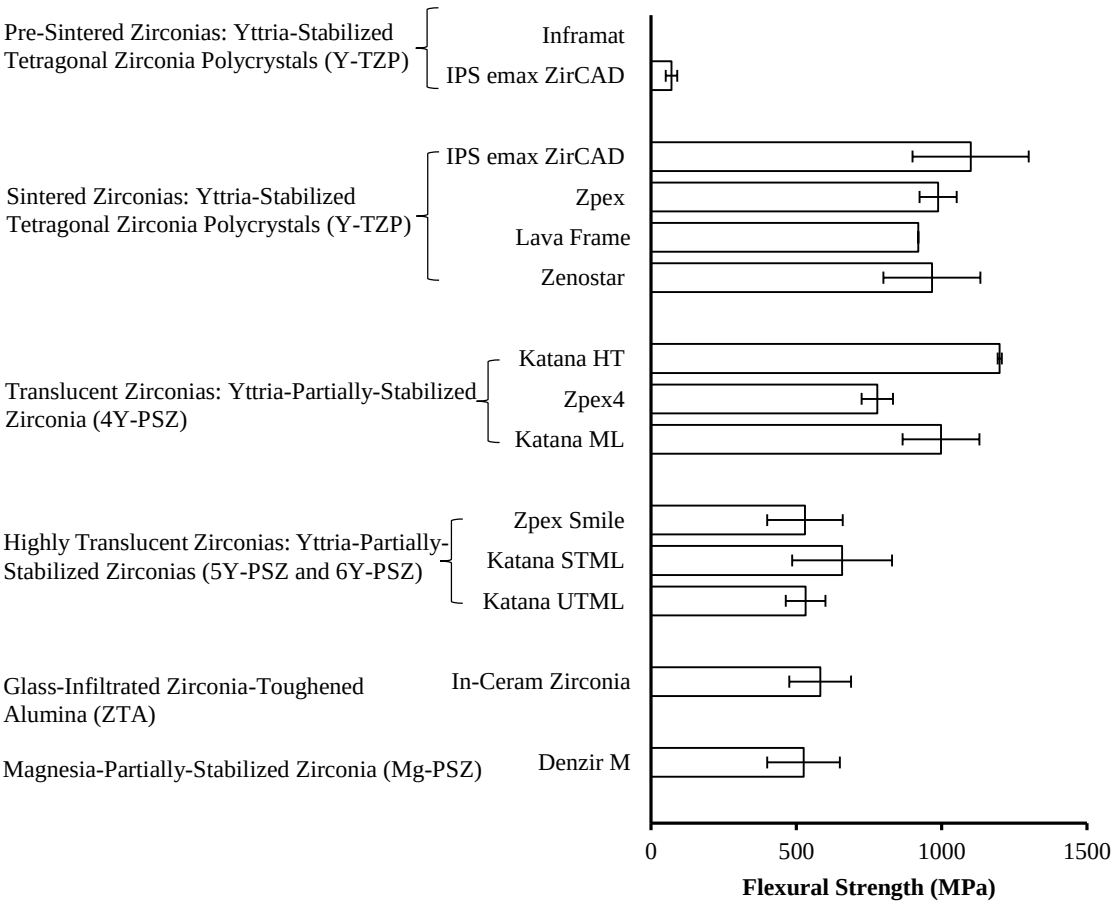

Fig. 2.6 Flexural strength of zirconia materials based on the values in Table 2.2.

The highly porous and weak bonding of zirconia crystals unavoidably yield the lowest strength for pre-sintered Y-TZP. The significantly lower strength of the highly translucent 5Y-PSZ and 6Y-PSZ compared with sintered Y-TZP may be attributed to the tetragonal-cubic (t-c) phase transition in zirconia microstructures. If the tetragonal phase is over-stabilized, it prevents the advantageous transformation toughening effect (Camposilvan et al., 2018), producing the low strength. A high volume tetragonal phase may yield a high strength while a high volume monoclinic phase results in lower strength (Kelly and Denry, 2008). This could partially explain the different strength values amongst the zirconia material. The higher monoclinic phase in sintered Mg-PSZ (64.22%) in comparison with sintered Y-TZP (0.85%) may explain the lower strength for the former than the latter (Soylemez et al., 2020).

2.3.4 Fracture Toughness

Fracture toughness measures the resistance of a material to the propagation of a crack (Homaei et al. 2016). It is determined by measuring the tensile stress at which a deliberately introduced crack in a material propagates under loading (Callister, 2007) or by indentation techniques, which may provide higher values than the former (Amat et al., 2020). Fig. 2.7 shows the fracture toughness of zirconia materials based on the values in Table 2.2. Pre-sintered Y-TZP has the lowest toughness of 0.7–0.8 MPa $m^{1/2}$ (Alao and Yin, 2016; Anand et al., 2018) while the indentation-measured values reach 2.4–2.8 MPa $m^{1/2}$ (Amat et al., 2020). Sintering Y-TZP materials have significantly higher fracture toughness up to 7.9 MPa $m^{1/2}$ (De Araújo-Júnior et al., 2020; Zhang et al., 2016) than pre-sintered state. However, the improved translucency reduces the fracture toughness, particularly for highly translucent zirconia (5Y-PSZ and 6Y-PSZ) materials in comparison with sintered Y-TZP (Fig. 2.7 and Table 2.2). ZTA has the same scale of the fracture toughness as translucent 4Y-PSZ, higher than highly translucent 5Y-PSZ and 6Y-PSZ but lower than sintered Y-TZP. Mg-PSZ has the highest toughness of 8–11.0 MPa $m^{1/2}$ (Piconi et al., 2014; Sundh and Sjögren, 2006).

The lowest fracture toughness for pre-sintered Y-TZP is attributed to its porous microstructure because pores act as a source of flaws (Rice, 1984) and may form sharp cracks that propagate through zirconia crystal boundaries. As porosities in sintered Y-ZTP materials are dramatically reduced, the materials become much tougher. For translucent 4Y-PSZ and highly translucent 5Y-PSZ and 6Y-PSZ, their lower fracture

toughness may also result from the lower beneficial influence of the transformation toughening mechanism (Cokic et al., 2020). ZTA has the lower fracture toughness than sintered Y-TZP may be attributed to the glassy matrix. The highest toughness for Mg-PSZ may be resulted from its nanoscale microstructure with lensed grain shapes of dimensions less than 200 nm (Kelly and Denry, 2008).

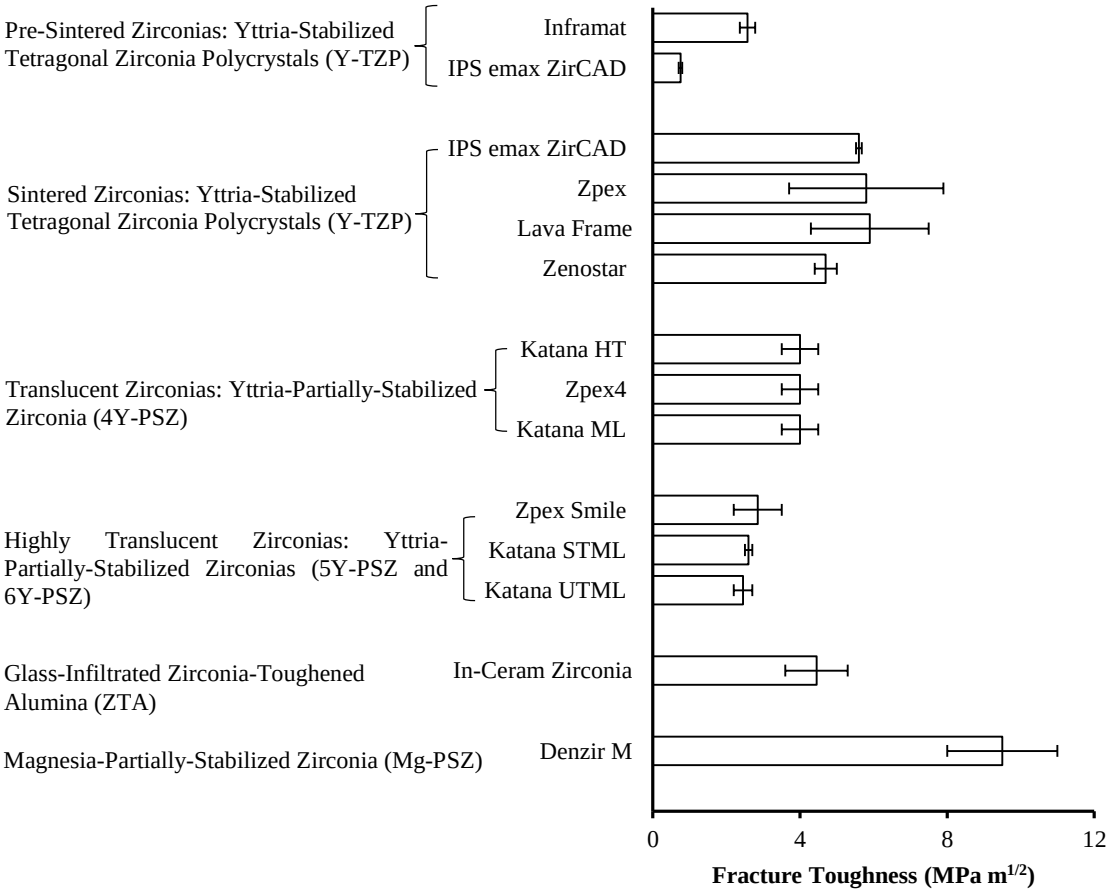

Fig. 2.7 Fracture toughness of zirconia materials based on the values of Table 2.2.

In comparison of all mechanical properties of zirconia materials shown in Table 2.2 and Figs. 2.4–2.7, the differences in their values are the results of the different compositions and microstructures. For instance, yttria addition not only ultimately augments the translucency of zirconias but also alters the mechanical strength (Fig. 2.6) and toughness (Fig. 2.7) of the materials (Yan et al. 2018). Glass infiltration in zirconias also make the materials less tough (Fig. 2.6) and strong (Fig. 2.7), but stiffer (Fig. 2.5). Magnesia addition enables zirconia to achieve the highest toughness (Fig. 2.7) but fails to make the strongest (Fig. 2.6). Highly porous pre-sintered zirconias reveal the poorest mechanical

properties because of their interconnected porous structures. All these properties play a key role in processing of zirconia materials.

2.4 Processing of Zirconia Materials

Zirconias must be shaped and processed using abrasive machining for their applications. Abrasive shaping of the material depends on their microstructures and mechanical properties. In general, pre-sintered zirconias with weak mechanical properties are shaped in soft machining first. The shaped materials are then sintered at high temperatures for densification and mechanical strengthening. However, sintering unavoidably induces shrinkages, which jeopardize accuracies of shapes and dimensions of zirconia restorations. Thus, hard machining of sintered zirconias is also practised using high-precision and high-stiffness machines, which is much more expensive than soft machining. As both soft and hard machining processes induce surface and subsurface damage to zirconia materials, surface and subsurface quality is a major issue in digital dentistry. Thus, it is critical to establish the property-processing relations for zirconia materials with respect to their machinability and brittleness determining their surface quality. To improve current CAD/CAM machining technologies in dentistry, some emerging manufacturing techniques, such as ultrasonic vibration-assisted machining, are being investigated.

2.4.1 Current CAD/CAM Machining

2.4.1.1 Digital Fabrication Processes

Dental CAD/CAM technology was developed in 1980 for the digital fabrication of restorative materials (Miyazaki et al., 2009). Since then, the technology has been improved and is capable of fabricating dental restorations from inlays, onlay, veneers, full-coverage crowns, and multi-unit bridges. Current CAD/CAM procedures for fabrication of dental fixed partial dentures shown in Fig. 2.8, consist of six parts, i.e., scanning, 3D reconstruction, CAD process, fabrication of numerical control (NC) data, CAM process, and post treatment (such as staining and grazing) (Beuer, 2008; Miyazaki et al., 2009; 2013). An oral impression of a diseased section is made through a digitization scanner that transforms the restoration geometry into 3D reconstruction of dentitions on a computer (Beuer, 2008; Miyazaki et al., 2013). Then, CAD software processes the

reconstruction data for the restoration design (Beuer, 2008; Miyazaki et al., 2013). Afterwards, NC data for machining paths need to be setup based on the CAD data (Beuer, 2008; Miyazaki et al., 2013). Next is the CAM processing of the restorative material to form the desired restoration shape (Beuer, 2008; Miyazaki et al., 2013). Finally, the post heat treatments, such as sintering, glazing, and staining, must be completed (Miyazaki et al., 2013). There are several commercial dental CAD/CAM systems are available, which can be used in dental laboratories or clinics as directly chairside systems or via centralized fabrication centres (Beuer, 2008; Miyazaki et al., 2009).

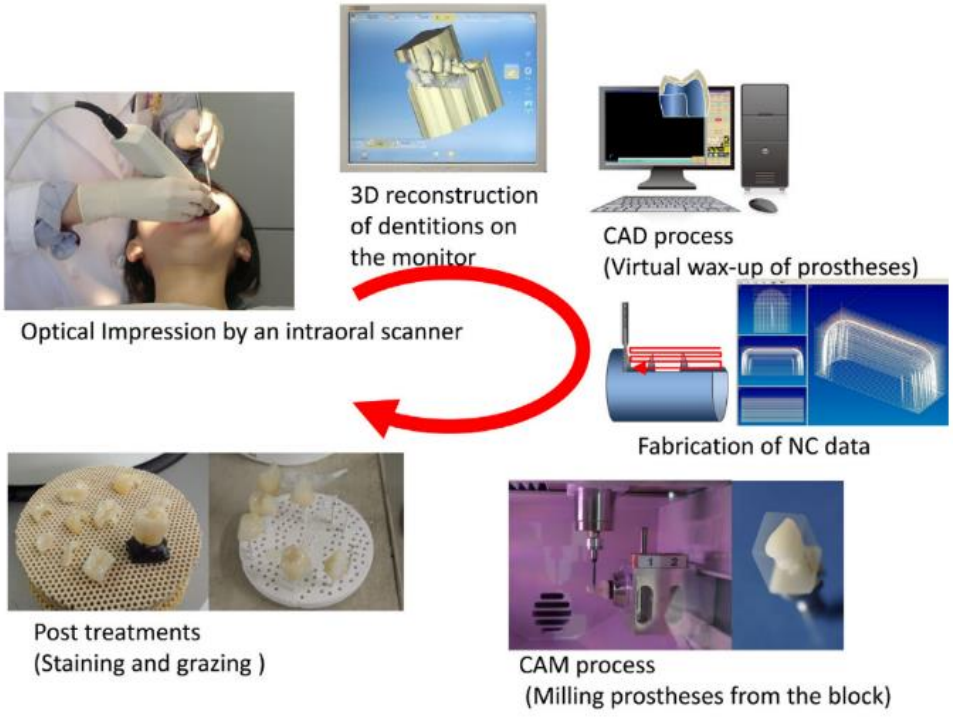

Fig. 2.8. Digital fabrication flow of fixed dental partial (Miyazaki et al., 2013).

4.1.2 Machinability Index

The material machinability measures the difficult degree of the material in abrasive machining processes. It is relevant to manufacturing costs and surface quality and determines the product performance. The machinability index *M* associated with the mechanical properties derived based on machining forces is expressed as (Song et al. 2016) as:

$$M = (K_{IC}^{\frac{4}{9}} H^{\frac{5}{9}})/(E/H)^{32/45} \quad (2.1)$$

where K_{IC} is the fracture toughness, H is the hardness and E is the Young's modulus. The higher the index ices, the more difficult and challenging it is for the material to be machined.

Fig. 2.9 shows the calculated machinability indices M for zirconia materials based on the average values of the mechanical properties in Table 2.2. Pre-sintered Y-TZP had the lowest machinability index with M of 5.8 MPa $m^{2/9}$. The machinability indices for sintered Y-TZP materials are significantly higher than pre-sintered Y-TZP materials. ZTA and some of highly translucent 5Y-PSZ and 6Y-PSZ materials have the indices of less than 50 MPa $m^{2/9}$. Sintered Y-TZP materials have the indices of approximately 34–63 MPa $m^{2/9}$. Mg-PSZ has the highest machinability index of 65 MPa $m^{2/9}$. These indices indicate that Mg-PSZ is the most difficult to machine and pre-sintered Y-TZP material is the easiest to machine, and other sintered Y-TZP, translucent 4Y-PSZ, highly translucent 5Y-PSZ and 6Y-PSZ, ZTA materials are intermediated between the two types of zirconia materials.

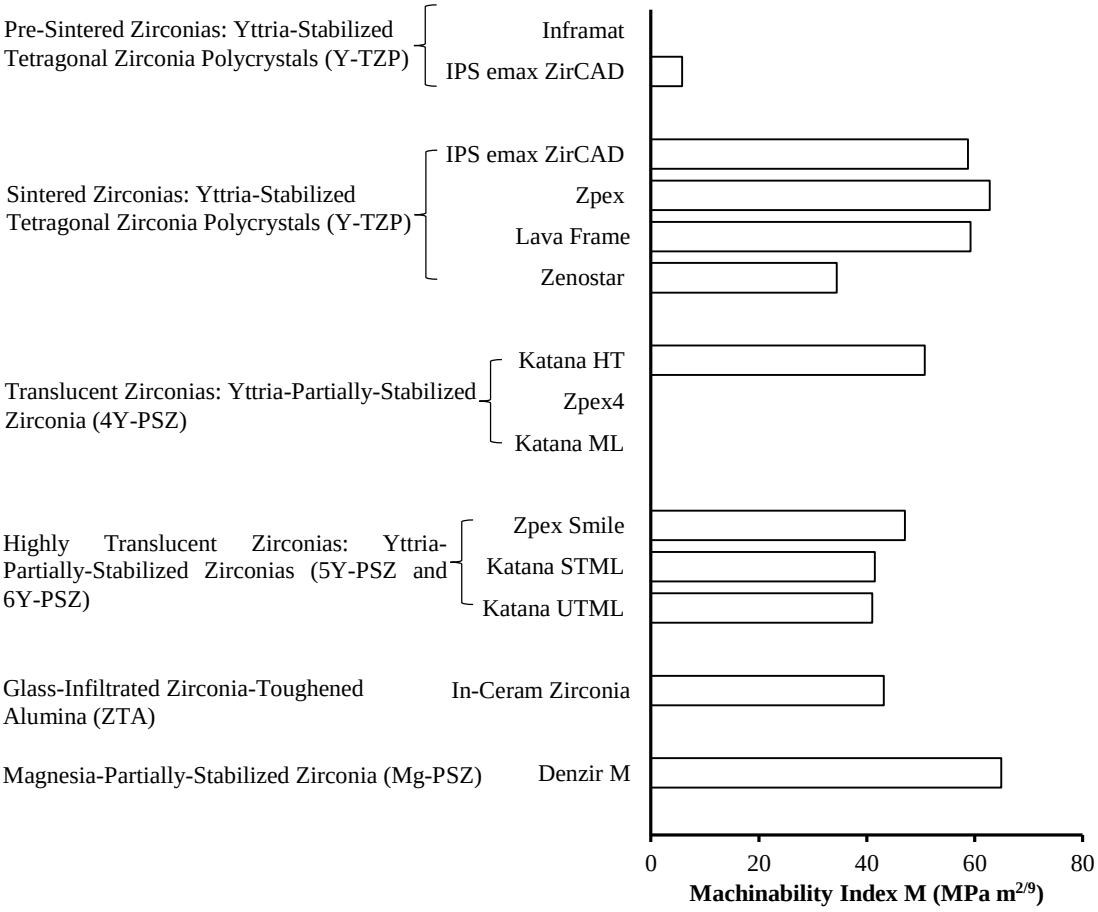

Fig. 2.9 Machinability index of zirconia materials determined by the average values in Table 2.2.

2. 4.2 Surface and subsurface quality

2. 4.2.1 Surface quality

The surface quality of the dental restoration is of utmost importance as it has a major impact on bacterial plaque build-up, color changes, wear, and the aesthetical representation of both indirect and direct restorations (Morgan 2004). Moreover, the patient can feel discomfort if a change in the order of 0.3 μm of surface roughness occurs; thus, a smooth surface can give the best restoration for patient's desires (Jones et al. 2004). Furthermore, increasing deposition of bacterial plaque is highly related to the high surface roughness of the restoration and it is a deciding factor in staining (Heintze et al. 2006). Consequently, achieving the lowest surface roughness on a fabricated dental material surfaces are the ongoing research of scholarly researchers. Surface quality is dependent on the material microstructure and mechanical properties.

In dental CAD/CAM milling of pre-sintered zirconia (Y-TZP), Alao et al. (2017) reported the machined surface had a very rough surface with severe fractures and cracks compared with sintered zirconia. This was due to the higher mechanical properties of sintered zirconia providing resistance to milling-induced damage (Alao et al., 2017). The grinding of pre-sintered zirconia, reveals the ground material surface had micro brittle fractures and surface cracks when it was grinded in both dry and wet conditions (Anand et al., 2018). Denkena et al. (2017) found that surface fractures in sintered zirconia due to machining flaws, along with phase transformation, thermal and residual stresses. High-speed grinding of yttria-stabilized zirconia (YSZ) reveals average surface roughness R_a of 2–4 μm at 100–200 μm down \feed, 0.5–2 m/min work speed, and 40–200 m/s wheel speed (Patidar et al., 2021). The ground yttria-stabilized zirconia (YSZ) surfaces reveal micro brittle fractures but it appears to be smoother than the alumina ground surfaces, which is due to the higher mechanical properties of YSZ compared with alumina (Patidar et al., 2021). These studies show that the reported zirconia machined surfaces are rough, and the mode of removal is a brittle fracture. This requires further advancement of the machining process to acquire a ductile mode or green machining of zirconia materials to produce a smooth high surface quality for zirconia restorations.

2.4.2.2 Subsurface Damage

Even though zirconia materials have excellent mechanical properties, their inherent brittleness nature is a challenge in the dental CAD/CAM abrasive machining process. The abrasive machining process involves the mechanical action of numerous diamond abrasives indenting, scratching, and removing a layer of the material surface. These mechanical actions inevitably induce severe surface and subsurface damage to the zirconia (Anand et al., 2018; Denkena et al., 2017). Subsurface damage has been reported to significantly influence the strength (Guazzato et al., 2005; Xu et al., 1997), fracture behaviour (Passos et al., 2015), toughness (Xu et al., 1997), and wear performance (Mitov et al., 2012) of zirconia restorations. Manual polishing is required to remove such damage, but it is a time-consuming and expensive process. Hence, subsurface damage in zirconia materials has become a huge obstacle in securing high productivity and service lifetime.

Edge chipping damage represents a critical type of surface and subsurface damage as it has a profound clinical impact on the mechanical functionality and reliability of zirconia restorations (Schmitter et al., 2012), resulting in restoration failure (Triwatana et al., 2012). Whilst, grinding sintered zirconia ceramic at 1.75–3.51 $\times 10^{-4}$ s^{-1} strain rates, extensive subsurface damage depths ranging from 20–85 µm were reported (Liu et al., 2022a). In abrasive machining of pre-sintered zirconia (Y-TZP), the edge chipping depths of 56.5–95.2 µm depending on the cutting conditions have been reported (Anand et al., 2018). Examination of grinding assessment damage and mechanical strength loss of sintered Y-TZP and alumina-zirconia ceramic has shown that sintered Y-TZP suffered chipping depth (12.7 ± 5.2 µm) with strength loss of 12%, whereas alumina-zirconia ceramic suffers deeper depth (56.8 ± 15.1 µm) and strength loss of 34% (Canneto et al., 2016). This shows that the mechanical properties of the materials influence machining damage, such that alumina-zirconia composite with a higher brittleness index compared with the sintered zirconia calculated in this study is more susceptible to machining damage. Sintering after machining of pre-sintered zirconia was reported to reduce mechanical residual stress from machining (Denry, 2013). However, the subsurface microcracks generated during machining of pre-sintered zirconia are not fully healed during final sintering (Kim et al., 2010), causing concern about the extensive damage in final crown adjustments and fitting for the patient. These studies show that machining-induced surface and subsurface damage are critical issues that need to be solved. Hence,

there is a compelling case for the development of ground-breaking manufacturing technologies to advance conventional diamond milling.

2.4.2.3 Brittleness Index

For machining concerns, the material brittleness relates to the machining surface and edge chipping damage. Brittleness is defined as a material susceptibility to deformation and fracture (Lawn and Marshall, 1979). The quantification of a material brittleness index provides a simple and easy evaluation of material response to brittle fracture and damage. Furthermore, the brittleness index can predict zirconia ceramic machining-induced surface and subsurface damage. This is because surface and subsurface damage is influenced by the zirconia inherent brittleness (Anand et al., 2018; Alao et al., 2017). Brittleness index B associated with the fracture toughness K_{IC}, the hardness H, and the Young's modulus E is expressed as (Quinn and Quinn, 1997):

$$B = EH/{K_{IC}}^2 \tag{2.2}$$

The higher these brittleness indices, the more susceptible the material is to fracture and damage. Thus, it is imperative to rank the brittleness indices of CAD/CAM zirconia materials zirconia materials to guide manufacturers to predict the machining quality.

Fig. 2.10 shows the calculated brittleness indices B for zirconia materials based on the average mechanical properties in Table 2.2. Mg-PSZ has the lowest brittleness index of 27 1/µ. It is followed by sintered Y-TZP materials with brittleness indices of approximately 56–67 1/µ. Next is pre-sintered Y-TZP has the brittleness index of 87 1/µ. Then, ZTA's brittleness index scales at 115 1/µ. Translucent 4Y-PSZ has a high index of 168 1/µ and highly translucent 5Y-PSZ and 6Y-PSZ have the highest brittleness indices of > 300 1/µ.

The ranking in Fig. 2.10 indicates that highly translucent zirconia materials (5Y-PSZ and 6Y-PSZ) are most brittle whereas Mg-PSZ is least brittle. This predicts that highly translucent zirconia materials may be most susceptible to fracture and suffer severe surface and subsurface damage compared with other zirconia materials. Although sintered Y-TZP, translucent and highly translucent zirconia materials share fairly similar hardness (Fig. 2.4) and Young's moduli (Fig. 2.5), the clear difference in their fracture

toughness (Fig. 2.7) make sintered Y-TZP materials less brittle than the ones with improved translucencies.

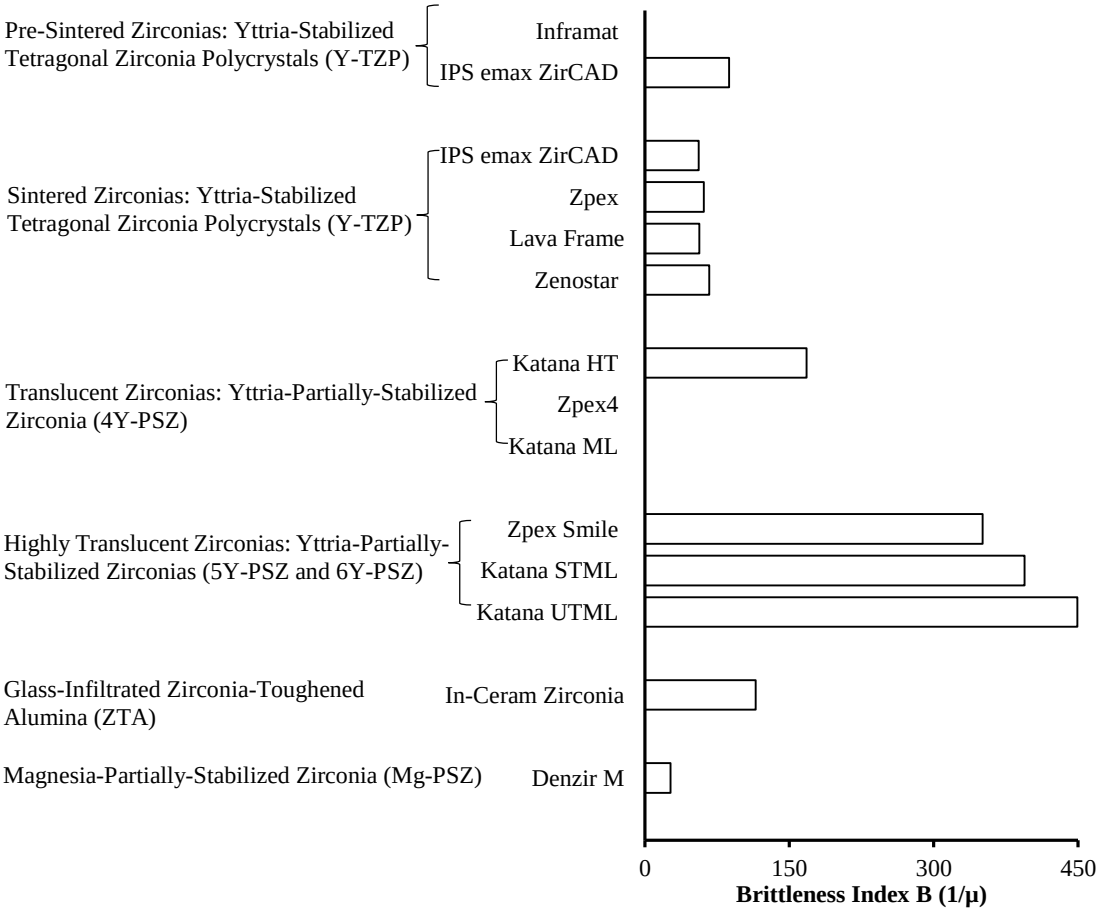

Fig. 2.10 Brittleness index of zirconia materials determined by the average values in Table 2.2.

The brittleness index can act as an indicator for machining-induced edge chipping responses, predicting translucent zirconia materials to generate more severe edge chipping than sintered Y-TZP. A comparative study revealed that a highly translucent multilayered zirconia (5Y-PSZ) with a high translucency factor of 9.96 yielded an edge chipping depth of 0.68 mm under a force of 200 N versus whereas sintered Y-TZP with a low translucency factor of 8.18 yielded the depth of 0.30 mm (Flask et al., 2021). The much more severe edge chipping in 5Y-PSZ was speculated due to its different phase composition with approximately 73% cubic zirconia in comparison with sintered Y-TZP with approximately 96.5% tetragonal phase (Flask et al., 2021). The selection of zirconia materials cannot simply depend on the mechanical properties. If translucency is important to a clinical application, e.g., an anterior crown, translucent zirconia may suffice.

However, a posterior crown with more strength requires the usage of sintered Y-TZP with less brittleness. Brittleness may be also associated with machinability (Boccaccini, 1997), which may predict Mg-PSZ to be the most difficult-to-machine (Fig. 2.9) but to have the least machining-induced brittle damage (Fig. 2.10).

2.4.3 Ultrasonic Vibration-Assisted Machining

The half-century history of dental CAD/CAM technology has played a significant role in digital dentistry. Manufacturing-induced damage in restorations has been the root-cause of failures of the restorations (Schmitter et al., 2012; Triwatana et al., 2012). Ultrasonic vibration-assisted machining (UVAM), as one of the emerging machining processes, introduces ultrasonic vibrations to the motion of a cutting tool tip to make intermittent material-tool contact (Xu and Zhang, 2015). Ultrasonic vibration cutting technology has been applied successfully to various difficult-to-machine materials such as hard steel (Kim and Loh, 2011), titanium (Tong et al., 2019), and ceramics (Abdo et al., 2019). Due to the advantage of UVAM, which can machine difficult-to-machine materials effectively, machinability studies into UVAM techniques have become a focal point of research into manufacturing technologies. In UVAM cutting, the maximum tooltip vibration speed in the cutting direction must exceed the tool feed rate for the ultrasonic vibration to be assisted in the cutting (Xu and Zhang, 2015). In a conventional diamond milling process, the material continuously interacts with the cutting tool tips causing a continuous contact interaction (Song et al., 2018). However, in UVAM, the applied vibration significantly changes the relative trajectory between the tool and the workpiece, thereby changing the material removal mechanism. When vibration is added, it breaks the continuous interaction of the material-tool tip interactions, creating a discontinuous tool-tip interaction (Li et al., 2018; Song et al., 2018). This helps with better chip flushing and cooling and hence results in a lower cutting force and less loading applied to the material surface (Li et al., 2018).

Recent studies show that properly added vibration can reduce cutting forces (Song et al., 2018), minimize burr formation (Kim and Loh, 2011), reduce surface roughness (Jia et al., 2019), lower machining-induced damage (Song et al., 2018; Tesfay et al., 2016) and reduce dimensional errors (Abdo et al., 2019). Kim and Loh (2011) show that elliptical vibration cutting is effective in reducing burr generation and obtaining better surface quality than ordinary cutting in micro/nano machining steel. Tong et al. (2019) found that

ultrasonic milling is more effective in reducing the machining force, surface roughness, and chatter mark heights of titanium alloys than conventional milling. Abdo et al. (2019) achieved surface roughness of microchannel surfaces and dimensional errors as low as 0.27 µm and 8 % respectively when using ultrasonic machine alumina bioceramic. Jia et al. (2019) used ultrasonic grinding to machine zirconia materials, resulting in reduced average surface roughness from 0.972 µm to 0.585 µm, by approximately 40% compared with conventional grinding. Song et al. (2018) report ultrasonic dental handpiece machining of mica-containing glass-ceramic has reduced machining-induced edge chipping damage by 65%. Tesfay et al. (2016) also showed ultrasonic vibration-assisted grinding has significantly reduced the edge chipping damage of alumina from 680 µm ± 30 µm to 70 µm ± 10 µm in comparison with conventional grinding, as shown in Fig. 2.11.

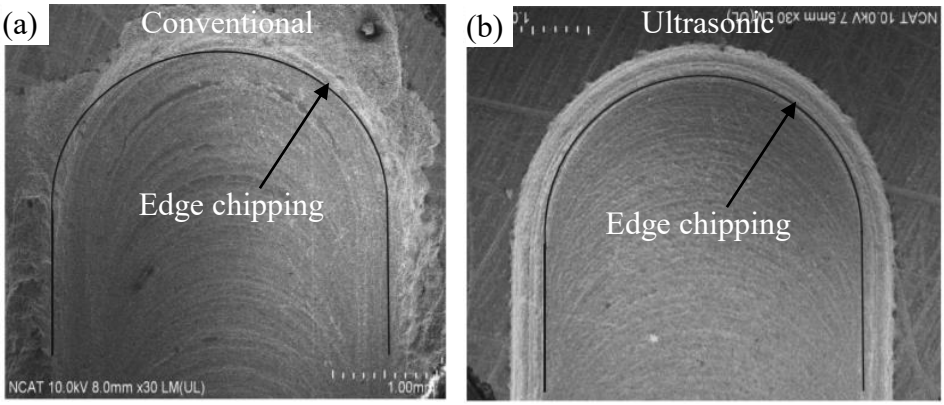

Fig. 2.11. SEM micrographs of machining-induced edge chipping damage induced in conventional and ultrasonic vibration assisted grinding (Tesfay et al., 2016).

2.5 Outlook

Efforts have been made to improve the clinical performances of dental CAD/CAM zirconia ceramics by the understanding of their microstructure, mechanical properties, and processing methods. However, each factor presents insufficient knowledge for future research trends in the fabrication and manufacture of zirconia restorations.

Various studies have reported on the material characterization of zirconia materials with different microstructures. However, by controlling sintering processes of zirconia materials, different microstructures can be produced. Since zirconia mechanical properties are largely dependent on their microstructures, it is important to understand

how the different microstructures of zirconia materials influence their mechanical properties. Investigations into the small scale mechanical testing of different zirconia microstructures may provide insights into the role of microstructures in controlling their mechanical properties. Further, since there are several types of zirconia-containing ceramic systems, as shown in Table 2.1, it is imperative to conduct material characterization of the different zirconia materials during small-scale testings under similar conditions, to thoroughly understand their damage and deformation mechanisms for insightful explanation of their mechanical properties and behavior.

As current machining-induced subsurface damage and poor surface quality of zirconia materials is a challenge and requires fresh solutions. Machining zirconia ceramics mainly involve brittle fracture modes of removal containing surface cracks and this could impose catastrophic failure in zirconia restoration during service. Even though polishing removes these cracks this process is time-consuming and also induces subsurface damage. Hence, there is a need to implement unconventional ultrasonic vibration-assisted technology in conventional dental CAD/CAM processing, enabling minimization of machining damage and poor surface quality. Few have reported on the significance of ultrasonic vibration assistance, but the information on zirconia materials using these systems and diamond tooling for high efficiency, low-cost production, and maximizing quality has not yet been widely introduced. Further, actual crowns fabrication using unconventional ultrasonic assistance and its marginal tolerances have not yet been fully determined.

2.6 Conclusions

Zirconia materials possess great mechanical properties and aesthetics. By controlling their material composition and microstructure different types of zirconia materials can be produced. However, their microstructures control their mechanical properties. Enhancing one aspect of aesthetics may influence their properties and hence depending on the particular application, their properties need to be chosen wisely. Further, their properties determine their processing characteristics, hence high mechanical properties present challenges during abrasive machining and in service due to unhealed damage. The understanding of this microstructure-property-process relation may help to develop new microstructure design of zirconia materials and to provide guidance in dental CAD/CAM zirconia-ceramic-based selections for restoration purposes. As restorations are expected to deliver longer lifetimes, and better aesthetics, fresh approaches are needed to bring

newer materials, newer mechanical characterization techniques and innovative manufacturing processes to improve the quality of zirconia restorations.

References

Abdo, B., Anwar, S., El-Tamimi, A. M., Abouel Nasr, E., 2019. Experimental analysis on the influence and optimization of μ-RUM parameters in machining alumina bioceramic. Mater. 12, 616. https://doi.org/10.3390/ma12040616.

Alao, A. R., Yin, L., 2014a. Nano-scale mechanical properties and behavior of pre-sintered zirconia. J. Mech. Behav. Biomed. Mater. 36, 21–31. https://doi.org/10.1016/j.jmbbm.2014.03.019.

Alao, A. R., Yin, L., 2014b. Loading rate effect on the mechanical behavior of zirconia in nanoindentation. Mater. Sci. Eng. A 619, 247–255. https://doi.org/10.1016/j.msea.2014.09.101.

Alao, A. R., Yin, L., 2016. Assessment of elasticity, plasticity and resistance to machining-induced damage of porous pre-sintered zirconia using nanoindentation techniques. J. Mater. Sci. Technol. 32, 402–410. https://doi.org/10.1016/j.jmst.2016.02.009.

Alao, A. R., Stoll, R., Song, X. F., Miyazaki, T., Hotta, Y., Shibata, Y., Yin, L., 2017. Surface quality of yttria-stabilized tetragonal zirconia polycrystal in CAD/CAM milling, sintering, polishing and sandblasting processes. J. Mech. Behav. Biomed. Mater. 65, 102–116. https://doi.org/10.1016/j.jmbbm.2016.08.021.

Amat, N. F., Muchtar, A., Yew, H. Z., Amril, M. S., Muhamud, R. L., 2020. Machinability of a newly developed pre-sintered zirconia block for dental crown applications. Mater. Lett. 261, 126996. https://doi.org/10.1016/j.matlet.2019.126996.

Anand, P. S. P., Arunachalam, N., Vijayaraghavan, L., 2018. Effect of grinding on subsurface modifications of pre-sintered zirconia under different cooling and lubrication conditions. J. Mech. Behav. Biomed. Mater. 86, 122–130. https://doi.org/10.1016/j.jmbbm.2018.06.026.

ArRejaie, A. S., Al-Hamdan, R. S., Basunbul, G. I., Abduljabbar, T., Al-Aali, K. A., Labban, N., 2019. Clinical performance of one-piece zirconia dental implants: A systematic review. J. Investig. Clin. Dent. 10, e12384. https://doi.org/10.1111/jicd.12384.

Audley, J. A., 1917. The use of zirconia as a refractory material. Nature 99, 375–376.

Belli, R., Wendler, M., de Ligny, D., Cicconi, M. R., Petschelt, A., Peterlik, H., Lohbauer, U., 2017. Chairside CAD/CAM materials. Part 1: Measurement of elastic constants and microstructural characterization. Dent. Mater. 33, 84–98. https://doi.org/10.1016/j.dental.2016.10.009.

Belli, R., Wendler, M., Petschelt, A., Lube, T., Lohbauer, U., 2018. Fracture toughness testing of biomedical ceramic-based materials using beams, plates and discs. J. Eur. Ceram. Soc. 38, 5533–5544. https://doi.org/10.1016/j.jeurceramsoc.2018.08.012.

Beuer, F., Schweiger, J., Edelhoff, D., 2008. Digital dentistry: an overview of recent developments for CAD/CAM generated restorations. Br. Dent. J. 204, 505–511. https://doi.org/10.1038/sj.bdj.2008.350.

Boccaccini, A. R., 1997. Machinability and brittleness of glass-ceramics. J. Mater. Process. Technol. 65, 302–304. https://doi.org/10.1016/S0924-0136(96)02275-3.

Borba, M., de Araújo, M. D., Fukushima, K. A., Yoshimura, H. N., Cesar, P. F., Griggs, J. A., Della Bona, Á., 2011. Effect of the microstructure on the lifetime of dental ceramics. Dent. Mater. 27, 710–721. https://doi.org/10.1016/j.dental.2011.04.003.

Callister, W. D., 2007. An introduction: material science and engineering. New York, 106, 139.

Clarke, I. C., Manaka, M., Green, D. D., Williams, P., Pezzotti, G., Kim, Y. H., Ries, M., Sugano, N., Sedel, L., Nissan, B., Gustafson, G. A., 2003. Current status of zirconia used in total hip implants. J. Bone. Joint. Surg. Am. 85, 73–84.

Canneto, J. J., Cattani-Lorente, M., Durual, S., Wiskott, A. H., Scherrer, S. S., 2016. Grinding damage assessment on four high-strength ceramics. Dent. Mater. 32, 171–182. https://doi.org/10.1016/j.dental.2015.11.028.

Camposilvan, E., Leone, R., Gremillard, L., Sorrentino, R., Zarone, F., Ferrari, M., Chevalier, J., 2018. Aging resistance, mechanical properties and translucency of different yttria-stabilized zirconia ceramics for monolithic dental crown applications. Dent. Mater. 34, 879–890. https://doi.org/10.1016/j.dental.2018.03.006.

Choi, Y. S., Kang, K. H., Att, W., 2020. Effect of aging process on some properties of conventional and multilayered translucent zirconia for monolithic

restorations. Ceram. Int. 46, 1854–1868. https://doi.org/10.1016/j.ceramint.2019.09.162.

Cokic, S. M., Vleugels, J., Van Meerbeek, B., Camargo, B., Willems, E., Li, M., Zhang, F., 2020. Mechanical properties, aging stability and translucency of speed-sintered zirconia for chairside restorations. Dent. Mater. 36, 959–972. https://doi.org/10.1016/j.dental.2020.04.026.

De Araújo-Júnior, E. N., Bergamo, E. T., Campos, T. M., Jalkh, E. B. B., Lopes, A. C., Monteiro, K. N., Cesar, P. F., Tognolo, F. C., Tanaka, R., Bonfante, E. A., 2020. Hydrothermal degradation methods affect the properties and phase transformation depth of translucent zirconia. J. Mech. Behav. Biomed. Mater. 112, 104021. https://doi.org/10.1016/j.jmbbm.2020.104021.

Denry, I., Kelly, J. R., 2008. State of the art of zirconia for dental applications. Dent. Mater. 24, 299–307. https://doi.org/10.1016/j.dental.2007.05.007.

Denry, I., 2013. How and when does fabrication damage adversely affect the clinical performance of ceramic restorations?. Dent. Mater. 29, 85–96. https://doi.org/10.1016/j.dental.2012.07.001.

Denkena, B., Breidenstein, B., Busemann, S., Lehr, C. M., 2017. Impact of hard machining on zirconia based ceramics for dental applications. Procedia CIRP 65, 248–252. https://doi.org/10.1016/j.procir.2017.04.055.

Duwez, P., Odell, F., Brown Jr, F. H., 1952. Stabilization of zirconia with calcia and magnesia. J. Am. Ceram. Soc. 35, 107–113. https://doi.org/10.1111/j.11512916.1952.tb13081.x.

Eldafrawy, M., Nguyen, J. F., Mainjot, A. K., Sadoun, M. J., 2018. A functionally graded PICN material for biomimetic CAD-CAM blocks. J. Dent. Res. 97, 1324–1330. https://doi.org/10.1177%2F0022034518785364.

Elias, A. B., Simão, R. A., Prado, M., Cesar, P. F., Dos Santos, G. B., da Silva, E. M., 2019. Effect of different times of nonthermal argon plasma treatment on the microtensile bond strength of self-adhesive resin cement to yttria-stabilized tetragonal zirconia polycrystal ceramic. J. Prosthet. Dent. 121, 485–491. https://doi.org/10.1016/j.prosdent.2018.03.025.

Elsaka, S. E., 2019. Optical and mechanical properties of newly developed monolithic multilayer zirconia. J. Prosthodont. 28, 279–284. https://doi.org/10.1111/jopr.12730

Flask, J. D., Thompson, G. A., Singh, M., Berzins, D. W., 2021. Edge chipping of translucent zirconia. J. Prosthet. Dent. https://doi.org/10.1016/j.prosdent.2020.12.009.

Garvie, R. C., Hannink, R. H., Pascoe, R. T., 1975. Ceramic steel?. Nature 258, 703–704. https://doi.org/10.1038/258703a0.

Guazzato, M., Albakry, M., Swain, M. V., Ironside, J., 2002. Mechanical properties of In-Ceram Alumina and In-Ceram Zirconia. Int. J. Prosthodont. 15, 339–346. https://pubmed.ncbi.nlm.nih.gov/12170847/#:~:text=Results%3A%20Mean%20biaxial%20flexure%20strengths,)%20for%20In%2DCeram%20Zirconia.

Guazzato, M., Albakry, M., Swain, M. V., Ringer, S. P., 2003. Microstructure of alumina- and alumina/zirconia-glass infiltrated dental ceramics. Bioceramics 15,879–82. https://doi.org/10.4028/www.scientific.net/KEM.240-242.879.

Guazzato, M., Albakry, M., Ringer, S. P., Swain, M. V., 2004. Strength, fracture toughness and microstructure of a selection of all-ceramic materials. Part II. Zirconia-based dental ceramics. Dent. Mater. 20, 449–456. https://doi.org/10.1016/j.dental.2003.05.002.

Guazzato, M., Quach, L., Albakry, M., Swain, M. V., 2005. Influence of surface and heat treatments on the flexural strength of Y-TZP dental ceramic. J. Dent. 33, 9–18. https://doi.org/10.1016/j.jdent.2004.07.001.

Gupta, T. K., Bechtold, J. H., Kuznicki, R. C., Cadoff, L. H., Rossing, B. R., 1977. Stabilization of tetragonal phase in polycrystalline zirconia. J. Mater. Sci. 12, 2421–2426. https://doi.org/10.1007/BF00553928.

Hanawa, T., 2020. Zirconia versus titanium in dentistry: A review. Dent. Mater. J. 39, 24–36. https://doi.org/10.4012/dmj.2019-172.

Hannink, R. H., Kelly, P. M., Muddle, B. C., 2000. Transformation toughening in zirconia-containing ceramics. J. Am. Ceram. Soc. 83, 461–487. https://doi.org/10.1111/j.1151-2916.2000.tb01221.x.

Heintze, S. D., Forjanic, M., Rousson, V., 2006. Surface roughness and gloss of dental materials as a function of force and polishing time in vitro. Dent. Mater. 22, 146–165. https://doi.org/10.1016/j.dental.2005.04.013.

Helmer, J. D., Driskell, T. D., 1969. Research on bioceramics. In Symposium on use of Ceramics as Surgical Implants. Clemson, SC: Clemson University.

Hisbergues, M., Vendeville, S., Vendeville, P., 2009. Zirconia: Established facts and perspectives for a biomaterial in dental implantology. J. Biomed. Mater. Res. B Appl. Biomater. 88, 519–529. https://doi.org/10.1002/jbm.b.31147.

Homaei, E., Farhangdoost, K., Tsoi, J. K. H., Matinlinna, J. P., Pow, E. H. N., 2016. Static and fatigue mechanical behavior of three dental CAD/CAM ceramics. J. Mech. Behav. Biomed. Mater. 59, 304–313. https://doi.org/10.1016/j.jmbbm.2016.01.023.

Inokoshi, M., Zhang, F., De Munck, J., Minakuchi, S., Naert, I., Vleugels, J., Merbeek, B. V., Vanmeensel, K., 2014. Influence of sintering conditions on low-temperature degradation of dental zirconia. Dent. Mater. 30, 669–678. https://doi.org/10.1016/j.dental.2014.03.005.

Inokoshi, M., Shimizu, H., Nozaki, K., Takagaki, T., Yoshihara, K., Nagaoka, N., Zhang, F., Vleugels, J., Meerbeek, B. V., Minakuchi, S., 2018. Crystallographic and morphological analysis of sandblasted highly translucent dental zirconia. Dent. Mater. 34, 508–518. https://doi.org/10.1016/j.dental.2017.12.008.

Inokoshi, M., Shimizubata, M., Nozaki, K., Takagaki, T., Yoshihara, K., Minakuchi, S., Vleugels, J., Meerbeek, B. V., Zhang, F., 2021. Impact of sandblasting on the flexural strength of highly translucent zirconia. J. Mech. Behav. Biomed. Mater. 115, 104268. https://doi.org/10.1016/j.jmbbm.2020.104268.

Jia, D., Li, C., Zhang, Y., Yang, M., Zhang, X., Li, R., Ji, H., 2019. Experimental evaluation of surface topographies of NMQL grinding ZrO_2 ceramics combining multiangle ultrasonic vibration. Int. J. Adv. Manuf. Technol. 100, 457–473. https://doi.org/10.1007/s00170-018-2718-y.

Jones, C. S., Billington, R. W., Pearson, G. J., 2004. The in vivo perception of roughness of restorations. Brit. Dent. J. 196, 42–45. https://doi.org/10.1038/sj.bdj.4810881.

Kelly, J. R., Denry, I., 2008. Stabilized zirconia as a structural ceramic: an overview. Dent. Mater. 24, 289–298. https://doi.org/10.1016/j.dental.2007.05.005.

Kim, J. W., Covel, N. S., Guess, P. C., Rekow, E. D., Zhang, Y., 2010. Concerns of hydrothermal degradation in CAD/CAM zirconia. J. Dent. Res. 89, 91–95. https://doi.org/10.1177%2F0022034509354193.

Kim, G. D., Loh, B. G., 2011. Direct machining of micro patterns on nickel alloy and mold steel by vibration assisted cutting. Int. J. Precis. Eng. Manuf. 12, 583–588. https://doi.org/10.1007/s12541-011-0075-y.

Kolakarnprasert, N., Kaizer, M. R., Kim, D. K., Zhang, Y., 2019. New multi-layered zirconias: Composition, microstructure and translucency. Dent. Mater. 35, 797–806. https://doi.org/10.1016/j.dental.2019.02.017.

Kwon, S. J., Lawson, N. C., McLaren, E. E., Nejat, A. H., Burgess, J. O., 2018. Comparison of the mechanical properties of translucent zirconia and lithium disilicate. J. Prosthet. Dent. 120, 132–137. https://doi.org/10.1016/j.prosdent.2017.08.004.

Lawn, B. R., Marshall, D. B., 1979. Hardness, toughness, and brittleness: an indentation analysis. J. Am. Ceram. Soc. 62, 347–350. https://doi.org/10.1111/j.11512916.1979.tb19075.x.

Li, R. W. K., Chow, T. W., Matinlinna, J. P., 2014. Ceramic dental biomaterials and CAD/CAM technology: state of the art. J. Prosthodont. Res. 58, 208–216. https://doi.org/10.1016/j.jpor.2014.07.003.

Li, J., Geng, D., Zhang, D., Qin, W., Jiang, Y., 2018. Ultrasonic vibration mill-grinding of single-crystal silicon carbide for pressure sensor diaphragms. Ceram. Int. 44, 3107–3112. https://doi.org/10.1016/j.ceramint.2017.11.077.

Liu, W., Tang, D., Gu, H., Wan, L., 2022a. Experimental study on the mechanism of strain rate on grinding damage of zirconia ceramics. Ceram. Int. https://doi.org/10.1016/j.ceramint.2022.04.142.

Liu, H., Inokoshi, M., Nozaki, K., Shimizubata, M., Nakai, H., Too, T. D. C., Minakuchi, S., 2022b. Influence of high-speed sintering protocols on translucency, mechanical properties, microstructure, crystallography, and low-temperature degradation of highly translucent zirconia. Dent. Mater. 38, 451–468. https://doi.org/10.1016/j.dental.2021.12.028.

Lughi, V., Sergo, V., 2010. Low temperature degradation-aging-of zirconia: A critical review of the relevant aspects in dentistry. Dent. Mater. 26, 807–820. https://www.sciencedirect.com/science/article/pii/S0109564110001132.

Marinis, A., Aquilino, S. A., Lund, P. S., Gratton, D. G., Stanford, C. M., Diaz-Arnold, A. M., Qian, F., 2013. Fracture toughness of yttria-stabilized zirconia sintered in conventional and microwave ovens. J. Prosthet. Dent. 109, 165–171. https://doi.org/10.1016/S0022-3913(13)60037-2.

Masaki, T., 1986. Mechanical properties of Y-PSZ after aging at low temperature. Int. J. High Technol. Ceram. 2, 85–98. https://doi.org/10.1016/0267-3762(86)90011-1.

Miura, S., Yamauchi, S., Kasahara, S., Katsuda, Y., Fujisawa, M., Egusa, H., 2021. Clinical evaluation of monolithic zirconia crowns: a failure analysis of clinically obtained cases from a 3.5-year study. J. Prosthodont. Res. 65, 148–154. https://doi.org/10.2186/jpr.JPOR_2019_643.

Mitov, G., Heintze, S. D., Walz, S., Woll, K., Muecklich, F., Pospiech, P., 2012. Wear behavior of dental Y-TZP ceramic against natural enamel after different finishing procedures. Dent. Mater. 28, 909–918. https://doi.org/10.1016/j.dental.2012.04.010.

Miyazaki, T., Hotta, Y., Kunii, J., Kuriyama, S., Tamaki, Y., 2009. A review of dental CAD/CAM: current status and future perspectives from 20 years of experience. Dent. Mater. J. 28, 44–56. https://doi.org/10.4012/dmj.28.44.

Miyazaki, T., Nakamura, T., Matsumura, H., Ban, S., Kobayashi, T., 2013. Current status of zirconia restoration. J. Prosthodont. Res. 57, 236–261. https://doi.org/10.1016/j.jpor.2013.09.001.

Monaco, C., Tucci, A., Esposito, L., Scotti, R., 2013. Microstructural changes produced by abrading Y-TZP in presintered and sintered conditions. J. Dent. 41, 121–126. https://doi.org/10.1016/j.jdent.2012.06.009.

Morgan, M., 2004. Finishing and polishing of direct posterior resin restorations. Pract. Proced. Aesthet. Dent. 16, 211–7. https://europepmc.org/article/med/15199696.

Mukhopadhyay, N. K., Paufler, P., 2006. Micro-and nanoindentation techniques for mechanical characterisation of materials. Int. Mater. Rev. 51, 209–245. https://doi.org/10.1179/174328006X102475.

Nakamura, K., Tarkeshi, A., Niklasson, A., Shishido, S., Svanborg, P., Barkarmo, S., Örtengren, U., 2022. Influence of crystalline phase transformation induced by airborne-particle abrasion and low-temperature degradation on mechanical properties of dental zirconia ceramics stabilized with over 5 mol% yttria. J. Mech. Behav. Biomed. Mater. 125, 104890. https://doi.org/10.1016/j.jmbbm.2021.104890.

Nagarajan, V. S., Jahanmir, S., 1996. The relationship between microstructure and wear of mica-containing glass-ceramics. Wear 200, 176–185. https://doi.org/10.1016/S0043-1648(96)07304-8.

Patidar, A., Mandal, A. K., Chaudhary, A. K., Jain, V., 2021. Surface roughness of sintered yttria stabilised zirconia (YSZ) using high speed moderate depth super-

abrasive grinding. Mater. Today Proc. 44, 2705–2709. https://doi.org/10.1016/j.matpr.2020.12.686.

Passos, S. P., Linke, B., Major, P. W., Nychka, J. A., 2015. The effect of air-abrasion and heat treatment on the fracture behavior of Y-TZP. Dent. Mater. 31, 1011–1021. https://doi.org/10.1016/j.dental.2015.05.008.

Peterson, I. M., Pajares, A., Lawn, B. R., Thompson, V. P., Rekow, E. D., 1998. Mechanical characterization of dental ceramics by Hertzian contacts. J. Dent. Res. 77, 589–602. https://doi.org/10.1177%2F00220345980770041201.

Piconi, C., Maccauro, G., 1999. Zirconia as a ceramic biomaterial. Biomaterials 20, 1–25. https://doi.org/10.1016/S0142-9612(98)00010-6.

Piconi, C., Condo, S. G., Kosmač, T., 2014. Alumina-and zirconia-based ceramics for load-bearing applications. Adv. Ceram. Dent. 219–253. https://doi.org/10.1016/B978-0-12-394619-5.00011-0.

Ponnilavan, V., Khan, M. I. K., Dhayalan, A., Kannan, S., 2019. Structure, luminescence, mechanical and in vitro behavior of zirconia toughened alumina due to terbium substitutions. Mater. Sci. Eng. C 102, 810–819. https://doi.org/10.1016/j.msec.2019.05.011.

Presenda, Á., Salvador, M. D., Penaranda-Foix, F. L., Moreno, R., Borrell, A., 2015. Effect of microwave sintering on microstructure and mechanical properties in Y-TZP materials used for dental applications. Ceram. Int. 41, 7125–7132. https://doi.org/10.1016/j.ceramint.2015.02.025.

Quinn, J. B., Quinn, G. D., 1997. Indentation brittleness of ceramics: a fresh approach. J. Mater. Sci. 32, 4331–4346. https://doi.org/10.1023/A:1018671823059.

Quinn, J. B., Sundar, V., Lloyd, I. K., 2003. Influence of microstructure and chemistry on the fracture toughness of dental ceramics. Dent. Mater. 19, 603–611. https://doi.org/10.1016/S0109-5641(03)00002-2.

Rekow, E. D., Silva, N. R. F. A., Coelho, P. G., Zhang, Y., Guess, P., Thompson, V. P., 2011. Performance of dental ceramics: challenges for improvements. J. Dent. Res. 90, 937–952. https://doi.org/10.1177%2F0022034510391795.

Rice, R. W., 1984. Pores as fracture origins in ceramics. J. Mater. Sci. 19, 895–914. https://doi.org/10.1007/BF00540460.

Ritzberger, C., Apel, E., Höland, W., Peschke, A., Rheinberger, V. M., 2010. Properties and clinical application of three types of dental glass-ceramics and ceramics for

CAD-CAM technologies. Mater. 3, 3700–3713. https://doi.org/10.3390/ma3063700.

Roy, M. E., Whiteside, L. A., Katerberg, B. J., Steiger, J. A., 2007. Phase transformation, roughness, and microhardness of artificially aged yttria-and magnesia-stabilized zirconia femoral heads. J. Biomed. Mater. Res. 83, 1096–1102. https://doi.org/10.1002/jbm.a.31438.

Schmitter, M., Mueller, D., Rues, S., 2012. Chipping behavior of all-ceramic crowns with zirconia framework and CAD/CAM manufactured veneer. J. Dent. 40, 154–162. https://doi.org/10.1016/j.jdent.2011.12.007.

Schünemann, F. H., Galárraga-Vinueza, M. E., Magini, R., Fredel, M., Silva, F., Souza, J. C., Zhang, Y., Henriques, B., 2019. Zirconia surface modifications for implant dentistry. Mater. Sci. Eng. C 98, 1294–1305. https://doi.org/10.1016/j.msec.2019.01.062.

Shi, J. L., Lu, Z. L., Gao, J. H., Zhu, G. Q., Li, L., Lai, T. R., 1998. Microstructure and micro-mechanical properties of Y-TZP and Y-TZP/Al2O3 composite after superplastic deformation. Acta Mater. 46, 1923–1932. https://doi.org/10.1016/S1359-6454(97)00424-2.

Song, X. F., Ren, H. T., Yin, L., 2016. Machinability of lithium disilicate glass ceramic in in vitro dental diamond bur adjusting process. J. Mech. Behav. Biomed. Mater. 53, 78–92. https://doi.org/10.1016/j.jmbbm.2015.08.003.

Song, X.F., Yang, J.J., Ren, H.T., Lin, B., Nakanishi, Y., Yin, L., 2018. Ultrasonic assisted high rotational speed diamond machining of dental glass ceramics. Int. J. Adv. Manuf. Tech. 96, 387–399. https://doi.org/10.1007/s00170-017-1571-8.

Soylemez, B., Sener, E., Yurdakul, A., Yurdakul, H., 2020. Fracture toughness enhancement of yttria-stabilized tetragonal zirconia polycrystalline ceramics through magnesia-partially stabilized zirconia addition. J. Sci. Adv. Mater. Devices 5, 527–534. https://doi.org/10.1016/j.jsamd.2020.09.003.

Sundh, A., Sjögren, G., 2006. Fracture resistance of all-ceramic zirconia bridges with differing phase stabilizers and quality of sintering. Dent. Mater. 22, 778–784. https://doi.org/10.1016/j.dental.2005.11.006.

Tesfay, H.D., Xu, Z., Li, Z.C., 2016. Ultrasonic vibration assisted grinding of bio-ceramic materials: an experimental study on edge chippings with Hertzian indentation tests. Int. J. Adv. Manuf. Tech. 86, 3483–3494. https://doi.org/10.1007/s00170-015-8326-1.

Triwatana, P., Nagaviroj, N., Tulapornchai, C., 2012. Clinical performance and failures of zirconia-based fixed partial dentures: a review literature. J. Adv. Prosthodont. 4, 76–83. https://doi.org/10.4047/jap.2012.4.2.76.

Too, T. D. C., Inokoshi, M., Nozaki, K., Shimizubata, M., Nakai, H., Liu, H., Minakuchi, S., 2021. Influence of sintering conditions on translucency, biaxial flexural strength, microstructure, and low-temperature degradation of highly translucent dental zirconia. Dent. Mater. J. 40, 1320–1328. https://doi.org/10.4012/dmj.2020-448.

Tong, J., Wei, G., Zhao, L., Wang, X., Ma, J., 2019. Surface microstructure of titanium alloy thin-walled parts at ultrasonic vibration-assisted milling. Int. J. Adv. Manuf. Technol. 101, 1007–1021. https://doi.org/10.1007/s00170-018-3005-7.

Vagkopoulou, T., Koutayas, S. O., Koidis, P., Strub, J. R., 2009. Zirconia in dentistry: Part 1. Discovering the nature of an upcoming bioceramic. Eur. J. Esthet. Dent. 4, 130–151.

Wang, J., Stevens, R., 1989. Zirconia-toughened alumina (ZTA) ceramics. J. Mater. Sci. 24, 3421–3440. https://doi.org/10.1007/BF02385721.

Wendler, M., Belli, R., Petschelt, A., Mevec, D., Harrer, W., Lube, T., Danzer, R., Lohbauer, U., 2017. Chairside CAD/CAM materials. Part 2: Flexural strength testing. Dent. Mater. 33, 99–109. https://doi.org/10.1016/j.dental.2016.10.008.

Xu, H. H., Jahanmir, S., Ives, L. K., 1997. Effect of grinding on strength of tetragonal zirconia and zirconia-toughened alumina. Mach. Sci. Technol. 1, 49–66. https://doi.org/10.1080/10940349708945637.

Xu, W. X., Zhang, L. C., 2015. Ultrasonic vibration-assisted machining: principle, design and application. Adv. Manuf. 3, 173–192. https://doi.org/10.1007/s40436-015-0115-4.

Yan, J., Kaizer, M. R., Zhang, Y., 2018. Load-bearing capacity of lithium disilicate and ultra-translucent zirconias. J. Mech. Behav. Biomed. Mater. 88, 170–175. https://doi.org/10.1016/j.jmbbm.2018.08.023.

Yilmaz, H., Aydin, C., Gul, B. E., 2007. Flexural strength and fracture toughness of dental core ceramics. J. Prosthet. Dent. 98, 120–128. https://doi.org/10.1016/S0022-3913(07)60045-6.

Yin, L., Jahanmir, S., Ives, L. K., 2003. Abrasive machining of porcelain and zirconia with a dental handpiece. Wear 255, 975–989. https://doi.org/10.1016/S0043-1648(03)001959.

Yin, L., Song, X. F., Song, Y. L., Huang, T., Li, J., 2006. An overview of in vitro abrasive finishing & CAD/CAM of bioceramics in restorative dentistry. Int. J. Mach. Tool. Manuf. 46, 1013–1026. https://doi.org/10.1016/j.ijmachtools.2005.07.045.

Zhang, F., Inokoshi, M., Batuk, M., Hadermann, J., Naert, I., Van Meerbeek, B., Vleugels, J., 2016. Strength, toughness and aging stability of highly-translucent Y-TZP ceramics for dental restorations. Dent. Mater. 32, e327–e337. https://doi.org/10.1016/j.dental.2016.09.025.

Zhang, Y., Lawn, B. R., 2018. Novel zirconia materials in dentistry. J. Dent. Res. 97, 140–147. https://doi.org/10.1177%2F0022034517737483.

Zhang, Y., Lawn, B. R., 2019. Evaluating dental zirconia. Dent. Mater. 35, 15–23. https://doi.org/10.1016/j.dental.2018.08.291.

Zhuang, Y., Zhu, Z., Jiao, T., Sun, J., 2019. Effect of aging time and thickness on low-temperature degradation of dental zirconia. J. Prosthodont. 28, e404–e410. https://doi.org/10.1111/jopr.12946.

Chapter 3 *In-situ* SEM Micropillar Compression

This chapter consists of the published journal article detailed below:

Juri, A. Z., Basak, A. K., Yin, L., 2022. In-situ SEM micropillar compression of porous and dense zirconia materials. J. Mech. Behav. Biomed. Mater. 105268. https://doi.org/10.1016/j.jmbbm.2022.105268.

Statement of Authorship

Title of Paper	*In-situ* SEM micropillar compression of porous and dense zirconia materials.
Publication status	■ Published ☐ Accepted for publication ☐ Submitted for publication ☐ Unpublished and unsuited work written in manuscript style
Publication details	*Juri, A. Z., Basak, A. K., Yin, L., 2022. In-situ SEM micropillar compression of porous and dense zirconia materials. J. Mech. Behav. Biomed. Mater. 105268. https://doi.org/10.1016/j.jmbbm.2022.105268.*

Principal Author

Name of Principal Author (Candidate)	Afifah Zakiyyah Juri		
Contribution to the Paper	Conceptualization, Methodology, Investigation, Formal analysis, Validation, Data curation, Writing - original draft, Funding acquisition (PhD scholarship).		
Overall percentage (%)	70		
Certification:	This paper reports on original research I conducted during the period of my Higher Degree by Research candidature and is not subject to any obligations or contractual agreements with a third party that would constrain its inclusion in this thesis. I am the primary author of this paper.		
Signature		Date	07/07/2022

Co-Author Contributions

By signing the Statement of Authorship, each author certifies that:

i. the candidate's stated contribution to the publication is accurate (as detailed above);
ii. permission is granted for the candidate in include the publication in the thesis; and
iii. the sum of all co-author contributions is equal to 100% less the candidate's stated contribution.

Name of Co-Author	Animesh Kumar Basak		
Contribution to the Paper	Writing – review and editing, Methodology, Investigation, Data curation.		
Signature		Date	08/06/2022

Name of Co-Author	Ling Yin		
Contribution to the Paper	Writing – review and editing, Validation, Supervision, Project administration, Methodology, Investigation, Funding acquisition, Formal analysis, Conceptualization.		
Signature		Date	07/07/2022

In-situ SEM micropillar compression of porous and dense zirconia materials

Afifah Z. Juri[1], Animesh K. Basak[2], Ling Yin[1,*]

[1]School of Mechanical Engineering, The University of Adelaide, Adelaide, SA 5005, Australia

[2]Adelaide Microscopy, The University of Adelaide, Adelaide, SA 5005, Australia

*Corresponding Author: afifah.juri@adelaide.edu.au, ling.yin@adelaide.edu.au

Abstract The reduction of failure rates of small-sized zirconia devices depends on the understanding of their micromechanical properties. This paper reports the micromechanical behaviors of porous and dense zirconia materials using *in-situ* micropillar compression with a flat diamond indenter in a scanning electron microscope (SEM). Porous and dense zirconia micropillars were made using focused ion beam (FIB) milling technique in the SEM. They were then subject to *in-situ* SEM compression to identify their Young's moduli, yield stresses, plastic deformation, compressive and fracture strengths, damage accumulations, and failure mechanisms. We found that while both porous and dense zirconia microstructures exhibited plastic behaviors, the former had much lower Young's moduli, strengths (yield, compression and fracture), resilience and toughness but higher ductility, resulting in significant buckling than the latter. In plastic regions, alternative strain softening and hardening may have caused stress variations in porous zirconia while dislocation movement contributed to strain hardening in dense zirconia. Although both zirconia materials had quasi-brittle failures, there were different damage mechanisms. The quasi-brittle failure for porous state was due to mushrooming buckling damage driven by breaking of weak interconnected pore networks, resulting in severe compaction and pulverization, microcracks and material piling. The quasi-brittle failure for dense state was identified as plastic crushing damage, involving microcrack initiation and propagation, cleavage and intergranular fractures, and delamination. The mechanical properties of porous and dense zirconia micropillars investigated contributed to the knowledge on deformation and damage mechanisms of zirconia materials at the small scale.

3.1 Introduction

The high strength and fracture toughness, excellent biocompatibility, low thermal conductivity, and aesthetic properties of zirconia make it promising as load bearing structures in engineering, medicine and dentistry (Chintapalli et al., 2012; Depprich et al., 2008; Manicone et al., 2007; Miyazaki et al., 2013; Rekow et al., 2011). The success of zirconia devices and structures, such as zirconia crowns, inlays, and onlays, and implants, i.e., small screws placed into jawbones (Miyazaki et al., 2013; Van Staden et al., 2006; Zinelis et al., 2010), depends on the microstructures and the micromechanical properties of zirconia materials (Camposilvan and Anglada, 2016). Hence, a deep understanding of the mechanical behavior, deformation and failure mechanisms of zirconia materials at small scales is utmost important to reduce failure rates of zirconia devices and structures.

Ex-situ and *in-situ* indentation techniques are commonly used to investigate the zirconia mechanical behavior at nano and micro scales in single and cyclic loading conditions (Juri et al., 2021; Kosai and Yan, 2020). The Oliver and Pharr method enabled the extraction of elastic properties of zirconia materials from unloading curves of indentations (Oliver and Pharr, 1992; 2004). Single nanoindentation of porous and dense zirconia materials also revealed the quasi-plastic deformation with different microstructural responses (Juri et al., 2021). Cyclic nanoindentation of sintered dense zirconia demonstrated the microstructural evolution under repetitive loading/unloading (Kosai and Yan, 2020). It is no doubt about that these indentation studies provided knowledge of microstructural changes and elastic properties of zirconia materials. However, the techniques fail to elucidate their brittle-ductile transitions, deformation (ductility), energy absorption (resilience, and toughness), and strength behaviors (yield, compression and fracture). Further, constrained conditions in indentation involving different geometrical indenters resulted in unavoidable strain gradients and complex stresses in indented zones (Han et al., 2009; Shin et al., 2013). During *in-situ* imaging using scanning electron microscopy (SEM), commonly used Berkovich diamond indenter tips often obstruct observations of deformation and damage of indented areas (Moser et al., 2005).

To overcome the limitations of indentation techniques, attempts have been made to conduct *in-situ* SEM micropillar compression, which has capabilities of investigating the mechanical properties, deformation and damage mechanisms in free surfaces (Basak et

al., 2019; Dehm et al., 2018). The technique involves the fabrication of micropillars using focused ion beam (FIB) milling of a material surface in an SEM and *in-situ* compression of the micropillars using a flat diamond indenter, which provides simpler stress states without stress gradients (Cho et al., 2018; Dehm et al., 2018; Ramachandramoorthy et al., 2021; Schwiedrzik et al., 2014). *In-situ* SEM video imaging of the compression process enables a clear and instantaneous observation of deformation and damage morphologies of the material, which can be correlated to stress-strain curves (Camposilvan and Anglada, 2016; Csanádi et al., 2019; Dang et al., 2018). The microscale stress-strain behavior of a material can be then determined under unconstrained conditions, including yield and strength properties, which may exhibit an extrinsic behavior when the material volumes are reduced, i.e., the size effect (Camposilvan and Anglada, 2016). Therefore, *in-situ* SEM micropillar compression has become another useful tool in micromechanics of materials (Basak et al., 2019; Dehm et al., 2018), such as bone (Schwiedrizik et al., 2014), ceramics (Cho et al., 2018), and composites (Basak et al., 2019).

In-situ micropillar compressions of brittle materials have focused on the size and plasticity effects on their behaviors because these materials are generally featured with brittleness in macroscale compressions (Camposilvan and Anglada, 2016). For example, *in-situ* micropillar compression of ZrB_2 in basal and prismatic orientations revealed the anisotropy of the yield and rupture strengths and the single slip activation of the microscale plasticity of the material (Csanádi et al., 2016). *In-situ* micropillar compression of sintered dense zirconia revealed the phase transformation-motivated plasticity and the length scale dependence of the plastic deformation of the material (Camposilvan and Anglada, 2016). Fracture properties of sintered porous zirconia materials with 33–63% porosities at different sintering temperatures were also investigated under microcompression, revealing the significant sintering temperature effects on both Young's moduli and fracture strength (Abaza et al., 2022). The study also indicates a brittle behavior transition from macrocracks to microcracks when increasing the porosity (Abaza et al., 2022).

Zirconia materials have porous and dense microstructures. However, little is known towards a thorough comparison of the small scale stress-strain behaviors of these microstructures, including brittle-ductile transitions, strength properties (yield, compressive and fracture), ductility and energy absorptions (resilience and toughness).

Thus, the small scale failure origins and deformation/damage mechanisms in zirconia devices and structures are not clearly elucidated, hence limiting the improvements of zirconia products and manufacturability. Therefore, this paper aims to investigate the *in-situ* SEM micropillar compression of porous and dense zirconia materials to understand their micromechanical properties, deformation and damage mechanisms. The stress-strain characteristics, deformation and damage modes of these materials can be used to study the overall responses and failures of other polycrystallized ceramics at the microscale.

3.2 Experimental Procedure

3.2.1 Materials and Specimen Preparation

A porous zirconia block of 15 mm × 15 mm × 50 mm (IPS e.max ZirCAD, Ivoclar Vivadent) was selected for this study. It contains approximately 87–95 wt% ZrO_2 and 4–6 wt% Y_2O_3 as primary compositions together with 1–5 wt% HfO_2 and 0.1–1 wt% Al_2O_3 as additives (Ritzberger et al., 2010). The material was fabricated from cold isostatic pressing of zirconia powders and a subsequent heat treatment at 850 °C to result in a highly porous microstructure (Amat et al., 2018; Denry and Kelly, 2008). Porous zirconia samples of 5 mm × 5 mm × 2 mm were obtained by cutting of the pre-sintered block using a low speed diamond saw (Struers Minitom, Struers Ins., USA). This is followed by standard metallographic grinding and polishing procedure with different grits of sand paper on a grinding/polishing machine (Struers Ins., USA). Initial rough grinding was conducted on sample top and bottom surfaces with 500 and 1200 grit sand papers for surface flatness and parallelism and water as a lubricant. Next top sample surfaces were polished using velvet cloth discs with diamond pastes of 6 µm, 1 µm and 0.5 µm grit sizes (Kemet Australia) at a rotational speed of 80 rpm with water as a lubricant. To ensure high surface quality, top sample surfaces were frequently checked by using an optical microscope. The reported material and mechanical properties of porous zirconia include the density of 3.0–3.21 g/cm^3, the porosity of 47.3–49.3 vol% (Ritzberger et al., 2010), the Young's modulus E of 34 GPa (Alao and Yin, 2014a), the hardness H of 1.5 GPa (Alao and Yin, 2014a), the fracture toughness K_{IC} of 0.8 MPa m$^{1/2}$ (Alao and Yin, 2016) and the flexural strength 50–90 MPa (Ritzberger et al., 2010).

Dense zirconia samples were obtained by sintering of polished porous zirconia samples at a temperature of 1300 °C for 2 hour at a heating rate of 10 °C/min in a furnace (MTI GSL1500X) (Alao and Yin, 2014b). The samples were then naturally cooled to room temperature as recommended by dental zirconia restoration specification (Denry and Holloway, 2010). As the sintering process altered the zirconia microstructure and surface morphology, further polishing of top surfaces was conducted following the same polishing procedure described for porous zirconia samples (Alao and Yin, 2014b). The reported material and mechanical properties of dense zirconia include the density of 6.09 g/cm^3, the porosity of less than 0.5% (Ritzberger et al., 2010), the Young's modulus *E* of 168 GPa (Alao and Yin, 2014b), the hardness *H* of 13.2 GPa (Alao and Yin, 2014b), the fracture toughness K_{IC} of 6 MPa m$^{1/2}$ (Sakoda et al., 2018) and the flexural strength 1300 MPa (Sakoda et al., 2018).

Both porous and dense zirconia samples were cleaned using ethanol and dried naturally. Then, they were carbon-coated for *in-situ* SEM micropillar compression.

3.2.2 *In-situ* SEM Micropillar Compression

A dual focused Ga-ion beam (FIB) was used to mill polished porous and dense zirconia sample surfaces at 30 kV in an SEM (FEI Helios Nanolab 600, Thermo Fisher Scientific, USA) to produce series cylindrical micropillars of 3 µm diameter and 9 µm height. In the first, rough milling with 6.5 nA beam current was performed to mill 30 µm diameter circular trenches to obtain 10 µm diameter posts. Then, fine milling was conducted in four steps in which the circular trenches were milled down to diameters of 6 µm, 5 µm, 3.8 µm and 3 µm with beam currents of 2.8 nA, 0.92 nA, 0.46 nA, and 90 pA, respectively. All fabricated micropillars were observed under the SEM at tilt angle of 30° for quality assurance.

In-situ micropillar compression was conducted using a quantitative picoindenter system (PI 88, Hysitron, USA) with a flat diamond indenter of 5 µm diameter inside the SEM. During compression at room temperature, a displacement-control mode was used at 3 nm/s loading rate and 50 nm/s unloading rate corresponding to a strain rate of 10^{-3}/s. Real-time SEM-imaging was performed to capture all small-scale mechanical events and microstructural evolution during micropillar compression for 500–700 s at a frame rate of 40 frame/s. Meanwhile, the picoindenter system automatically recorded all force-

displacement data. For each material, at least three repeated micropillar compressions were conducted. After compressions, all damaged micropillars were also observed under the SEM at tilt angle of 30°.

3.2.3 Mechanical Properties

The micromechanical properties of porous and dense zirconia micropillars were determined using the stress-strain curves converted from the force-displacement data (Wang and Stanford, 2015; Frick et al., 2008). The engineering stress was calculated by the following equation:

$$\sigma = \frac{F}{A_0} \tag{3.1}$$

where F was the compressive force and A_0 was the cross-sectional area of a micropillar. To calculate the engineering strain, the recorded displacements u_{total} must be corrected due to the Sneddon effect (Sneddon, 1965), which equals to the sum of the micropillar length change Δl and the Sneddon-effected displacement $u_{Sneddon}$ as follows (Wang and Stanford, 2015):

$$u_{total} = \Delta l + u_{Sneddon} \tag{3.2}$$

As $u_{Sneddon}$ representes the elastic penetration of the micropillar to its sample substrate, the corrected micropillar length change $\Delta l_{corrected}$ can be written as (Wang and Stanford, 2015; Sneddon, 1965; Frick et al., 2008):

$$\Delta l_{corrected} = u_{total} - \frac{(1-v_{indenter}^2)F}{E_{indenter}D_{bottom}} - \frac{\left(1-v_{sample}^2\right)F}{E_{sample}D_{top}} \tag{3.3}$$

where $v_{indenter}$ and v_{sample} are the Poisson's ratios of the indenter and the sample, $E_{indenter}$ and E_{sample} are the Young's moduli of the indenter and the samples, and D_{bottom} and D_{top} are the micropillar bottom and top diameters. For a standard diamond indenter tip, $v_{indenter}$ = 0.07 and $E_{indenter}$ = 1140 GPa (Oliver and Pharr, 1992). Thus, the engineering strain can be determined using the following expression:

$$\varepsilon = \frac{\Delta l_{corrected}}{l_0} \tag{3.4}$$

where l_0 is the initial micropillar height.

The Young's modulus was determined from the slope of the linear relationship in the elastic region of the stress-strain curves. The yield strength was taken from the stress at 0.002 strain offset following the same slope of the linear relationship in the elastic region. The compressive strength was obtained from the highest stress value. The fracture strength was obtained from the stress at the failure. The ductility was taken from the plastic strain of the stress-strain curve, by taking the elastic strain from the full strain value at the failure. The resilience was computed from the area under the stress-strain curve taken to yielding. The toughness was computed from the area under the stress-strain curve taken to failure. All mean values and standard deviations of the mechanical properties for each material were obtained from three repeated micropillar compressions. A paired *t*-test was also conducted at a 5% significance level to examine the material effect on these properties. All calculations were conducted using Excel software.

3.3 Results

3.3.1 *In-situ* SEM Micropillar Compression

Figs. 3.1(a) and 3.1(b) show SEM micrographs of series porous and dense zirconia micropillars in 30 μm crater centers of sample surfaces, respectively. Figs. 3.1(c) and 3.1(d) reveal detailed porous and dense micropillar geometries with 3 μm nominal diameter and vertical error angles of 0.8° and 1.8°, respectively. Porous zirconia (Fig. 3.1(c)) had an isolated or interconnected pore structure with visible individual submicron zirconia grains. Dense zirconia (Fig. 3.1(d)) had a compact submicron structure.

Fig. 3.2 shows a series of *in-situ* SEM images of deformation and damage of porous zirconia micropillar compression and its corresponding stress-strain curve. In the elastic region (Fig. 3.2(a)), the flat diamond indenter perfectly contacted and compressed the top surface of the porous zirconia micropillar. After the yield (Fig. 3.2(b)), the porous zirconia structure sheared at a shear angle of approximately 30°, the microstructural buckling initiated. With the continuing compression, severe bucking occurred (Fig. 3.2(c)). Further progression of the indenter resulted in the accumulated zirconia crystals pushing outward (Fig. 3.2(d)). At the end of plastic deformation (Fig. 3.2(e)), significant material accumulated zirconia crystals were pushing out, creating mushrooming buckling damage. At the fracture (Fig. 3.2(f)), part of the deformed and damage micropillar was pulled off.

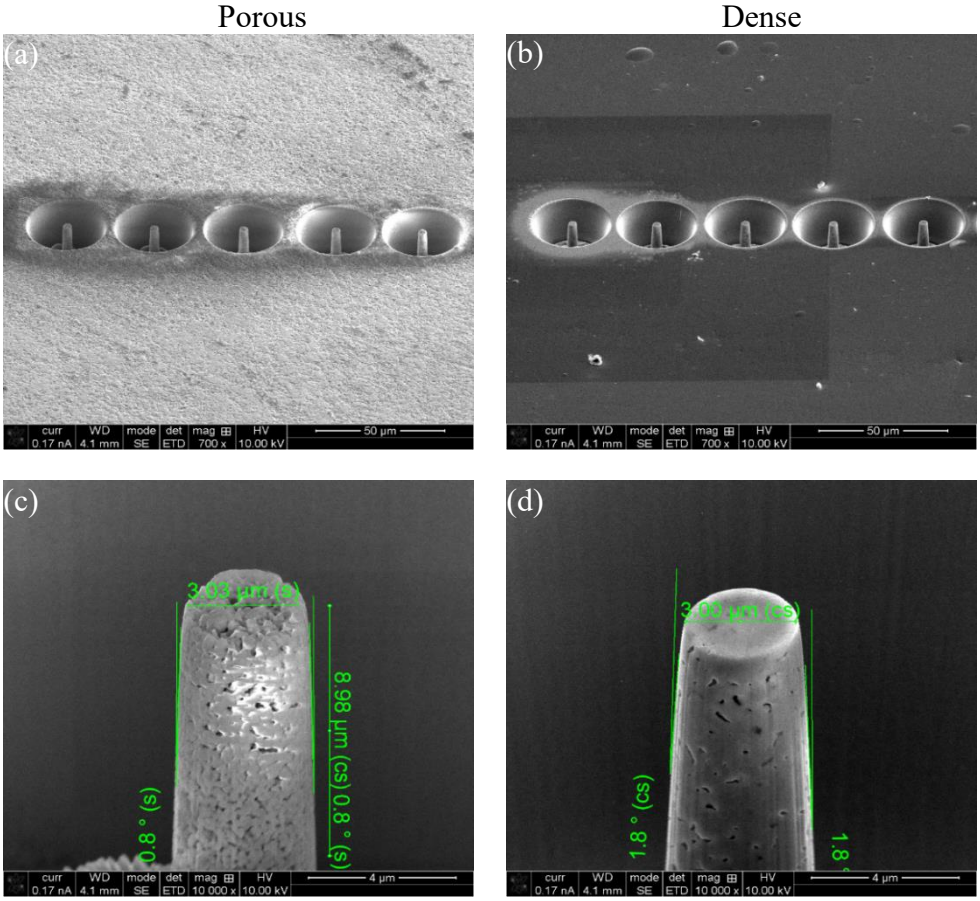

Fig. 3.1. SEM micrographs of a series fabricated (a) porous and (b) dense zirconia micropillars and their detailed geometries for (c) porous and (d) dense micropillars.

Fig. 3.3 shows a series of *in-situ* SEM images of deformation and damage of dense zirconia micropillar compression and its corresponding stress-strain curve. Fig. 3.3(a) shows the perfect elastic deformation of the dense zirconia micropillar compressed by the flat diamond indenter. In the elastic region (Fig. 3.3(b)), no visible changes at the microstructural level but microscale horizontal expansion can be observed. After the yield (Fig. 3.3(c)), microcracks initiated. Zirconia crystals slipped around grain boundaries to propagate the microcracks (Fig. 3.3(d)). Prior to the micropillar failure (Fig. 3.3(e)), more zirconia crystals slipped around grain boundaries, resulting in more microcracks and delamination in the vicinity of the indenter. At the failure point (Fig. 3.3(f)), the crack propagation led to the pushing outward of the zirconia material, the falling off of the damaged top micropillar, and then the zirconia piling up to side of the micropillar.

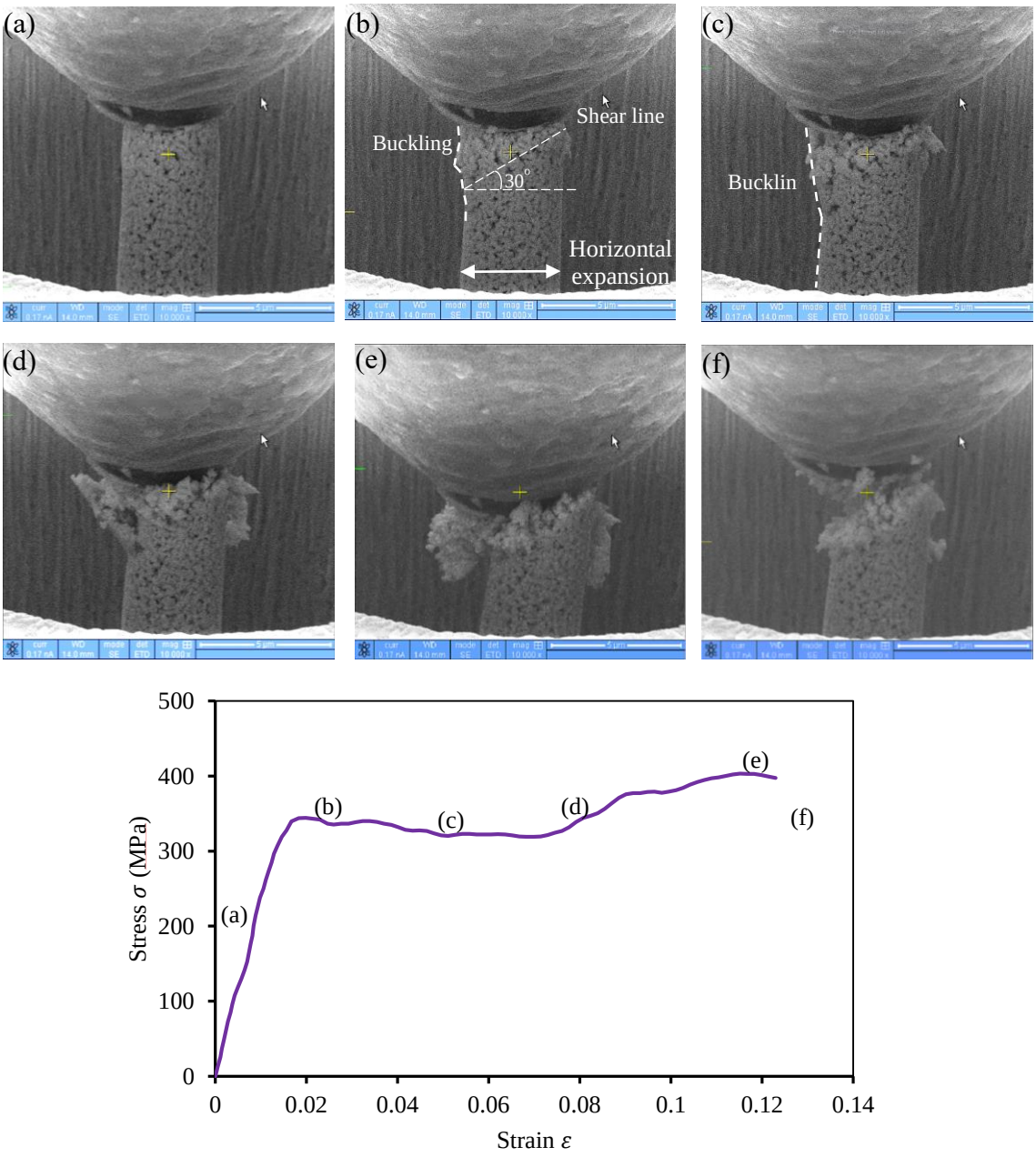

Fig. 3.2. A series of SEM micrographs of in-situ porous zirconia micropillar compression and its corresponding stress-strain curve, reflecting (a) the elastic region, (b) the post yield with buckling with horizontal expansion and shear deformation initiation, (c) the plastic region with severe buckling, (d) zirconia crystals pushing outward, and (e) zirconia crystals pushing out with mushrooming damage, and (f) the fracture point.

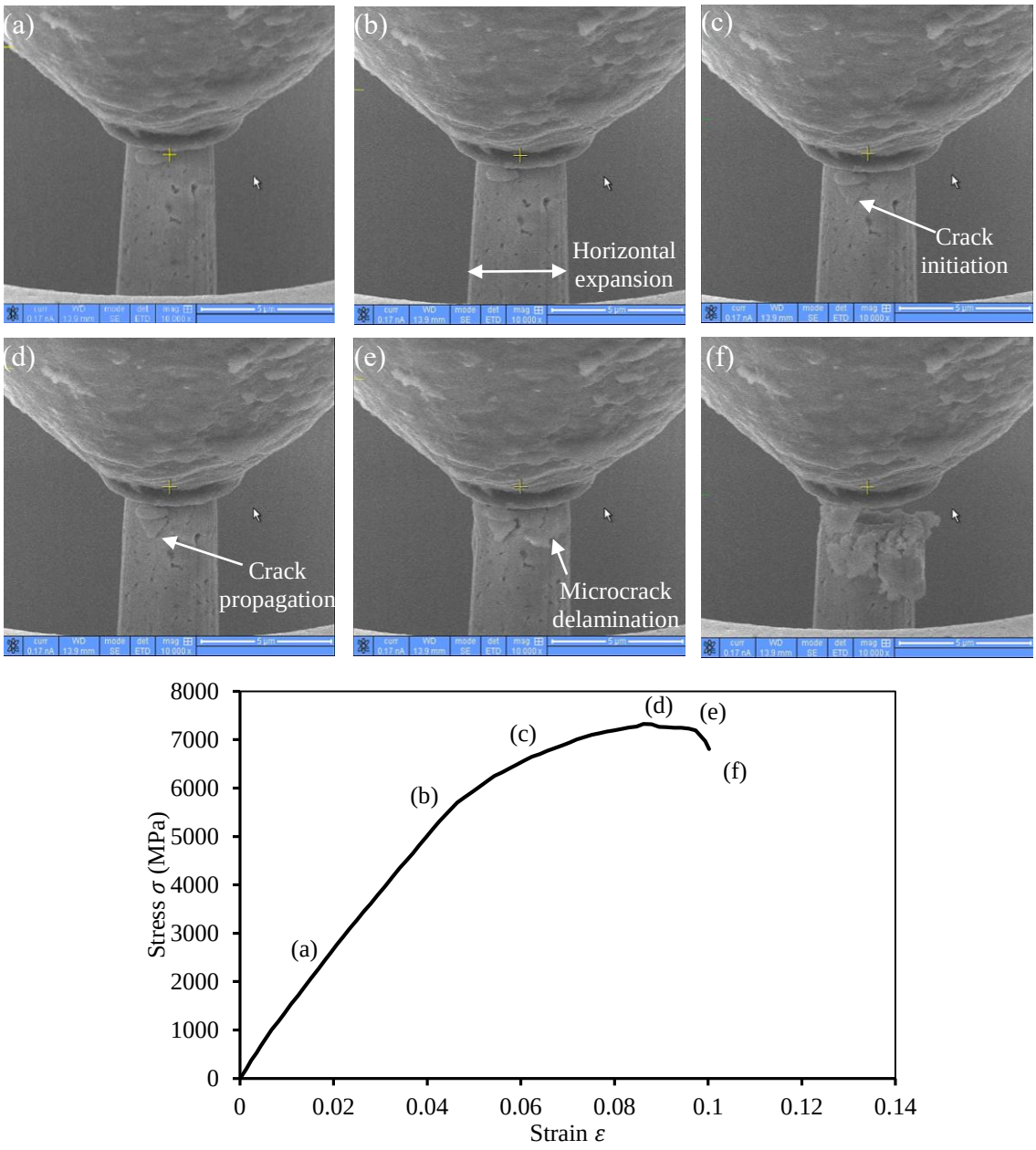

Fig. 3.3. A series of SEM micrographs of in-situ dense zirconia micropillar compression and its corresponding stress-strain curve, reflecting (a) the elastic region, (b) the elastic deformation with horizontal expansion, (c) the plastic region with microcrack initiation, (d) microcrack propagation, (e) microcrack delamination, and (f) the fracture point. Arrows indicate microcrack and delamination.

3.3.2 Mechanical Properties

Fig. 3.4 displays the stress-strain curves for three porous and dense micropillar compressions. For porous zirconia (Fig. 3.4(a)), the initial parts of the curves showed

nearly identical elastic slopes followed by significant deviations for their yield, compressive strength and fracture strength points. After the yield points, there were multiple stress variations as indicated by arrows and more irregularities, indicating complex plastic deformation in the material. For dense zirconia (Fig. 3.4(b)), the initial parts of the curves showed steeper elastic slopes. After the yields, the material had smooth plastic deformation with smooth stress-strain curves. After reaching the compressive strength values, all stresses dropped as indicated by arrows, resulting in lower fracture strength values. In comparison between the two materials, porous zirconia revealed much lower elastic moduli, compressive and fracture strengths but more ductile than dense state.

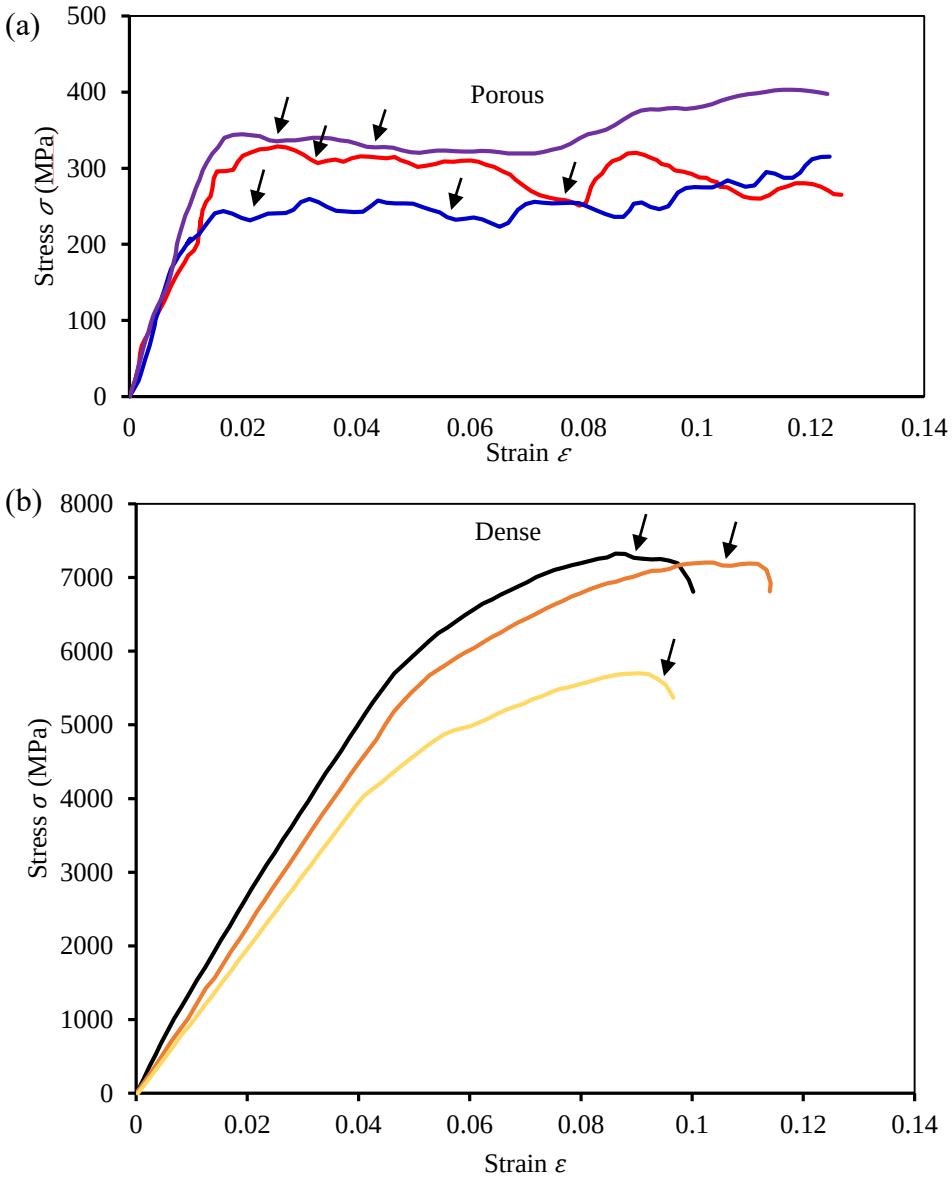

Fig. 3.4. Three repeated stress-strain curves of (a) porous and (b) dense zirconia micropillars. Arrows indicate stress drops.

Fig. 3.5 shows the mechanical properties of porous and dense zirconia materials. The Young's moduli (Fig. 3.5(a)) for dense zirconia ranged 110 ± 18 GPa, at least 3 times more than those of 23 ± 9 GPa for porous zirconia. Fig. 3.5(b) reveals that dense zirconia had the yield strength of 5383 ± 855 MPa, approximately 21 times higher than porous state of 285 ± 65 MPa. It also shows that the fracture strength for dense zirconia scaled 6330 ± 833 MPa, more than 20 times higher than those of 329 ± 64 MPa for porous zirconia. The compressive strength for dense zirconia scaled 6737 ± 902 MPa, more than 20 times higher than those of 351 ± 46 MPa for porous zirconia. Fig. 3.5(c) demonstrates the ductility of 10.8% ± 0.6% for porous zirconia, nearly doubled those of 4.7 ± 0.7% for dense zirconia. Fig. 3.5(d) indicates that dense zirconia had the resilience of 200.3 ± 69.5 J/m^3, nearly 76 times those of 2.5 ± 1.1 J/m^3 for porous zirconia. It also reveals the toughness of 525.4 ± 90.8 J/m^3 for dense state, nearly 25 times higher than those of 30.1 ± 10.1 J/m^3 for porous state.

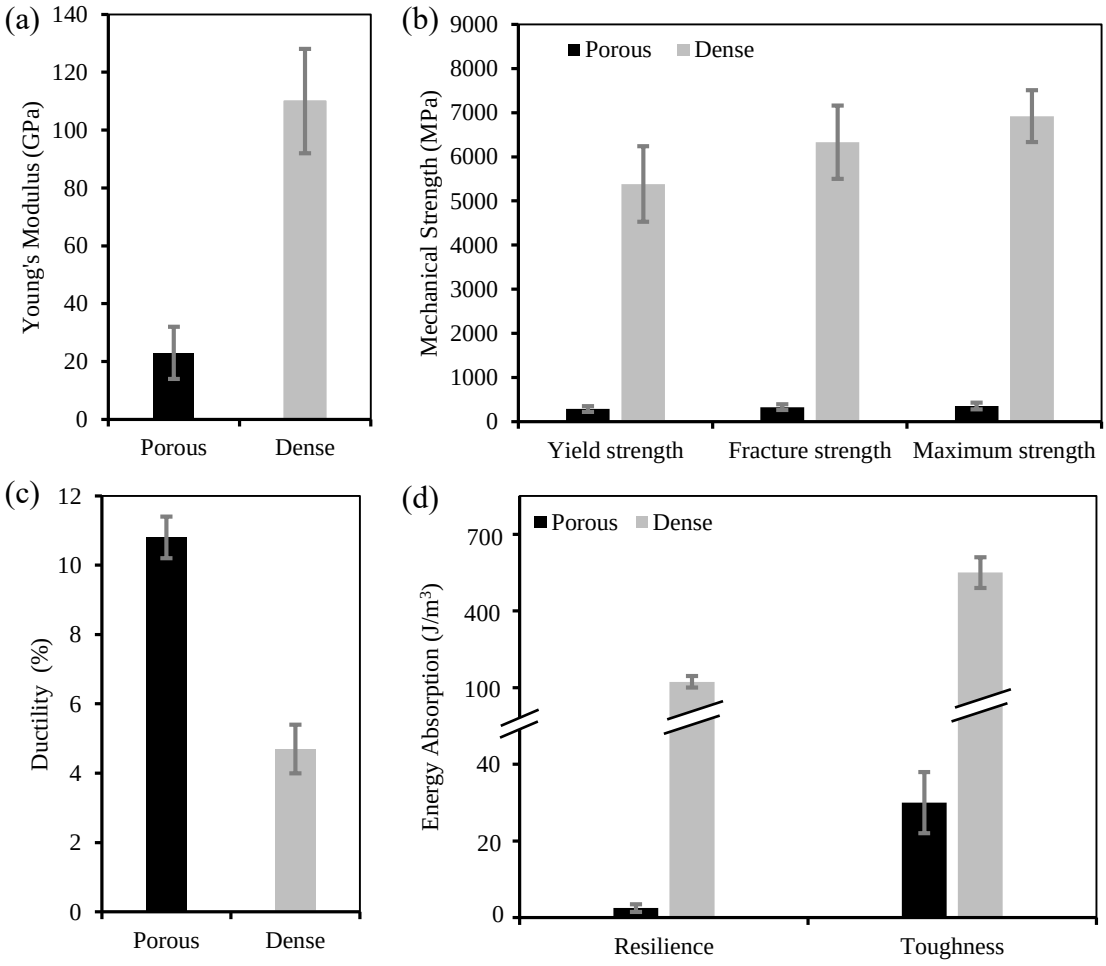

Fig. 3.5. Mechanical properties of porous and dense zirconia micropillars: (a) The Young's modulus, (b) Mechanical strength, (c) Ductility, and (d) Energy absorption.

3.3.3 Micropillar Deformation and Damage Morphology

Fig. 3.6 shows SEM micrographs of an original, and deformed and damaged porous zirconia micropillar. The original micropillar (Fig. 3.6(a)) with a highly interconnected pore network microstructure with zirconia crystals separated by pores straightly stood in its crater center. The micropillar buckled and fractured after the compression (Fig. 3.6(b)). Intergranular fracture occurred along pore networks (Fig. 3.6(c)). There were extensive microcracks, delamination, and pore condensation around fractured pore networks (Fig. 3.6(d)).

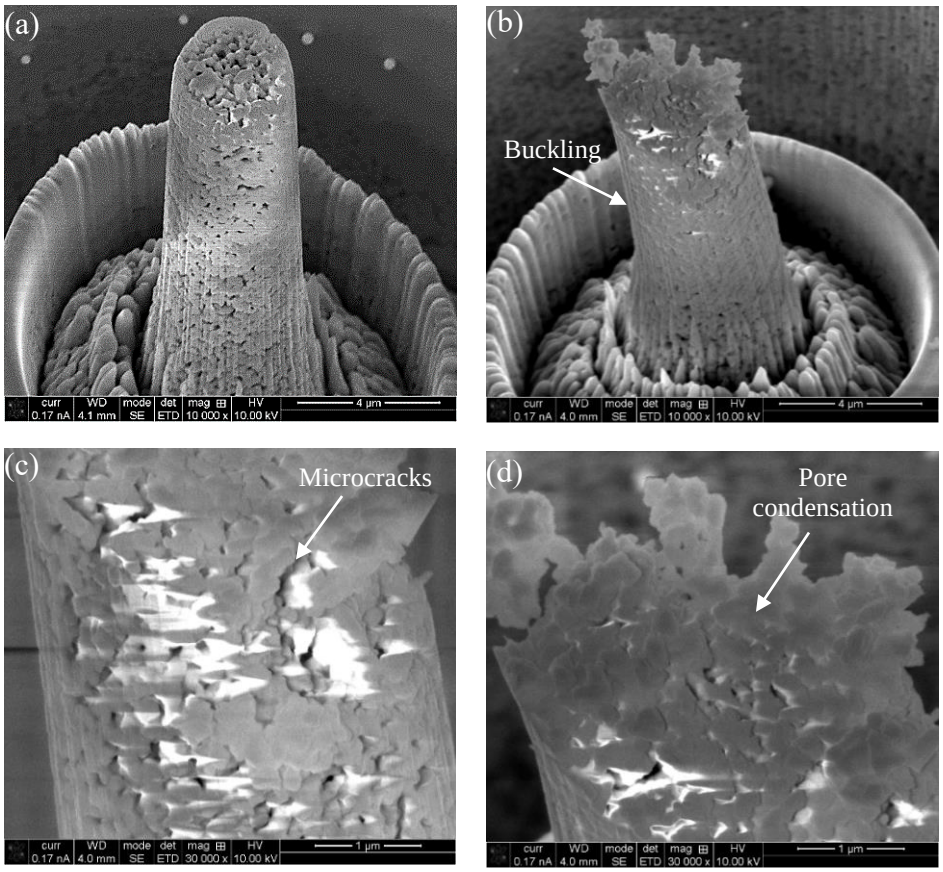

Fig. 3.6. SEM micrographs of an original, and deformed and damaged porous zirconia micropillar: (a) Original morphology, (b) Buckling fracture, (c) Microcracks, delamination and pulverization, and (d) Microcracks, delamination and pore condensation.

Fig. 3.7 shows SEM micrographs of an original, and deformed and damaged dense zirconia micropillar. The original micropillar (Fig. 3.7(a)) having very smooth surfaces with very low porosity and less clearer grain boundaries straightly stood in its crater

center. After compression, the fractured section (Fig. 3.7(b)) still straightly stood in its crater center without visible buckling. In the fractured area, extensive microcracks, delamination and pulverization were observed in (Fig. 3.7(c)). Meanwhile, cleavage and intergranular fracture were also visible (Fig. 3.7(d)).

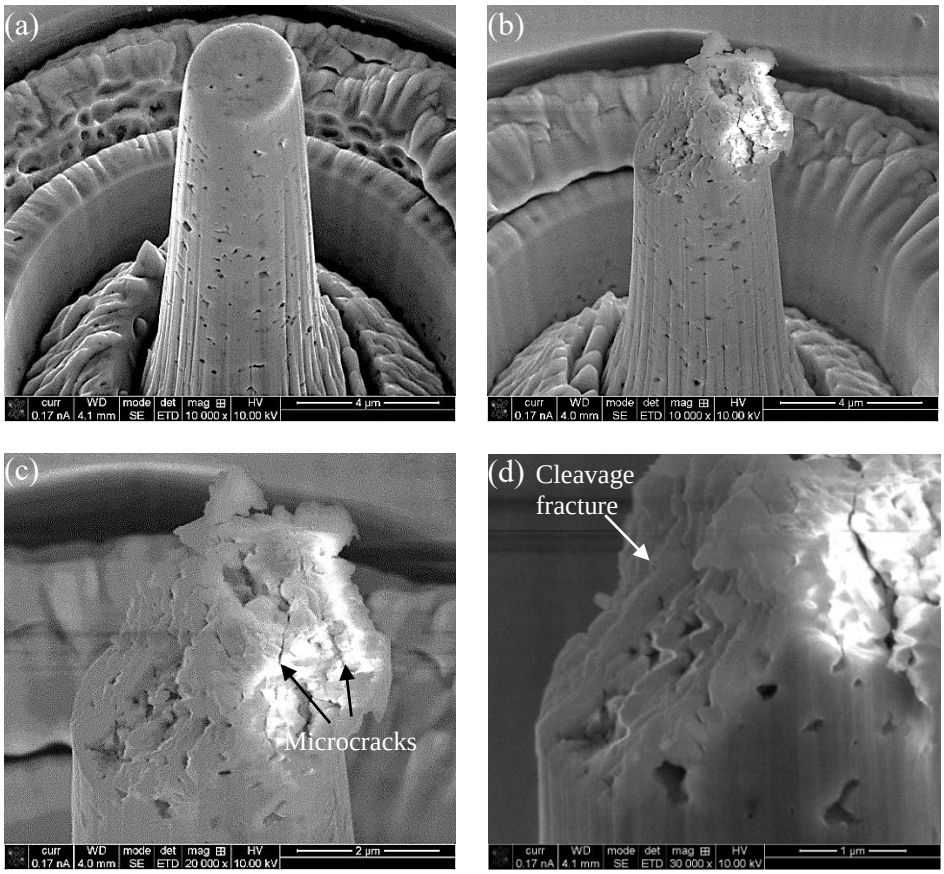

Fig. 3.7. SEM micrographs of an original, and deformed and damaged dense zirconia micropillar: (a) Original morphology, (b) Quasi-brittle fracture, (c) Microcracks, delamination and pulverization, and (d) Cleavage and intergranular fracture.

3.4 Discussion

This study has studied the mechanical behaviors of porous and dense zirconia micropillars in compression using *in-situ* SEM techniques, revealing a significant microstructural effect on their properties, deformation and damage mechanisms.

This study applied dual focused Ga-ion beam (FIB) milling for the micropillar production. Studies have found radiation damage in ferroelectric capacitors produced by focused Ga-ion beam at 50 kV (Stanishevsky et al., 2002). Significant modification of the

chemical composition of the damaged layer of 5–10 nm was discovered on the FIB-processed capacitor surfaces (Stanishevsky et al., 2002). In the current study, porous and dense zirconia micropillars were FIB-processed using dual focused Ga-ion beam at 30 kV. Based on the SEM observations of the produced porous and dense micropillars at the micron scale, they all revealed high structural and surface integrity (Fig. 3.1). Therefore, the FIB-induced surface layer composition changes in porous and dense zirconia micropillars may be negligible for the microscale mechanical compressions conducted in this study.

Although both materials had stress-strain curves with initial elastic regions, yield points, plastic regions and fracture points (Figs. 3.2 and 3.3), they demonstrated distinct mechanical properties. Porous zirconia had shallower elastic slopes and early yield points around 0.02 strain (Fig. 3.2) whereas dense state yielded steeper elastic slopes and later yield points around 0.06 strain (Fig. 3.3). These differences were attributed to their different microstructures, resulting in the significant different mechanical properties (Fig. 3.5). The significantly higher Young's moduli for dense zirconia than porous zirconia (Fig. 3.5(a)) enabled the dense state to be stiff without visible buckling during compression (Figs. 3.3 and 3.7(b)). In contrast, porous zirconia with the significantly lower Young's moduli (Fig. 3.5(a)) led to zirconia crystal shear at approximately 30° shear angle (Fig. 3.2) and severe buckling of the material in compression (Figs. 3.2 and 3.6(b)).

Further, it is of interest to compare the measured Young's moduli of porous and dense zirconia micropillars with those obtained in nanoindentation with a Berkovich diamond indenter (Alao and Yin, 2014a; 2014b). The current moduli were underestimated by 22% and 35% for porous and dense states, respectively (Alao and Yin, 2014a; 2014b). The reasons for the underestimations may be due to the difference between micropillar compression and nanoindentation. Micropillar compression did not present confining pressures surrounding the micropillar except the vertical compression while nanoindentation with a Berkovich diamond indenter was accompanied with confining pressured beneath the indenter. A previous study by Espinosa et al. (2019) also found that that doubling micropillar sizes of sea urchin teeth had the higher Young's moduli by 30%. Further studies of the size effect on the Young's moduli for porous and dense zirconia micropillars will be conducted in the future.

The higher yield strength for dense zirconia than porous zirconia (Fig. 3.5(b)) enables the dense state to bear higher stresses without plastic deformation than the porous state. The higher fracture and compressive strengths for dense zirconia (Fig. 3.5(b)) indicates that the material is more capable of bearing more stresses than porous state. In comparison with strength properties for porous and dense zirconia materials measured at different scales, current micropillars had significantly higher values than those obtained in macro compressions. For instance, ice-templated porous zirconia materials with porosities of 35.3–75% had the compressive strength values from 197.1 ± 50.4 MPa to 4.5 ± 0.5 MPa (Zou et al., 2021), which were significantly lower than the compressive strength of 351 ± 46 MPa for the porous zirconia micropillars with porosity of 47.3–49.3 % (Fig. 3.5(b)). For dense zirconia, macro compression produced the yield strength from 2 GPa to 3.3 GPa depending on compressive conditions (Subhash and Nemat-Nasser, 1993), which were also significantly lower than of the yield strength of 6.7 ± 0.9 GPa for the dense zirconia micropillars (Fig. 3.5(b)). All these results indicate a clear size effect in the assessment of the mechanical strength of zirconia materials, highlighting the importance of testing volumes in the material properties (Composilvan and Anglada, 2016).

The significantly higher resilience for dense zirconia (Fig. 3.5(d)) enabled the material to absorb more energy in the elastic region than porous zirconia. While dense zirconia had much less ductility than porous state (Fig. 3.5(c)), the former had much higher toughness than the latter to absorb more energy prior to failure (Fig. 3.5(d)). This is in agreement with the much higher plane strain fracture toughness K_{IC} of 6.0 MPa $m^{1/2}$ for dense zirconia (Sakoda et al., 2018) than that of 0.8 MPa $m^{1/2}$ for porous state (Alao and Yin, 2016).

Plastic regions for porous and dense zirconia materials (Fig. 3.4) reveal stress variations, which may be associated with different deformation and strain mechanisms. For porous zirconia, they were correlated to zirconia crystals pushing outward and breakage near the shear surface (Fig. 3.2). The multiple stress variations may also be associated with alternative strain softening and hardening mechanisms (Fig. 3.4(a)). This is because pore network collapses and condensation in the plastic region alternatively occurred and continuous loading eventually led to more zirconia crystals pushing outward and the micropillar breaking (Fig. 3.2). The strain softening was also studied in micropillar compression of Al-Al_3Sc multilayer at displacement rate of 2 nm s^{-1} (Han et al., 2009).

The alternative strain softening and hardening for porous zirconia may be a new observation due to its weak pore network microstructure. There is a possibility of the strain softening in porous zirconia due to densification, which will be further studied.

For sintered zirconia, plastic deformation may be companied with dislocation movements by slipping around zirconia crystal boundaries, providing more dense structure and temporarily increased strength (or stain hardening) (Fig. 3.4(b)). The increased stresses resulted in zirconia crystals moving and rearranging. This strain hardening mechanism was also observed in single loading indentation of sintered zirconia at 10 mN peak load to lead to the plastic deformation (Alao et al., 2014b). Once the stresses exceeded the compressive strength, the stress drops occurred which may be correlated to microcrack propagation (Figs. 3.3 and 3.4(b)). With the increased microcrack propagation and delamination, the material eventually fractured (Figs. 3.3 and 3.4(b)).

Both porous and dense zirconia materials exhibited quasi-brittle failures in micropillar compression processes (Figs. 3.2, 3.3, 3.6 and 3.7). The quasi-brittle response is a mode where both plasticity and cracking deformation occurred before the material failure (Schwiedrzik et al., 2014). The plasticity could be defined as measurable deformation before failure takes place (Tandon and Faber, 1993). The quasi-brittle response has been observed in micropillar compressions of lamellar bone (Schwiedrzik et al., 2014) and cement (Shahrin and Bobko, 2019). In this study, both porous and dense zirconia micropillars revealed their ductility (Fig. 3.5(c)) as the measurable deformations prior to their failures. However, different quasi-brittle failure modes were observed for the two zirconia materials from analyses of their micropillar compression processes, deformations and damages (Figs. 3.2, 3.3, 3.6 and 3.7).

For porous zirconia, micropillar failures had mushroom buckling damage shapes along shear planes with localized cracking and delamination (Figs. 3.2 and 3.6). With the loading progression, high compressive stresses broke pore networks between zirconia crystals, fractured individual zirconia crystals and resulted in fragmentation and pulverization (Fig. 3.6). These broken pore networks acted as shear faults to initiate plastic buckling (Fig. 3.2(c)) and resulted in microcracks initiation and propagation, and fatal collapsing of the interconnected pore networks and (Fig. 3.6). Disseminated zirconia crystals moved and filled pores, resulting in zirconia crystals coalescence (Fig. 3.6). Buckling fracture was also found in macro compression of ice-templated porous zirconia

during which porosity played a key role in controlling the transition of a buckling fracture to brittle fracture (Zou et al., 2021). In nanoindentation of porous zirconia using a Berkovich tip, kink bands were observed in indentation imprints which were a form of plastic buckling (Alao and Yin, 2014a). The mushroom shape deformation was also detected when compress TiSiN/Ag multilayer coatings at ~ 4 $\times 10^{-3}$ s^{-1} strain rate (Dang et al., 2018).

For sintered zirconia, micropillar failures reveal a plastic crushing phenomenon emerged with plastic deformation, then originated with interganular and transgranular fractures and followed by delamination under uniaxial compression (Figs. 3.3 and 3.7). The material underwent the dislocation-dominate plastic deformation with increased micropillar diameters (Fig. 3.3). With increased stresses, dense zirconia micropillars had intergranular and transgranular microfractures, crack initiation and propagation (Fig. 3.7). These distributed microcracks resulted in the quasi-brittle fracture of zirconia crystals once the compressive stress exceeded the material strength (Figs. 3.7). The plastic crushing phenomenon was also found in micropillar compression of calcium-silicate-hydrates (C-S-H) as cement paste (Shahrin and Bobko, 2019).

The schematic models for porous and dense zirconia micropillar compression processes were proposed in Figs. 3.8. For porous zirconia (Fig. 3.8(a)), the mushroom buckling damage underwent elastic compression (Left), plastic buckling with horizontal expansion and pore networks breaking (Middle), and pore networks collapsing and buckling fracture (Right). For sintered zirconia (Fig. 3.8(b)), the plastic crushing phenomenon emerged from elastic compression (Left), plastic deformation with horizontal expansion (Middle), and interganular and transgranular fractures and delamination (Right). The mechanical properties of porous and dense zirconia micropillars investigated may provide useful knowledge on deformation and damage mechanisms of zirconia materials at the small scale. In the future, granular mechanics may be approached to better understand the mechanical behaviour of zirconia materials.

3.5 Conclusions

This study conducted *in-situ* SEM porous and dense zirconia micropillar compressions and the main conclusions are summarized as follows:

(a) Zirconia microstructures significantly influenced their micropillar compressive behaviors, revealing distinct quasi-brittle deformation and damage mechanisms. For porous zirconia, the quasi-brittle deformation and damage featured with mushroom buckling damage along shear planes with localized cracking and delamination resulted from weak interconnected pore networks breaking. For dense zirconia, the mechanism was reflected with a plastic crushing phenomenon of plastic deformation and microcrack initiation, cleavage and intergranular fractures, and delamination.

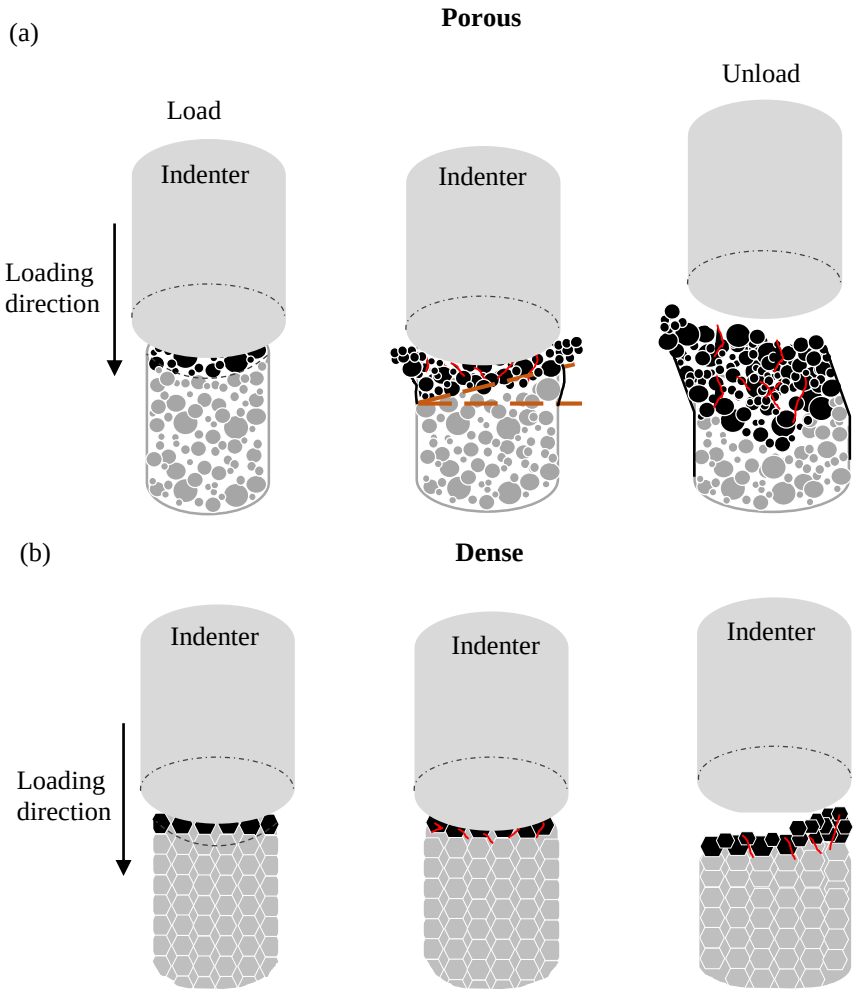

Fig. 3.8. Compression mechanics models for (a) porous and (b) dense zirconia micropillars.

(b) Stress variations in plastic regions were attributed to alternative strain softening and hardening mechanisms for porous zirconia and dislocation-induced strain hardening for dense zirconia.

(c) Dense zirconia yielded significantly higher Young's moduli, strengths (yield, fracture and compressive), resilience and toughness but much lower ductility than porous zirconia.

Credit Authorship Contribution Statement

Afifah Z. Juri: Conceptualization, Methodology, Investigation, Formal analysis, Validation, Data curation, Writing - original draft, Funding acquisition (PhD Scholarship, The University of Adelaide, Australia). **Animesh K. Basak**: Methodology, Investigation, Data curation, Writing - review & editing. **Ling Yin**: Conceptualization, Methodology, Validation, Writing - review & editing, Supervision, Project administration, Funding acquisition (Seed Grant, The University of Adelaide, Australia).

Declaration of Competing Interest

The authors declare that they have no known competing financial interests or personal relationships that could have appeared to influence the work reported in this paper.

Acknowledgements

This work was supported by a PhD scholarship and a seed grant in manufacturing and bio-manufacturing from the University of Adelaide.

References

Abaza, A., Laurencin, J., Nakajo, A., Hubert, M., David, T., Monaco, F., Lencer, C., Meille, S., 2022. Fracture properties of porous yttria-stabilized zirconia under micro-compression testing. J. Eur. Ceram. Soc. 42, 1656–1669. https://doi.org/10.1016/j.jeurceramsoc.2021.11.051.

Alao, A. R., Yin, L., 2014a. Nano-scale mechanical properties and behavior of pre-sintered zirconia. J. Mech.Behav. Biomed. Mater. 36, 21–31. https://doi.org/10.1016/j.jmbbm.2014.03.019.

Alao, A. R., Yin, L., 2014b. Loading rate effect on the mechanical behavior of zirconia in nanoindentation. Mater. Sci. Eng. 619, 247–255. https://doi.org/10.1016/j.msea.2014.09.101.

Alao, A. R., Yin, L., 2016. Assessment of elasticity, plasticity and resistance to machining-induced damage of porous pre-sintered zirconia using nanoindentation

techniques. J. Mater. Sci.Technol. 32, 402–410. https://doi.org/10.1016/j.jmst.2016.02.009.

Amat, N. F., Muchtar, A., Amril, M. S., Ghazali, M. J., Yahaya, N., 2018. Preparation of presintered zirconia blocks for dental restorations through colloidal dispersion and cold isostatic pressing. Ceramics International. 44, 6409–6416. https://doi.org/10.1016/j.ceramint.2018.01.035.

Basak, A. K., Pramanik, A., Prakash, C., 2019. Deformation and strengthening of SiC reinforced Al-MMCs during in-situ micro-pillar compression. Mater. Sci. Eng. A. 763, 138141. https://doi.org/10.1016/j.msea.2019.138141.

Camposilvan, E., Anglada, M., 2016. Size and plasticity effects in zirconia micropillars compression. Acta Mater. 103, 882–892. https://doi.org/10.1016/j.actamat.2015.10.047.

Chintapalli, R. K., Jimenez-Pique, E., Marro, F. G., Yan, H., Reece, M., Anglada, M., 2012. Spherical instrumented indentation of porous nanocrystalline zirconia. J. Eur. Ceram. Soc 32, 123–132. https://doi.org/10.1016/j.jeurceramsoc.2011.07.037.

Cho, J., Li, Q., Wang, H., Fan, Z., Li, J., Xue, S., Vikrant, K. S. N., Wang, H., Holland, T. B., Mukherjee, A. K., García, R. E., Zhang, X., 2018. High temperature deformability of ductile flash-sintered ceramics via in-situ compression. Nat. Commun. 9, 1–9. https://doi.org/10.1038/s41467-018-04333-2.

Csanádi, T., Szommer, P., Chinh, N. Q., Grasso, S., Dusza, J., Reece, M., 2016. Plasticity in ZrB_2 micropillars induced by anomalous slip activation. J. Eur. Ceram. Soc. 36, 389–394. https://doi.org/10.1016/j.jeurceramsoc.2015.10.035.

Csanádi, T., Wehrs, J., Grasso, S., Reece, M., Michler, J., Dusza, J., 2019. Anomalous slip of ZrB_2 ceramic grains during in-situ micropillar compression up to 500 C. Int. J. Refract. Hard Met. 80, 270–276. https://doi.org/10.1016/j.ijrmhm.2019.01.021.

Dang, C., Olugbade, T., Fan, S., Zhang, H., Gao, L., Li, J., Lu, Y., 2018. Direct quantification of mechanical responses of TiSiN/Ag multilayer coatings through uniaxial compression of micropillars. Vacuum. 156, 310–316. https://doi.org/10.1016/j.vacuum.2018.07.048.

Dehm, G., Jaya, B. N., Raghavan, R., Kirchlechner, C., 2018. Overview on micro-and nanomechanical testing: New insights in interface plasticity and fracture at small

length scales. Acta Mater. 142, 248–282. https://doi.org/10.1016/j.actamat.2017.06.019.

Depprich, R., Zipprich, H., Ommerborn, M., Mahn, E., Lammers, L., Handschel, J., Naujoks, C., Wiesmann, H. P., Kübler, N. R., Meyer, U., 2008. Osseointegration of zirconia implants: an SEM observation of the bone-implant interface. Head Face Med. 4, 1–7. https://doi.org/10.1186/1746-160X-4-25.

Denry, I., Kelly, J.R., 2008. State of the art of zirconia for dental applications. Dent. Mater. 24, 299–307. https://doi.org/10.1016/j.dental.2007.05.007.

Denry, I., Holloway, J. A., 2010. Ceramics for dental applications: a review. Mater. 3, 351–368. https://doi.org/10.3390/ma3010351.

Espinosa, H. D., Zaheri, A., Nguyen, H., Restrepo, D., Daly, M., Frank, M., McKittrick, J., 2019. In situ wear study reveals role of microstructure on self-sharpening mechanism in sea urchin teeth. Matter 1, 1246–1261. https://doi.org/10.1016/j.matt.2019.08.015.

Frick, C. P., Clark, B. G., Orso, S., Schneider, A. S., Arzt, E., 2008. Size effect on strength and strain hardening of small-scale [111] nickel compression pillars. Mater. Sci. Eng. 489, 319–329. https://doi.org/10.1016/j.msea.2007.12.038.

Han, S. M., Phillips, M. A., Nix, W. D., 2009. Study of strain softening behavior of Al–Al_3Sc multilayers using microcompression testing. Acta Mater. 57, 4473–4490. https://doi.org/10.1016/j.actamat.2009.06.007.

Juri, A. Z., Basak, A. K., Yin, L., 2021. Microstructural responses of zirconia materials to in-situ SEM nanoindentation. J. Mech. Behav. Biomed. Mater. 118, 104450. https://doi.org/10.1016/j.jmbbm.2021.104450.

Kosai, K., Yan, J., 2020. Effects of cyclic loading on subsurface microstructural changes of zirconia polycrystals in nanoscale mechanical processing. Int. J. Mach. Tools Manuf. 159, 103626. https://doi.org/10.1016/j.ijmachtools.2020.103626.

Manicone, P.F., Iommetti, P.R., Raffaelli, L., 2007. An overview of zirconia ceramics: basic properties and clinical applications. J. Dent. 35, 819–826. https://doi.org/10.1016/j.jdent.2007.07.008

Miyazaki, T., Nakamura, T., Matsumura, H., Ban, S., Kobayashi, T., 2013. Current status of zirconia restoration. J. Prosthodont. Res. 57, 236–261. https://doi.org/10.1016/j.jpor.2013.09.001

Moser, B., Kuebler, J., Meinhard, H., Muster, W., Michler, J., 2005. Observation of instabilities during plastic deformation by in-situ SEM indentation experiments. Adv. Eng. Mater. 7, 388–392. https://doi.org/10.1002/adem.200500049.

Oliver, W.C., Pharr, G.M., 1992. An improved technique for determining hardness and elastic modulus using load and displacement sensing indentation experiments. J. Mater. Res. 7, 1564–1583. https://doi.org/10.1557/JMR.1992.1564.

Oliver, W. C., Pharr, G. M., 2004. Measurement of hardness and elastic modulus by instrumented indentation: Advances in understanding and refinements to methodology. J. Mater. Res. 19, 3–20. https://doi.org/10.1557/jmr.2004.19.1.3.

Ramachandramoorthy, R., Yang, F., Casari, D., Stolpe, M., Jain, M., Schwiedrzik, J., Best, J. P., 2021. High strain rate in situ micropillar compression of a Zr-based metallic glass. J. Mater. Res. 1–12. https://doi.org/10.1557/s43578-021-00187-5.

Rekow, E.D., Silva, N.R.F.A., Coelho, P.G., Zhang, Y., Guess, P., Thompson, V.P., 2011. Performance of dental ceramics: challenges for improvements. J. Dent. Res. 90, 937–952. https://doi.org/10.1177/0022034510391795.

Ritzberger, C., Apel, E., Höland, W., Peschke, A., Rheinberger, V.M., 2010. Properties and clinical application of three types of dental glass-ceramics and ceramics for CAD-CAM technologies. Materials 3, 3700–3713. https://dx.doi.org/10.3390%2Fma3063700.

Sakoda, S., Nakao, N., Watanabe, I., 2018. The effect of abrading and cutting instruments on machinability of dental ceramics. J. Mater. Sci. Mater. Med. 29, 34. https://doi.org/10.1007/s10856-018-6031-y.

Schwiedrzik, J., Raghavan, R., Bürki, A., LeNader, V., Wolfram, U., Michler, J., Zysset, P., 2014. In situ micropillar compression reveals superior strength and ductility but an absence of damage in lamellar bone. Nat. Mater. 13, 740–747. https://doi.org/10.1038/nmat3959.

Shahrin, R., Bobko, C. P., 2019. Micropillar compression investigation of size effect on microscale strength and failure mechanism of Calcium-Silicate-Hydrates (CSH) in cement paste. Cement Concrete Res. 125, 105863. https://doi.org/10.1016/j.cemconres.2019.105863.

Shin, C., Jin, H. H., Sung, H., Kim, D. J., Choi, Y. S., Oh, K., 2013. Evaluation of irradiation effects on fracture strength of silicon carbide using micropillar compression tests. Exp. Mech. 53, 687–697. https://doi.org/10.1007/s11340-012-9678-1.

Sneddon, I. N., 1965. The relation between load and penetration in the axisymmetric Boussinesq problem for a punch of arbitrary profile. Int. J. Eng. Sci. 3, 47–57. https://doi.org/10.1016/0020-7225(65)90019-4.

Stanishevsky, A., Nagaraj, B., Melngailis, J., Ramesh, R., Khriachtchev, L., McDaniel, E., 2002. Radiation damage and its recovery in focused ion beam fabricated ferroelectric capacitors. J. Appl. Phy. 92, 3275–3278. https://doi.org/10.1063/1.1489069.

Subhash, G., Nemat-Nasser, S., 1993. Dynamic stress-induced transformation and texture formation in uniaxial compression of zirconia ceramics. J. Am. Ceram. Soc. 76, 153–165. https://doi.org/10.1111/j.1151-2916.1993.tb03701.x.

Tandon, S., Faber, K. T., 1993. Fracture of brittle and quasi-brittle engineering materials. 209–239. https://resolver.caltech.edu/CaltechAUTHORS:20140919-144538556.

Van Staden, R. C., Guan, H., Loo, Y. C., 2006. Application of the finite element method in dental implant research. Comput. Methods Biomech. Biomed. Eng. 9, 257–270. https://doi.org/10.1080/10255840600837074.

Wang, J., Stanford, N., 2015. Investigation of precipitate hardening of slip and twinning in Mg5% Zn by micropillar compression. Acta Mater. 100, 53–63. https://doi.org/10.1016/j.actamat.2015.08.012.

Zinelis, S., Thomas, A., Syres, K., Silikas, N., Eliades, G., 2010. Surface characterization of zirconia dental implants. Dent. Mater. 26, 295–305. https://doi.org/10.1016/j.dental.2009.11.079.

Zou, J., Xiong, H., Huang, Y., Zhou, K., Zhang, D., 2021. Fracture mode and compressive strength of ice-templated porous zirconia. Ceram. Int. 47, 17373–17382. https://doi.org/10.1016/j.ceramint.2021.03.051.

Chapter 4 *In-situ* SEM Nanoindentation

This chapter consists of the published journal article detailed below:

Juri, A. Z., Basak, A. K., Yin, L., 2021. Microstructural responses of Zirconia materials to in-situ SEM nanoindentation. J. Mech. Behav. Biomed. Mater. 118, 104450. https://doi.org/10.1016/j.jmbbm.2021.104450.

Statement of Authorship

Title of Paper	Microstructural responses of Zirconia materials to *in-situ* SEM nanoindentation.
Publication status	■ Published ☐ Accepted for publication ☐ Submitted for publication ☐ Unpublished and unsuited work written in manuscript style
Publication details	*Juri, A. Z., Basak, A. K., Yin, L., 2021. Microstructural responses of Zirconia materials to in-situ SEM nanoindentation. J. Mech. Behav. Biomed. Mater. 118, 104450. https://doi.org/10.1016/j.jmbbm.2021.104450*

Principal Author

Name of Principal Author (Candidate)	Afifah Zakiyyah Juri
Contribution to the Paper	Conceptualization, Methodology, Investigation, Formal analysis, Validation, Data curation, Writing - original draft, Funding acquisition (PhD scholarship).
Overall percentage (%)	70
Certification:	This paper reports on original research I conducted during the period of my Higher Degree by Research candidature and is not subject to any obligations or contractual agreements with a third party that would constrain its inclusion in this thesis. I am the primary author of this paper.
Signature	Date 07/07/2022

Co-Author Contributions

By signing the Statement of Authorship, each author certifies that:

i. the candidate's stated contribution to the publication is accurate (as detailed above);
ii. permission is granted for the candidate in include the publication in the thesis; and
iii. the sum of all co-author contributions is equal to 100% less the candidate's stated contribution.

Name of Co-Author	Animesh Kumar Basak		
Contribution to the Paper	Writing – review and editing, Methodology, Investigation, Data curation.		
Signature		ate	08/06/2022

Name of Co-Author	Ling Yin		
Contribution to the Paper	Writing – review and editing, Validation, Supervision, Project administration, Methodology, Investigation, Funding acquisition, Formal analysis, Conceptualization.		
Signature		Date	07/07/2022

Microstructural responses of Zirconia materials to in-situ SEM nanoindentation

Afifah Z. Juri[1], Animesh K. Basak[2], Ling Yin[1,*]

[1]School of Mechanical Engineering, The University of Adelaide, Adelaide, SA 5005, Australia

[2]Adelaide Microscopy, The University of Adelaide, Adelaide, SA 5005, Australia

*Corresponding Author: afifah.juri@adelaide.edu.au, ling.yin@adelaide.edu.au

Abstract Development of optimal shaping processes for pre-sintered and sintered zirconia materials requires a fundamental understanding of damage and deformation mechanisms at small-scale contacts with diamond tools. This paper reports on responses of zirconia materials with distinct microstructures to nanoindentation associated with diamond machining using a Berkovich diamond indenter. *In-situ* nanoindentation was performed in a scanning electron microscope (SEM) and in-process filmed to record small contact events. Indentation morphology was SEM-mapped at high-magnifications. Although both pre-sintered porous and sintered dense zirconia materials mechanically revealed the quasi-plastic behavior in indentation, there were distinct responses of the two materials to quasi-plasticity at the microstructural level. For pre-sintered porous zirconia, the quasi-plasticity was attributed to shear faults resulting from breaking pore networks as microstructurally discrete interfaces, to lead to compression, fragmentation, pulverization and microcracking of zirconia crystals in indentation imprints. In contrast, sintered dense zirconia had shear band-induced quasi-plastic deformation, accompanied with localized tensile microfracture. A material index associated with the mechanical properties ranked the lower quasi-plasticity for pre-sintered porous zirconia than its sintered dense state, predicting more machining-induced damage in the former than the latter. Significantly higher indentation imprint volumes induced in indented pre-sintered porous zirconia than sintered dense state previses higher machining efficiency for the former than the latter. The microstructure-dependent indentation mechanisms provide the fundamental knowledge into micromechanics of abrasive machining of zirconia materials and may lead to a new microstructural design for zirconia materials to achieve a balanced machining efficiency and damage control.

4.1 Introduction

Zirconia is an outstandingly strong ceramic and has been extensively applied as dental restorative material for crowns and bridges (Kelly and Benetti, 2011; Rekow et al., 2011). This is due to its high strength and fracture toughness, excellent biocompatibility, high iconic conductivity and low thermal conductivity (Denry and Kelly, 2008; Manicone et al., 2007; Miyazaki et al., 2013). The enhanced mechanical properties of zirconia is due to its transformation toughening mechanism in its microstructure (Garvie et al., 1975; Piconi and Maccauro, 1999; Guazzato et al., 2004; Garvie and Nicholson, 1972). This mechanism results in the formation of a transformation zone, which protects propagating crack tips and prevents further crack propagation. Thus, zirconia has the highest fracture toughness in the ceramic family (Denry and Kelly, 2008).

Zirconia is available in its pre-sintered porous or sintered dense state (Denry and Kelly, 2008). It is manufactured for dental restorations using dental computer-assisted design and manufacturing (CAD/CAM) systems (Alao et al., 2017; Miyazaki et al., 2013). Different processes are applied to pre-sintered porous and sintered dense zirconia materials due to their differences in microstructure and mechanical properties. Pre-sintered porous zirconia with a porous microstructure has a low strength of 70 ± 20 MPa (Ritzberger et al., 2010), and thus is machined in soft machining process with low stiffness machines (Alao et al., 2017). Sintered dense zirconia with a dense microstructure has a high strength of 1050 ± 150 MPa (Wendler et al., 2017), and therefore is machined in hard machining process with high stiffness machines (Yin and Huang, 2004).

To advance machining processes and uncover wear performance of advanced materials, a comprehensive understanding of damage mechanisms at small-scale contacts is required. This is because the basic science of attendant deformation and removal modes in contact events is the first step towards the optimization of removal processes and wear performance of materials (Lawn et al., 2021). Indentation testing as an essential technique plays a key role in studies of micromechanics of materials subject to abrasive invasions (Reece at el., 1992; Dey and Mukhopadhyay, 2014; Zhang and Basak, 2013). It mimics the scenarios of contact and hydrostatic stresses that exert on materials during abrasive machining or wear process (Malkin and Hwang, 1996; Basak and Zhang, 2018). Therefore, indentation testing is representative of the mechanics involved in dental CAD/CAM diamond machining processes (Xu et al., 1996).

Previous indentation studies of zirconia have been conducted at micro- (Li et al., 2020a; Werbach et al., 2019; Zhang and Lawn, 2019) and nano-scales (Alao and Yin, 2014a, 2014b, 2015, 2016). In particular, the indentation behavior of zirconia at the nano-scale is vital because similar contact conditions took place in diamond abrasive machining during which each diamond abrasive acts as a cutting tip. *Ex-situ* indentation and scanning probe microscopy (SPM) imaging techniques were applied to nanoindentation of pre-sintered porous and sintered dense zirconia materials at the maximum peak load of 10 mN and loading rates of 0.1–2 mN/s (Alao and Yin, 2014a, 2014b, 2015, 2016). The investigated properties include contact hardness, Young's modulus, and resistance to plasticity. Pop-in events were observed in these zirconia materials, corresponding to pore closure and opening and kink band formation for porous zirconia and nanoindentation-induced strain softening for dense zirconia (Alao and Yin, 2014a, 2014b). These studies have provided insights into the nano-scale mechanical behavior of these zirconia materials. However, the microstructural responses of these materials to indentation are not yet understood because SPM is not sensitive to material microstructures although it has high (sometimes atomic) resolution for geometrical scanning and imaging. In addition, induced deformation and damage in the materials during indentation cannot be simultaneously observed, which limits the elucidation of how the materials behave during the process.

Nanoindentation techniques have also been applied to determine the mechanical properties of zirconia materials after laser patterning, indicating slightly reduced hardness and Young's modulus due to laser-induced microcracking (Roitero et al., 2018). In nanoindentation studies of the effect of accelerated aging on sintered zirconia materials at peak loads of 5000–6000 μN, likely cracking events were found on the loading curves and aging had no effect on the Young's modulus and hardness aging (De Souza et al., 2017). Additionally, the mechanical properties of glass-glazed sintered zirconia (Campos et al., 2021) and sol-gel silica coated sintered zirconia (Reis et al., 2019) were measured using nanoindentation.

Further, micro pop-in events were reported during nanoindentation at 10–1000 mN in zirconia toughened alumina ceramic composites containing different concentrations of Y_2O_3 stabilized zirconia (Maiti et al., 2019a, 2019b; 2020). In these studies, field emission scanning electron microscopy (FESEM) was applied to reveal shear induced deformation

and microcracking related to pop-in events in loading and unloading curves. Indentation size effects on these materials were also studied (Maiti et al., 2019a; 2020). This high-magnification imaging technique has not been widely used to analyze other nanoindentation imprints, which, in fact, is a great tool to reveal nanoindentation behavior at the microstructural level.

In-situ nanoindentation is conducted inside a scanning electron microscope (SEM). The technique enables indentation-induced deformation and damage to be captured and viewed in real time under the SEM to understand the material behavior in micro- or nano-scale loading and unloading conditions by a diamond indenter (Huang and Zhao, 2014; Ghisleni et al., 2009). The indentation process can correlate any discontinuous events in loading and unloading curves with physical explanations (Nili et al., 2013; Nowak et al., 2010). *In-situ* indentation studies have performed for thin films (Rabe et al., 2004; Rzepiejewska-Malyska et al., 2009; Wasmer et al., 2013) and bulk materials (Moser et al., 2005; Deuschle et al., 2008). For example, Rabe at al. (2004) conducted *in-situ* indentation on TiN/SiN_x coatings and diamond-like carbon films using a cube corner indenter. The series of real-time SEM micrographs during the indentation provided insights into the material deformation behavior, such as cracks and pile ups for TiN/SiN_x coatings and significant pop-in for diamond-like carbon films. Wasmer et al., (2013) used wedge and conical indenters on gallium arsenide wafers. The results provide the correlation of nanoindentation cracking events to the occurrence of pop-ins in the force-displacement curves. These studies have provided a valuable understanding and knowledge of the capabilities of *in-situ* indentation techniques for various materials.

Although extensive studies on nanoindentation of zirconia (e.g., Alao and Yin, 2014a, 2014b; De Souza et al., 2017; Roitero et al., 2018; Reis et al., 2019; Campos et al., 2021) and zirconia-related materials (e.g., Maiti et al., 20019a, 2019b; 2020) have been studied. However, microstructural responses of two important pre-sintered porous and sintered dense zirconia materials widely used in dentistry to nanoindentation have not been in-process investigated during nanoindentation using high magnification imaging techniques. The deep analysis of nanoscale deformation mechanisms bridging induced deformation characteristics and microstructural features is missing, which jeopardizes the development of new manufacturing techniques for these materials for high quality and durability. Therefore, the potential to uncover the nanoindentation behavior and

respective deformation and damage mechanisms for zirconia materials with distinct microstructures remains unaccomplished. Further, from the machinability aspect of zirconia materials in dental CAD/CAM abrasive machining processes, the investigation of indentation mechanisms is essential because fundamental machining mechanics of the materials can be mimicked in a simplified way through *in-situ* nanoindentation.

This paper aims to investigate the indentation behavior of pre-sintered porous and sintered dense zirconia materials using *in-situ* SEM nanoindentation techniques. All indentation processes were performed in a SEM, which simultaneously filmed all phenomena occurring in the indentation processes to understand small contact mechanics events linking to force-displacement curves. Residual indentation imprints were further analyzed at high-magnifications under the SEM to reveal the role of microstructure in indentation deformation and damage mechanisms for the two materials. Notably, our results show that both zirconia materials exhibited a quasi-plastic response to indentation, with distinctions at the microstructural level. The behavior in the porous state was related to shear faults arising from breaking pore networks as microstructurally discrete interfaces, to lead to compression, fragmentation, pulverization and microcracking of zirconia crystals. In contrast, the dense state was featured with the shear band formation to result in plastic deformation and localized tensile microfracture of zirconia crystals. These mechanisms were synergistically associated with the material removal and damage tolerance in CAD/CAM diamond abrasive machining, and are important to the application of zirconia materials subject to the abrasion, erosion and wear processes as dental materials.

4.2 Experimental Procedure

4.2.1 Materials and Specimen Preparation

Porous zirconia was selected from a pre-sintered zirconia block with dimensions of 15 mm × 15 mm × 50 mm (IPS e.max ZirCAD, Ivoclar Vivadent), which is a machinable pre-sintered yttria-stabilized zirconia polycrystal designed for dental CAD/CAM milling units to make crowns and bridges (Denry and Kelly, 2008). The material consists of approximately 87–95 wt% ZrO_2 and 4–6 wt% Y_2O_3 as primary compositions together with 1–5 wt% HfO_2 and 0.1–1 wt% Al_2O_3 as additives (Ritzberger et al., 2010). Pre-sintered zirconia is generally fabricated by cold isostatic pressing of zirconia powders,

followed by pre-sintering heat treatment at temperatures of approximately 850°C to obtain pre-sintered blank with high porosity (Amat et al., 2018; Denry and Kelly 2008). For indentation studies, porous zirconia specimens were obtained by cutting the pre-sintered block into 2 mm thick slices using a low speed diamond saw machine (Struers Minitom, Struers Inc., USA) with water as both a coolant and a lubricant, detailed in Alao and Yin, 2014a. A diamond saw blade, 450 μm thick and 125 mm in diameter was used to slice specimens at a cutting pressure of 300 g and a cutting speed of 250 rpm. To avoid surface tilting during indentations, top and bottom surfaces of 15 mm × 15 mm in sliced specimens were precisely ground using 600-grit alumina abrasives to ensure their parallelity for 5–10 min using a grinding/polishing machine (Northern Petrographics Pty. Ltd, Australia). Prior to polishing, ground specimens were ultrasonically bathed in water. Top specimen surfaces were polished to obtain an optical surface quality using the grinding/polishing machine with a wool cloth polishing disc with diamond pastes of 0.5–1 μm grit sizes and water as a polishing lubricant. The polishing was conducted at a disk rotational speed of 80 rpm and an applied load of 2 kg. All polished surfaces were assessed using SPM (NT-MDT NTEGRA, Hysitron, USA), achieving the root-mean-squared surface roughness, S_q, of approximately 72 nm in scanned areas of 50 × 50 μm (Alao and Yin, 2014a). For microstructural analysis, a fractured pre-sintered zirconia specimen was also obtained from the pre-sintered block.

Dense zirconia specimens were obtained by sintering of polished pre-sintered specimens in a furnace (MTI GSL1500X, USA) to 1300 °C for 2 h at 10 °C/min heating rate and then naturally cooled to room temperature following the specifications for dental zirconia restorations (Denry and Holloway, 2010). For indentation testing, sintered dense zirconia specimens were repolished using the same polishing procedures for pre-sintered zirconia to remove sintering-induced morphology changes due to grain coarsening, shrinkage, residual stresses and monoclinic to tetragonal phase transformation (Alao and Yin, 2014b). Repolished zirconia surfaces were assessed using the SPM, obtaining the root-mean-squared surface roughness, R_q, of approximately 7.7 nm in scan areas of 50 μm × 50 μm (Alao and Yin, 2014b). For microstructural analysis, a fractured sintered dense zirconia specimen was also obtained from a sintered specimen.

SEMs (FEI Helios Nanolab 600 and FEI Quanta 450 FEG ESEM, Thermo Fisher SCIENTIFIC, USA) were used to observe microstructures of polished and fractured pre-

sintered porous and sintered dense specimens, respectively. Fig. 4.1(a) shows SEM micrographs of the pre-sintered porous zirconia microstructure and morphology after polishing (left) and after fracture (right), revealing its isolated and interconnected porous microstructure with approximately 300 nm grains in diameter. The reported porosity is 47.3–49.3 vol.% porosity and density is 3.0–3.21 g/cm^3 (Ritzberger et al., 2010). Reported mechanical properties of pre-sintered porous zirconia include the biaxial strength of approximately 50–90 MPa (Ritzberger et al., 2010), the fracture toughness of 0.8 MPa.m$^{1/2}$ (Alao and Yin, 2016), and the Poisson's ratio of 0.235 provided by Ivoclar Vivadent. Fig. 4.1(b) shows SEM micrograph of sintered dense zirconia microstructure after polishing (left) and after fracture (right), demonstrating a highly dense microstructure with grain sizes of 300–500 nm in diameter. The reported porosity is less than 0.5% and density is 6.09 g/cm^3 (Ritzberger et al., 2010). Reported mechanical properties of sintered dense zirconia include the biaxial strength of approximately 1300 MPa (Sakoda et al., 2018), the fracture toughness of 6.0 MPa.m$^{1/2}$ (Sakoda et al., 2018), and the Poisson's ratio of 0.3 (Ereifej, et al., 2011).

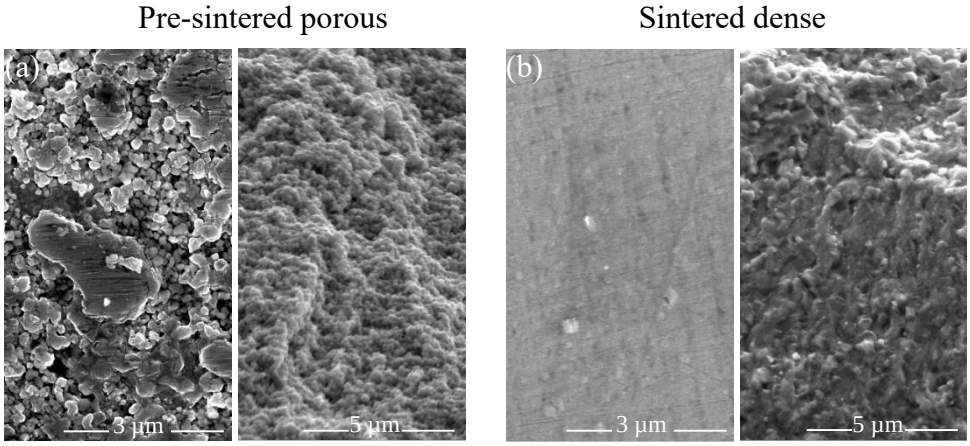

Fig. 4.1. SEM micrographs of (a) polished (left) and fractured (right) surfaces of pre-sintered porous zirconia and (b) polished (left) and fractured (right) surfaces of sintered dense zirconia.

Both pre-sintered porous and sintered dense zirconia specimens were further cut into dimensions of 5 mm × 5 mm × 2 mm to meet the *in-situ* indentation specimen size requirement using a diamond saw. They were cleaned using acetone and dried naturally prior to the testing.

4.2.2 *In-situ* SEM Nanoindentation

In-situ nanoindentation was conducted using an SEM picoindententer system (PI 88, Hysitron, USA) installed with a Berkovich diamond indenter inside the SEM (FEI Helios Nanolab 600, Thermo Fisher SCIENTIFIC, USA). The indentation system contains a control module with 78 kHz feedback rate and data acquisition up to 39 kHz to capture transient events in indentation processes. It is also equipped with a specimen tile in a rotation stage with 5 degrees of freedom, a load cell with a maximum load of 500 mN, an electrical characterization module enabling simultaneous measurement of electrical and mechanical properties in indentations processes. Prior to the testing, the indentation system was calibrated using standard fused silica.

In-situ nanoindentation tests were performed under a load-controlled mode on both pre-sintered porous and sintered dense zirconia specimens at 500 mN peak load and 2 mN/s loading and unloading rate. Each indentation process was real-time filmed to capture all mechanical characteristics of the process using the SEM. Two magnifications of 2,500 × and 5,000 × were selected to film indentation processes for pre-sintered porous and sintered dense zirconia materials, respectively, to have clear observations of larger indentation imprints in the former and smaller in the latter. Each SEM film for an indentation was shot during a diamond loading-unloading process for 500 s at a frame rate of 25 frame/s, and thus contained 12,500 frames. Three films for three repeated indentations at different locations of each material specimen were shot. In total, 6 films were shot with 75,000 SEM frames. Meanwhile, all loading-unloading force-displacement curves were automatically recorded by the picoindentation system.

4.2.3 Nanoindentation Properties

The mechanical properties and indentation geometries for both pre-sintered porous and sintered porous zirconia materials were determined through TriboScan software loaded on the *in-situ* nanoindentation system based on the Oliver-Pharr method (Oliver and Pharr, 1992). These included the contact hardness H_c and the Young's modulus E, as well as the contact indentation depth h_c, the maximum indentation depth h_{max}, and the final indentation depth h_f. The contact depth h_c was determined from the intercept of the unloading slope against the displacement axis (Oliver and Pharr, 1992). The contact hardness can be determined by the following equation (Oliver and Pharr, 1992):

$$H_c = \frac{P_{max}}{A(h_c)} \quad (4.1)$$

where H_c is the contact hardness, P_{max} is the maximum force, and $A(h_c)$ is the contact area, which is a function of the contact depth h_c. The reduced modulus E_r, determined from the slope of the unloading curve at the maximum load and the contact area, is also related to the Young's modulus of the specimen as (Stillwell and Tabor, 1961):

$$\frac{1}{E_r} = \frac{1 - v_{specimen}^2}{E_{specimen}} + \frac{1 - v_{indenter}^2}{E_{indenter}} \quad (4.2)$$

where $E_{specimen}$ and $v_{specimen}$ are the Young's modulus and the Poisson's ratio of the specimen, respectively, whereas $E_{indenter}$ and $v_{indenter}$ are the Young's modulus and the Poisson's ratio of the indenter, respectively. For a standard diamond indenter probe, $E_{indenter}$ is 1140 GPa and $v_{indenter}$ is 0.07 (Oliver and Pharr, 1992). For pre-sintered porous and sintered dense zirconia the v_{sample} are 0.235, which was provided by Ivoclar Vivadent, and 0.3 (Ereifej, et al., 2011), respectively. The Young's modulus of the indented specimen can be calculated using the following expression:

$$E_{specimen} = (1 - v^2)\left[\frac{1}{E_r} - \frac{(1 - v_{indenter}^2)}{E_{indenter}}\right]^{-1} \quad (4.3)$$

The mean values and standard deviations of indentation depths and properties were obtained from the three repeated indentations in each material specimen. *T*-test at 5% significant level was conducted to compare the measured indentation depths and properties between the two zirconia materials.

4.2.4 High-Magnification SEM Nanoindentation Morphology

After *in-situ* nanoindentations, microstructural changes of indented specimens were also observed under the SEM at high magnifications of up to 20,000 ×. Indentation apexes, diagonals, corners, edges and areas were analysed to understand the indentation mechanics at the microstructural level for the two materials.

4.3 Results

4.3.1 *In-situ* SEM indentations

Viewing of the large amount of *in-situ* SEM nanoindentation images did not find visible pop-in and pop-out sudden events, such as cracks and fractures, for both pre-sintered porous and sintered dense zirconia materials during indentation processes at the magnifications applied. Figs. 4.2(a), 4.2(c) and 4.2(e) reveal a typical loading and unloading cycle on a pre-sintered porous zirconia specimen using the Berkovich diamond indenter. During loading (Figs. 4.2(a) and 4.2(c)), the Berkovich diamond indenter tip revealing a large curvature radius bluntly penetrated into the material with hardly any deformation visible in the vicinity of the indentation. As shown in Fig. 4.2(e), a plastically deformed indentation residual imprint appeared without visible cracks during unloading at the applied magnification of 2,500 ×. Figs. 4.2(b), 4.2(d) and 4.2(f) demonstrate a typical loading and unloading cycle on a sintered dense zirconia specimen using the Berkovich diamond indenter. During loading (Figs. 4.2(b) and 4.2(d)), there is no visible deformation of the material during the blunt penetration by the Berkovich diamond indenter tip. During unloading (Fig. 4.2(f)), a much smaller plastic indention imprint with clear edge pile-ups was revealed. No cracks can be found at the applied magnification of 5,000 ×.

4.3.2 Nanoindentation Properties

Fig. 4.3 shows the force-displacement curves for the three nanoindentations at 500 mN peak load and 2 mN/s loading for pre-sintered porous and sintered dense zirconia materials, respectively. All curves for the two materials show smooth with no noticeable discontinuities such as pop-in and pop-out events. This smooth feature of the force-displacement curves reflects the plastic behavior of the materials.

Fig. 4.4 shows the final indentation depths (h_f), the contact indentation depths (h_c) and the maximum indentation depths (h_{max}) of pre-sintered porous and sintered dense zirconia materials, respectively. The final indentation depths ranged 3300 ± 200 nm for pre-sintered porous zirconia, at least 4 times more than the ones of 758 ± 162 nm for sintered dense zirconia. The contact indentation depths scaled 4483 ± 214 nm for pre-sintered porous zirconia, 3 times more than the ones of 1416 ± 172 nm for sintered dense zirconia.

The maximum indentation depths reached 5076 ± 183 nm for pre-sintered zirconia, approximately 2.5 times more than the ones of 2038 ± 65 nm for sintered dense zirconia. The paired *t*-tests reveal all significant differences between pre-sintered porous and dense zirconia materials with respect to the final, contact, and maximum indentation depths under the applied load condition ($p < 0.05$).

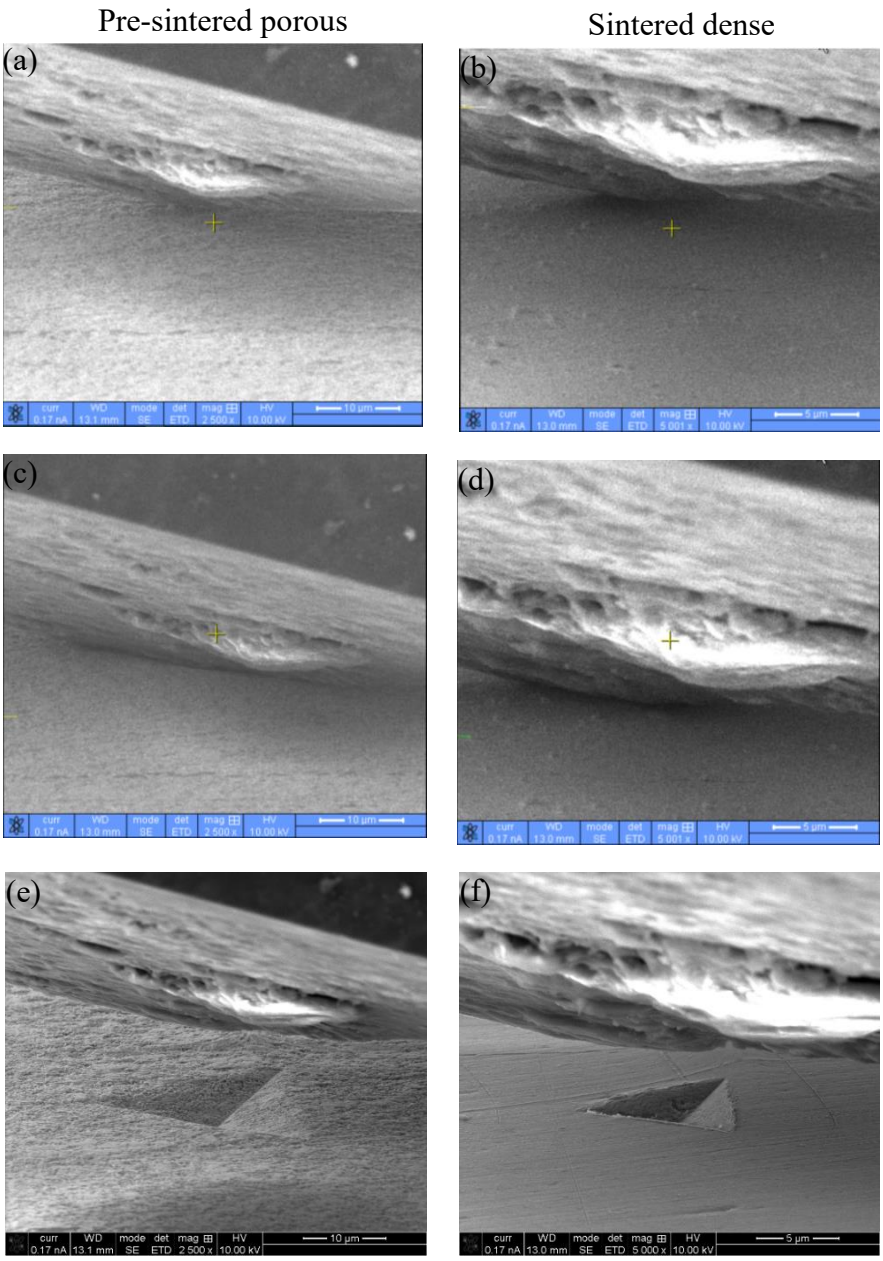

Fig. 4.2. In-situ SEM micrographs. Initial loading contacts between the Berkovich tip and the surfaces of (a) pre-sintered porous and (b) sintered dense zirconia materials; Peak load contacts between the Berkovich tip and the surfaces of (c) pre-sintered porous and (d) sintered dense zirconia materials; Indentation residual imprints of (e) pre-sintered porous and (f) sintered dense zirconia materials.

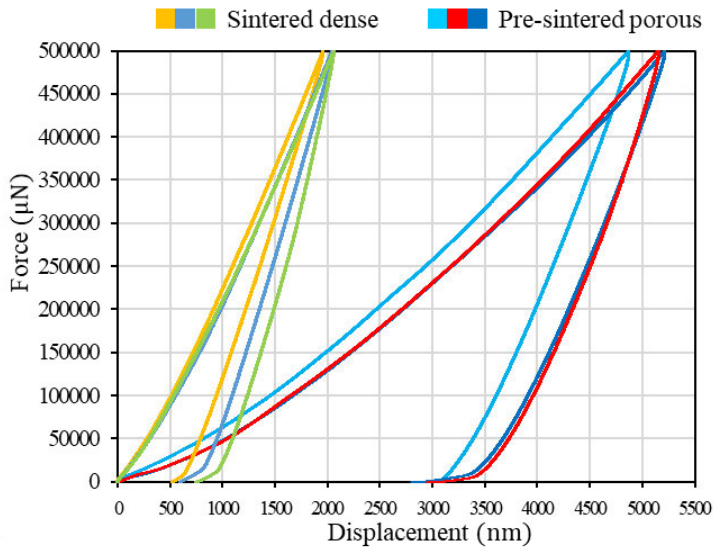

Fig. 4.3. Force-displacement curves of in-situ nanoindentation of pre-sintered porous and sintered dense zirconia materials.

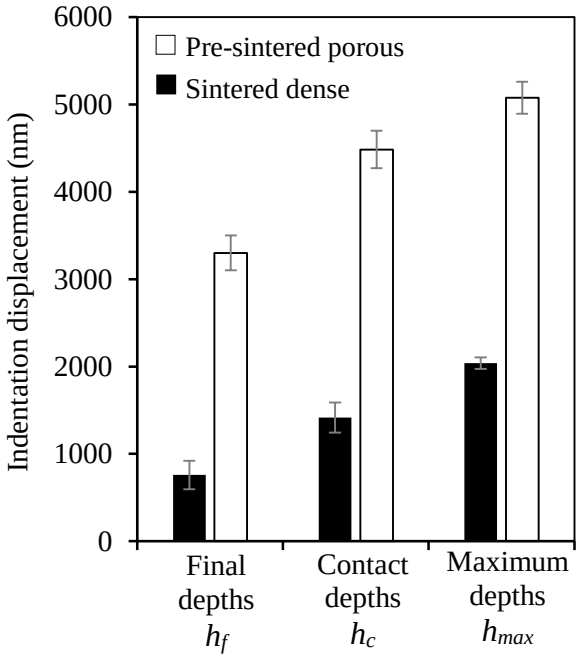

Fig. 4.4. Indentation displacements of final depths (h_f), contact depths (h_c) and maximum depths (h_{max}) for pre-sintered porous and sintered dense zirconia materials.

Fig. 4.5 shows the contact hardness and Young's modulus values for pre-sintered porous and sintered dense zirconia materials. The hardness for the latter was valued at 21.09 ± 4.20 GPa, approximately 11 times higher than the former at 1.92 ± 0.22 GPa. The modulus for the latter scaled 111.6 ± 10.9, more than 3 times higher than the former with 32.6 ± 5.3 GPa.

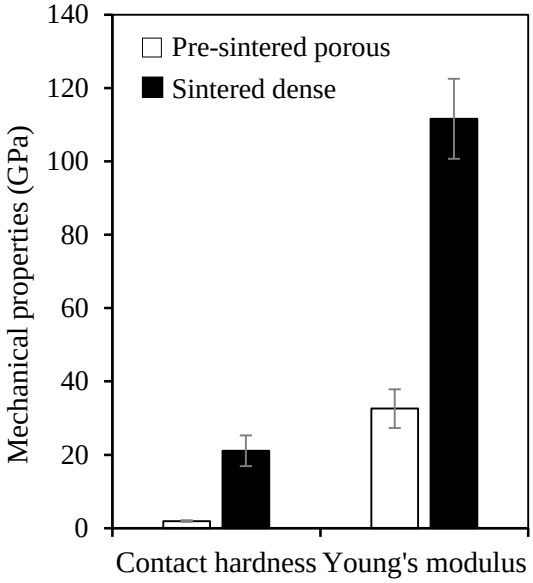

Fig. 4.5. Mechanical properties of the contact hardness and the Young's modulus values of pre-sintered porous and sintered dense zirconia materials.

4.3.3 High-Magnification SEM Nanoindentation Morphology

Fig. 4.6 shows a series of high-magnification SEM micrographs of a nanoindentation imprint in pre-sintered porous zirconia. Fig. 4.6(a) shows an overview of the indentation with fragmentation and pulverization of zirconia crystals. Fig. 4.6(b) shows severe compressed, fragmented and pulverized zirconia crystals at the indentation apex, where the highest indentation stress from the diamond indenter tip was concentrated. Big vacancies were also formed due to the zirconia crystal removal. Fig. 4.6(c) also reveals compression, fragmentation and pulverization of zirconia crystals along an indentation diagonal and cracks of zirconia pore networks in the vicinity of the diagonal. Dark coloured regions indicate grain removal from the diagonal. At a corner of the indentation in Fig. 4.6(d), interparticle and intraparticle collapses were evidenced. Compression and fragmentation were observed along its diagonal and cracks of pore networks were found in the vicinity of the indentation corner. Meanwhile, no crack extending from the corner region could observed. Fig. 4.6(e) reveals several intergranular cracks at zirconia crystal boundaries and pore networks along an indentation edge and compression and fragmentation of zirconia crystals inside an indented area.

Fig. 4.7 shows a series of high-magnification SEM micrographs of a nanoindentation imprint in sintered dense zirconia. Fig. 4.7(a) shows an overview of the indentation with plastic shear bands, edge pile-ups and localized microfractures. Figs. 4.7(b) and 4.7(c)

detail shear bands and ductile microfractures at the apex and along a diagonal of the indentation, respectively. Meanwhile, ductile fracture at the edge of the indentation was also found in Fig. 4.7(c). In the corner of the indentation shown in Fig. 4.7(d), no distinct crack extending the indentation was observed. Fig. 4.7(e) shows clearly shear bands and shear-induced plastic pile-ups at an edge of the indentation.

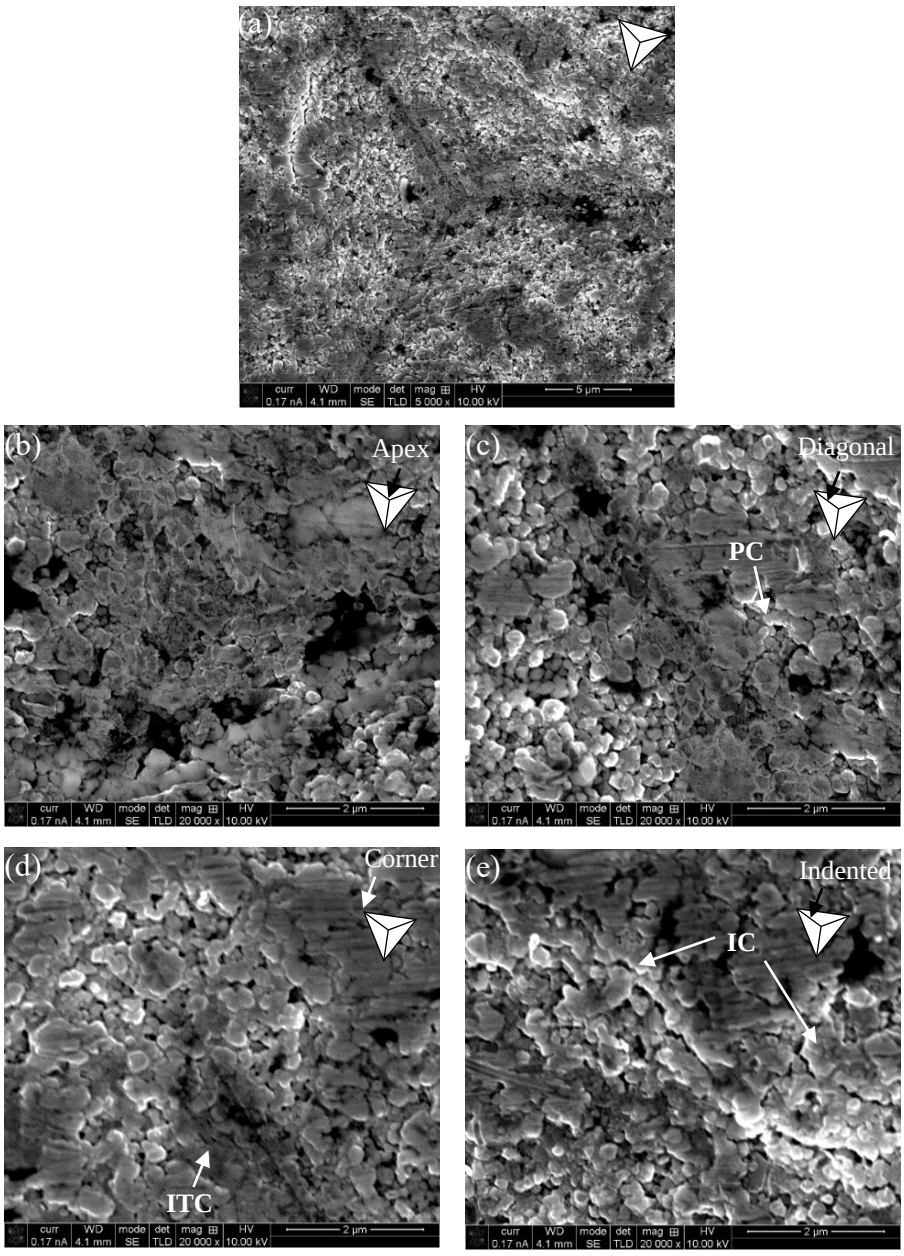

Fig. 4.6. High-magnification SEM micrographs of an indented residual imprint in pre-sintered porous zirconia. (a) Overall indented morphology, (b) Morphology at the apex, (c) Morphology along a diagonal length with pore cracks (PC), (d) Morphology at a corner with intergranular and transgranular collapses (ITC), and (e) Morphology of an indented edge area with intergranular cracks (IC).

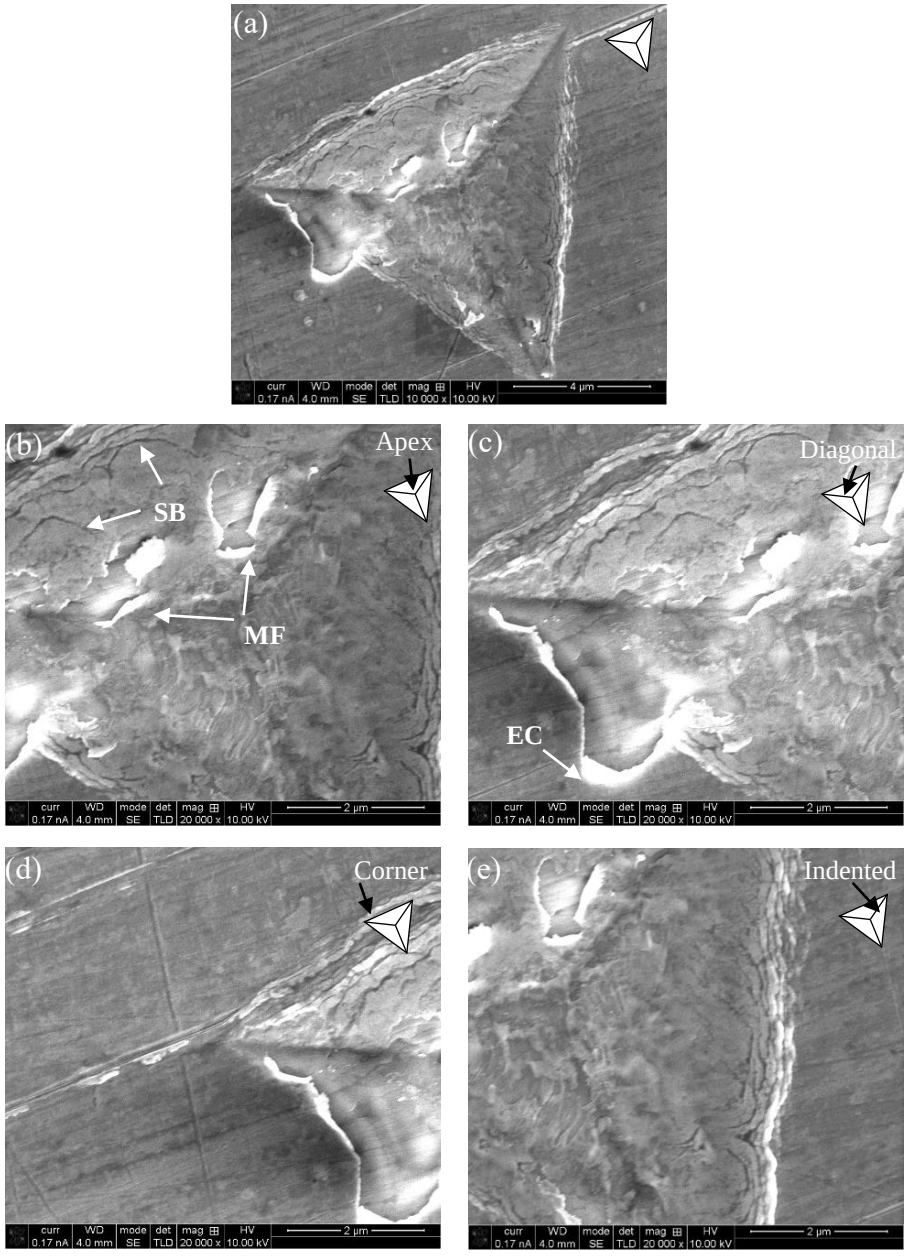

Fig. 4.7. High-magnification SEM micrographs of an indented residual imprint in sintered dense zirconia. (a) Overall indented morphology, (b) Morphology at the apex with microfracture (MF) and shear bands (SB), (c) Morphology at a diagonal length with shear bands (SB) and edge cracking (EC), and (d) Morphology at a corner with shear bands (SB), and (e) Morphology in an indented edge area with shear bands (SB).

4.4 Discussion

This study has revealed distinct microstructural responses of loosely pre-sintered porous and closely packed dense zirconia materials to nanoindentation with respect to deformation and damage, mechanical properties and indentation imprint geometries.

In-situ SEM observations of indentation processes for the two materials in Fig. 4.2 featured plastic deformation at the applied indentation conditions. This feature was also confirmed by the continuous and smooth force-displacement curves without pop-in and pop-out events for the two materials, as in Fig. 4.3. Generally, smooth force-displacement curves imply plastic deformation without cracking occurring during indentations. Even though no distinct discontinuities are shown in Fig. 4.3, but at the microstructural level, the plastic deformation for the two material reflects entirely different indentation mechanisms. Although *in-situ* SEM indentation images (e.g., Fig. 4.2(e)) for pre-sintered porous zirconia reveal yield zones, these zones contained microcracked, fragmented and pulverized zirconia crystals under indentation stresses due to intergranular and transgranular fractures (Fig. 4.6). This indicates that the indentation mode for pre-sintered porous zirconia is quasi-plastic. For sintered dense zirconia, the indentation mechanics is featured with more typical plastic deformation with shear-band localization generated by contact stresses (Fig. 4.7). Shear-induced localized edge cracking (Fig. 4.7(c)) and inner microfracture (Fig. 4.7(b)) are also observed. These damages may have mainly resulted from intergranular fracture as evidenced in the high-magnification SEM micrographs of the indentation morphologies in the dense microstructure (Fig. 4.7). Thus, sintered dense zirconia also exhibits a quasi-plastic response to nanoindentation.

In pre-sintered porous zirconia, the weak interfaces are interconnected pore networks, which were compressed and broken to form discrete zirconia crystals under indentation stresses (Fig. 4.6). These broken pore networks functioned as shear faults to result in quasi-plastic deformation of zirconia crystals in indentation processes (Fig. 4.2(e)). High stress concentrations revealing darker grey at the indentation apex (Fig. 4.6(b)), diagonal (Fig. 4.6(c)) and corner (Fig. 4.6(d)) have created a gradient in indentation deformation in contrast to relatively more homogeneous deformed sides of the imprint. Because of the high indentation stresses, more zirconia crystals were fragmented and pulverized in comparison with only interconnected pore network fractures in sides of the imprint with less indentation stresses (Fig. 4.6). The continuous loading of the indenter to pre-sintered

porous zirconia enabled the accumulation, compression and densification of these fragmented and pulverized zirconia crystals to form darkened grey areas in Fig. 4.6. Therefore, it is noted that high internal residual stresses in these discrete zirconia crystals led to intergranular and transgranular fractures and collapses, pore filling and densification to form fragmented and pulverized layers with cracking in the deformed indentation area (Fig. 4.6). The pore-densification-induced quasi-plasticity was also studied in spherical indentations of $ZrTiO_4$-TiO_2 porous ceramic at 5–200 N (Bhaskar et al., 2016), porous nanocrystalline zirconia at 630-mN load (Chintapalli et al., 2012), porous alumina ceramics at loads up to 2000 N (Latella et al., 1997).

Intergranular cracking was observed in indented pre-sintered porous zirconia (Fig. 4.6(e)). This may be attributed to localized shear stresses and microstructural strains generated in response to the indentation event. Microstructural cracking occurs when the shear stress generated exceeds the material shear strength (Dey and Mukhopadhyay, 2014). Studies of the inelastic behavior of nanoindentation of porous hydroxyapatite using a spherical indenter also confirms that higher contact loads led to a larger plastic core with more damage in the form of cracks and fracture of sintered necks (He, et al., 2008). However, no cracking was observed extending the current indent imprints (Fig. 4.2(e)). This implies that indentation-induced shear stresses were strictly constrained in the localized indentation imprint due to the discrete zirconia crystals as stress shields at the indentation edges. Therefore, conventional radial cracking resulting from crack propagation at indentation corners did not occur in porous zirconia.

In contrast, the quasi-plasticity in indented sintered dense zirconia featured the shear-band plastic mode, as shown in Figs. 4.2 and 4.7. The shear bands might be triggered due to slight deviation from orthogonality (Keryvin, 2007) between the indenter and sintered dense zirconia. The imperfect orthogonality may have led to the nucleation of shear bands and pileups. With increasingly loading, the nucleation may have spread in the indentation imprint to create complete shear band patterns. The high load may provide enough strain field to some extent that results in the shear bands intersecting the surface, thus generated the shear bands beneath the indenter. Further, the shear-band induced plastic deformation in sintered dense zirconia may have caused micro-tensile stresses in zirconia crystals through crystal rearrangement dislocations, whose movements were constraint at the grain boundaries (Subhash et al., 2008). At high indentation stress concentration sites,

such as indentation apexes, diagonals and edges, these stresses may have exceeded the tensile strength of zirconia, consequently leading to the microstructural cracking as shown in Fig. 4.7.

The quasi-plasticity is a mode containing a yield zone of distributed shear-driven faults or microcracks in the subsurface (Rhee et al., 2001) and it's response occurs due to micro-cracking and/or densification mechanisms (Staub et al., 2016). The quasi-plasticity can be detrimental as it can reduce the material strength (Lawn et al., 1998; Coldea et al., 2014). The quasi-plasticity has been observed in indentations of dense polycrystalline ceramics, such as sintered silicon nitride and zirconia, and glass ceramics, such as mica glass ceramics, at the macro indentation load level, e.g., 2200 N, and can be featured at multi-length scales (Lee et al., 2000). Although the behavior in dense ceramics has a similar shear-induced plastic deformation of metal materials at the macroscale, the deformation in these brittle materials is driven by internal residual stresses and occurs via dissipative slip at microstructurally discrete weak particle/interfaces as shear faults (Fischer-Cripps and Lawn 1996).

All damages induced by the indenter to both pre-sintered porous and sintered dense zirconia materials were limited within the indentation imprint perimeters and did not extend outside the imprint perimeters after complete retractions of the indenter. No classical radial cracks that are formed in purely brittle materials (Lawn, 1998) were found in all indentation imprints in both pre-sintered porous and dense zirconia materials (Figs. 4.2, 4.6 and 4.7). This may explain why no pop-in steps or discontinuities could be seen in the force-displacement curves. The induced indentation damages to the two materials at 500 mN peak load and 2 mN/s loading and unloading rate might not be enough to cause discontinuities in the curves when the load has been completely removed from the material surfaces (Lawn and Swain, 1975). Previous nanoindentation studies of the same materials at 10 mN peak load and 0.1–2 mN/s loading rates have revealed much less pop-in events in the resulted force-displacement curves at higher loading rates compared to lower rates for both materials (Alao and Yin, 2014a, b). These may suggest that visible pop-in events may only occur at very low loading rates for pre-sintered porous and dense zirconia materials. This may be because low loading rates might provide force-displacement curves with enough time to capture different discrete physical events beneath indenter tips while high loading rates might be insufficient for the curves to

capture such events and cause discontinuities. Further, Wasmer et al. (2013) reported that discontinuities in load-displacement curves are related to microcracking events when indenting gallium arsenide. Similarly, serrations in load-displacement curves were also reported to be associated to initiations and propagations of microcracking when indenting zirconia toughened alumina composites (Maiti et al., 2019a, 2019b; 2020). This indicates that visible pop-in events may also be sensitive to materials.

The distinct microstructures and indentation behaviours between pre-sintered porous and sintered dense zirconia materials enabled the former to yield larger indentation displacements and weaker mechanical properties than the latter as shown in Figs. 4.3 and 4.4. These also indicate a significant material dependent nature of indentation mechanics for the two zirconia materials. For pre-sintered porous zirconia with interconnected porosity and loosely packed crystal microstructure (Fig. 4.1(a)), the indentation forces exerted by the indenter may have pushed discrete zirconia crystals to the next layer resulting in material accumulating beneath the indenter to begin a compaction process. The force exerted might have also allowed a layer of potential material to crash and fall not only to the next layer beneath the fractured layer but also to fall to the layers of pores until the load is removed, resulting in higher indentation displacements. This deformation phenomenon was also observed when indenting an ordered foamed silica film on a substrate using a Berkovich indenter (Toivola et al., 2004). In contrast, densely sintered zirconia with closely packed crystal microstructure (Fig. 4.1(b)) had high resistance to plastic deformation, resulting in less indentation displacements and higher contact hardness and Young's modulus values (Figs. 4.3–4.5).

In addition, the occurrence of the increase in spatial density in microstructural damages may provide higher chances of interactions between an indenter and a material to result in higher penetration depths (Chakraborty et al., 2012). Pre-sintered porous zirconia with a weaker mechanical strength had higher spatial density of microstructural damage than sintered dense zirconia, thus it was penetrated much deeper by the diamond indenter than the latter. This is evidenced from the microstructural cracking observed at the indented area in pre-sintered porous zirconia (Fig. 4.6(e)) whereas no microstructural cracking was observed in dense sintered zirconia (Fig. 4.7(e)) indent imprint.

To quantify the quasi-plasticity for ceramics, a brittleness index ratio P_y/P_c corresponding to the critical load at initial yielding (P_y) and cracking (P_c) in indentation is used, which is defined as (Rhee et al., 2001):

$$\frac{P_y}{P_c} = \left(\frac{D}{A}\right)\left(\frac{H}{E'}\right)\left(\frac{H}{K_{IC}}\right)^2 r' \tag{4.4}$$

where D and A are constants and respectively equal to 0.848 and 8.63×10^3, H is the hardness, K_{IC} is the fracture toughness, r' is the contact radius of curvature assuming equal to 3.18 mm and E' is the effective modulus. E' can be calculated as (Rhee et al., 2001):

$$\frac{1}{E'} = \frac{1}{E} + \frac{1}{E_i} \tag{4.5}$$

Where E is the material Young's modulus and E_i is the indenter Young's modulus (i.e., equal to 1140 GPa for a Berkovich indenter). When $P_y/P_c > 1$, it indicates that the material contact response is brittle, whereas if $P_y/P_c < 1$, the response is quasi-plastic (Rhee et al., 2001). Further, a smaller brittleness index ratio P_y/P_c implies that the material is more plastic. For pre-sintered porous zirconia with the mechanical properties of H = 1.6 GPa (Alao and Yin, 2014a), E = 28.0 GPa (Alao and Yin. 2014a) and K_{IC} = 0.8 MPa.m$^{1/2}$ (Alao and Yin, 2016), $(P_y/P_c)_{pre\text{-}sintered\ porous}$ is calculated as 7.3×10^{-2}. For sintered dense zirconia with the mechanical properties of H = 9.3 GPa (Alao and Yin, 2014b), E = 157.5 GPa (Alao and Yin, 2014b) and K_{IC} = 6.0 MPa.m$^{1/2}$ (Sakoda et al., 2018), $(P_y/P_c)_{sintered\ dense}$ is calculated as 5.1×10^{-2}. Thus, the brittleness index ratios for both materials are

$$\left(\frac{P_y}{P_c}\right)_{pre-sintered\ porous} < 1 \tag{4.6}$$

$$\left(\frac{P_y}{P_c}\right)_{sintered\ dense} < 1 \tag{4.7}$$

These indicate that both pre-sintered porous zirconia and sintered dense zirconia materials had quasi-plastic contact response in nanoindentation. Further, a material index (M) for the brittleness associated with the hardness H, the effective modulus E' and the fracture toughness K_{IC} can be derived based on Eq. 4.8 and expressed as (Rhee et al., 2001):

$$M = \left(\frac{H}{E'}\right)\left(\frac{H}{K_{IC}}\right)^2 \tag{4.8}$$

A higher index means that the material is more brittle and vice versa. The material indexes for pre-sintered porous and sintered dense zirconia materials are $M_{pre\text{-}sintered\ porous} = 2.3 \times 10^7$ and $M_{sintered\ dense} = 1.6 \times 10^7$. The comparison of both the brittleness index ratios and the material indices between pre-sintered porous and sintered dense zirconia materials is given by

$$\left(\frac{P_y}{P_c}\right)_{pre-sintered\ porous} > \left(\frac{P_y}{P_c}\right)_{sintered\ dense} \tag{4.9}$$

$$M_{pre-sintered\ porous} > M_{sintered\ dense} \tag{4.10}$$

These indicate that pre-sintered porous zirconia is more brittle or less quasi-plastic than sintered dense zirconia.

It is of interest to compare the *in-situ* indentation properties at the peak load of 500 mN with the *ex-situ* studies at the peak load of 10 mN for pre-sintered and sintered zirconia materials. For the former, this study obtained 36% higher hardness value and a reasonably good agreement for the Young's modulus value while for the latter, the current hardness was 38% higher and the Young's modulus was 34% lower (Alao and Yin, 2014a, b). A reversible indentation size effect may be considered with the respect to the hardness values for both materials measured using the two methods, higher applied indentation loads yield higher hardness values. The similarly effect was also reported on other ceramic materials (Sangwal, 2009). These could be due to the penetration depth of an indenter. At a high load, the indenter penetrates deeper into the inner layer and a bulk material effect becomes dominant. Whereas at a low load, the indenter penetrates only into the surface layer and a surface effect is dominating (Alao and Bujang, 2020).

In general, the mechanical properties obtained in nanoindentation represent the surface properties of bulk materials (Bell et al., 1991) or small volumes of bulk materials (Field and Swain, 1995; Swain, 1998). Therefore, the measured properties in *in-situ* nanoindentation in this study, may only represent the surface behavior of zirconia materials. They may differ from bulk properties using bulk tests (Broitman, 2017). In practice, not only the indentation size effect significantly influences the measured mechanical properties, but also indenter shapes and materials remarkably affect their interactions with tested specimens (Pharr et al., 2010).

The Oliver and Pharr method is based on purely elastic-plastic response of a material (Oliver and Pharr, 1992). It is of interest to discuss whether the quasi-plastic responses observed in zirconia materials studied influence their properties determined using the method. For pre-sintered porous zirconia, the densification-formed quasi-plastic response would not influence the mechanical properties determined using the method as reported by Li et al. (2020b). Further, the indentation-induced microcracking in the material did not extend outside of the indentation imprints (Figs. 4.6 and 4.7) to cause any discontinuities in the load-displacement curves (Fig. 4.3). Thus, the contact stiffness and hardness determined would not be affected, and the method is still applicable to porous zirconia studied. For sintered dense zirconia, the shear-band formed quasi-plastic response (Fig. 4.7) can lead to pile-ups (Chen et al., 2019; Xie and George, 2008), which may affect the Oliver-Pharr model to result in overestimated hardness and Young's modulus values (Qiu et al., 2018).

Further, *in-situ* indentation is generally conducted inside a SEM at acceleration voltage of 5–15 KV (Deuschle et al., 2008). In the current investigation, 10 kV was used, which is different from the *ex-situ* studies conducted only in the mechanical environment and may affect the property measurement in nanoindentation. Given the sensitivity of the nano-scale behavior of materials, the electro-mechanical coupling effect on *in-situ* nanoindentation needs to be understood. In addition, the machine compliance of the indentation instrument and the tip area function calibration is crucial for the measurement. In *ex-situ* indentation, silica is generally used as a calibration specimen (Oliver and Pharr 1992). In *in-situ* indentation studies, sapphire is also recommended as a calibration specimen, particularly for measured specimens with a high modulus (Chudoba et al., 2006). Due to the limitation of the current *in-situ* study in which the calibration was only conducted using silica, the accuracy of the measured mechanical properties may be compromised. Nevertheless, the advantage of the study was the *in situ* imaging capability of the SEM to provide a direct observation of indentation processes and phenomena, which the traditional *ex-situ* indentation is not able to directly account for.

The responses of pre-sintered porous and sintered dense zirconia materials to a sharp three side pyramidal indenter provide fundamental knowledge into dental CAD/CAM abrasive machining processes for zirconia restorations. In machining, a zirconia workpiece is subject to indentations and scratches by numerous diamond abrasives to remove a layer

of material. Hence, for a single abrasive, the exerted machining force can be very low in the range of millinewton scale, which is associated with the peak load used in this study. The high peak load applied in this study indicates that ductile regime machining is possible for both pre-sintered and sintered zirconia materials. The indentation responses of pre-sintered porous and dense sintered zirconia materials can be linked to their machinability by comparing their indentation volumes relating to material removal rates. With a Berkovich diamond indenter, an indentation volume can be expressed as (Randall, 2002):

$$V = \frac{1}{3} A_p h_f \tag{4.11}$$

where V is the volume indentation, A_p is the plastic contact area which can be estimated from the force-displacement curve and h_f is the final depth. Note that, this indentation volume might not accurately represent the actual indentation volume as the contact area taken for this calculation does not take into consideration of any elastic recovery of the surface nor any sink-in or pile up effect (Randall, 2002). However, it is sufficient to act as an indication of a comparison of the two materials. Taking respective A_p of $(26.3 \pm 2.9) \times 10^7$ nm^2 and $(2.4 \pm 0.48) \times 10^7$ nm^2 for pre-sintered porous and sintered dense zirconia materials, the indentation volumes for the two materials are calculated as $(290.9 \pm 49.4) \times 10^9$ nm^3 and $(6.4 \pm 2.5) \times 10^9$ nm^3, respectively. This indicates that the removal rate for pre-sintered porous zirconia might be 45 times that for sintered dense zirconia. On the other hand, the indentation mechanics of pre-sintered porous and sintered dense zirconia materials in Figs. 4.6 and 4.7 may predict machining damage in zirconia, which affects the fatigue and wear performance of zirconia restorations.

In relevance with current dental CAD/CAM machining of pre-sintered porous and sintered dense zirconia materials, induced-surface and subsurface damage can lead to restoration failure. In particular, machining-induced edge chipping damage as the most severe quality problem, is easily triggered from surface defects, such as microstructural cracking, and stress concentrations at the edges. As indicated in Figs. 4.6 and 4.7, microstructural cracking observed in indent imprint of pre-sintered porous zirconia was much more severe in sintered dense zirconia. This means that surface/subsurface and edge damage prevails more easily in pre-sintered porous zirconia than sintered dense zirconia. In comparison, the closely packed crystal dense microstructure in sintered dense zirconia

can provide high resistance to machining damage than pre-sintered zirconia. Therefore, it might be an optimal choice to alter the microstructure of pre-sintered porous zirconia by sintering at low temperatures for balanced machining efficiency and damage, which will be our future studies. This may overcome disadvantages in current soft and hard machining of pre-sintered porous and sintered dense zirconia materials applied for ceramic restorations. In addition, our findings and analysis may also be used in zirconia structures in engineering (e.g., bearings) and medicine (e.g., joints) where sintered zirconia materials are subject to abrasive wear and erosion. Indentation-induced damage in zirconia structures may act as a stress concentrator to lead to catastrophic failure. Hence, the insights of this study on the nanoscale contact-induced deformation and damage may lead to the development of ductile removal machining techniques to prevent machining damage, improving the strength and service life of zirconia products. This is critical and significant for manufacturing of dental ceramic restorations.

4.5 Conclusions

In-situ SEM nanoindentation and high-magnification of indentation morphology analysis of zirconia materials with distinct pre-sintered porous and sintered dense microstructures offer the micromechanics prospect of a predictive basis for CAD/CAM diamond shaping of zirconia restorations. This work demonstrated that microstructure has played a key role in controlling zirconia responses to nanoindentation by a Berkovich diamond indenter. Although *in-situ* SEM indentation images and force-displacement curves for both materials revealed smooth and continuing plastic deformation without classical radial cracks, the underlying deformation and damage mechanisms were microstructurally different. For pre-sintered porous zirconia, quasi-plastic deformation was dominant and accompanied with compression, fragmentation, pulverization and microcracking of zirconia crystals, resulting from shear faults at broken pore networks as microstructurally discrete interfaces. For sintered dense zirconia, metal-like shear band-induced quasi-plastic deformation was governing and presented with localized tensile microfracture. The higher ranked brittleness index ratio and material index for pre-sintered porous zirconia suggested it more brittle and less quasi-plastic than sintered dense state and predicted it more prone to machining damage. The pore-induced weak interfaces in pre-sintered porous zirconia yielded 45 times the indentation imprint volumes in sintered dense state, forecasting extremely higher machining removal rates for pre-sintered state

than sintered zirconia in diamond machining. The indention deformation and fracture mechanics studied may be used as the fundamental knowledge tool for tailoring of zirconia microstructures to achieve machining efficiency and damage tolerance in CAD/CAM dental milling.

Credit Authorship Contribution Statement

Afifah Z. Juri: Conceptualization, Methodology, Investigation, Formal analysis, Validation, Data curation, Writing - original draft, Funding acquisition (PhD Scholarship, The University of Adelaide, Australia). **Animesh K. Basak:** Methodology, Investigation, Data curation, Writing - review & editing. **Ling Yin:** Conceptualization, Methodology, Validation, Writing - review & editing, Supervision, Project administration, Funding acquisition (Seed Grant, The University of Adelaide, Australia).

Declaration of Competing Interest

The authors declare that they have no known competing financial interests or personal relationships that could have appeared to influence the work reported in this paper.

Acknowledgements

This work was supported by a PhD scholarship and a seed grant in manufacturing and bio-manufacturing from the University of Adelaide.

References

Alao, A.-R., Yin, L., 2014a. Nano-scale mechanical properties and behavior of pre-sintered zirconia. J. Mech. Behav. Biomed. Mater. 36, 21–31. https://doi.org/10.1016/j.jmbbm.2014.03.019

Alao, A.-R., Yin, L., 2014b. Loading rate effect on the mechanical behavior of zirconia in nanoindentation. Mater. Sci. Eng. 619, 247–255. https://doi.org/10.1016/j.msea.2014.09.101

Alao, A.-R., Yin, L., 2015. Nanoindentation characterization of the elasticity, plasticity and machinability of zirconia. Mater. Sci. Eng. 628, 181–187. https://doi.org/10.1016/j.msea.2015.01.051

Alao, A.-R., Yin, L., 2016. Assessment of elasticity, plasticity and resistance to machining-induced damage of porous pre-sintered zirconia using nanoindentation techniques. J. Mater. Sci. Technol. 32, 402–410. https://doi.org/10.016/j.jmst.2016.02.009

Alao, A.-R., Stoll, R., Song, X.-F., Miyazaki, T., Hotta, Y., Shibata, Y., Yin, L., 2017. Surface quality of yttria-stabilized tetragonal zirconia polycrystal in CAD/CAM milling, sintering, polishing and sandblasting processes. J. Mech. Behav. Biomed. Mater. 65, 102–116. https://doi.org/10.1016/j.jmbbm.2016.08.021

Alao, A.-R., Bujang, M.H.D., 2020. Load effect on the mechanical behaviour of zirconia-reinforced lithium silicate glass ceramics. Ceram. Int. 47, 1353–1363. https://doi.org/10.1016/j.ceramint.2020.08.257

Amat, N. F., Muchtar, A., Amril, M. S., Ghazali, M. J., Yahaya, N., 2018. Preparation of presintered zirconia blocks for dental restorations through colloidal dispersion and cold isostatic pressing. Ceramics International. 44, 6409–6416. https://doi.org/10.1016/j.ceramint.2018.01.035

Basak, A.-K., Zhang, L., 2018. Deformation of Ti-Based bulk metallic glass under a cutting tip. Tribol. Lett. 66, 1–8. https://doi.org/10.1007/s11249-017-0975-9

Bell, T.J., Bendeli, A., Field, J.S., Swain, M.V., Thwaite, E.G., 1991. The determination of surface plastic and elastic properties by ultra micro-indentation. Metrologia 28, 463–469. https://iopscience.iop.org/article/10.1088/0026-1394/28/6/004/meta

Bhaskar, S., Park, J. G., Lee, K. S., Kim, S. Y., Kim, I. J., 2016. Thermal and mechanical behavior of ZrTiO4-TiO2 porous ceramics by direct foaming. Ceram. Int. 42, 14395–14402. https://doi.org/10.1016/j.ceramint.2016.06.019

Broitman, E., 2017. Indentation Hardness Measurements at Macro-, Micro-, and Nanoscale: A Critical Overview. Tribol Lett 65, 23. https://doi.org/10.1007/s11249-016-0805-5

Campos, T. M. B., de Melo Marinho, R. M., Ribeiro, A. D. O. P., do Amaral Montanheiro, T. L., da Silva, A. C., Thim, G. P., 2021. Microstructure and mechanical properties of fully sintered zirconia glazed with an experimental glass J. Mech. Behav. Biomed. Mater. 113, 104093. https://doi.org/10.1016/j.jmbbm.2020.104093

Chakraborty, R., Dey, A., Mukhopadhyay, A.K., Joshi, K.D., Rav, A., Mandal, A.K., Gupta, S.C., 2012. Indentation size effect of alumina ceramic shocked at 12 GPa.

Int. J. Refract. Hard. Met. 33, 22–32. https://doi.org/10.1016/j.ijrmhm.2012.02.003

Chen, H., Levitas, V. I., Xiong, L., 2019. Amorphization induced by 60° shuffle dislocation pileup against different grain boundaries in silicon bicrystal under shear. Acta Mater. 179, 287–295. https://doi.org/10.1016/j.actamat.2019.08.023

Chintapalli, R. K., Jimenez-Pique, E., Marro, F. G., Yan, H., Reece, M., Anglada, M., 2012. Spherical instrumented indentation of porous nanocrystalline zirconia. J. Eur. Ceram. Soc. 32, 123–132. https://doi.org/10.1016/j.jeurceramsoc.2011.07.037

Chudoba, T., Schwaller, P., Rabe, R., Breguet, J.M., Michler, J., 2006. Comparison of nanoindentation results obtained with Berkovich and cube-corner indenters. Philos. Mag. 86, 5265–5283. https://doi.org/10.1080/14786430600746424

Coldea, A., Swain, M. V., Thiel, N., 2014. Hertzian contact response and damage tolerance of dental ceramics. J. Mech. Behav. Biomed. Mater. 34, 124–133. https://doi.org/10.1016/j.jmbbm.2014.02.002

De Souza, G. M., Zykus, A., Ghahnavyeh, R. R., Lawrence, S. K., Bahr, D. F., 2017. Effect of accelerated aging on dental zirconia-based materials. J. Mech. Behav. Biomed. Mater. 65, 256– 263. https://doi.org/10.1016/j.jmbbm.2016.08.023

Denry, I., Holloway, J. A., 2010. Ceramics for dental applications: a review. Materials 3, 351–368. https://dx.doi.org/10.3390%2Fma3010351

Denry, I., Kelly, J.R., 2008. State of the art of zirconia for dental applications. Dent. Mater. 24, 299–307. https://doi.org/10.1016/j.dental.2007.05.007

Dey, A., Mukhopadhyay, A.K., 2014. Nanoindentation of brittle solids. CRC Press, Boca Raton.

Deuschle, J.K., Buerki, G., Deuschle, H.M., Enders, S., Michler, J., Arzt, E., 2008. In situ indentation testing of elastomers. Acta. Mater. 56, 4390–4401. https://doi.org/10.1016/j.actamat.2008.05.003

Ereifej, N., Rodrigues, F.P., Silikas, N., Watts, D.C., 2011. Experimental and FE shear-bonding strength at core/veneer interfaces in bilayered ceramics. Dent. Mater. 27, 590–597. https://doi.org/10.1016/j.dental.2011.03.001

Field, J.S., Swain, M.V., 1995. Determining the mechanical properties of small volumes of material from submicrometer spherical indentations. J. Mater. Res. 10, 101–112. https://doi.org/10.1557/JMR.1995.0101

Fischer-Cripps, A.C., Lawn, B.R., 1996. Stress analysis of contact deformation in quasi-plastic ceramics. J. Am. Ceram. Soc. 79, 2609–2618. https://doi.org/10.1111/j.11512916.1996.tb09023.x

Garvie, R.C., Hannink, R.H., Pascoe, R.T., 1975. Ceramic steel?. Nature 258, 703–704. https://doi.org/10.1038/258703a0

Garvie, R.C., Nicholson, P.S., 1972. Phase analysis in zirconia systems. J. Am. Ceram. Soc. 55, 303–305. https://doi.org/10.1111/j.1151-2916.1972.tb11290.x

Ghisleni, R., Rzepiejewska-Malyska, K., Philippe, L., Schwaller, P., Michler, J., 2009. In situ SEM indentation experiments: Instruments, methodology, and applications. Microsc. Res. Tech. 72, 242–249. https://doi.org/10.1002/jemt.20677

Guazzato, M., Albakry, M., Ringer, S.P., Swain, M.V., 2004. Strength, fracture toughness and microstructure of a selection of all-ceramic materials. Part II. Zirconia-based dental ceramics. Dent. Mater. 20, 449–456. https://doi.org/10.1016/j.dental.2003.05.002

He, L. H., Standard, O. C., Huang, T. T. Y., Latella, B. A., Swain, M. V., 2008. Mechanical behaviour of porous hydroxyapatite. Acta Biomater. 4, 577–586. https://doi.org/10.1016/j.actbio.2007.11.002

Huang, H., Zhao, H., 2014. In situ nanoindentation and scratch testing inside scanning electron microscopes: opportunities and challenges. Sci. Adv. Mater. 6, 875–889. https://doi.org/10.1166/sam.2014.1868

Kelly, J.R., Benetti, P., 2011. Ceramic materials in dentistry: historical evolution and current practice. Aust. Dent. J. 56, 84–96. https://doi.org/10.1111/j.1834-7819.2010.01299.x

Keryvin, V., 2007. Indentation of bulk metallic glasses: Relationships between shear bands observed around the prints and hardness. Acta. Mater. 55, 2565–2578. https://doi.org/10.1016/j.actamat.2006.12.005

Latella, B. A., OConnor, B. H., Padture, N. P., Lawn, B. R., 1997. Hertzian contact damage in porous alumina ceramics. J. Am. Ceram. Soc. 80, 1027–1031. https://doi.org/10.1111/j.1151-2916.1997.tb02940.x

Lawn, B.R., 1998. Indentation of ceramics with spheres: a century after Hertz. J. Am. Ceram. Soc. 81, 1977–1994. https://doi.org/10.1111/j.1151-2916.1998.tb02580.x

Lawn, B. R., Lee, S. K., Peterson, I. M., Wuttiphan, S., 1998. Model of strength degradation from Hertzian contact damage in tough ceramics. J. Am. Ceram. Soc. 81, 1509–1520. https://doi.org/10.1111/j.1151-2916.1998.tb02510.x

Lawn, B.R., Borrero-Lopez, O., Huang, H., Zhang, Y., 2021. Micromechanics of machining and wear in hard and brittle materials. J. Am. Ceram. Soc. 104, 5–22. https://doi.org/10.1111/jace.17502

Lawn, B.R., Swain, M.V., 1975. Microfracture beneath point indentations in brittle solids. J. Mater. Sci. 10, 113–122. https://doi.org/10.1007/BF00541038.

Lee, K.S., Jung, Y.G., Peterson, I.M., Lawn, B.R., Kim, D.K., Kun Lee, S., 2000. Model for cyclic fatigue of quasi-plastic ceramics in contact with spheres. J. Am. Ceram. Soc. 83, 2255–2262. https://doi.org/10.1111/j.1151-2916.2000.tb01544.x

Li, L., Wan, L., Zhou, Q., 2020a. Crack propagation during Vickers indentation of zirconia ceramics. Ceram. Int. 46, 21311–21318. https://doi.org/10.1016/j.ceramint.2020.05.225

Li, C., Zhang, L., Sun, L., Wu, C., Duan, D., Lin, Q., Jiang, Z., 2020b. A finite element study on the effects of densification on fused silica under indentation. Ceram. Int. 46, 26861–26870. https://doi.org/10.1016/j.ceramint.2020.07.162

Maiti, P., Bhattacharya, M., Das, P. S., Ghosh, J., Mukhopadhyay, A. K., 2019a. A critical note on nanoscale plasticity in 20 ZTA ceramics. Ceram. Int. 45, 25034–25043. https://doi.org/10.1016/j.ceramint.2019.05.189

Maiti, P., Eqbal, A., Bhattacharya, M., Das, P. S., Ghosh, J., Mukhopadhyay, A. K., 2019b. Micro pop-in issues in nanoindentation behaviour of 10 ZTA ceramics. Ceram. Int. 45, 8204–8215. https://doi.org/10.1016/j.ceramint.2019.01.123

Maiti, P., Ghosh, J., Mukhopadhyay, A. K., 2020. New observations and critical assessments of incipient plasticity events and indentation size effect in nanoindentation of ceramic nanocomposites. Ceramics International. 46, 3144–3165. https://doi.org/10.1016/j.ceramint.2019.10.019

Malkin, S., Hwang, T. W., 1996. Grinding mechanisms for ceramics. CIRP Annals 45, 569–580. https://doi.org/10.1016/S0007-8506(07)60511-3

Manicone, P.F., Iommetti, P.R., Raffaelli, L., 2007. An overview of zirconia ceramics: basic properties and clinical applications. J. Dent. 35, 819–826. https://doi.org/10.1016/j.jdent.2007.07.008

Miyazaki, T., Nakamura, T., Matsumura, H., Ban, S., Kobayashi, T., 2013. Current status of zirconia restoration. J. Prosthodont. Res. 57, 236–261. https://doi.org/10.1016/j.jpor.2013.09.001

Moser, B., Kuebler, J., Meinhard, H., Muster, W., Michler, J., 2005. Observation of instabilities during plastic deformation by in-situ SEM indentation experiments. Adv. Eng. Mater. 7, 388–392. https://doi.org/10.1002/adem.200500049

Nili, H., Kalantar-Zadeh, K., Bhaskaran, M., Sriram, S., 2013. In situ nanoindentation: probing nanoscale multifunctionality. Prog. Mater. Sci. 58, 1–29. https://doi.org/10.1016/j.pmatsci.2012.08.001

Nowak, J.D., Rzepiejewska-Malyska, K.A., Major, R.C., Warren, O.L., Michler, J., 2010. In-situ nanoindentation in the SEM. Mater. Today 12, 44–45. https://doi.org/10.1016/S1369-7021(10)70144-9

Oliver, W.C., Pharr, G.M., 1992. An improved technique for determining hardness and elastic modulus using load and displacement sensing indentation experiments. J. Mater. Res. 7, 1564–1583. https://doi.org/10.1557/JMR.1992.1564

Pharr, G.M., Herbert, E.G., Gao, Y., 2010. The indentation size effect: a critical examination of experimental observations and mechanistic interpretations. Ann Rev Mater Res 40, 271–292. https://doi.org/10.1146/annurev-matsci-070909-104456

Piconi, C., Maccauro, G., 1999. Zirconia as a ceramic biomaterial. Biomaterials 20, 1–25. https://doi.org/10.1016/S0142-9612(98)00010-6

Qiu, Y. H., Bai, Q., Fu, E. G., Wang, P. P., Du, J. L., Chen, X. F., Wang, X. J., 2018. A novel approach to extracting hardness of copper/niobium (Cu/Nb) multilayer films by removing the substrate effect. Mater. Sci. Eng. A. 724, 60–68. https://doi.org/10.1016/j.msea.2018.03.047

Rabe, R., Breguet, J.M., Schwaller, P., Stauss, S., Haug, F.J., Patscheider, J., Michler, J., 2004. Observation of fracture and plastic deformation during indentation and scratching inside the scanning electron microscope. Thin Solid Films 469, 206–213. https://doi.org/10.1016/j.tsf.2004.08.096

Randall, N.X., 2002. Direct measurement of residual contact area and volume during the nanoindentation of coated materials as an alternative method of calculating hardness. Philos. Mag. A. 82, 1883–1892. https://doi.org/10.1080/01418610208235700

Rekow, E.D., Silva, N.R.F.A., Coelho, P.G., Zhang, Y., Guess, P., Thompson, V.P., 2011. Performance of dental ceramics: challenges for improvements. J. Dent. Res. 90, 937–952. https://doi.org/10.1177/0022034510391795

Reece, M.J., Tetlow, P.L., Galiotis, C., 1992. Phase transformation around indentations in zirconia. J. Mater. Sci. Lett. 11, 575–577. https://doi.org/10.1007/BF00728613

Reis, A. F. N., Ramos, G. F., Campos, T. M. B., Prado, P. H. C. O., Vasconcelos, G., Borges, A. L. S., de Melo, R. M., 2019. The performance of sol-gel silica coated Y-TZP for veneered and monolithic dental restorations. J. Mech. Behav. Biomed. Mater. 90, 515–522. https://doi.org/10.1016/j.jmbbm.2018.09.023

Rhee, Y.W., Kim, H.W., Deng, Y., Lawn, B.R., 2001. Brittle fracture versus quasi plasticity in ceramics: a simple predictive index. J. Am. Ceram. Soc. 84, 561–565. https://doi.org/10.1111/j.1151-2916.2001.tb00698.x

Roitero, E., Anglada, M., Mücklich, F., Jiménez-Piqué, E., 2018. Mechanical reliability of dental grade zirconia after laser patterning. J. Mech. Behav. Biomed. Mater. 86, 257–263. https://doi.org/10.1016/j.jmbbm.2018.06.039

Ritzberger, C., Apel, E., Höland, W., Peschke, A., Rheinberger, V.M., 2010. Properties and clinical application of three types of dental glass-ceramics and ceramics for CAD-CAM technologies. Materials 3, 3700–3713. https://dx.doi.org/10.3390%2Fma3063700

Rzepiejewska-Malyska, K., Parlinska-Wojtan, M., Wasmer, K., Hejduk, K., Michler, J., 2009. In-situ SEM indentation studies of the deformation mechanisms in TiN, CrN and TiN/CrN. Micron 40, 22–27. https://doi.org/10.1016/j.micron.2008.02.013

Sakoda, S., Nakao, N., Watanabe, I., 2018. The effect of abrading and cutting instruments on machinability of dental ceramics. J. Mater. Sci. Mater. Med. 29, 34. https://doi.org/10.1007/s10856-018-6031-y

Sangwal, K., 2009. Indentation size effect, indentation cracks and microhardness measurement of brittle crystalline solids–some basic concepts and trends. Cryst. Res. Technol. 44, 1019–1037. https://doi.org/10.1002/crat.200900385

Stilwell, N.A., Tabor, D., 1961. Elastic recovery of conical indentations. Proc. Phys. Soc. 78, 169–179. https://doi.org/10.1088/0370-1328%2F78%2F2%2F302

Staub, D., Meille, S., Le Corre, V., Rouleau, L., Chevalier, J., 2016. Identification of a damage criterion of a highly porous alumina ceramic. Acta. Mater. 107, 261–272. https://doi.org/10.1016/j.actamat.2016.01.071

Subhash, G., Maiti, S., Geubelle, P.H., Ghosh, D., 2008. Recent advances in dynamic indentation fracture, impact damage and fragmentation of ceramics. J. Am. Ceram. Soc. 91, 2777–2791. https://doi.org/10.1111/j.1551-2916.2008.02624.x

Swain, M.V., 1998. Mechanical property characterisation of small volumes of brittle materials with spherical tipped indenters. Mater. Sci. Eng. A, 253, 160–166. https://doi.org/10.1016/S0921-5093(98)00725-4

Toivola, Y., Stein, A., Cook, R. F., 2004. Depth-sensing indentation response of ordered silica foam. J. Mater. Res. 19, 260–271. https://doi.org/10.1557/jmr.2004.19.1.260

Wasmer, K., Pouvreau, C., Breguet, J.M., Michler, J., Schulz, D., Giovanola, J.H., 2013. Nanoindentation cracking in gallium arsenide: Part I. In situ SEM nanoindentation. J. Mater. Res. 28, 2785–2798. https://doi.org/10.1557/jmr.2013.252

Werbach, K., Hummel, S., Ebner, C., Lohbauer, U., Peterlik, H., 2019. Pitfalls of determining the elastic properties of stabilized zirconia with indentation methods. Ceram. Int. 45, 9491–9496. https://doi.org/10.1016/j.ceramint.2018.09.128

Wendler, M., Belli, R., Petschelt, A., Mevec, D., Harrer, W., Lube, T., Lohbauer, U., 2017. Chairside CAD/CAM materials. Part 2: flexural strength testing. Dent. Mater. 33, 99–109. https://doi.org/10.1016/j.dental.2016.10.008

Xie, S., George, E. P., 2008. Hardness and shear band evolution in bulk metallic glasses after plastic deformation and annealing. Acta. Mater. 56, 5202–5213. https://doi.org/10.1016/j.actamat.2008.07.009

Xu, H.H., Smith, D.T., Jahanmir, S., 1996. Influence of microstructure on indentation and machining of dental glass-ceramics. J. Mater. Res. 11, 2325–2337. https://doi.org/10.1557/JMR.1996.0296

Yin, L., Huang, H., 2004. Ceramic response to high speed grinding. Mach. Sci. Technol. 8, 21–37. https://doi.org/10.1081/MST-120034240

Zhang, Y., Lawn, B.R., 2019. Evaluating dental zirconia. Dent. Mater. 35, 15–23. https://doi.org/10.1016/j.dental.2018.08.291

Zhang, L., Basak, A., 2013. Quantitative prediction of phase transformations in silicon during nanoindentation. Philos. Mag. Lett. 93, 448–456. https://doi.org/10.1080/09500839.2013.798441

Chapter 5 *In-situ* SEM Cyclic Nanoindentation

This chapter consists of the published journal article detailed below:

Juri, A. Z., Basak, A. K., Yin, L., 2022. In-situ SEM cyclic nanoindentation of pre-sintered and sintered zirconia materials. J. Mech. Behav. Biomed. Mater. 126, 105068. https://doi.org/10.1016/j.jmbbm.2021.105068

Statement of Authorship

Title of Paper	*In-situ* SEM cyclic nanoindentation of pre-sintered and sintered zirconia materials
Publication status	■ Published ☐ Accepted for publication ☐ Submitted for publication ☐ Unpublished and unsuited work written in manuscript style
Publication details	*Juri, A. Z., Basak, A. K., Yin, L., 2022. In-situ SEM cyclic nanoindentation of pre-sintered and sintered zirconia materials. J. Mech. Behav. Biomed. Mater. 126, 105068. https://doi.org/10.1016/j.jmbbm.2021.105068*

Principal Author

Name of Principal Author (Candidate)	Afifah Zakiyyah Juri
Contribution to the Paper	Conceptualization, Methodology, Investigation, Formal analysis, Validation, Data curation, Writing - original draft, Funding acquisition (PhD scholarship).
Overall percentage (%)	70
Certification:	This paper reports on original research I conducted during the period of my Higher Degree by Research candidature and is not subject to any obligations or contractual agreements with a third party that would constrain its inclusion in this thesis. I am the primary author of this paper.
Signature	Date: 08/06/2022

Co-Author Contributions

By signing the Statement of Authorship, each author certifies that:

i. the candidate's stated contribution to the publication is accurate (as detailed above);
ii. permission is granted for the candidate in include the publication in the thesis; and
iii. the sum of all co-author contributions is equal to 100% less the candidate's stated contribution

Name of Co-Author	Ling Yin
Contribution to the Paper	Writing – review and editing, Validation, Supervision, Project administration, Methodology, Investigation, Funding acquisition, Formal analysis, Conceptualization.
Signature	Date 08/06/2022

Name of Co-Author	Animesh Kumar Basak
Contribution to the Paper	Writing – review and editing, Methodology, Investigation, Data curation.
Signature	Date 08/06/2022

In-situ SEM cyclic nanoindentation of pre-sintered and sintered zirconia materials

Afifah Z. Juri[1], Animesh K. Basak[2], Ling Yin[1,*]

[1]School of Mechanical Engineering, The University of Adelaide, Adelaide, SA 5005, Australia

[2]Adelaide Microscopy, The University of Adelaide, Adelaide, SA 5005, Australia

*Corresponding Author: afifah.juri@adelaide.edu.au, ling.yin@adelaide.edu.au

Abstract Efficient diamond machining of zirconia requires a comprehensive understanding of repetitive diamond indentation mechanics. This paper reports on *in-situ* cyclic nanoindentations of pre-sintered and sintered zirconia materials performed inside a scanning electron microscope (SEM). *In-situ* SEM imaging of cyclic indentation processes and high-magnification SEM mapping of indentation imprints were conducted. The elastic and plastic behaviors of pre-sintered and sintered zirconia materials were investigated as a function of the cyclic nanoindentation number using the Sakai and Sakai-Nowak models. For pre-sintered zirconia, cyclic nanoindentation induced quasi-plastic deformation, causing localized agglomeration of zirconia crystals with microcracks and large cracking along the indentation edge. Severely compressed, fragmented, and pulverized zirconia crystals along with smeared surfaces were also observed. For sintered zirconia, shear bands dominated the quasi-plastic deformation with the formation of edge pile-ups and localized microfractures occurred at indentation apex and diagonals. All elastic and plastic behaviors for pre-sintered and sintered zirconia materials revealed significantly microstructure-dependent. Pre-sintered zirconia yielded significantly lower contact hardness, Young's moduli, resistance to plasticity, elastic deformation components, and resistance to machining-induced cracking, and higher elastic and plastic displacements than sintered state. Meanwhile, all the behaviors for the two materials were independent from the cyclic nanoindentation number. A model was proposed for cyclic nanoindentation mechanics, revealing their cyclic indentation-induced microstructural changes in the two zirconia materials. This study advances the fundamental understanding of nanoindentation mechanics of zirconia materials.

5.1 Introduction

Zirconia has high fracture toughness and mechanical strength, attractive biocompatibility, and excellent aesthetics (Chevalier et al., 2009; Garvie et al., 1975; Zhang and Lawn, 2018). Consequently, it has been extensively used in engineering, medicine and dentistry for load-bearing products, such as dental crowns and bridges (Kohorst et al., 2008; Schriwer et al., 2017). Pure zirconia is featured with a temperature dependency, leading to phase transformation and volume-expansion-induced cracking during high temperature heating and cooling (Meirowitz et al., 2019). Thus, doping stabilizers are often applied to produce partially stabilized zirconia (PSZ) materials. For instance, CaO-doped PSZ processed by microwave heating technology significantly improved the stability of zirconia materials (Ling et al., 2021). Such treatments also improve the mechanical properties of zirconia materials (Meirowitz et al., 2019). However, because of their good mechanical properties, zirconia materials are difficult to machine (Lambert et al., 2017; Zhong, 2020). To shape zirconia products, soft and hard digital abrasive machining processes for pre-sintered porous and sintered dense states are respectively conducted, both of which induce extensive fracture damage to zirconia materials (Alao et al., 2017; Denry and Kelly, 2008).

To suppress fracture damage induced in abrasive machining of brittle solids, crack initiation beneath multiple microcontacts and the role of indentation mechanics associated with material microstructures need to be understood (Lawn et al., 2021). Although abrasive machining is dynamically, thermally and geometrically different from quasi-static indentations, similar microfracture and deformation events have been observed in both indentation and abrasive machining processes for these materials (Lawn et al., 2021; Malkin and Hwang, 1996; Xu et al., 1996). The indentation load corresponds to the machining normal force per grit, the loading/unloading rate mimics the machining cutting speed and the indenter shape simplifies the cutting tool geometry (Yan et al., 2006). The fixed depth in indentation representing the normal displacement is parallel to the normal displacement known as the depth of cut measured in abrasive machining (Xu et al., 1996). Therefore, the deformation and damage induced in indentation processes predict the material machinability and determine the removal modes (Malkin and Hwang, 1996; Lawn et al., 2021).

Accordingly, extensive *ex-situ* nanoindentation studies of pre-sintered and sintered zirconia materials were conducted together with scanning probe microscopy. The results have revealed load-rate dependent mechanical properties in both materials and indentation behaviors, such as the elasticity, the plasticity and the resistance to machining-induced damage (Alao and Yin, 2015; 2016). Although these results provide useful insights about the small-scale contact mechanical behaviour associated with the wear and machinability of zirconia materials, they lacked understanding of the indentation-induced deformations and failures in zirconia materials at a microstructural level. This is because scanning probe microscopy can only image the deformation geometrical topographies but cannot clearly identify the material microstructures.

Moreover, abrasive machining involves repetitive diamond indentations and scratches in a work materials, i.e., the work material material is subject to cyclic loading/unloading impact from abrasives. The understanding of abrasive machining processes is technological difficult due to real time high speed dynamic interactions of diamond abrasives and a material surface as well as complicated heat generation and tool wear (Kosai and Yan, 2020). As nanoindentation techniques offer the simplicity testing of repetitive loading/unloading conditions for a diamond indenter to penetrate a material, excluding complicated heat generation and the indenter wear, cyclic nanoindentation mechanics can better mimics abrasive machining (Lawn et al., 2021; Kosai and Yan, 2020). Even though the two processes are not completely similar with respect to strain rates, speeds, material removal rates, cutting tool shapes, the understanding of nanoindentations can provide generic knowledge of materials removal mechanisms (Kosai and Yan, 2020; Malkin and Hwang, 1996).

For sintered zirconia, cyclic nanoindentation promoted a tetragonal-to-monoclinic (t-m) phase transformation and yielded higher pile-ups resulting from shear deformation, microcracking and surface spalling unlike to single nanoindentation (Kosai and Yan, 2020). Cyclic nanoindentation was also conducted on zirconia-containing lithium silicate glass-ceramic, degrading the material strength (Springall and Yin, 2019). In cyclic nanoindentation of TiNi thin film, the second indentation resulted in a notable hardness upsurge, which gradually declined in the subsequent cycles, and finally stabilized in the 7–12 indentation cycles (Pan et al., 2014). To some extent, cyclic nanoindentation mimics fatigue processes. Therefore, the hardness increase may be attributed to work hardening

and the hardness decreases may result from work softening. The hardness eventually stabilizes when reaching the fatigue limit. Thus, cyclic indentation results in a work softening effect on zirconia-containing lithium silicate glass-ceramic in which hardness decreases during subsequent loading (Springall and Yin, 2019). Regarding the cyclic indentation-induced hardness of TiNi film, the work hardening effect and a consequent softening effect from reaching the fatigue limit occurred (Pan et al. 2014). However, there remains insufficient knowledge on cyclic nanoindentation of zirconia ceramics because little is known towards the cyclic nanoindentation behavior of pre-sintered zirconia and the microstructural response of sintered zirconia.

In-situ nanoindentation inside a high-resolution scanning electron microscope (SEM) is a powerful technique to capture real-time indentation-induced deformation and damage and correlating load-displacement curves (Nautiyal et al., 2020; Nili et al., 2013). Juri et al. (2021a) have reported the microstructure-dependent quasi-plastic deformation mechanisms of porous and dense zirconia materials in nanoindentation using the technique. However, the technique has not been applied to cyclic nanoindentation studies of both pre-sintered and sintered zirconia materials.

In spite of extensive studies on nanoindentation of zirconia-related materials in single loading (Alao and Yin, 2015; 2016) and cyclic loading (Kosai and Yan, 2020; Pan et al., 2014; Springall and Yin, 2019), research gaps still remain. Firstly, there is a lack of *in-situ* SEM cyclic nanoindentation studies of zirconia materials. Secondly, in-depth microstructural analysis of elasticplastic fracture mechanics for pre-sintered and sintered zirconia materials in cyclic nanoindentation is missing, which is central to abrasive machining and wear functions of these materials.

Therefore, this paper aimed to investigate the cyclic nanoindentation behavior of pre-sintered porous and sintered dense zirconia materials at the microstructural level using *in-situ* SEM techniques. High-magnification SEM was also used to map indentation imprints. The Sakai model was used to characterize the elastic and plastic behavior of the two zirconia materials.

5.2 Experimental Procedure

5.2.1 Materials, Sample Preparation, Baseline Imaging and Mechanical Properties

Pre-sintered zirconia (IPS e.max ZirCAD, Ivoclar Vivadent) was selected, as it is machinable for the fabrication of monolithic dental crowns and bridges using dental CAD/CAM milling systems. The material contains approximately 87–95 wt% ZrO_2, 4–6 wt% Y_2O_3, 1–5 wt% HfO_2, and 0.1–1 wt% Al_2O_3 (Ritzberger et al., 2010). Samples of 15 mm × 15 mm × 2 mm were sliced and polished to obtain semi-mirror finished surfaces with a root-mean-squared R_q of approximately 72 nm measured using scanning probe imaging (NT-MDT NTEGRA, Hysitron, USA) (Alao and Yin, 2014a). Prior to polishing, a sliced sample was broken to obtain fractured surfaces for microstructural analysis.

Sintered zirconia was obtained by sintering the polished pre-sintered zirconia samples in a furnace (MTI GSL1500X, USA) at 1300 ^oC for 2 h at 10 ^oC/min followed by natural cooling to room temperature (Alao and Yin, 2014b). A sintered zirconia sample was broken to obtain fractured surfaces for microstructural analysis. Other sintered samples were polished again to reduce the sintering-induced roughness and obtain a root-mean-squared R_q of approximately 7.7 nm evaluated using scanning probe imaging (Alao and Yin, 2014b).

SEM (FEI Helios Nanolab 600, Thermo Fisher SCIENTIFIC, USA) was used to view polished and fractured pre-sintered and sintered zirconia samples for microstructural analyses. Fig. 5.1(a) shows the microstructure of polished and fractured pre-sintered zirconia samples, consisting highly isolated and interconnected porous structures with zirconia crystal sizes of approximately 300 nm. Fig. 5.1(b) shows the microstructure of polished and fractured sintered zirconia, containing a dense structure with zirconia crystal sizes of 300–500 nm. Table 5.1 provides the physical and material properties of these two zirconia materials.

In-situ SEM cyclic nanoindentation samples of pre-sintered and sintered zirconia materials with dimensions of 5 mm × 5 mm × 2 mm were obtained by cutting the polished pre-sintered and sintered zirconia materials to 15 mm × 15 mm × 2 mm. Prior to the testing, the small samples were ethanol-cleaned and dried naturally.

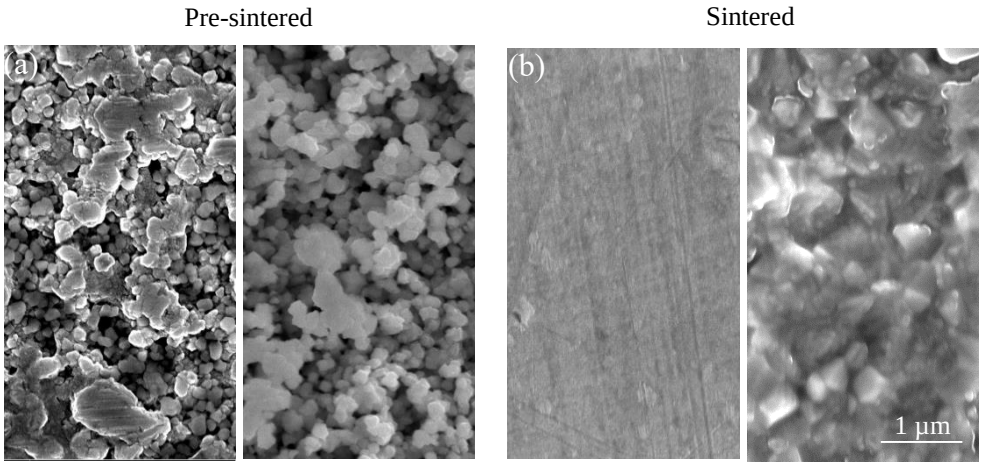

Fig. 5.1. SEM micrographs of (a) polished (left) and fractured (right) of pre-sintered zirconia and (b) polished (left) and fractured (right) of sintered zirconia surfaces.

Table 5.1. Physical and material properties of pre-sintered and sintered zirconia materials.

Material (Brand)	Porosity vol%	Density g/cm^3	Fracture Toughness (MPa m$^{1/2}$)	Flexural strength (MPa)	Poisson's ratio
Pre-sintered Zirconia (IPS e.max ZirCAD)	47.3–49.3 [a]	3.0–3.21 [a]	0.8 [b]	50–90 [a]	0.235 [c]
Sintered Zirconia (IPS e.max ZirCAD)	< 0.5 [a]	6.09 [a]	6.0 [d]	1300 [d]	0.3 [e]

[a] Data from Ritzberger et al. (2010)

[b] Data from Alao and Yin (2016)

[c] Data from Ivoclar Vivadent

[d] Data from Sakoda et al. (2018)

[e] Data from Ereifej et al. (2011)

5.2.2 *In-situ* Cyclic Nanoindentation

In-situ cyclic nanoindentation was performed using a picoindenter system (PI 88, Hysitron, USA) and a Berkovich diamond indenter tip of radius 150 nm inside the SEM in a vacuum environment. The picoindenter system is connected to an advanced control module with a 78 kHz feedback rate and data acquisition up to 39 kHz to record real-time indentation process events. It also includes a 3-axis sample positioning stage, an extended range load cell with a maximum load of 500 mN, and an electrical module allowing

simultaneous measurement of the mechanical properties during the nanoindentation process. Prior to the indentation testing, the picoindenter system calibration was performed using standard fused silica.

During *in-situ* cyclic nanoindentation, the diamond indenter tip was positioned perpendicular to a sample surface, which was mounted on the sample positioning stage tilted at 20^{o}. The testing was conducted at 10 loading and unloading cycles at 500 mN maximum peak load and a 2 mN/s loading and unloading rate. Each cycle was unloaded to 10% of the peak load. Force-displacement curves in all 10 cyclic loading and unloading processes were in-process recorded by the picoindenter system. Meanwhile, SEM imaging of each 10 cyclic indentation process was shot at 2,500× for pre-sintered zirconia and 5,000× for sintered zirconia for 4,080 seconds at a frame rate of 5 frame/s (i.e., a total 20,400 frames of SEM micrographs for each 10 cyclic indentation process). At each indentation condition, three repeated indentations were repeated at three different locations.

5.2.3 SEM Mapping of Nanoindentation Imprints

Cyclic nanoindentation imprints were mapped at high magnifications using the SEM to understand the microstructural deformation and damage at indentation apexes, diagonals, corners, and edges.

5.2.4 Nanoindentation Properties

The Oliver-Pharr method was used to determine the indentation properties, including the contact indentation depth h_c, the final indentation depth h_f, the maximum indentation depth h_{max}, the contact hardness H_c and the Young's modulus E (Oliver and Phar, 1992). The contact depth h_c was defined as the intercept value of the initial unloading slope to the displacement axis (Oliver and Phar, 1992). Briefly, the contact hardness H_c is expressed as (Oliver and Phar, 1992):

$$H_c = \frac{P_{max}}{A(h_c)} \tag{5.1}$$

where P_{max} is the maximum peak load and $A(h_c)$ is the indented projected area defined as a function of the contact depth. The reduced modulus is determined as (Oliver and Phar, 1992):

$$E_r = \frac{S\beta\sqrt{\pi}}{2\sqrt{A}} \tag{5.2}$$

where $\beta$is the correction factor which is 1 ± 0.05 and S is the initial unloading stiffness measured by the slope of the unloading curve *(dP/dh)* at the maximum indentation displacement. The Young's modulus is related to the reduced modulus E_r by the following relationship (Oliver and Phar, 1992):

$$E = (1 - v^2)\left[\frac{1}{E_r} - \frac{(1-v_i^2}{E_i}\right]^{-1} \tag{5.3}$$

where v is the sample's Poisson's ratio, E_i and v_i are the indenter's Young's modulus and Poisson's ratios, respectively. For the Berkovich indenter, E_i = 1141 GPa and v_i = 0.07 (Oliver and Phar, 1992).

Further, the elastic-plastic behavior was measured based on the Sakai model (Sakai, 1999). Briefly, the total contact displacement h_t is the sum of the elastic h_e and plastic h_p displacements as follows (Sakai, 1999):

$$h_t = h_e + h_p \tag{5.4}$$

Eq. 5.4 can be written as (Sakai, 1999; Oyen, 2006)

$$h_t = \sqrt{\frac{P_{max}}{\alpha_2 E'}} + \sqrt{\frac{P_{max}}{\alpha_1 H_T}} \tag{5.5}$$

where α_2 is a geometric constant and equal to 4.4 for the Berkovich indenter, E' is the plastic strain and expressed as $E' = E/(1 - v^2)$, α_1 is a non-dimensional constant and equal to 24.5 for the Berkovich indenter, and H_T is the resistance to plasticity. Hence, the resistance to plasticity H_T is determined using (Alao and Yin, 2016):

$$H_T = \frac{H_c \alpha_2 E'}{(\sqrt{\alpha_2 E'} - \sqrt{\alpha_1 H_c})^2} \tag{5.6}$$

The elastic h_e and plastic h_p displacements are calculated using (Alao and Yin, 2016):

$$h_e = \sqrt{\frac{P_{max}}{\alpha_2 E'}} \tag{5.7}$$

$$h_p = \sqrt{\frac{P_{max}}{\alpha_1 H_T}} \tag{5.8}$$

Thus, the elastic $h_e/(h_e + h_p)$ and plastic $h_p/(h_e + h_p)$ deformation components can also be calculated using Eqs. 5.7 and 5.8.

The resistance to machining-induced cracking *M* can be determined using the Sakai and Nowak model in terms of the fracture toughness K_{IC}, the plastic strain E' and the ductility index *D* as (Sakai and Nowak, 1992):

$$M = \frac{{K_{IC}}^2}{E'(1-D)} \tag{5.9}$$

where D can be expressed as h_f/h_{max} (Sakai, 1999).

The mean values and standard deviations of all nanoindentation properties were determined from three repeated tests under each condition. A single-factor analysis of variance (ANOVA) at a 5% significance level was performed to examine the significant influence of the nanoindentation cyclic number on the indentation properties. A paired *t*-test was also conducted at a 5% significance level to examine the material effect on these properties.

5.3 Results

5.3.1 *In-situ* Cyclic Nanoindentation

Fig. 5.2 shows the *in-situ* cyclic nanoindentation processing SEM images and the corresponding force-displacement curve with 10 loading-unloading cycles at 500 mN peak load and 2 mN/s loading/unloading rate for pre-sintered zirconia. From the initial loading (Fig. 5.2(a)) to the 1st peak load (Fig. 5.2(b)), the corresponding loading curve indicates a smooth indentation process without visible pop-in and pop-out events. In the following indentation cycles, a large amount of *in-situ* SEM nanoindentation images also revealed smooth indentation processes with one of the images at 10th peak load (Fig. 5.2(c)) as an example. Correspondingly, the cyclic force-displacement curves did not show visible pop-in and pop-out events. At the end of the unloading of 10th cycles, Fig. 5.2(d) demonstrates a perfectly plastically deformation indentation imprint of pre-sintered zirconia evidenced by being crack-free at the indentation corners and edges.

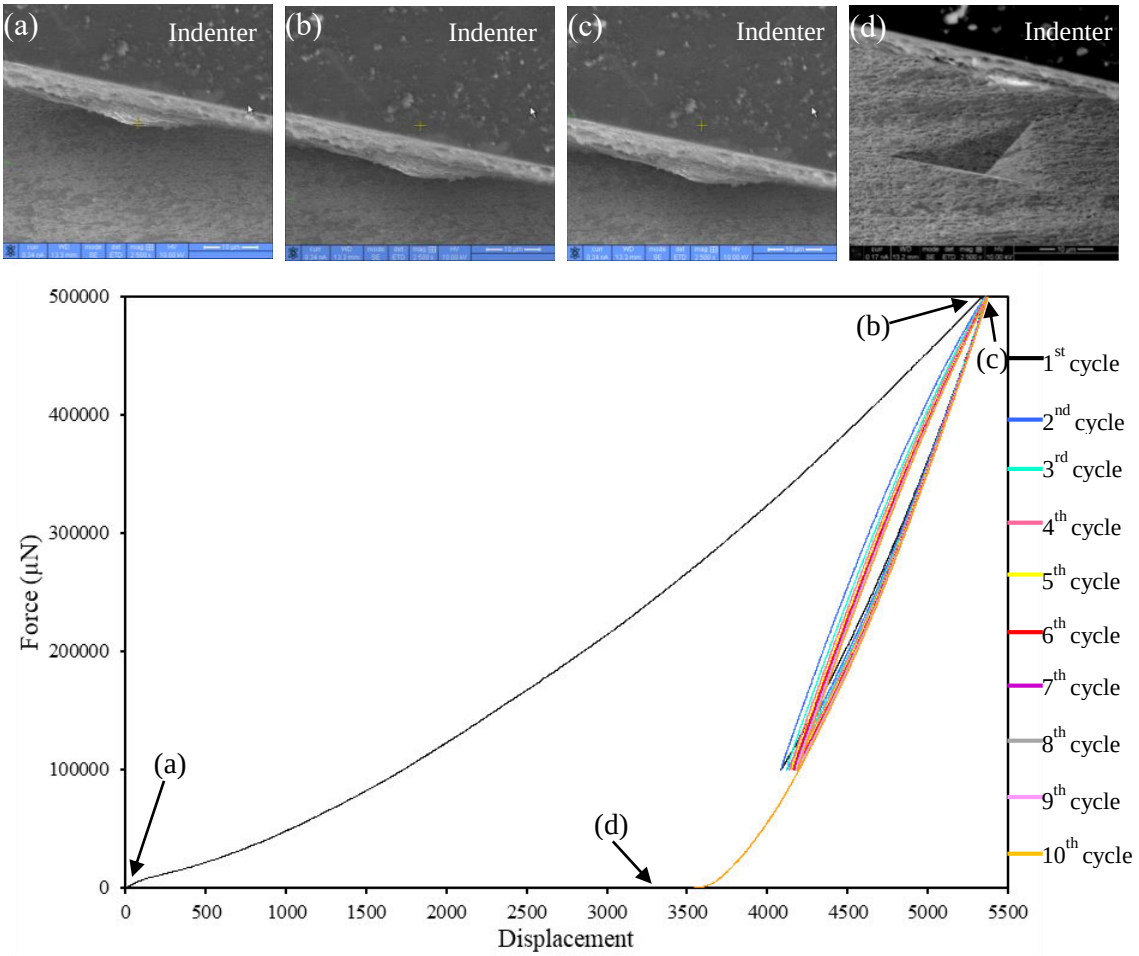

Fig. 5.2. In-situ cyclic nanoindentation processing SEM images and the force-displacement curve with 10 loading-unloading cycles for pre-sintered zirconia. (a) Initial loading contact; (b) 1st cyclic peak load contact; (c) 10th cyclic peak load contact; and (d) The final indentation imprint.

Fig. 5.3 shows the in-situ cyclic nanoindentation processing SEM images and the corresponding force-displacement curve with 10 loading-unloading cycles at 500 mN peak load and 2 mN/s loading/unloading rate for sintered zirconia. From the initial loading (Fig. 5.3(a)) to the 1st peak load (Fig. 5.3(b)), the corresponding loading curve also reveal a smooth indentation process without visible pop-in and pop-out events. In the following indentation cycles, a large amount of *in-situ* SEM nanoindentation images also showed smooth indentation processes with one of the images at the 10th peak load (Fig. 5.3(c)) as an example. Correspondingly, the cyclic force-displacement curves did not show visible pop-in and pop-out events. At the end of the unloading of the 10th cycles, Fig. 5.3(d) demonstrates a perfectly plastically deformation indentation imprint of

sintered zirconia with edge pile-ups but without visible cracks at the indentation corners and edges.

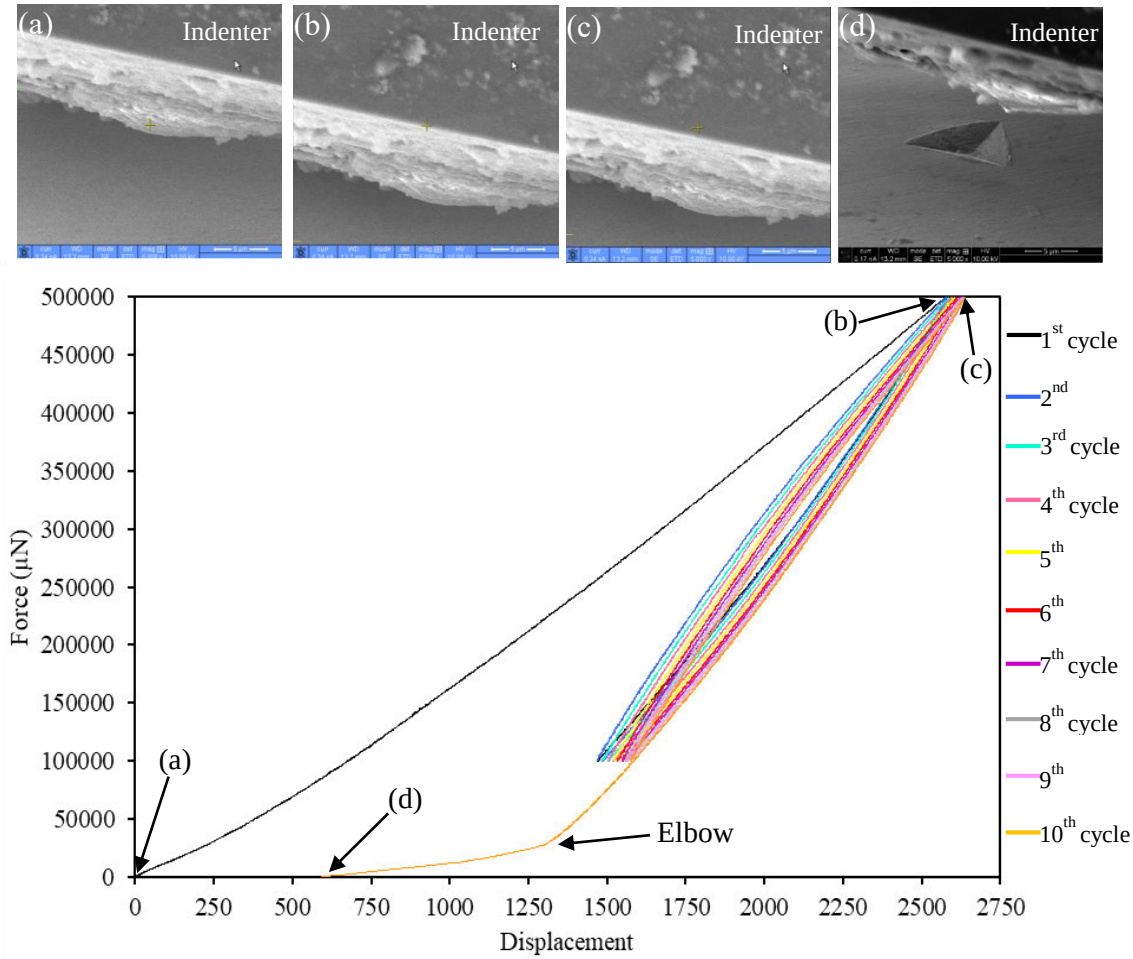

Fig. 5.3. In-situ cyclic nanoindentation processing SEM images and the force-displacement curve with 10 loading-unloading cycles for sintered zirconia. (a) Initial loading contact; (b) 1st cyclic peak load contact; (c) 10th cyclic peak load contact; and (d) The final indentation imprint.

Fig. 5.4 shows the final indentation depths h_f, the indentation contact depths h_c, and the maximum indentation depths h_{max} for pre-sintered and sintered zirconia materials versus the nanoindentation cyclic number. These values for both materials slightly increased with the cyclic number (ANOVA, $p > 0.05$). Indented pre-sintered zirconia had 3641.0 ± 82.4 nm to 3937.1 ± 224.8 nm for h_f, 4548.1 ± 115.8 nm to 4721.4 ± 234.6 nm for h_c and 5479.3 ± 117.5 nm to 5624.5 ± 226.8 nm for h_{max}. In contrast, indented sintered zirconia had 1102.8 ± 28.3 nm to 1167.2 ± 168.1 nm for h_f, 1778.9 ± 24.6 nm to 1790.6 ± 107.4 nm for h_c and 2623.4 ± 33.2 nm to 2627.4 ± 82.4 nm for h_{max}.

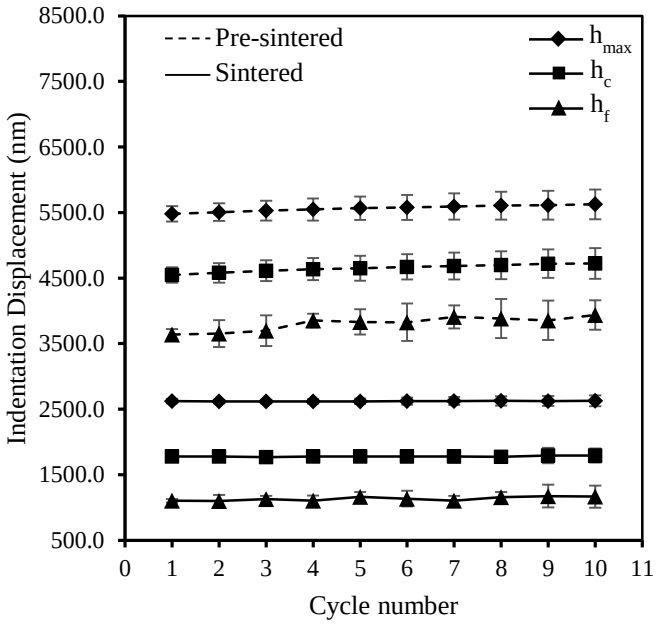

Fig. 5.4. Indentation displacements of the final depths h_f, the contact depths h_c and the maximum depths h_{max} for pre-sintered and sintered zirconia materials versus nanoindentation cycles.

5.3.2 Nanomechanical Properties

Fig. 5.5 show the nanomechanical properties of pre-sintered and sintered zirconia materials versus nanoindentation cycles. The contact hardness H_c (Fig. 5.5(a)) for both materials slightly increased with the cyclic number (ANOVA, $p > 0.05$). Sintered zirconia had a hardness ranging from 13.84 ± 0.36 GPa to 13.99 ± 0.70 GPa, approximately 11 times higher than pre-sintered state with values from 1.78 ± 0.14 GPa to 1.83 ± 0.49 GPa. Similarly, the Young's moduli E (Fig. 5.5(b)) did not vary significantly with the cyclic number (ANOVA, $p > 0.05$). Sintered zirconia had mean moduli scaling from 112.67 ± 12.00 GPa to 122.60 ± 16.32 GPa, 6 times higher than in its pre-sintered state ranging from 20.45 ± 1.49 GPa to 21.96 ± 3.31 GPa, as well as much larger standard deviations. The resistance to plasticity H_T values (Fig. 5.5(c)) were insignificantly affected by the cyclic number (ANOVA, $p > 0.05$) but they were significantly influenced by the material microstructure (t-test, $p < 0.05$). The H_T values for pre-sintered zirconia ranged from 15.12 ± 5.30 GPa to 19.11 ± 11.26 GPa, which were significantly lower than those for sintered zirconia varying from 244.34 ± 53.73 GPa to 341.34 ± 118.68 GPa with larger standard deviations. The elastic h_e and plastic h_p displacements (Fig. 5.5(d)) were flat with the cyclic number (ANOVA, $p > 0.05$). However, pre-sintered zirconia had

approximately two times larger elastic and plastic displacements than sintered zirconia (*t*-test, $p < 0.05$). For each material, its elastic displacements were significantly larger than its plastic ones (*t*-test, $p < 0.05$). The elastic $h_e/(h_e + h_p)$ and plastic $h_p/(h_e + h_p)$ deformation components (Fig. 5.5(e)) also reveal insignificant changes with the cyclic number (ANOVA, $p > 0.05$) but a strong material effect (*t*-test, $p < 0.05$). The elastic components for sintered zirconia were significantly higher than those in a pre-sintered state (*t*-test, $p < 0.05$) while the plastic components for the former were significantly lower than those for the latter (*t*-test, $p < 0.05$). Meanwhile, for each material, its elastic deformation components were also significantly larger than its plastic deformation components (*t*-test, $p < 0.05$). The resistances to machining-induced cracking M (Fig. 5.5(f)) did not obviously change with the cyclic number (ANOVA, $p > 0.05$). Sintered zirconia exhibited resistances ranging from 441.54 ± 73.27 GPa to 488.16 ± 57.95 GPa, more than three times larger than those in the range of 136.77 ± 7.58 GPa to 155.33 ± 21.80 GPa for pre-sintered state, indicating a significant material effect (*t*-test, $p < 0.05$).

5.3.3 SEM Mapping of Nanoindentation Imprints

Fig. 5.6 shows high-magnification SEM micrographs of a nanoindentation imprint in pre-sintered zirconia after ten indentation cycles. Fig. 5.6(a) reveals an overall view of the indentation imprint. At the apex region (Fig. 5.6(b)), where the highest stress concentration was induced by the indenter, there were severely compressed, fragmented, and pulverized zirconia crystals. Localized agglomerated zirconia crystals and smeared marks with significant pores reduction were formed due to the impact of the cyclic loading and unloading process. In a diagonal vicinity (Fig. 5.6(c)), there were compressed, fragmented, pulverized, and localized agglomerated zirconia crystals. At an indentation corner (Fig. 5.6(d)), microfractures and cracks, along with smeared crystals were observed. Near the corner, densification, fragmentation, and agglomeration of zirconia crystals were found. However, no crack extending the indented corner was observed. Near an edge of the indentation imprint (Fig. 5.6(e)), there were large edge cracks resulting from irregular fractures, as well as compressed, pulverized, and smeared agglomerated zirconia crystals.

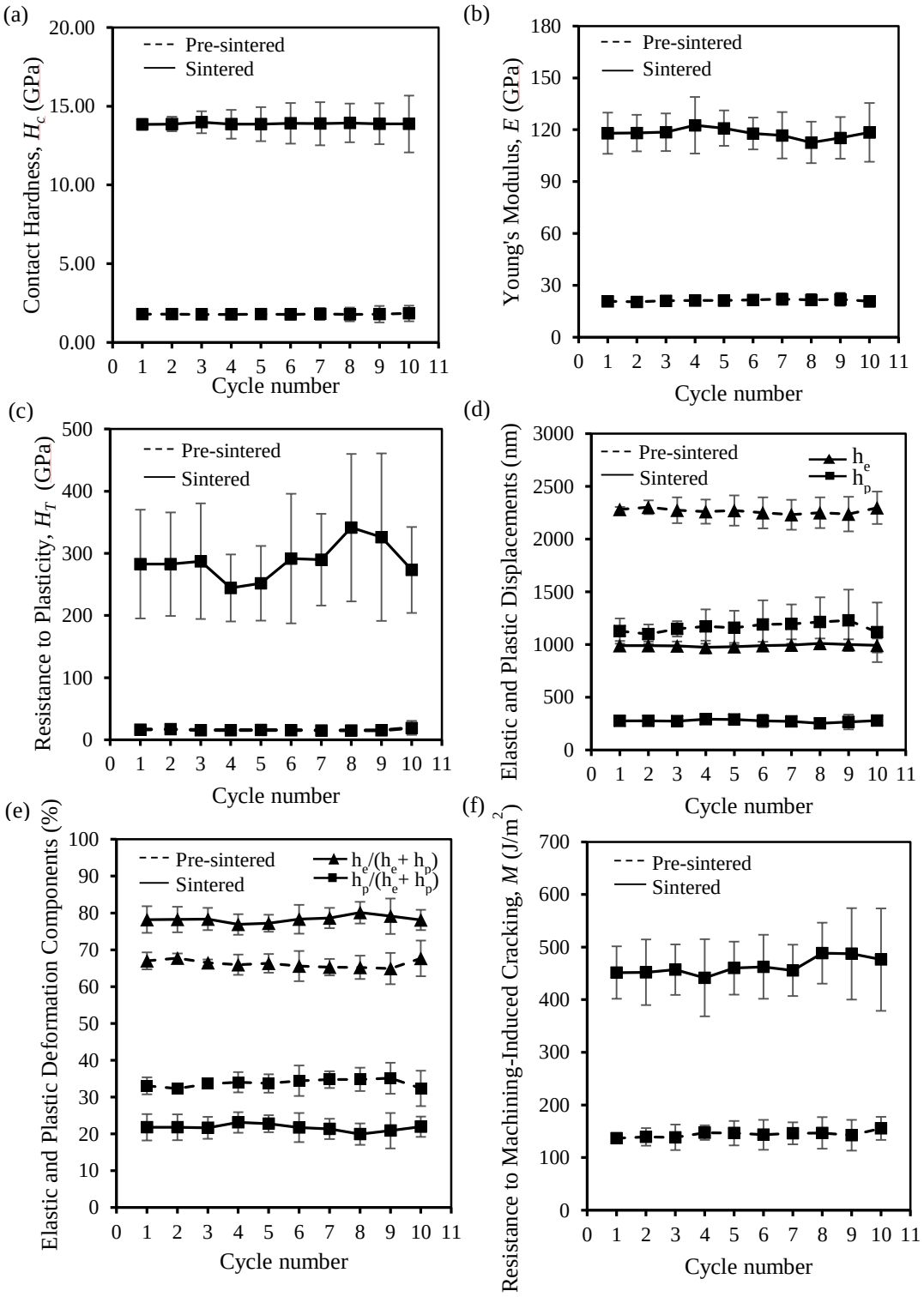

Fig. 5.5 The nanomechanical properties of pre-sintered and sintered zirconia materials versus nanoindentation cycles, including (a) contact hardness H_c, (b) Young's moduli E, (c) resistance to plasticity H_T, (d) elastic h_e and plastic h_p displacements, (e) elastic h_e / (h_e + h_p) and plastic h_p / (h_e + h_p) deformation components, and (f) resistance to machining-induced cracking M.

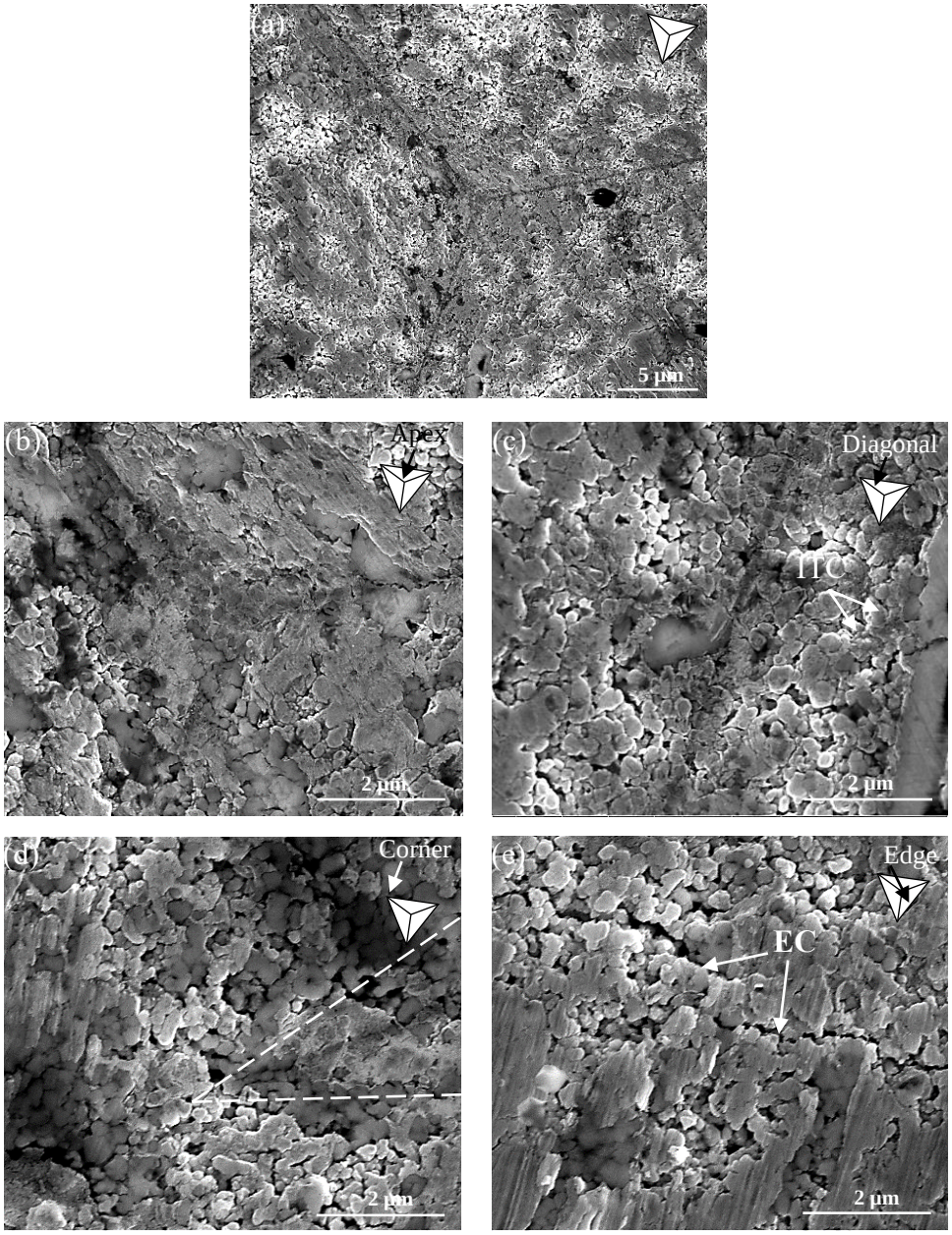

Fig. 5.6. High-magnification SEM micrographs of a final indentation imprint after 10 cycles in pre-sintered zirconia. (a) Overall indented morphology, (b) Morphology at the apex, (c) Morphology along a diagonal, (d) Morphology at a corner, and (e) Morphology of an indented area. “ITC” denotes intergranular cracks. “EC” denotes edge cracks.

Fig. 5.7 shows high-magnification SEM micrographs of a nanoindentation imprint in sintered zirconia after ten indentation cycles. Fig. 5.7(a) shows an overall view of the indentation imprint with visible plastic shear bands and edge pile-ups. Detailed shear bands and localized microfractures are observed at the apex (Fig. 5.7(b)) and along a diagonal (Fig. 5.7(c)) of the indentation. At an indentation corner (Fig. 5.7d), localized

microfractures and shear bands coexisted. In an edge area (Fig. 5.7(e)), there were shear bands, localized microfractures, and shear-band induced edge pile-ups.

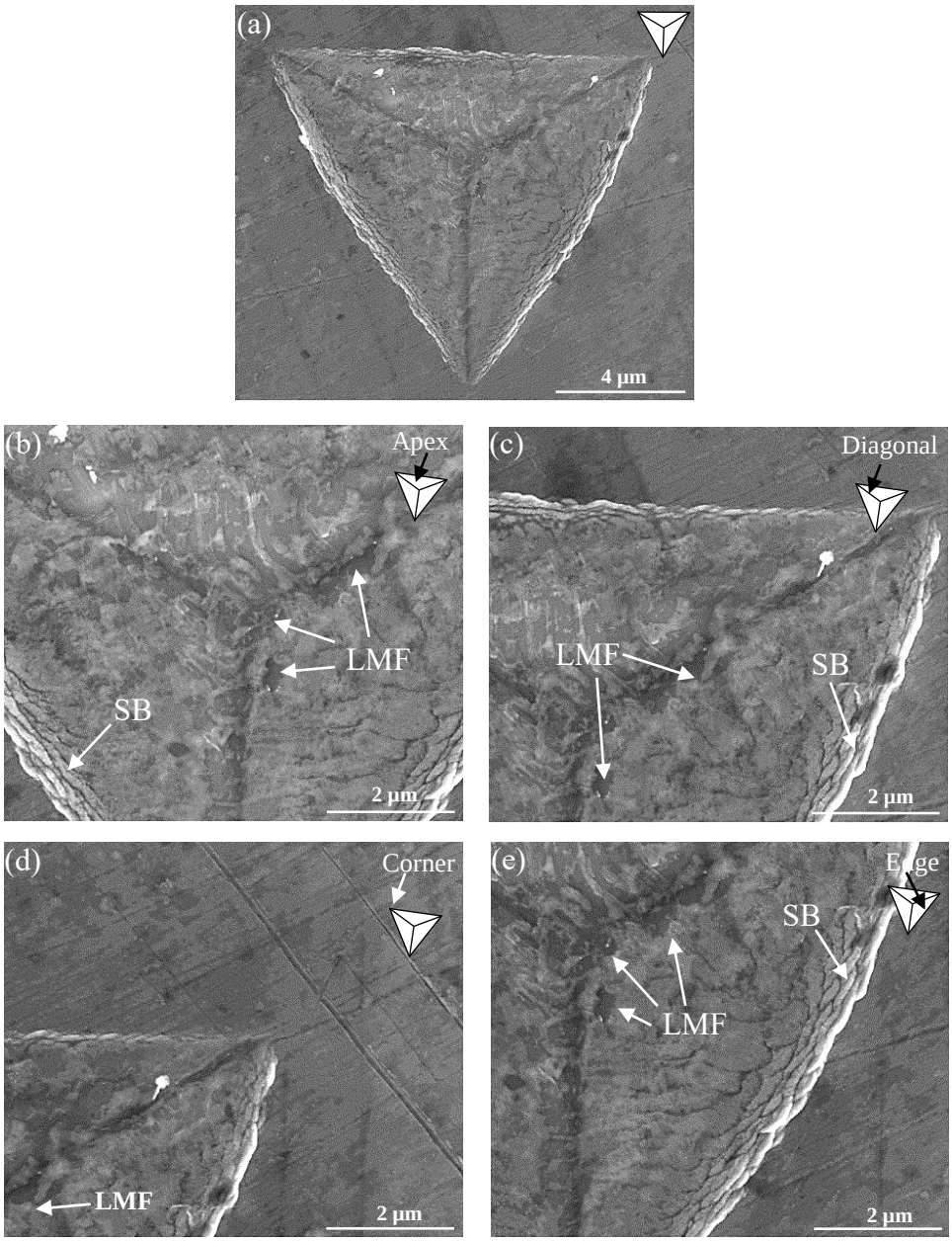

Fig. 5.7. High-magnification SEM micrographs of a final indentation imprint after 10 cycles in sintered zirconia. (a) Overall indented morphology, (b) Morphology at the apex, (c) Morphology along a diagonal, (d) Morphology at a corner and (e) Morphology of an indented area. “SB” denotes shear band. “LMF” denotes localized microfractures.

5.4 Discussion

The results of this study have revealed a strong zirconia microstructural effect on the cyclic nanoindentation responses of pre-sintered and sintered states.

In-situ SEM observations of both cyclic nanoindentation processes and smooth force-displacement curves without any discontinuities for pre-sintered (Fig. 5.2) and sintered (Fig. 5.3) zirconia states demonstrate the plastic deformation of the two materials. Although both cyclic force-displacement curves for pre-sintered and sintered zirconia materials show smoothly continuous lines, the loading-unloading curves for sintered zirconia (Fig. 5.3) are obviously steeper than those for pre-sintered zirconia (Fig. 5.2). In addition, the cyclic indentation imprint for sintered zirconia (Fig. 5.3d) exhibited as much smaller than that for pre-sintered zirconia (Fig. 5.2(d)) at the same magnification of 5,000×. The much larger h_f, h_c and h_{max} values for pre-sintered zirconia than those for sintered zirconia reflect a significant material effect on these indentation depths (*t*-test, $p < 0.05$). Further, on the unloading curves of sintered zirconia (Fig. 5.3), a sudden slope transition known as an elbow was observed, which was absent on the force-displacement curves for pre-sintered zirconia (Fig. 5.2). The elbow observed could have ascribed to the formation of edge pile-ups (Figs. 5.3(d) and 5.7) in sintered zirconia with a dense microstructure (Fig. 5.1(b)) due to the volume expansions under cyclic nanoindentation forces. This elbow phenomenon was also observed in a single indention of silicon (Zhang and Basak, 2013) and cyclic indentation of sintered zirconia (Kosai and Yan, 2020), which occurrences were also volume expansions. Gaillard et al., (2009) suggested that the pile-ups formed around indentations may have also resulted from volume expansions through the phase transformation mechanism when indenting sintered zirconia. In highly porous pre-sintered zirconia (Fig. 5.1(a)), the indentation-induced volume expansion may be consumed by the pore filling and moving because of the weak pore networks. Therefore, no visible edge pile-ups can be observed around the indentation imprints (Figs. 5.2(d) and 5.6) and the elbow phenomenon is not shown in the unloading curves of pre-sintered zirconia (Fig. 5.2).

Plastic deformation revealed in smooth and continuing force-displacement curves (Figs. 5.2 and 5.3) and nanoindentation imprints (Figs. 5.2(d) and 5.3(d)) for both pre-sintered and sintered zirconia materials at lower magnification need to be further analyzed. Although no visible crack extending from the indentation imprints are observed, the high-

magnification SEM mapping of both indentation imprints showed localized brittle damage inside both indented materials (Figs. 5.6 and 5.7). At the microstructural level, the cyclic nanoindentation responses of the two zirconia materials may be more precisely described as quasi-plastic deformation. This is evidenced by indentation-induced microcracks, edge cracks, microfractures, fragmentation, and pulverized zirconia crystals in porous pre-sintered zirconia (Fig. 5.6) and shear bands and localized microfractures in sintered zirconia (Fig. 5.7). Although similar quasi-plastic deformation was observed in single indentation of the two materials (Juri et al., 2021a), there were different damage mechanisms under cyclic nanoindentation.

In pre-sintered zirconia, cyclic nanoindentation induced quasi-plastic deformation may have encased a population of discrete microcracks, resulting in much-reduced porosity and severely compressed, accumulated, and agglomerated zirconia crystals and microcracks together with edge microcracks (Fig. 5.6). Weak interfaces of the interconnected pore network in the porous material can easily be broken by initial loading and compassing of the indenter, forming fragmented and pulverized zirconia crystals. These broken pore networks might have acted as shear faults in the following cyclic indentations, contributing to the quasi-plastic deformation of the porous material. The repeated cyclic loading/unloading of the indenter may have further fragmented and pulverized zirconia crystals, resulting in accumulated fine zirconia crystals (Fig. 5.6(b)). Furthermore, high indentation stresses from repeated loading and unloading of the indenter produced not only microcracks (Fig. 5.6(c)) inside the indent imprint but also large edge cracking (Fig. 5.6(e)). Lawn et al. (2021) suggested that shear fault within a quasi-plastic deformation zone could act as a source of crack initiation. Therefore, the broken pore networks in porous zirconia as shear faults may have enabled the cyclic indentation-induced damage to expand and densify further to form large edge cracks, microcracks and compressed densification (Fig. 5.6).

In sintered zirconia, cyclic nanoindentation-induced quasi-plastic deformation was dominated by shear bands because dislocation nucleation and interaction may prevail in the strong interfaces between zirconia crystals. Shear band and pile-up formations surrounding the indentation contact boundaries could be ascribed to the dislocation network and volume expansion (phase transformation), as observed by Gaillard et al. (2009) and Kosai and Yan (2020) in sintered zirconia polycrystals. In contrast to single

nanoindentation (Juri et al., 2021a), cyclic indentation yielded higher pile-ups (Fig. 5.3), larger shear bands, and localized microfractures along the diagonal length (Fig. 5.7). Further, cyclic nanoindentation induced smaller localized microfractures at the apex and diagonal with high stresses of the residual indentation imprint (Fig. 5.7). In comparison, single indentation produced microfractures around the indented region, resulting from material sticking to the indenter and then pulling out during unloading (Juri et al., 2021a). Edge cracks in single indentation (Juri et al., 2021a) did not occur during cyclic indentation. This may be due to strain hardening in cyclic indentation, resulting in higher yield and fracture strength for sintered zirconia. Cyclic indentation may have promoted the material plastic flow, producing larger shear bands and pile-ups (Fig. 5.7). Therefore, the primary deformation mechanism could include zirconia crystal boundary sliding, pushing zirconia crystals against each other with a dislocation motion, and forming shear bands and pile-ups during subsequent loading and unloading. Grain boundary sliding deformation was also studied in the Berkovich indentation of zirconia-based ceramics under constant strain rates of 0.01–0.2 s^{-1} (Liu et al., 2015). Much fewer surface defects are shown in sintered zirconia (Fig. 5.1(b)) than pre-sintered zirconia (Fig. 5.1(a)) exhibits higher resistance to cyclic loading and unloading for the former than the latter.

The independence of contact hardness H_c values for both zirconia materials from indentation cycles (Fig. 5.5(a)) may be attributed to strain hardening. In general, cyclic indentation may have enhanced the contact depths to result in lower hardness based on Eq. 5.1. Due to the strain hardening, all contact depths remained fairly similar through all the indentation cycles (Fig. 5.4). These were also proved by load-displacement curves with very close gaps of the loading/unloading curves between each cycle for both materials (Figs. 5.2 and 5.3). For pre-sintered zirconia, the strain hardening may be ascribed to accumulated zirconia crystals filling the pores, providing resistance to indentation loads and movements of zirconia crystals. The relative consistency of the hardness values for the two zirconia materials could predict their fatigue behavior and limits. This strain hardening of both pre-sintered and sintered zirconia materials is in stark contrast with the strain softening of pre-crystallized zirconia-reinforced lithium silicate glass ceramics (Springall and Yin, 2019).

The independence of Young's moduli for the materials from indentation cycles (Fig. 5.5(b)) may be because Young's modulus is dependent on the contact area and the

contact stiffness (Eq. 5.2). The contact stiffness depends on the maximum and final depths, and the unloading exponent, which are relatively similar (Figs. 5.2 and 5.3). In addition, the indentation deformation modes for both materials were quasi-plastic. Consequently, the contact stiffness shows insignificant variation due to quasi-plastic deformation.

The much higher resistance to plasticity H_T for the sintered state over the pre-sintered state (Fig. 5.5c) may be due to the elastic and plastic deformation components in Fig. 5.5(e) revealing that the former had higher elastic deformation components and lower plastic deformation components than the latter. This means that sintered zirconia would have more elastic deformation than the pre-sintered state during cyclic indentations. In addition, the compact and dense microstructure of sintered zirconia (Fig. 5.1(b)) might have provided a high resistance to deformation and caused significantly higher resistance to plasticity H_T than pre-sintered zirconia. The independence of the elastic deformation components (Fig. 5.5(e)) to cyclic loading/unloading processes could be explained in terms of the maximum shear stresses induced in the elastic-plastic transition. The maximum shear stresses can be estimated by the following relationship (Packard and Schuh, 2007):

$$\tau_{max} = 0.45 \left(\frac{16 P_c E_r^2}{9\pi^3 R^2}\right)^{1/3} \tag{5.10}$$

where P_c is the critical load to initiate plasticity E_r is the reduced modulus and R is the indenter radius (~ 150 nm for the Berkovich diamond indenter tip). The critical load P_c corresponds to the first pop-in event that occurred in the loading curve where the elastic-plastic transition occurs. However, this study shows that for both pre-sintered and sintered zirconia materials, the loading curves are smooth (Figs. 5.2 and 5.3) without any evidence of discontinuities. Moreover, plastic discontinuities (pop-in events) are more easily observed at low peak loads and small indentation displacements (Oyen and Cook, 2009). Therefore, by applying the Hertzian elastic prediction of the load-displacement relationship, a load P can be described as follows (Lawn, 1998):

$$P = \frac{4}{3} E_r R^{\frac{1}{2}} h^{\frac{3}{2}} \tag{5.11}$$

where h is the instantaneous indentation depth. At the elastic-plastic transition, the sharp Berkovich indenter may inevitably blunt, and the geometry can be approximated as spherical. Hence, in this study, the critical load P_c can be predicted using the Hertzian law and the total elastic contact displacements h_e be seen represent an elastic portion of the indentation depth as:

$$P_c = \frac{4}{3} E_r R^{1/2} h_e^{3/2} \tag{5.12}$$

Fig. 5.8 shows the maximum shear stresses for pre-sintered and sintered zirconia materials versus the nanoindentation cycle number, ranging from 12.73 ± 1.28 GPa to 13.30 ± 1.32 GPa for the former and 43.49 ± 3.11 GPa to 46.00 ± 4.16 GPa for the latter. The independence of the maximum shear stresses for both materials from the indentation cycles reconfirms the independent elastic and plastic deformation against the number of cyclic loading. Hence, the maximum shear stress must exceed the material theoretical shear strength to induce plastic deformation. The material theoretical shear strength can be determined as follows (Shaw, 1995):

$$\tau_{theoretical} = \frac{G}{2v} \tag{5.13}$$

where G is the shear modulus and is expressed by (Callister and Rethwisch, 2018) :

$$G = \frac{E}{2(1+v)} \tag{5.14}$$

The calculated shear moduli over 10 indentation cycles ranged from 8.15 ± 0.78 GPa to 8.76 ± 1.50 GPa for pre-sintered zirconia and 43.33 ± 4.61 GPa to 47.16 ± 6.28 GPa for sintered zirconia. The calculated theoretical shear strength over 10 indentation cycles ranged from 1.30 ± 0.12 GPa to 1.39 ± 0.25 GPa for pre-sintered zirconia and 6.90 ± 0.73 GPa to 7.50 ± 1.00 GPa for sintered zirconia. In comparison with the maximum shear stresses induced in cyclic indentations, it is obtained as

$$\tau_{\max(pre-sintered)} > \tau_{theoretical(pre-sintered)} \tag{5.15}$$

$$\tau_{\max(sintered)} > \tau_{theoretical(sintered)} \tag{5.16}$$

Hence, sufficient shear stresses were induced to produce plastic deformation for both zirconia materials.

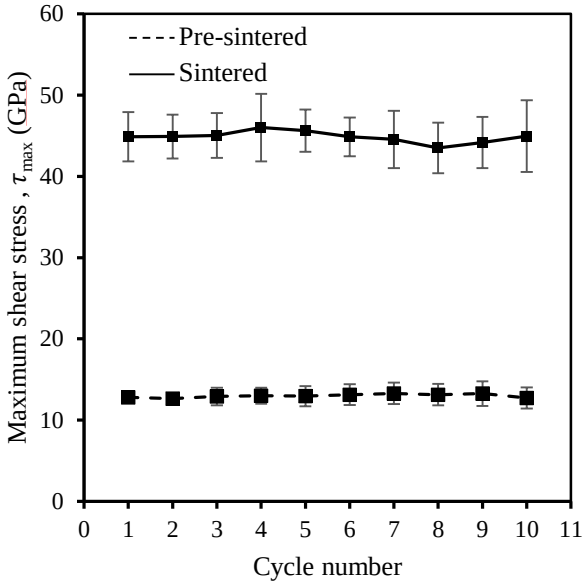

Fig. 5.8. Maximum shear stresses τ_{max} for pre-sintered and sintered zirconia materials versus nanoindentation cycles.

The significantly lower resistance to machining-induced cracking *M* of pre-sintered zirconia (Fig. 5.5(f)) may be attributed to its single (isolated) and multiple (interconnected) porous microstructure (Fig. 5.1(a)). Rice (1984) treats pores as fracture origins in polycrystalline ceramics to form equatorial cracks that could become sharp flaws, and propagate across the ceramic crystals. This is evidenced by the indentation-induced microfractures and edge cracks (Fig. 5.6). Repeated loading forces might have broken pore necks between zirconia crystals and allowed microcracks to generate and propagate from one layer of zirconia crystal boundaries to another, resulting in edge cracking. In contrast, sintered zirconia with its compact microstructure (Fig. 5.1(b)) had strong interface boundaries to resist cyclic indentation forces, resulted in less surface damage (Fig. 5.7). Therefore, pre-sintered zirconia is more vulnerable to machining-induced edge chipping than sintered zirconia. This is consistent with diamond machining during which pre-sintered zirconia suffered more severe edge chipping damage than sintered zirconia (Juri et al., 2021b), which is a bottleneck to zirconia restoration.

Fig. 5.9 schematically describes the cyclic indentation mechanics models for the two zirconia materials. In porous pre-sintered zirconia (Fig. 5.9(a)), the first indentation

pressed weak interface boundaries of the material and broke them into discrete zirconia crystals to form a deformed zone with reduced porosity, and fragmented and pulverized zirconia crystals. In the following indentation cycles, discrete zirconia crystals were further compressed and broken to produce more discrete zirconia crystals and pore fillings, resulting in a larger deformation zone with significant pore reduction and accumulation of pulverized zirconia crystals. In dense sintered zirconia (Fig. 5.9(b)), the first indentation resulted in shear-band induced edge pile-ups and a plastic deformation zone with localized microfractures. In the subsequent indentation cycles, zirconia crystals were further pushed, leading to a larger shear-band plastic zone with higher edge pile-ups and more localized microfractures.

In comparison with single indentation of the two zirconia materials (Juri et al., 2021a), cyclic indentations produced much larger indentation sizes (Figs. 5.2 and 5.3) and higher indentation displacements (Fig. 5.4) for both materials. This suggests that in repetitive diamond indenting processes, such as diamond milling and grinding, pre-sintered zirconia can be more easily removed with higher removal rates than sintered zirconia. The cyclic indentation models in Fig. 5.9 can liken the machining mechanisms for the two materials, in which sintered zirconia yields significantly less machining-induced edge chipping than pre-sintered zirconia.

What do our results mean to clinical application of zirconia restorations? Both dental CAD/CAM milling and manual handpiece adjusting/polishing processes for zirconia materials can largely influence their long-term performance (Wu et al., 2021). Our study has shown that the different microstructural responses of pre-sintered and sintered zirconia materials to cyclic nanoindentation with quasi-plastic deformation and damage characteristics. These cyclic nano-scale mechanical behaviors predict the diamond machining mechanisms and machinability of pre-sintered and sintered zirconia materials, making the former easier to machine but more susceptible to machining-induced damage than the latter. Our findings indicate that incipient cracks induced inside quasi-plastic zones are controlled by zirconia microstructures under mechanical loading. This may lay a foundation for the understanding of the role of zirconia microstructures in controlling their mechanical properties to achieve efficient machining processes for durable zirconia restorations. Microstructural optimization by applying different sintering conditions to zirconia blanks may be our next step to improve machinability of zirconia materials

without compromising strength by machining-induced damage. Moreover, our results may also be applicable to zirconia products as load-bearing mechanical components subjected to contact problems leading to abrasive wear and erosion. The cyclic indentation induced quasi-plastic damage in zirconia products may act as wear damage and stress concentrators, leading to subsequent catastrophic fatigue failures.

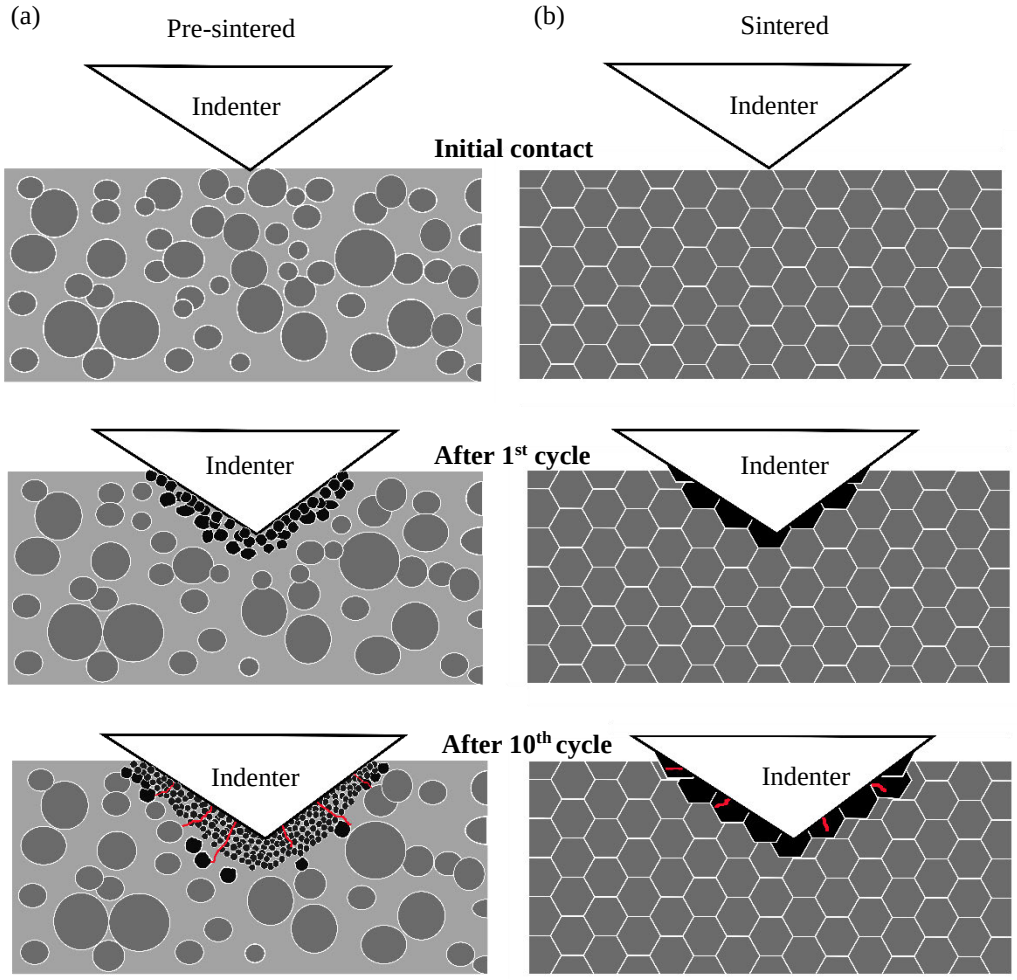

Fig. 5.9. Cyclic indentation mechanics models for (a) pre-sintered and (b) sintered zirconia materials.

5.5 Conclusions

This study conducted *in-situ* SEM cyclic nanoindentation of pre-sintered and sintered zirconia materials. The following conclusions can be drawn from the results:

a) The elastic and plastic properties (contact hardness, Young's moduli, resistance to plasticity, elastic and plastic displacements, elastic and plastic deformation

components, and resistance to machining-induced cracking) are microstructure-dependent.

b) Pre-sintered zirconia yielded significantly lower contact hardness, Young's moduli, resistance to plasticity, elastic deformation components, and resistance to machining-induced cracking, and higher elastic and plastic displacements than sintered state.

c) For porous pre-sintered zirconia, cyclic nanoindentation were featured with the quasi-plastic deformation in the form of pore network breaking, fragmentation and pulverization of zirconia crystals, resulting in compressed pulverized layers mixed with microfractures and large edge cracks. For dense sintered zirconia, cyclic nanoindentation induced shear-band dominated quasi-plastic deformation with minor localized microfractures at stress concentration sites (the indentation apex and diagonals) and edge pile-ups.

d) All the behaviors for pre-sintered and sintered zirconia materials were independent from the cyclic nanoindentation number due to cyclic loading-induced strain hardening which stabilized the nanomechanical properties when increasing indentation cycles.

Credit Authorship Contribution Statement

Afifah Z. Juri: Conceptualization, Methodology, Investigation, Formal analysis, Validation, Data curation, Writing - original draft, Funding acquisition (PhD Scholarship, The University of Adelaide, Australia). **Animesh K. Basak:** Methodology, Investigation, Data curation, Writing - review & editing. **Ling Yin:** Conceptualization, Methodology, Validation, Writing - review & editing, Supervision, Project administration, Funding acquisition (Seed Grant, The University of Adelaide, Australia).

Declaration of Competing Interests

The authors declare that they have no known competing financial personal interests that could have appeared to influence the work reported in this paper.

Acknowledgments

This work was supported by a Ph.D. scholarship and a seed grant in manufacturing and bio-manufacturing from the University of Adelaide.

References

Alao, A. R., Yin, L., 2014a. Nano-scale mechanical properties and behavior of pre-sintered zirconia. J. Mech. Behav. Biomed. Mater. 36, 21–31. https://doi.org/10.1016/j.jmbbm.2014.03.019.

Alao, A. R., Yin, L., 2014b. Loading rate effect on the mechanical behavior of zirconia in nanoindentation. Mater. Sci. Eng. A 619, 247–255. https://doi.org/10.1016/j.msea.2014.09.101.

Alao, A. R., Yin, L., 2015. Nanoindentation characterization of the elasticity, plasticity and machinability of zirconia. Mater. Sci. Eng. A 628, 181–187. https://doi.org/10.1016/j.msea.2015.01.051.

Alao, A. R., Yin, L., 2016. Assessment of elasticity, plasticity and resistance to machining-induced damage of porous pre-sintered zirconia using nanoindentation techniques. J. Mater. Sci. Technol. 32, 402–410. https://doi.org/10.1016/j.jmst.2016.02.009.

Callister, W. D., Rethwisch, D. G., 2018. Materials science and engineering: an introduction. Wiley, New York, NY.

Chevalier, J., Gremillard, L., Virkar, A. V., Clarke, D. R., 2009. The tetragonal-monoclinic transformation in zirconia: lessons learned and future trends. J. Am. Ceram. Soc. 92, 1901–1920. https://doi.org/10.1111/j.15512916.2009.03278.x.

Denry, I., Kelly, J. R., 2008. State of the art of zirconia for dental applications. Dent. Mater. 24, 299–307. https://doi.org/10.1016/j.dental.2007.05.007.

Ereifej, N., Rodrigues, F. P., Silikas, N., Watts, D. C., 2011. Experimental and FE shear-bonding strength at core/veneer interfaces in bilayered ceramics. Dent. Mater. 27, 590-597. https://doi.org/10.1016/j.dental.2011.03.001.

Gaillard, Y., Anglada, M., Jiménez-Piqué, E., 2009. Nanoindentation of yttria-doped zirconia: effect of crystallographic structure on deformation mechanisms. J. Mater Res. 24, 719–727. https://doi.org/10.1557/jmr.2009.0091.

Garvie, R. C., Hannink, R. H., Pascoe, R. T., 1975. Ceramic steel? Nature 258, 703–704. https://doi.org/10.1038/258703a0.

Juri, A. Z., Basak, A. K., Yin, L., 2021a. Microstructural responses of Zirconia materials to in-situ SEM nanoindentation. J. Mech. Behav. Biomed. Mater. 118, 104450. https://doi.org/10.1016/j.jmbbm.2021.104450.

Juri, A. Z., Zhang, Y., Kotousov, A., Yin, L., 2021b. Zirconia Responses to Edge Chipping Damage Induced in Conventional and Ultrasonic Vibration-Assisted Diamond Machining. J. Mater. Res. Technol. 13, 573–589. https://doi.org/10.1016/j.jmrt.2021.05.005.

Kohorst, P., Dittmer, M. P., Borchers, L., Stiesch-Scholz, M., 2008. Influence of cyclic fatigue in water on the load-bearing capacity of dental bridges made of zirconia. Acta Biomater. 4, 1440–1447. https://doi.org/10.1016/j.actbio.2008.04.012.

Kosai, K., Yan, J., 2020. Effects of cyclic loading on subsurface microstructural changes of zirconia polycrystals in nanoscale mechanical processing. Int. J. Mach. Tools Manuf. 159, 103626. https://doi.org/10.1016/j.ijmachtools.2020.103626.

Lambert, H., Durand, J. C., Jacquot, B., Fages, M., 2017. Dental biomaterials for chairside CAD/CAM: State of the art. J Adv. Prosthodont. 9, 486–495. https://doi.org/10.4047/jap.2017.9.6.486.

Lawn, B. R., 1998. Indentation of ceramics with spheres: a century after Hertz. J. Am. Ceram. Soc. 81, 1977–1994. https://doi.org/10.1111/j.11512916.1998.tb02580.x.

Lawn, B. R., Borrero, O., Huang, H., Zhang, Y., 2021. Micromechanics of machining and wear in hard and brittle materials. J. Am. Ceram. Soc. 104, 5–22. https://doi.org/10.1111/jace.17502.

Ling, Y., Li, Q., Zheng, H., Omran, M., Gao, L., Chen, J., Chen, G., 2021. Optimisation on the stability of CaO-doped partially stabilised zirconia by microwave heating. Ceram. Int. 47, 8067–8074. https://doi.org/10.1016/j.ceramint.2020.11.161.

Liu, E., Wang, H., Xiao, G., Yuan, G., Shu, X., 2015. Creep-related micromechanical behavior of zirconia-based ceramics investigated by nanoindentation. Ceram. Int. 41, 12939–12944. https://doi.org/10.1016/j.ceramint.2015.06.136.

Malkin, S., Hwang, T. W., 1996. Grinding mechanisms for ceramics. CIRP Ann. 45, 569–580. https://doi.org/10.1016/S0007-8506(07)60511-3.

Meirowitz, A., Bitterman, Y., Levy, S., Mijiritsky, E., Dolev, E., 2019. An in vitro evaluation of marginal fit zirconia crowns fabricated by a CAD-CAM dental laboratory and a milling center. BMC oral health, 19, 1–6. https://doi.org/10.1186/s12903-019-0810-9.

Nautiyal, P., Boesl, B., Agarwal, A., 2020. Test Methods for In-Situ Mechanical Characterization. In *In-situ* Mechanics of Materials. Springer Nature Switzerland AG, Switzerland, CH. https://doi.org/10.1007/978-3-030-43320-8_3.

Nili, H., Kalantar-zadeh, K., Bhaskaran, M., Sriram, S., 2013. In situ nanoindentation: Probing nanoscale multifunctionality. Prog. Mater. Sci. 58, 1–29. https://doi.org/10.1016/j.pmatsci.2012.08.001.

Oliver, W. C., Pharr, G. M., 1992. An improved technique for determining hardness and elastic modulus using load and displacement sensing indentation experiments. J. Mater. Res. 7, 1564–1583. https://doi.org/10.1557/JMR.1992.1564.

Oyen, M. L., 2006. Nanoindentation hardness of mineralized tissues. J. Biomech. 39, 2699–2702. https://doi.org/10.1016/j.jbiomech.2005.09.011.

Oyen, M. L., Cook, R. F., 2009. A practical guide for analysis of nanoindentation data. J. Mech. Behav. Biomed. Mater. 2, 396–407. https://doi.org/10.1016/j.jmbbm.2008.10.002.

Packard, C. E., Schuh, C. A., 2007. Initiation of shear bands near a stress concentration in metallic glass. Acta Mater. 55, 5348–5358. https://doi.org/10.1016/j.actamat.2007.05.054.

Pan, G., Cao, Z., Wei, M., Xu, L., Shi, J., Meng, X., 2014. Superelasticity of TiNi thin films induced by cyclic nanoindentation deformation at nanoscale. Mater. Sci. Eng. A 600, 8–11. https://doi.org/10.1016/j.msea.2014.02.019.

Rice, R. W., 1984. Pores as fracture origins in ceramics. J. Mater. Sci. 19, 895–914. https://doi.org/10.1007/BF00540460.

Ritzberger, C., Apel, E., Höland, W., Peschke, A., Rheinberger, V. M., 2010. Properties and clinical application of three types of dental glass-ceramics and ceramics for CAD-CAM technologies. Materials 3, 3700–3713. https://doi.org/10.3390/ma3063700.

Sakai, M., Nowak, R., 1992. Fracture toughness and brittleness of ceramic materials, Ceramics Adding the Value 2, 922–931.

Sakai, M., 1999. The Meyer hardness: A measure for plasticity? J. Mater. Res. 14, 3630–3639. https://doi.org/10.1557/JMR.1999.0490.

Sakoda, S., Nakao, N., Watanabe, I., 2018. The effect of abrading and cutting instruments on machinability of dental ceramics. J. Mater. Sci. Mater. Med. 29, 1–8. https://doi.org/10.1007/s10856-018-6031-y.

Schriwer, C., Skjold, A., Gjerdet, N. R., & Øilo, M., 2017. Monolithic zirconia dental crowns. Internal fit, margin quality, fracture mode and load at fracture. Dent. Mater. 33, 1012–1020. https://doi.org/10.1016/j.dental.2017.06.009.

Shaw, M. C., 1995. Precision finishing. CIRP Ann. 44, 343–348. https://doi.org/10.1016/S0007-8506(07)62339-7.

Springall, G. A., Yin, L., 2019. Response of pre-crystallized CAD/CAM zirconia-reinforced lithium silicate glass ceramic to cyclic nanoindentation. J. Mech. Behav. Biomed. Mater. 92, 58–70. https://doi.org/10.1016/j.jmbbm.2019.01.004.

Wu, L., Sun, Z., Zhao, J., Zheng, Y., 2021. Retrospective clinical study of monolithic zirconia crowns fabricated with a straightforward completely digital workflow. J. Prosthet. Dent. In press. https://doi.org/10.1016/j.prosdent.2021.01.018.

Xu, H. H., Smith, D. T., Jahanmir, S., 1996. Influence of microstructure on indentation and machining of dental glass-ceramics. J. Mater. Res. 11, 2325–2337. https://doi.org/10.1557/JMR.1996.0296.

Yan, J., Takahashi, H., Gai, X., Harada, H., Tamaki, J. I., Kuriyagawa, T., 2006. Load effects on the phase transformation of single-crystal silicon during nanoindentation tests. Mater. Sci. Eng. A 423, 19–23. https://doi.org/10.1016/j.msea.2005.09.120.

Zhang, L., Basak, A., 2013. Quantitative prediction of phase transformations in silicon during nanoindentation. Philos. Mag. Lett. 93, 448–456. https://doi.org/10.1080/09500839.201.3.798441.

Zhang, Y., Lawn, B. R., 2018. Novel zirconia materials in dentistry. J. Dent. Res. 97, 140–147. https://doi.org/10.1177%2F0022034517737483.

Zhong, Z. W., 2020. Advanced polishing, grinding and finishing processes for various manufacturing applications: a review. Mater. Manuf. Process. 35, 1279–1303. https://doi.org/10.1080/10426914.2020.1772481.

Chapter 6 Edge Chipping in Conventional and Ultrasonic Milling

This chapter consists of the published journal article detailed below:

Juri, A. Z., Zhang, Y., Kotousov, A., Yin, L., 2021. Zirconia responses to edge chipping damage induced in conventional and ultrasonic vibration-assisted diamond machining. J. Mater. Res. Technol. 13, 573–589.https://doi.org/10.1016/j.jmrt.2021.05.005.

Statement of Authorship

Title of Paper	Zirconia responses to edge chipping damage induced in conventional and ultrasonic vibration-assisted diamond machining.
Publication status	■ Published ☐ Accepted for publication ☐ Submitted for publication ☐ Unpublished and unsuited work written in manuscript style
Publication details	*Juri, A. Z., Zhang, Y., Kotousov, A., Yin, L., 2021. Zirconia responses to edge chipping damage induced in conventional and ultrasonic vibration-assisted diamond machining. J. Mater. Res. Technol. 13, 573–589.https://doi.org/10.1016/j.jmrt.2021.05.005.*

Principal Author

Name of Principal Author (Candidate)	Afifah Zakiyyah Juri		
Contribution to the Paper	Conceptualization, Methodology, Investigation, Formal analysis, Validation, Data curation, Writing - original draft, Funding acquisition (PhD scholarship).		
Overall percentage (%)	60		
Certification:	This paper reports on original research I conducted during the period of my Higher Degree by Research candidature and is not subject to any obligations or contractual agreements with a third party that would constrain its inclusion in this thesis. I am the primary author of this paper.		
Signature		Date	30/5/2022

Co-Author Contributions

By signing the Statement of Authorship, each author certifies that:

i. the candidate's stated contribution to the publication is accurate (as detailed above);
ii. permission is granted for the candidate in include the publication in the thesis; and
iii. the sum of all co-author contributions is equal to 100% less the candidate's stated contribution

Name of Co-Author	Yanzhong Zhang
Contribution to the Paper	Methodology, Investigation, Data curation.
Signature	Date 26/May/2022

Name of Co-Author	Andrei Kotousov
Contribution to the Paper	Writing – review & editing, Validation, Investigation, Data curation.
Signature	Date 30/05/2022

Name of Co-Author	Ling Yin
Contribution to the Paper	Writing – review & editing, Validation, Supervision, Project administration, Methodology, Investigation, Funding acquisition, Formal analysis, Conceptualization.
Signature	Date 30/5/2022

Zirconia responses to edge chipping damage induced in conventional and ultrasonic vibration-assisted diamond machining

Afifah Z. Juri, Yanzhong Zhang, Andrei Kotousov, Ling Yin*

School of Mechanical Engineering, The University of Adelaide, Adelaide, SA 5005, Australia

*Corresponding Author: ling.yin@adelaide.edu.au

Abstract Machining-induced edge chipping damage represents a common challenge in ceramic applications. This paper reports on responses of zirconia materials with porous and dense microstructures to edge chipping damage induced in conventional and ultrasonic vibration-assisted diamond machining. The machining-induced damage was evaluated using optical and scanning electron microscopies. The results show that edge chipping damage produced in these processes was associated with brittle fracture and depends on the material microstructure and the vibration amplitude. Pre-sintered porous zirconia with a high brittleness index yielded significantly larger edge chipping damage than sintered dense zirconia with a low index in these processes. Ultrasonic machining at an optimal vibration amplitude minimized the scale of brittle fracture at the micro level, and thus significantly diminished edge chipping damage in zirconia materials with distinct microstructures. The investigation underpins the transition from conventional to ultrasonic vibration-assisted machining for manufacturing of ceramics to achieve better product quality.

6.1 Introduction

Zirconia is an attractive structural material widely applied in engineering and medicine due to its high strength and fracture toughness, low thermal conductivity, and good wear and corrosion resistance (Denry and Kelly, 2008; Garvie et al., 1975; Piconi and Maccauro, 1999). Excellent biocompatibility, aesthetic appearance, and optimal osseointegration has made this material very popular for dental applications (Amarante et al., 2019; Belli et al., 2017; Manicone et al., 2007; Schriwer et al., 2017; Schünemann et al., 2019; Zhang and Lawn, 2019). However, zirconia's brittleness, poor

manufactureability and susceptibility to machining-induced damage are main challenges and thus hinder its wider use.

Zirconia has porous and dense microstructures depending on sintering conditions and is subject to diamond machining to form precise shapes and sizes. Pre-sintered zirconia has a porous microstructure and low mechanical strength of 50–90 MPa (Ritzberger et al., 2010), thus can be rapidly and economically machined using inexpensive and low stiffness tools (Denry, 2013; Fraga et al., 2017; Lambert et al., 2017; Meirowitz et al., 2019). However, sintering must be processed to densify its porous structure and increase its mechanical strength, which induces approximately 20% bulk volume shrinkages (Reich et al., 2005; Sailer et al., 2007), resulting in geometrical distortions for zirconia products. Thus, shrinkage compensations must be included in initial design as well as diamond machining, and polishing processes, making manufacturing processes more complex and less precise (Miyazaki et al., 2013). Sintered zirconia has a dense microstructure and high mechanical strength of 1100 ± 200 MPa (Schriwer et al., 2017; Wendler et al., 2017), and can be machined for precise and accurate profiles using high-precision and high-stiffness tools (Abduo et al., 2010), leading to high machining costs, low efficiency and severe wear of diamond tools (Miyazaki et al., 2013).

Although zirconia is considered as ‘‘ceramic steel” (Garvie et al., 1975), it is much more brittle than steels. As both porous and dense zirconia materials undergo diamond indentations and abrasion in fabrication processes, which unavoidably produce surface and subsurface damage to zirconia materials (Anand et al., 2018a; Denkena et al., 2017). In particular, edge chipping damage representing the most severe type of mechanical damage. It has a significant impact on the mechanical functionality and reliability of zirconia products, such as zirconia crowns and bridges (Schmitter et al., 2012), and leads to fractures and failures of the products (Triwatana et al., 2012). Therefore, machining-induced damage in pre-sintered porous and sintered dense zirconia materials has recently become a focal point of research related to zirconia applications (Alao et al., 2017; Anand et al., 2018a; Denkena et al., 2017). In machining of pre-sintered porous zirconia, cooling and lubrication also affected the generation of subsurface edge chipping damage in the material (Anand et al., 2018a). However, the evaluation of the damage is yet to be investigated. In machining of sintered dense zirconia, subsurface damage and edge chipping of 15–44 μm deep in the material surfaces have been reported (Luthardt et al.,

2004; Xu et al., 1997), which depends on machining parameters. In spite of the importance of machining processes for zirconia materials, the quantitative studies of machining-induced edge chipping damage in zirconia materials with distinct porous and dense microstructures has not been documented. As mentioned above, machining-induced surface and subsurface defects were found to significantly affect the strength (Guazzato et al., 2005; Xu et al., 1997), toughness (Xu et al., 1997), hardness (Anand et al., 2018b), fatigue and reliability (Denry and Holloway, 2006; Kosmač et al., 1999), fracture behavior (Passos et al., 2015) and wear performance (Mitov et al., 2012) of zirconia products. The problem of damage mitigation/reduction can be addressed with non-conventional machining processes, such as ultrasonic vibration-assisted machining.

Ultrasonic vibration-assisted machining as one of the emerging machining techniques, is a process to assist conventional machining by adding ultrasonic vibration to the motion of a cutting tool tip to make discontinuous tool-workpiece interactions (Xu and Zhang, 2015; Yang et al., 2020). Ultrasonic machining has been used to machine hard steels and alloys (Chen et al., 2019; Goiogana et al., 2018; Lotfi et al., 2019) and brittle materials (Alkawaz et al., 2018; Bhosale et al., 2014; Song et al., 2018; Tesfay et al., 2016; Yang et al., 2019). For brittle materials, ultrasonic machining of pre-sintered porous alumina has resulted in a significant edge chipping reduction from 680 ± 30 μm to 70 ± 10 μm in comparison with conventional machining (Tesfay et al., 2016). For feldspar-containing glass ceramics, ultrasonic dental handpeice machining has reduced edge chipping by 65% (Song et al., 2018). Although these studies have provided insights into applications of ultrasonic machining for several materials, its potential to reduce edge chipping damage for brittle materials remains unclear and needs further investigation.

This paper aims to systematically study machining-induced edge chipping damage in zirconia materials with porous and dense microstructures by using conventional and ultrasonic vibration-assisted diamond milling processes. Optical and scanning electron microscopies were applied to characterize edge chipping damage depths and areas, and morphology features. Overall, the current research facilitates the development of a transition to new manufacturing processes to improve diamond machining for reliable zirconia products.

6.2 Experimental Procedure

6.2.1 Materials

A cylindrical blank of translucent pre-sintered zirconia with 98.5 mm diameter and 14 mm thickness (ZENOSTAR Zr Translucent, Wieland Dental+Technik GmbH & Co. KG, Pforzheim, Germany) was selected for this study. This material is generally utilized for dental CAD/CAM systems to produce zirconia crowns and bridges. It contains 91 wt% ZrO_2, 5 wt% Y_2O_3 as a stabilizer for retention of tetragonal grains at room temperature, 2 wt% HfO_2 as a binder for ZrO_2 powders (Monaco et al., 2013) and 0.05 wt% Al_2O_3 as an agent to reduce the susceptibility of zirconia to low-temperature degradation (Denry and Kelly, 2008; Hallmann et al., 2012). Fig. 6.1(a) shows the microstructure of fractured pre-sintered zirconia using scanning electron microscopy (SEM, FEI Helios Nanolab 600, Thermo Fisher Scientific, USA). An interconnected and isolated porous microstructure of approximately 200 nm zirconia crystals was observed. The material porosity is in the range of 47.3–49.3 vol% (Ritzberger et al., 2010). The mechanical properties of the material include the Young's modulus E of 34 GPa (Alao and Yin, 2014a), the hardness H of 1.5 GPa (Alao and Yin, 2014a), the fracture toughness K_{IC} of 0.8 MPa $m^{1/2}$ (Alao and Yin, 2016) and flexural strength of 50–90 MPa (Ritzberger et al., 2010).

Dense zirconia with a bulk density of more than 99% was achieved in a sintering process at a temperature of 1530 °C for 4 h 30 min using a digital dental furnace (Programat S1, Ivoclar Vivadent, Liechtenstein) at John Griffiths Dental Laboratory Australia. Fig. 6.1(b) shows the microstructures of fractured sintered zirconia using the SEM, revealing a highly dense and compacted microstructure of enlarged zirconia crystals of approximately 400 nm. The mechanical properties of the material include the Young's modulus E of 168 GPa (Alao and Yin, 2014b), the hardness H of 13.2 GPa (Alao and Yin, 2014b), the fracture toughness K_{IC} of 6 MPa $m^{1/2}$ (Sakoda et al., 2018), and the flexural strength of 1300 MPa (Sakoda et al., 2018).

Both pre-sintered porous and sintered dense zirconia samples were cut into rectangular blocks with dimensions of 10 × 10 × 2 mm using a diamond saw machine with a metal-bond 70 μm grit diamond disk of 450 μm thickness and 125 mm diameter (Struers Minitom, Denmark). The saw operated at a low speed with tap water as a coolant. Subsequently, top and bottom surfaces of 10 × 10 mm of each sample were polished using

a polishing machine with 1200 grit silicon carbide grinding paper on a lap disc (Struers, Denmark) to parallel the two surfaces. Both surfaces were then progressively polished using 9–6 μm diamond pastes on wool cloth disks to achieve fine surfaces. Finally, all polished samples were cleaned using acetone. Top and bottom polished surfaces were observed under optical microscopy (OM) to ensure all existing cracks or flaws were removed for subsequent machining processes.

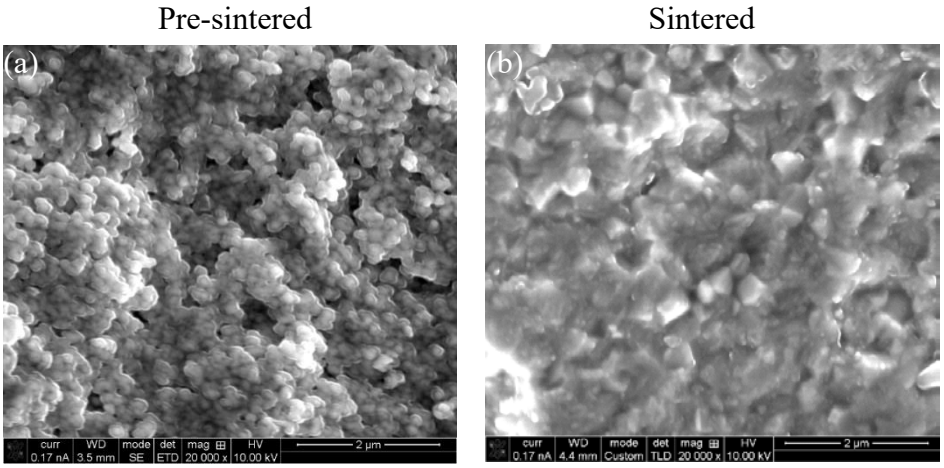

Fig. 6.1. High magnification (20,000 ×) SEM micrographs revealing the microstructures of (a) fractured pre-sintered porous and (b) sintered dense zirconia materials.

6.2.2 Conventional and Ultrasonic Vibration-Assisted Diamond Milling

Conventional and ultrasonic vibration-assisted diamond machining of zirconia materials were conducted using an ultrasonic high speed grinding/milling machine (Fig. 6.2) (Ultrasonic 20 Linear, DMG Mori Seiki CO., Ltd, Japan). The machine is a five-axis computer-controlled, high-speed, high-precision, high-efficiency grinding/milling unit integrated with an ultrasonic oscillation mechanism, enabling the maximum spindle rotational speed of 60,000 rpm for conventional machining and 50,000 rpm for ultrasonic vibration-assisted machining. The key machine structures shown in Fig. 6.2(a) includes a spindle system, an ultrasonic transducer, a tool holder installed with a diamond tool, a coolant nozzle, and a sample holder. The ultrasonic transducer driven by a piezoelectric actuator converts high-frequency electrical signals to high-frequency linear mechanical vibrations of the diamond tool along the spindle axis at 20–50 kHz frequencies and up to 10 μm vibration amplitudes. The cooling system supplies a coolant fluid into the machining zone for cooling and cleaning of machining debris.

Fig. 6.2(b) illustrates sample-diamond tool movements for surface machining, in which the diamond tool was initially positioned parallel to the 10 × 2 mm sample surface and then rotated at a machining speed of v_s along a 10 × 2 mm surface of the sample. A feed rate v_w parallel to the machined surface and a depth of cut a perpendicular to the machined surface were applied to remove a layer of material. In ultrasonic machining, the diamond tool also simultaneously rotated and axially vibrated at a frequency f and an amplitude A. The selected diamond tool had a cutting portion of 2 mm diameter and 4 mm length electroplated with 53 μm diamond grits (Schott, Diamantwerkzeuge GmbH, Germany). The selected conventional machining (i.e., vibration amplitude A = 0 as control) conditions for zirconia materials included a spindle speed v_s of 25,000 rpm, a feed rate v_w of 500 mm/min, and a depth of cut a of 50 μm. In addition to ultrasonic machining, vibration amplitudes of 3–9 μm at the harmonic frequency of the diamond tool 25 kHz were selected. During conventional and ultrasonic machining, a coolant (ECOCOOL 700 NBF (M), Fuchs Lubricants Australiasia Pty Ltd, Australia) was injected to the sample-tool contact area at a pressure of 4 bars to prevent tool overheating and jamming, and to wash away debris.

6.2.3 Characterization of Edge Chipping Damage

At each machining condition, 100 milling passes for each material were completed to obtain new machined surfaces. During machining, edge chipping damage was visible on both top and bottom polished surfaces perpendicular to the machined surface, as shown in Fig. 6.2(b). After machining, all samples were cleaned using acetone.

Edge chipping damage in top and bottom surfaces illustrated in Fig. 6.2(b), were first imaged using OM (ZEISS, Germany) installed with a camera and digital image processing software (AXIOvision software, ZEISS, Germany). On each top and bottom surface containing edge chipping damage, multiple images were continuously taken along a full edge length of 10 mm of a sample. Using Adobe Photoshop software, multiple images of edge chipping along the full length of each sample were merged. As shown in Fig. 6.2(b), an edge chipping damage depth is defined as the vertical length between the damage bottom and the damage edge on a top or bottom surface. Under each machining condition, three largest edge chipping damage depths on each top or bottom surface were measured to obtain the average and the standard deviation of the measurement (Song et al., 2018) using AXIOvision software.

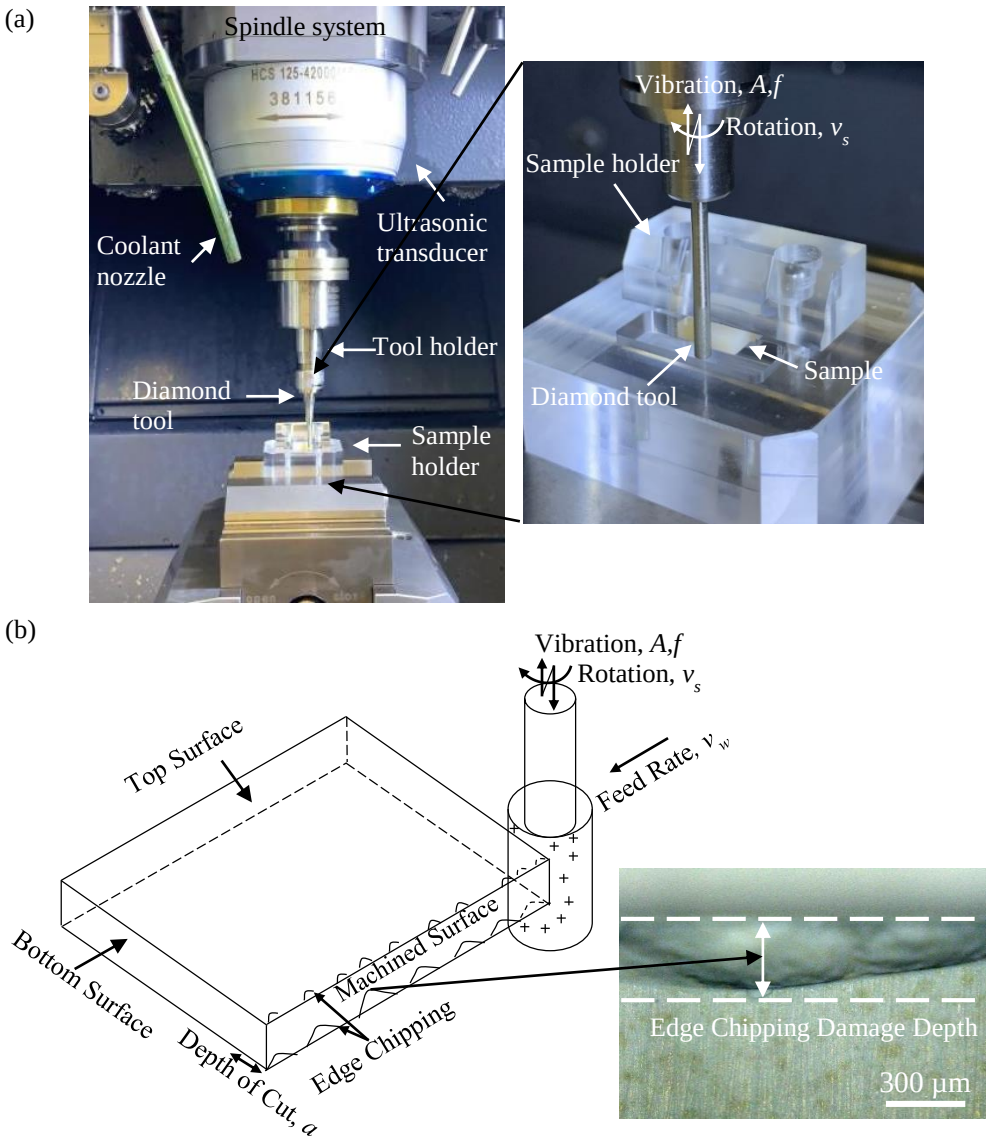

Fig. 6.2. (a) Experimental setup for conventional and ultrasonic vibration-assisted diamond machining and (b) Sample-diamond tool movements for surface machining, machining-induced edge chipping damage on both top and bottom sample surfaces perpendicular to the machined surface, and edge chipping damage depth measurement.

Based on the OM observation and measurement, ultrasonic machining at 3 µm vibration amplitude yielded least edge chipping damage to both materials. Then, top and bottom pre-sintered and sintered zirconia surfaces containing edge chipping damage produced in conventional and ultrasonic machining at 3 µm vibration amplitude were carbon-coated and examined using SEM (FEI Quanta 450 FEG ESEM, Thermo Fisher Scientific, USA).

A two-way analysis of variance (ANOVA) with replication at a 5% confidence interval was applied to examine the effects of edge surface locations and ultrasonic vibration

amplitudes as independent variables on edge chipping damage depths. The paired *t*-test was also performed at 5% confidence to examine the influence of each material on edge chipping damage depths. The probability value, or the *p* value, was used to evaluate the significant results.

6.3 Results

6.3.1 Edge Chipping Damage Depths

Fig. 6.3 shows edge chipping damage depths on top and bottom surfaces of pre-sintered porous and sintered dense zirconia materials produced in conventional (i.e., vibration amplitude = 0 as control) and ultrasonic machining at different vibration amplitudes. The data in Fig. 6.3 are also summarized in Table 6.1.

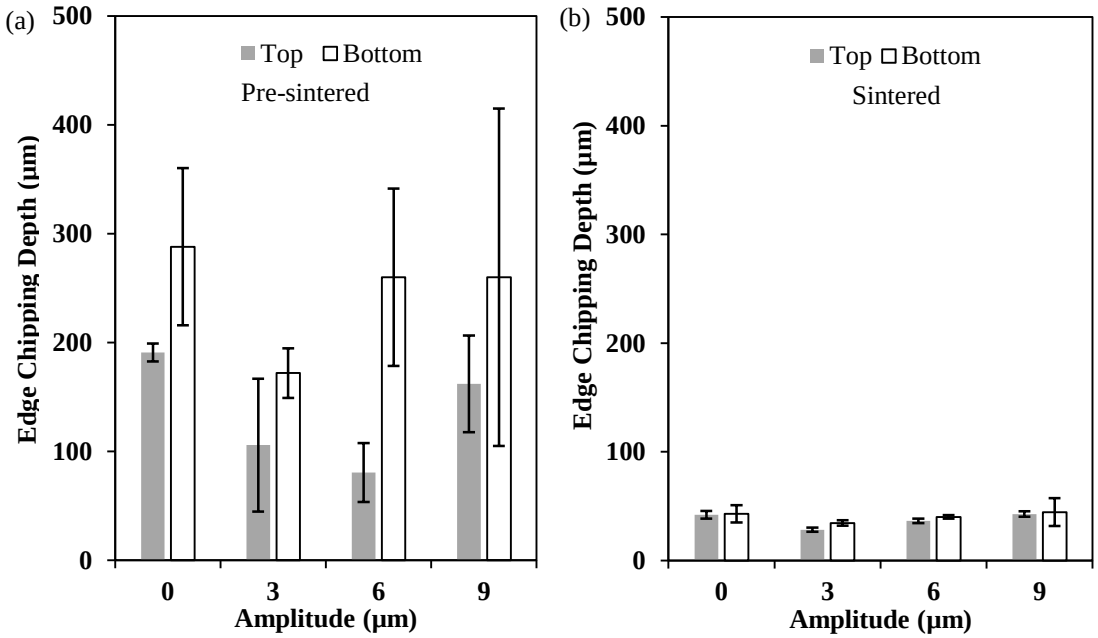

Fig. 6.3. Edge chipping damage depths on top and bottom surfaces of (a) pre-sintered porous and (b) sintered dense zirconia materials produced by conventional and ultrasonic machining at different vibration amplitudes. Note that zero amplitude means conventional machining.

For pre-sintered porous zirconia in Fig. 6.3(a), conventional machining produced edge chipping damage depths of 191 ± 8 μm and 288 ± 72 μm on top and bottom surfaces, respectively. In comparison, ultrasonic machining at 3 μm vibration amplitude reduced edge damage depths to 106 ± 61 μm by 45% and to 172 ± 23 μm by 40% on top and

bottom surfaces, respectively. Table 6.2 shows the two-way ANOVA with replication for comparison of edge chipping damage depths in top and bottom surfaces in the porous material produced in conventional and ultrasonic machining at 3 μm vibration amplitude. It indicates that ultrasonic machining at such a vibration amplitude significantly reduced edge chipping damage depths than conventional machining (ANOVA, $p < 0.01$). It also shows that top and bottom edge chipping damage depths in both processes were significantly different (ANOVA, $p = 0.02 < 0.05$). Ultrasonic machining at 6 μm vibration amplitude, edge chipping damage depths decreased to 81 ± 27 μm by 58% and to 260 ± 81 μm by 9% on top and bottom surfaces in comparison with conventional machining, respectively. Ultrasonic machining at 9 μm vibration amplitude, edge chipping damage depths decreased to 162 ± 44 μm by 15% and to 260 ± 155 μm by 9% on top and bottom surfaces in comparison with conventional machining, respectively. Table 6.3 shows the two-way ANOVA with replication for comparison of edge chipping damage depths in top and bottom surfaces in pre-sintered porous zirconia produced in conventional and ultrasonic machining at 6 μm and 9 μm vibration amplitudes. It indicates that that ultrasonic machining at such vibration amplitudes yielded insignificantly different edge chipping damage depths from conventional machining (ANOVA, $p = 0.37 > 0.05$). However, the top and bottom edge damage depths produced in these processes were significantly different (ANOVA, $p = 0.01 < 0.05$). All edge chipping damage on bottom surfaces in pre-sintered porous zirconia produced in conventional and ultrasonic machining were 1.5–3.3 times more severe than that on its top surfaces.

Table 6.1. Edge chipping damage depths (μm) in conventional and ultrasonic machining.

Ultrasonic vibration amplitude	Pre-sintered porous zirconia		Sintered dense zirconia	
	Top	Bottom	Top	Bottom
0 (Conventional)	191 ± 8	288 ± 72	42 ± 4	43 ± 8
3 μm	106 ± 61	172 ± 23	28 ± 2	35 ± 3
6 μm	81 ± 27	260 ± 81	37 ± 2	40 ± 2
9 μm	162 ± 44	260 ± 155	42 ± 2	44 ± 13

Table 6.2. Two-way ANOVA with replication for comparison of edge chipping damage depths on top and bottom surfaces of pre-sintered porous zirconia produced in conventional and ultrasonic machining at 3 μm vibration amplitude

Source of variation	Sum of square (SS)	DF	Mean sum of square (MS)	*F*-test	*p*-value	*F* crit
Edge location	19,983	1	19,983	8.38	0.02	5.32
Vibration amplitude	30,338	1	30,338	12.73	0.00	5.32
Interaction	719	1	719	0.30	0.60	5.32
Within	19,071	8	2,384			
Total	70,111	11				

Table 6.3. Two-way ANOVA with replication for comparison of edge chipping damage depths on top and bottom surfaces of pre-sintered porous zirconia produced in conventional and ultrasonic machining at 6 μm and 9 μm vibration amplitudes

Source of variation	Sum of square (SS)	DF	Mean sum of square (MS)	*F*-test	*p*-value	*F* crit
Edge location	70,566	1	70,566	10.93	0.01	4.75
Vibration amplitude	14,167	2	7,084	1.10	0.37	3.89
Interaction	6,935	2	3,468	0.54	0.60	3.89
Within	77,492	12	6,458			
Total	169,162	17				

For sintered dense zirconia in Fig. 6.3(b), conventional machining produced edge chipping damage depths of 42 ± 4 μm and 43 ± 8 μm on top and bottom surfaces, respectively. In comparison, ultrasonic machining at 3 μm vibration amplitude reduced edge damage depths to 28 ± 2 μm by 33% and to 35 ± 3 μm by 19% on top and bottom surfaces, respectively. Table 6.4 shows the two-way ANOVA with replication for comparison of edge chipping damage depths in top and bottom surfaces of sintered dense zirconia produced in conventional and ultrasonic machining at 3 μm vibration amplitude. It indicates that ultrasonic machining at such a vibration amplitude significantly reduced edge chipping damage depths than conventional machining (ANOVA, $p < 0.01$). However, top and bottom edge chipping damage depths produced in both processes were insignificantly different (ANOVA, $p = 0.26 > 0.05$). Ultrasonic machining at 6 μm

vibration amplitude, edge chipping damage depths decreased to 37 ± 2 μm by 12% and to 40 ± 2 μm by 7% on top and bottom surfaces in comparison with conventional machining, respectively. Ultrasonic machining at 9 μm vibration amplitude, edge chipping damage depths unchanged and slightly increased to 44 ± 13 μm by 5% on top and bottom surfaces in comparison with conventional machining, respectively. Table 6.5 shows the two-way ANOVA with replication for comparison of edge chipping damage depths in top and bottom surfaces of sintered dense zirconia produced in conventional and ultrasonic machining at 6 μm and 9 μm vibration amplitudes. It indicates that that ultrasonic machining at such vibration amplitudes yielded insignificantly different edge chipping damage depths from conventional machining (ANOVA, $p = 0.45 > 0.05$). Further, the top and bottom edge damage depths produced in these processes were also insignificantly different (ANOVA, $p = 0.54 > 0.05$).

Table 6.4. Two-way ANOVA with replication for comparison of edge chipping damage depths on in top and bottom surfaces of sintered dense zirconia produced in conventional and ultrasonic machining at 3 μm vibration amplitude.

Source of variation	Sum of square (SS)	DF	Mean sum of square (MS)	*F*-test	*p*-value	*F* crit
Edge location	34	1	34	1.49	0.26	5.32
Vibration amplitude	373	1	373	16.52	0.00	5.32
Interaction	23	1	23	1.00	0.35	5.32
Within	181	8	23			
Total	610	11				

Comparing pre-sintered porous and sintered dense zirconia materials in Figs. 6.3(a) and 6.3(b), conventional machining-induced edge chipping damage depths in the former top and bottom surfaces were 4.5 and 6.7 times those in the latter top and bottom surfaces, respectively. Ultrasonic machining-induced damage depths in the former top and bottom surfaces were 2.2–3.9 times and 4.9–5.9 times those in the latter top and bottom surfaces, respectively. Table 6.6 shows the *t*-test results for comparison of edge chipping damage depths in the two materials with two distinct microstructures produced in all machining

conditions at all edge surface locations. It indicates that the material microstructure had a significant effect on edge chipping damage depths in the materials (*t*-test, $p < 0.01$).

Table 6.5. Two-way ANOVA with replication for comparison of edge chipping damage depths on top and bottom surfaces of sintered dense zirconia produced in conventional and ultrasonic machining at 6 μm and 9 μm vibration amplitudes

Source of variation	Sum of square (SS)	DF	Mean sum of square (MS)	*F*-test	*p*-value	*F* crit
Edge location	17	1	17	0.40	0.54	4.75
Vibration amplitude	74	2	37	0.85	0.45	3.89
Interaction	6	2	3	0.07	0.93	3.89
Within	520	12	43			
Total	618	17				

Table 6.6. A paired *t*-test for edge chipping damage depths between pre-sintered porous and sintered dense zirconia materials produced in all machining conditions and at both top and bottom locations

	Pre-sintered zirconia	Sintered zirconia
Mean	190	39
Variance	8917	49
Observations	24	24
Pooled Variance	4483	
Hypothesized Mean Difference	0	
Degree of freedom	46	
t Statistic	8	
p(T<=t) one-tail	0	
t Critical one-tail	2	
p(T<=t) two-tail	0	
t Critical two-tail	2	

6.3.2 SEM Edge Chipping Damage Morphology

Fig. 6.4 shows low-magnification (100×) SEM micrographs of edge chipping damage on top and bottom surfaces of pre-sintered porous and sintered dense zirconia materials produced by conventional and ultrasonic machining at 3 μm vibration amplitude. For pre-sintered porous zirconia shown in Fig. 6.4(a)–6.4(d), ultrasonic machining significantly reduced the maximum damage depth from 216 μm to 158 μm, by 27%, and from 381 μm to 171 μm, by 55%, on its top and bottom surfaces, respectively. For sintered dense zirconia shown in Figs. 6.4(e)–6.4(h), minimum conventional and ultrasonic machining-induced edge chipping damage can be observed on its top and bottom surfaces.

Fig. 6.5 shows higher magnification SEM micrographs of edge chipping damage features in pre-sintered porous zirconia produced by conventional and ultrasonic machining at 3 μm vibration amplitude. Fig. 6.5(a) reveals significant secondary edge chipping occurring in conventional machining, enhancing the original maximum chipping depth from 136 μm to 205 μm, by 51%. Fig. 6.5(b) reveals that ultrasonic machining produced smaller secondary edge chipping, increasing the original maximum chipping depth from 136 μm to 150 μm, by 10%. Both arrest lines and convex shell-like fractures in edge chipping scars are observed in conventional (Fig. 6.5(c)) and ultrasonic machining (Fig. 6.5(d)), respectively. Fig. 6.5(e) reveals a nearly identical conventional and ultrasonic machining-induced edge chipping damage morphology with irregular fractures and porous morphology.

Fig. 6.6 shows higher magnification SEM micrographs of edge chipping damage in top and bottom surfaces of sintered dense zirconia produced by conventional and ultrasonic machining at 3 μm vibration amplitude. On top damaged surfaces shown in Figs. 6.6(a) and 6b, ultrasonic machining reduced the maximum damage depth from 41 μm to 29 μm, by 29%. On bottom damaged surfaces revealed in Figs. 6.6(c) and 6.6(d), ultrasonic machining reduced the maximum damage depth from 45 μm to 36 μm, by 20%. Arrest lines and convex shell-like fractures were observed in these damaged scars. Fig. 6.6(e) reveals large cracks resulting from irregular fractures produced in conventional machining. Fig. 6.6(f) shows localized micro fractures created in ultrasonic machining, indicating reduced scales of edge chipping damage in the dense structure by ultrasonic machining.

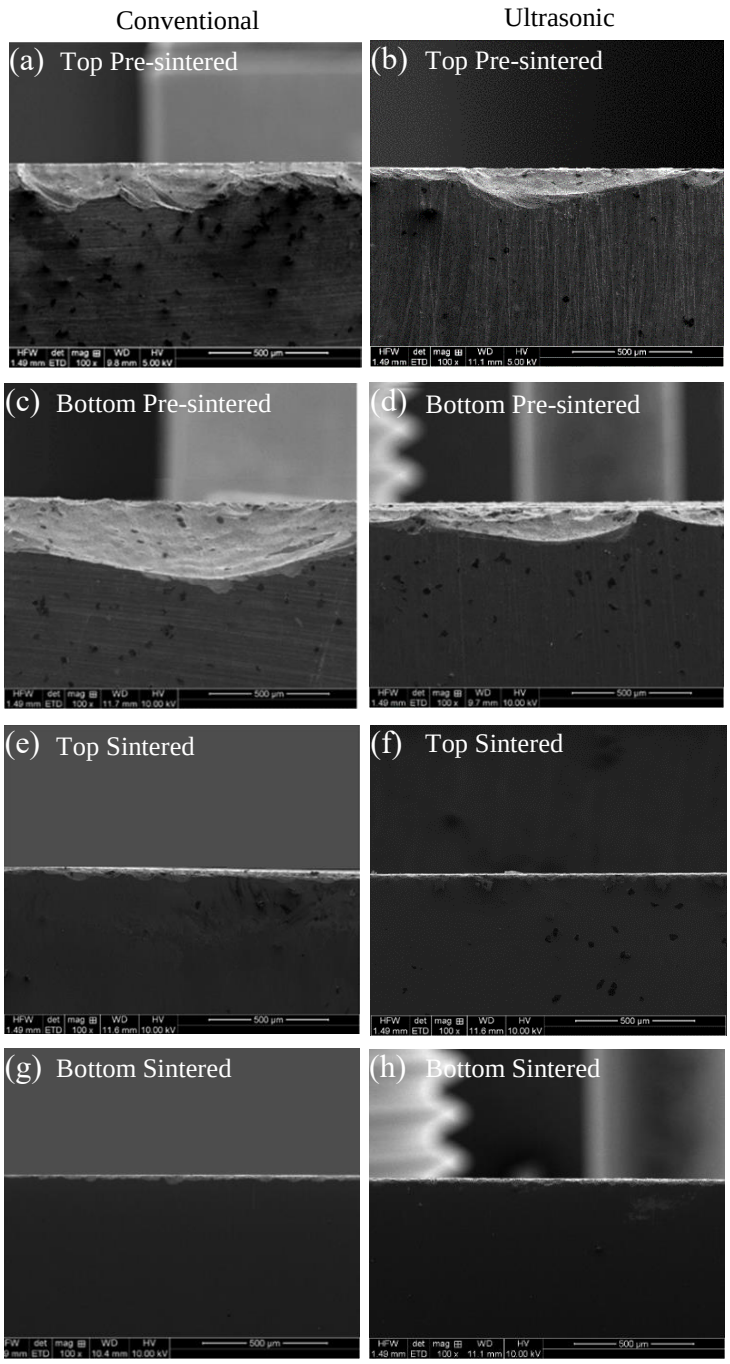

Fig. 6.4. Low-magnification (100×) SEM micrographs of edge chipping damage in zirconia materials produced in conventional and ultrasonic machining at 3 □m vibration amplitude. (a) and (b) Top pre-sintered porous zirconia surfaces produced by conventional and ultrasonic machining, respectively; (c) and (d) Bottom pre-sintered porous zirconia surfaces produced by conventional and ultrasonic machining, respectively; (e) and (f) Top sintered dense zirconia surfaces produced by conventional and ultrasonic machining, respectively; (g) and (h) Bottom sintered dense zirconia surfaces produced by conventional and ultrasonic machining, respectively.

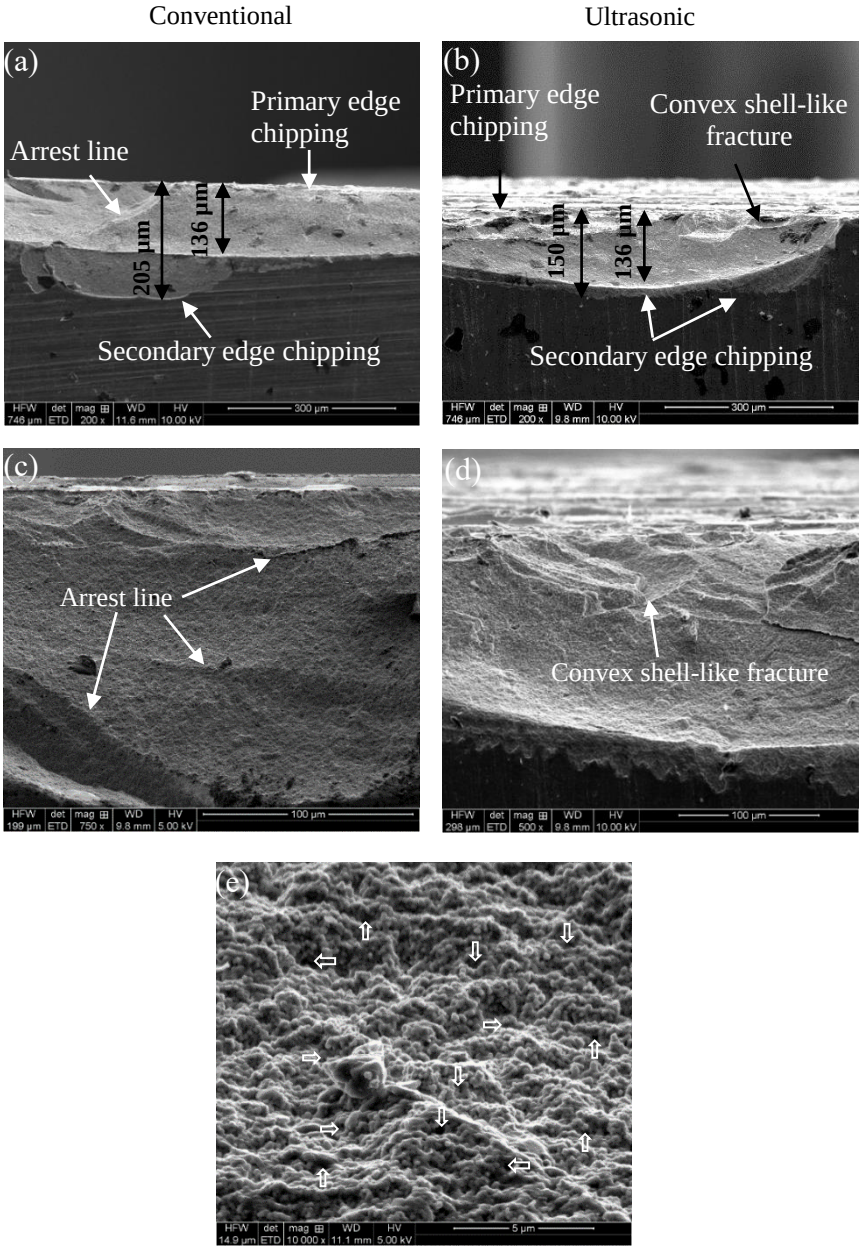

Fig. 6.5. Higher-magnification SEM micrographs of edge chipping damage features in pre-sintered porous zirconia surfaces produced in conventional and ultrasonic machining at 3 μm vibration amplitude. (a) Significant secondary edge chipping damage below primary edge chipping damage produced in conventional machining; (b) Minor secondary edge chipping damage below primary edge chipping damage produced in ultrasonic machining; (c) Arrest lines in edge chipping damage produced in conventional machining; (d) Convex shell-like fractures in edge chipping damage produced in ultrasonic machining; (e) Nearly identical conventional and ultrasonic machining-induced edge chipping damage morphology of irregular fractures and porous microstructure. Arrows indicate pores.

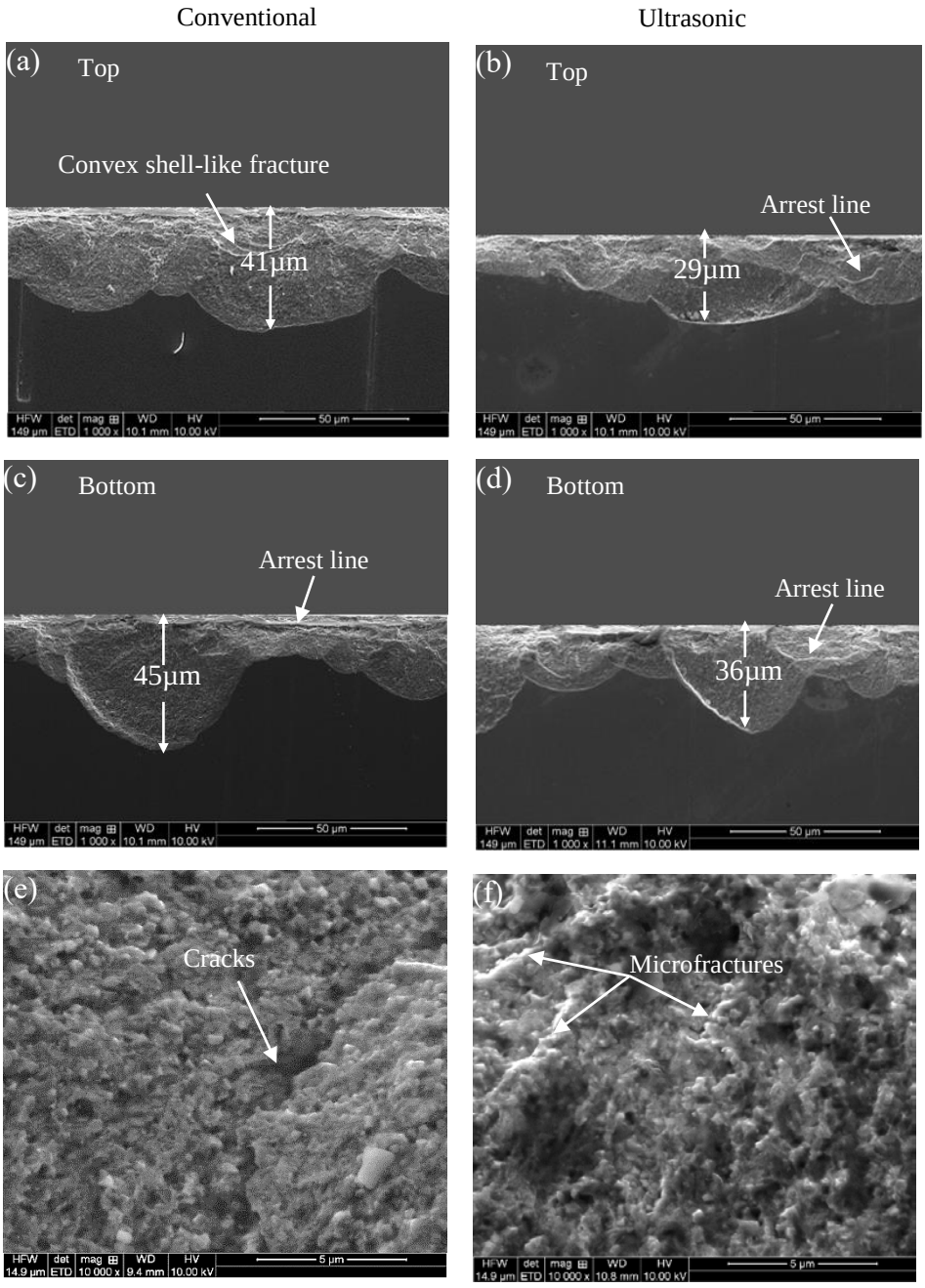

Fig. 6.6. Higher-magnification SEM micrographs of edge chipping damage in top and bottom sintered dense zirconia surfaces produced by conventional and ultrasonic machining at 3 μm vibration amplitude. (a) and (b) Top surfaces with arrest lines and convex shell-like fracture produced by conventional and ultrasonic machining, respectively; (c) and (d) Bottom surfaces with arrest lines and convex shell-like fracture produced by conventional and ultrasonic machining, respectively; (e) Dense morphology and large cracks resulted from irregular fractures by conventional machining; and (f) Dense morphology and localized micro fracture produced by ultrasonic machining.

6.4 Discussion

The results of this study have some intriguing implementations concerning the application of ultrasonic vibration assistance to CAD/CAM diamond machining of pre-sintered porous and sintered dense zirconia materials. Particularly, edge chipping damage depths in the two materials with distinct microstructures in conventional and ultrasonic diamond machining have been compared in terms of maximum depths using OM and SEM, which are commonly used for damage studies at different resolutions (Anand et al., 2018a; Song et al., 2018). Secondary chipping and detailed chipping morphologies and features, which were hardly visible using OM but clearly observed under SEM, contributed edge chipping damage degrees and reflect fracture mechanisms as shown in Figs. 6.4–6.6. All edge chipping damages cover damage areas. To reflect this areal feature, a Java-based image processing program (ImageJ, NIH Image, USA) was applied to measure edge chipping damage areas based on SEM micrographs in pre-sintered porous and sintered dense zirconia surfaces in Figs. 6.4 and 6.6. In the measurement, three repeats were conducted to obtain the means and standard deviations of the measured damage areas.

Fig. 6.7 shows the measurement of edge chipping damage areas in top and bottom surfaces of pre-sintered porous and sintered dense zirconia materials produced in conventional and ultrasonic machining at 3 μm vibration amplitude. Table 6.7 summarizes these damage area data, revealing that the ultrasonic machining-induced damage areas on top and bottom pre-sintered porous zirconia surfaces were reduced by 27% and 59%, respectively, whereas for sintered dense zirconia, the damage areas on top and bottom surfaces were decreased by 30% and 13%, respectively. A specific edge chipping damage area, i.e., edge chipping damage area per unit machining length ($\mu m^2/\mu m$), is used to compare maximum damage depths. Fig. 6.8 demonstrates specific edge chipping damage areas for top and bottom surfaces of pre-sintered porous and sintered dense zirconia materials produced in conventional and ultrasonic machining at 3 μm vibration amplitude. For pre-sintered porous zirconia, ultrasonic machining achieved significant reductions in specific edge chipping areas from 126 ± 5 $\mu m^2/\mu m$ to 92 ± 2 $\mu m^2/\mu m$, by 27%, and from 298 ± 2 $\mu m^2/\mu m$ to 121 ± 2 $\mu m^2/\mu m$, by 59%, on top and bottom surfaces, respectively. For sintered dense zirconia material, the corresponding reductions were obtained from 26 ± 1 $\mu m^2/\mu m$ to 19 ± 1 $\mu m^2/\mu m$, by 27%, and from 26 ± 1 $\mu m^2/\mu m$ to 22 ± 0 $\mu m^2/\mu m$, by 15%, on the latter top and bottom surfaces,

respectively. This analysis reveals a similar trend to maximum edge chipping damage depths (Fig. 6.3) but reflects the true areal damage nature of edge chipping.

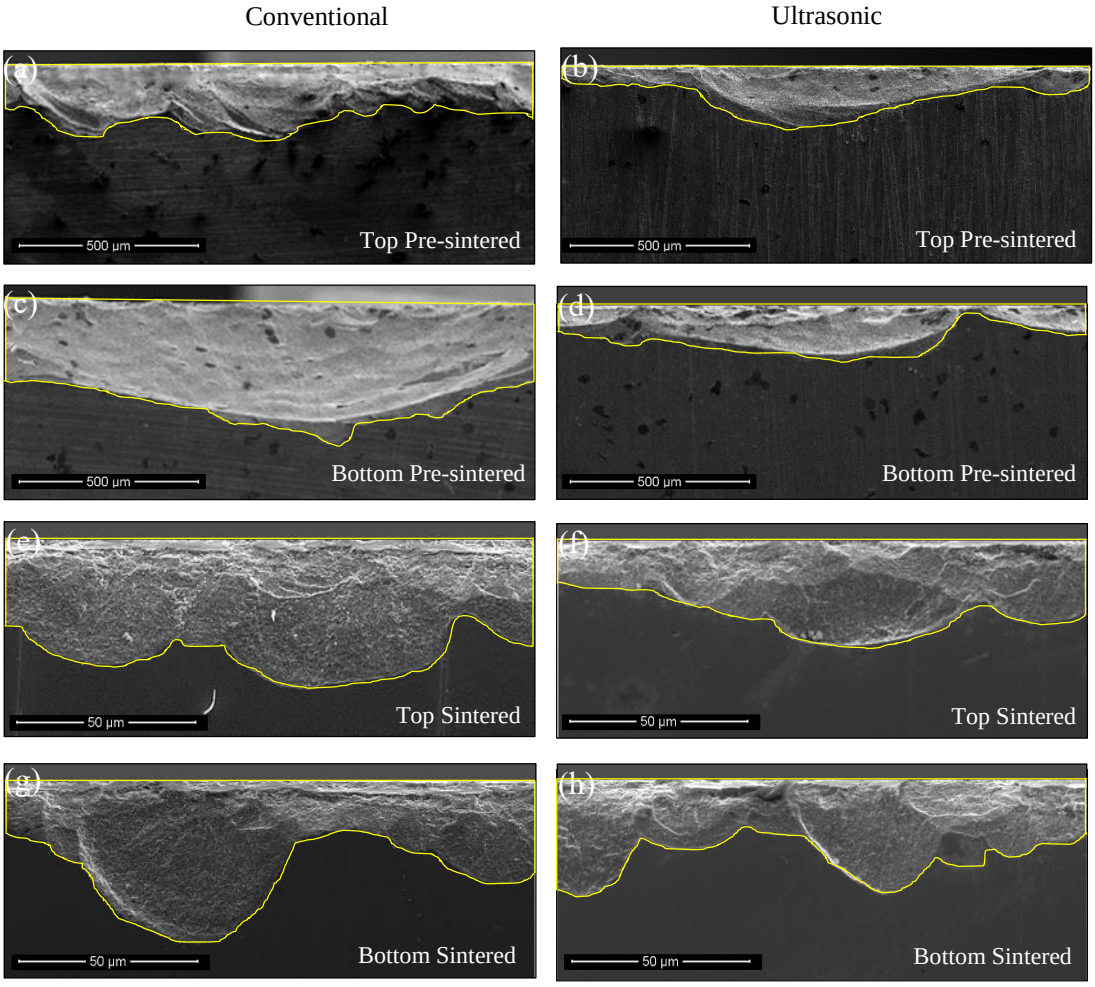

Fig. 6.7. Measurement of edge chipping damage areas in zirconia materials induced by conventional and ultrasonic machining at 3 µm vibration amplitude. (a) and (b) Damages in top pre-sintered porous zirconia surfaces produced by conventional and ultrasonic machining, respectively; (c) and (d) Damages in bottom pre-sintered porous surfaces produced by conventional and ultrasonic machining, respectively; (e) and (f) Damages in top sintered dense zirconia surfaces produced by conventional and ultrasonic machining, respectively; (g) and (h) Damages in bottom sintered dense zirconia surfaces produced by conventional and ultrasonic machining, respectively.

Figs. 6.3 and 6.4 show that pre-sintered porous zirconia yielded much more severe edge chipping damage than sintered dense zirconia in conventional and ultrasonic machining, indicating a significant material microstructure dependent nature of edge chipping damage formation as shown in Table 6.6 (t-test, $p < 0.01$). This is in agreement with

studies on edge toughness studies of dental ceramics (Quinn et al., 2000). The material behavior affecting edge chipping damage is generally associated with its brittleness index expressed as (Quinn and Quinn, 1997):

$$B = \frac{EH}{{K_{IC}}^2} \tag{6.1}$$

where H is the hardness, E is the Young's modulus, and K_{IC} is the fracture toughness. The brittleness indices of pre-sintered porous and sintered dense zirconia materials are calculated as 78 1/μ and 61 1/μ, respectively. A material with a higher brittleness index is more susceptible to brittle fracture. This means that pre-sintered porous zirconia is more susceptible to edge chipping damage than sintered dense zirconia in both conventional and ultrasonic machining, resulting in significantly deeper damage depths than those in sintered dense zirconia surfaces, as shown in Fig. 6.4. Sintering at high temperatures significantly influences zirconia microstructures by reducing porosity and increasing density, which, in turn, improve the mechanical properties (Inokoshi et al., 2014; Kim et al., 2013; Ruiz and Readey, 1996). Thus, sintered dense zirconia with much higher Young's modulus, hardness, fracture toughness and strength than its pre-sintered state, ultimately restrained edge chipping damage in conventional and ultrasonic machining. In addition, edge chipping occurs due to the existence of initial surface defects as crack origins to propagate under the action of machining forces, leading to fracture. Given the highly porous microstructure of pre-sintered zirconia (Fig. 6.5(e)), pores in the material also acted as initial surface defects, which easily nucleated, propagated and fractured to form edge chipping damage in diamond machining. In contrast, densely sintered zirconia with much less material defects revealed more resistance to edge chipping damage.

Table 6.7. Conventional and 3 μm vibration amplitude ultrasonic machining-induced damage areas (10^3 μm^2) on top and bottom surfaces of pre-sintered porous and sintered dense zirconia materials

Ultrasonic vibration amplitude	Pre-sintered porous zirconia		Sintered dense zirconia	
	Top	Bottom	Top	Bottom
0 (Conventional)	185.3 ± 7.2	438.3 ± 3.2	3.9 ± 0.1	3.8 ± 0.1
3 μm	134.8 ± 3.0	178.1 ± 3.6	2.7 ± 0.1	3.3 ± 0.1

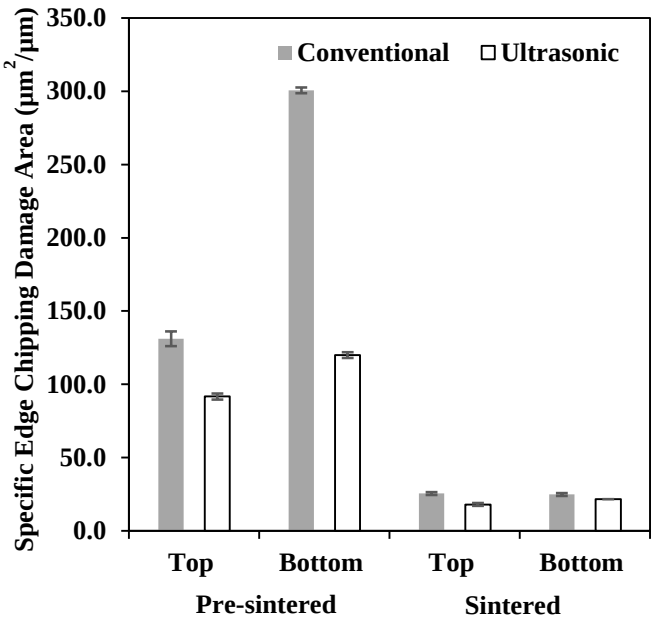

Fig. 6.8. Specific edge chipping damage areas on top and bottom surfaces of zirconia materials produced in conventional and ultrasonic machining at 3 μm vibration amplitude.

Ultrasonic machining at 3 μm vibration amplitude yielded least edge chipping depths for the two materials with distinct microstructures (ANOVA, $p < 0.05$) as shown in Figs. 6.3–6.6 and Tables 6.2 and 6.4, indicating the benefit of ultrasonic vibration assistance to diamond machining. Therefore, it is of great interest to elucidate the role of ultrasonic vibration in diamond machining and mechanisms to lead to less edge damage in terms of dynamic and kinematic analysis and finite element analysis (FEA) simulation. Firstly, from the dynamic and kinematic point of view, this study applied a one-dimensional ultrasonic vibration to the diamond tool axis direction, which was perpendicular to the feed direction, as shown in Fig. 6.9(a). In conventional machining, diamond grains moved toward a zirconia surface at a rotational milling speed of v_s, a tool feed rate of v_w and a depth of cut of a to remove a layer of the material, as shown in Fig. 6.9(b). In ultrasonic machining, an ultrasonic vibration with an amplitude of A and a frequency of f added to conventional machining. The trajectory of a single diamond grain in conventional and ultrasonic machining can be parametrically described as (Xiao et al., 2016):

$$\begin{aligned} x &= v_w t + \frac{d}{2} cos\left(\frac{2\pi v_s}{60} t\right) \\ y &= \frac{d}{2} sin\left(\frac{2\pi v_s}{60} t\right) \\ z &= H_0 + A\, sin(2\pi f t) \end{aligned} \tag{6.2}$$

where d is the tool diameter, t is the cutting time and H_0 is the original height of the diamond grit. The cutting trajectory of a single diamond grain in conventional machining followed nearly a circular arc while the trajectory in ultrasonic machining traced a sinusoidal oscillation, as shown in Fig. 6.9(c). Consequently, the relative motion relationship between the diamond tool and the zirconia surface in ultrasonic machining was changed to result in different material removal mechanisms from conventional machining.

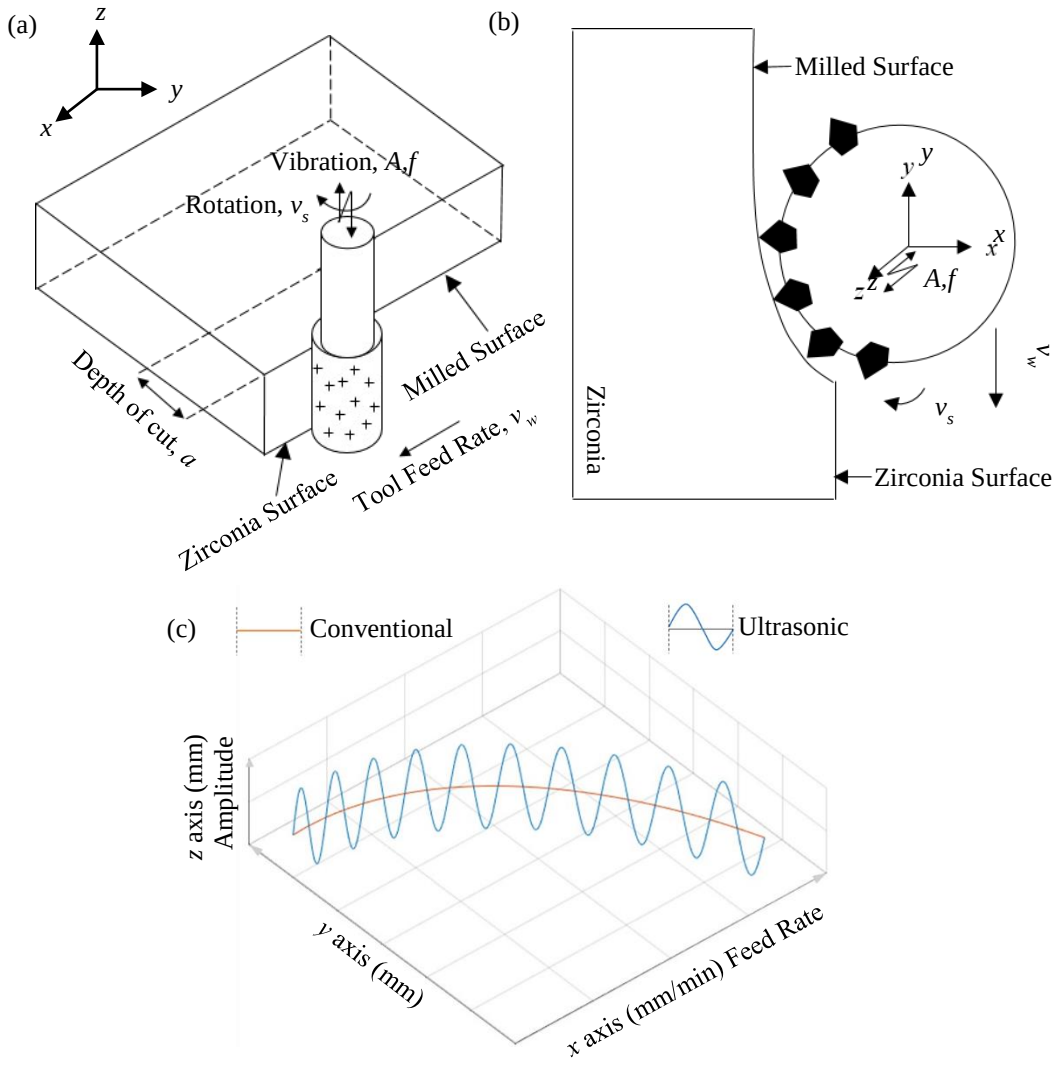

Fig. 6.9. Illustration of conventional and ultrasonic machining processes. (a) 3D diamond machining; (b) 2D diamond grains-zirconia surface contact; and (c) Diamond grains trajectories in conventional and ultrasonic machining.

Further, a mathematical model for ultrasonic vibration-assisted machining has identified an effective machining time for the period of diamond grain-workpiece contact with soda-lime glass as (El-Taybany and El-Hofy, 2019):

$$t_{eff} = \frac{g}{2Af} \tag{6.3}$$

where t_{eff} is the effective cutting time, A is the vibration amplitude, f is the vibration frequency, and g is the diamond gain penetration depth. In ultrasonic vibration-assisted machining of brittle solids, each diamond grain may have indented and hammered a zirconia surface at a penetration depth for a period of effective machining time in a single ultrasonic vibration cycle. On the contrary, for conventional machining each diamond grain may have continuously contacted the zirconia surface. Accordingly, ultrasonic assisted machining has longer trajectory lengths than conventional machining, as shown in Fig. 6.9(c).

In conventional machining, the interaction between the diamond tool and the zirconia surface was continuous. The interaction in ultrasonic machining was non-continuous due to sinusoidal oscillation trajectory-induced reciprocating separations between the diamond tool and the zirconia surface. This discontinuity was also confirmed in ultrasonic grinding of sintered zirconia using a CBN tool (Yang et al., 2019b). The high-frequency ultrasonic vibration inputting into the diamond grains allowed them to contact with the zirconia surface at shorter cutting times and to penetrate the surface at shallower depths during abrading. As a result of reciprocating separations and discontinuous interactions between the diamond tool and the zirconia surface in ultrasonic machining, contact frictions and machining forces might have been significantly reduced to yield shallower machining-induced edge chipping damage depths (Song et al., 2018). This finding is also supported by experimental results for alumina and silicon carbide ceramics (Ahmed et al., 2012; Li et al., 2006; Zeng et al., 2005).

Secondly, previous FEA simulation studies on edge chipping in rotary ultrasonic machining of alumina have predicted edge chipping initiation (Jiao et al., 2005) based on the Withney-Nuismer point stress criterion (Whitney and Nuismer, 1974). The FEA model indicates that the scale of edge chipping damage in alumina was determined by controllable machining variables, i.e., machining speed, ultrasonic vibration amplitude, and feed rate (Jiao et al., 2005). However, the model has not compared the edge chipping

damage in conventional and ultrasonic vibration-assisted machining. Efforts will be made to establish FEA modelling for comparison and prediction of edge chipping damage depths in both conventional and ultrasonic machining of pre-sintered porous and sintered dense zirconia materials.

Ultrasonic machining at 3 μm vibration amplitude might have altered material removal mechanisms for both zirconia materials. For pre-sintered porous zirconia, secondary edge chipping in conventional machining (Fig. 6.5(a)) was significantly larger than that in ultrasonic machining (Fig. 6.5(b)). For sintered dense zirconia, conventional machining induced large cracks on the chipping morphology (Fig. 6.6(e)) was not found in ultrasonic machining (Fig. 6.6(f)). These suggest that in ultrasonic machining, discontinuous interactions between diamond grains and zirconia surfaces might have contributed to reduced fracture scales for both materials in comparison to conventional machining. Fig. 6.10 shows removal mechanisms for conventional and ultrasonic machining processes, respectively. Conventional machining might have yielded larger scales of fractures and cracks as shown in Fig. 6.10(a). In ultrasonic machining, microscale high-frequency ultrasonic vibrations applied to diamond grains might have impacted on the zirconia surface at higher active speeds and reduced forces, resulting in more microfractures and microcracks on the machined surface as shown in Fig. 6.10(b). These distinct material removal mechanisms in conventional and ultrasonic machining may help to explain why ultrasonic machining at 3 μm vibration amplitude achieved least edge chipping damage for both zirconia materials. However, the fracture feature as the main material removal mode reflects the nature of conventional and ultrasonic machining both materials. Evidenced with arrest lines in Figs. 6.5 and 6.6, discontinuous crack propagations were observed in both materials produced by conventional and ultrasonic machining.

Higher vibration amplitudes of 6 μm and 9 μm might have scaled up microfracture and microcrack to larger fractures and cracks, leading to less or insignificant edge chipping damage reductions for both materials (ANOVA, $p > 0.05$) as shown in Fig. 6.3, Tables 6.3 and 6.5. Increased vibration amplitudes may have resulted in increased hammering actions of the diamond grains (Tsai et al., 2016) on both material surfaces, inducing more chipping damage. This finding agrees with previous studies in which increased vibration amplitudes resulted in higher cutting forces and worse surface quality

(Abdo et al., 2019; Li et al., 2017). Hence, the selection of the ultrasonic vibration amplitude is crucial to improve the edge quality for zirconia materials and the vibration assistance at 3 μm vibration amplitude might be optimal for effective machining in this study.

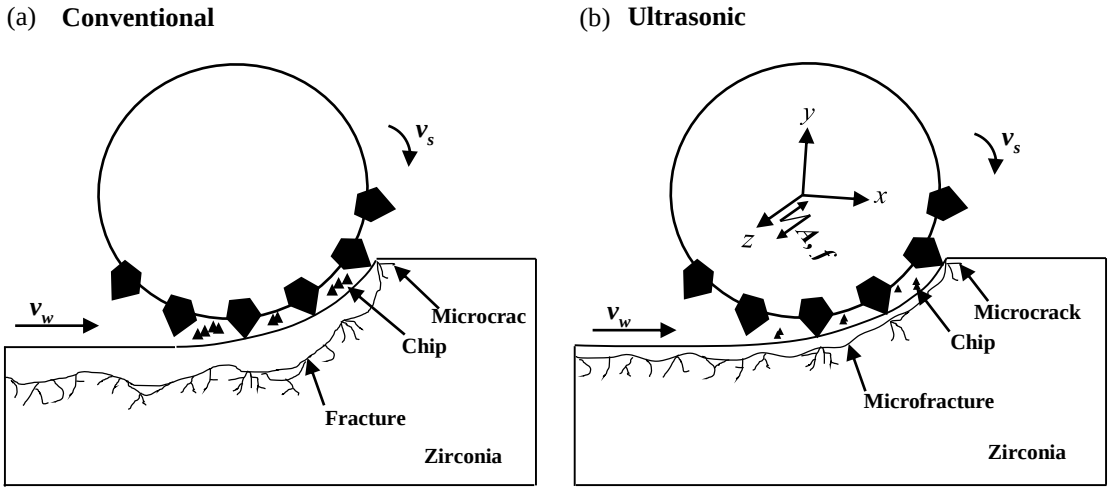

Fig. 6.10. Illustration of removal mechanisms for (a) conventional and (b) ultrasonic machining.

Generally, ultrasonic vibration-assisted machining is performed at high frequency (typically 20 kHz) (Liu et al., 2012). The current study applied 25 kHz, the harmonic frequency of the diamond tool determined by the machine. The application of such a harmonic frequency was recommended by the machine manufacturer and the studies on ultrasonic vibration-assisted machining of a carbon fiber reinforced polymer (CFRP) composite using the same machine (Kuruc et al., 2017). Some optimality studies have predicted the increased material removal rates with the increased ultrasonic vibration frequency in the range of 10–40 kHz (Rao et al., 2010). This paper has focused on the amplitude effect on the ultrasonic vibration-assisted machining of zirconia materials with distinct microstructure. The frequency effect in the machining processes will be studied in the future.

Although ultrasonic machining at 3 μm vibration amplitude significantly decreased edge chipping damage for both pre-sintered porous and sintered dense zirconia materials, the reduction rates for the former were significantly higher than the latter as shown in Figs. 6.3, 6.4, and 6.6. This may be attributed to the two materials with different

machinability indices associated with their mechanical properties as follows (Song et al., 2016):

$$M = \frac{(K_{IC}^{\frac{1}{2}} H^{\frac{9}{10}})}{E^{2/5}} \tag{6.4}$$

where M is the machinability index, K_{IC} is the fracture toughness, H is the hardness and E is the elastic modulus. A higher machinability index indicates that the material is more difficult to machine. The machinability indices for pre-sintered porous and sintered dense zirconia materials are 4.3 MPa $m^{1/4}$ and 124.1 MPa $m^{1/4}$, respectively, indicating that the former is more machinable than the latter and the removal of edge chipping damage in the latter is much more difficult than the former. Therefore, any reduction in edge chipping damage in sintered dense zirconia would be very beneficial for post processing with respect to time and cost effectiveness.

Most previous edge chipping damage was observed or measured on single surfaces (Song et al., 2018). For the pre-sintered porous zirconia, edge chipping damage on bottom surfaces was found significantly larger than that on top surfaces in conventional and ultrasonic machining (ANOVA, $p < 0.05$) as shown in Figs. 6.3 and 6.4, and Tables 6.2 and 6.3. For the sintered dense zirconia, the damage scales on top and bottom surfaces in conventional and ultrasonic machining were similar (ANOVA, $p > 0.05$) as shown in Figs. 6.3 and 6.6, and Tables 6.4 and 6.5. In general, there are certain limitations in machining of brittle materials. Most studies have focused on fully dense solids with high hardness and Young's moduli, yielding higher cutting forces (Malkin and Hwang, 1996). In conjunction with the low machine and tool stiffness, the forces produce deflections which negatively impact the dimensional accuracy of machined workpieces (Malkin and Hwang, 1996). However, the machine used in this study (Fig. 6.2) is designed for high-precision machining of a wide range of materials from standard metals to difficult-to-cut materials of ceramics. Therefore, during machining of both zirconia materials, the machining-induced spindle-tool deflections was minimum.

Both pre-sintered porous and sintered dense zirconia materials were machined in the same machining conditions but significant different edge chipping depths on top and bottom surfaces were only measured for the former. Hence, the source of the difference may not favour the machining-induced spindle tool deflections in machining but may be attributed to the mechanical properties of the materials. The extreme low Young's modulus of

34 GPa (Alao and Yin, 2014a) for the highly porous pre-sintered zirconia reflects its low resistance to the elastic deformation, which may have caused its machining-induced elastic deflections, leading to more severe edge chipping damage on bottom surfaces. The much higher Young's modulus of 168 GPa of the sintered dense zirconia (Alao and Yin, 2014b) enables the material to have a higher resistance to the elastic deformation under machining, causing insignificant elastic defections. Thus, similar scales of machining-induced damages occurred on its top and bottom surfaces. Furthermore, little is known about machining-induced elastic deformation and deflections in soft, porous brittle solids, further studies are needed towards these issues.

6.5 Conclusions

This study reveals the microstructure-mechanical behavior-processing-induced edge damage relation in zirconia materials in conventional and ultrasonic vibration-assisted diamond machining. This research provides useful scientific fundamentals for the application of ultrasonic vibration assistance to diamond machining, enabling a potential improvement of conventional machining techniques for ceramic products. The following conclusions are drawn below:

(a) Pre-sintered porous zirconia with a high brittleness index yielded 4.5–6.7 and 2.2–5.9 times edge chipping damage than sintered dense zirconia with a low index in conventional and ultrasonic machining processes, respectively. The low elastic modulus of porous zirconia caused more chipping damage on bottom than top edges in both conventional and ultrasonic machining processes while such an edge location effect did not occur in the high elastic modulus of dense zirconia.

(b) Ultrasonic assisted machining at an optimal vibration amplitude of 3 μm achieved significant reductions in maximum edge chipping damage depths in pre-sintered porous and sintered dense zirconia materials by 40–45% and 19–33%, respectively.

(c) Caution must be taken in ultrasonic machining during which a suitable micro-scale vibration amplitude needs to be selected to enable the alteration of the material removal mechanisms for both materials from fracture to microscale fracture, leading to diminished subsurface edge chipping damage.

(d) A new concept of specific edge chipping area was proposed, which may be used as a precise assessment of edge chipping damage for all ceramics.

Declaration of Competing Interests

The authors declare that they have no known competing financial personal interests that could have appeared to influence the work reported in this paper.

Acknowledgments

The authors would like to thank Dr. Animesh Basak of the Adelaide Microscopy Centre and Mr. Evan Johnson of the Institute for Photonics & Advanced Sensing at the University of Adelaide (UoA) for experimental assistance. This work was supported by the UoA PhD Scholarship and seed grant, and the Australian Research Council Grant No. DP200102300.

References

Abduo, J., Lyons, K., Swain, M., 2010. Fit of zirconia fixed partial denture: a systematic review. J. Oral Rehabil. 37, 866–876. https://doi.org/10.1111/j.13652842.2010.02113.x.

Abdo, B. M., Anwar, S., El-Tamimi, A., 2019. Machinability study of biolox forte ceramic by milling microchannels using rotary ultrasonic machining. J. Manuf. Process. 43, 175–191. https://doi.org/10.1016/j.jmapro.2019.05.031.

Alao, A. R., Yin, L., 2014a. Nano-scale mechanical properties and behavior of pre-sintered zirconia. J. Mech. Behav. Biomed. Mater. 36, 21–31. https://doi.org/10.1016/j.jmbbm.2014.03.019.

Alao, A. R., Yin, L., 2014b. Loading rate effect on the mechanical behavior of zirconia in nanoindentation. Mater. Sci. Eng. A 619, 247–255. https://doi.org/10.1016/j.msea.2014.09.101.

Alao, A. R., Yin, L., 2016. Assessment of elasticity, plasticity and resistance to machining-induced damage of porous pre-sintered zirconia using nanoindentation techniques. J. Mater. Sci. Technol. 32, 402–410. https://doi.org/10.1016/j.jmst.2016.02.009.

Alao, A. R., Stoll, R., Song, X. F., Miyazaki, T., Hotta, Y., Shibata, Y., Yin, L., 2017. Surface quality of yttria-stabilized tetragonal zirconia polycrystal in CAD/CAM milling, sintering, polishing and sandblasting processes. J. Mech. Behav. Biomed. Mater. 65, 102–116. https://doi.org/10.1016/j.jmbbm.2016.08.021.

Alkawaz, M., Hafiz, M. S. A., Kasim, M. S., Izamshah, R., 2018. Study of Dental Zirconia Milling Using Rotary Ultrasonic Ma-chining. Int. J. Eng. Technol. 7, 181–183. https://www.sciencepubco.com/index.php/%20IJET/article/view/22881.

Ahmed, Y., Cong, W. L., Stanco, M. R., Xu, Z. G., Pei, Z. J., Treadwell, C., Zhu, Y. L., Li, Z. C., 2012. Rotary ultrasonic machining of alumina dental ceramics: a preliminary experimental study on surface and subsurface damages. J. Manuf. Sci. Eng. Trans. ASME 134, 064501. https://doi.org/10.1115/1.4007711.

Amarante, J. E. V., Pereira, M. V. S., De Souza, G. M., Pais Alves, M. F. R., Simba, B. G., dos Santos, C., 2019. Roughness and its effects on flexural strength of dental yttria-stabilized zirconia ceramics. Mater. Sci. Eng. A 739,149–157. https://doi.org/10.1016/j.msea.2018.10.027.

Anand, P. S. P., Arunachalam, N., Vijayaraghavan, L., 2018a. Effect of grinding on subsurface modifications of pre-sintered zirconia under different cooling and lubrication conditions. J. Mech. Behav. Biomed. Mater. 86, 122–130. https://doi.org/10.1016/j.jmbbm.2018.06.026

Anand, P. S. P., Arunachalam, N., Vijayaraghavan, L., 2018b. Study on grinding of pre-sintered zirconia using diamond wheel. Mater. Manuf. Process. 33, 634–643. https://doi.org/10.1080/10426914.2017.1364761.

Belli, R., Wendler, M., Ligny, D., Cicconi, M. R., Petschelt, A., Peterlik, H., Lohbauer, U., 2017. Chairside CAD/CAM materials. Part 1: Measurement of elastic constants and microstructural characterization. Dent. Mater. 33, 84–98. https://doi.org/10.1016/j.dental.2016.10.009.

Bhosale, S. B., Pawade, R. S., Brahmankar, P. K., 2014. Effect of process parameters on MRR, TWR and surface topography in ultrasonic machining of alumina–zirconia ceramic composite. Ceram. Int. 40, 12831–12836. https://doi.org/10.1016/j.ceramint.2014.04.137.

Chen, S., Zou, P., Tian, Y., Duan, J., Wang, W., 2019. Study on modal analysis and chip breaking mechanism of Inconel 718 by ultrasonic vibration-assisted drilling. Int.

J. Adv. Manuf. Technol. 105, 177–191. https://doi.org/10.1007/s00170-01904155-6.

Denkena, B., Breidenstein, B., Busemann, S., Lehr, C. M., 2017. Impact of hard machining on zirconia based ceramics for dental applications. Procedia CIRP 65, 248–252. https://doi.org/10.1016/j.procir.2017.04.055.

Denry, I. L., Holloway, J. A., 2006. Microstructural and crystallographic surface changes after grinding zirconia-based dental ceramics. J. Biomed. Mater. Res. B Appl. Biomater. 76, 440–448. https://doi.org/10.1002/jbm.b.30382.

Denry, I., Kelly, J. R., 2008. State of the art of zirconia for dental applications. Dent. Mater. 24, 299–307. https://doi.org/10.1016/j.dental.2007.05.007.

Denry, I., 2013. How and when does fabrication damage adversely affect the clinical performance of ceramic restorations?. Dent. Mater. 29, 85–96. https://doi.org/10.1016/j.dental.2012.07.001.

El-Taybany, Y., El-Hofy, H., 2019. Mathematical model for cutting force in ultrasonic-assisted milling of soda-lime glass. Int. J. Adv. Manuf. Technol. 103, 3953–3968. https://link.springer.com/article/10.1007/s00170-019-03399-6.

Fraga, S., Amaral, M., Bottino, M. A., Valandro, L. F., Kleverlaan, C. J., May, L. G., 2017. Impact of machining on the flexural fatigue strength of glass and polycrystalline CAD/CAM ceramics. Dent. Mater. 33, 1286–1297. https://doi.org/10.1016/j.dental.2017.07.019

Garvie, R. C., Hannink, R. H., Pascoe, R. T., 1975. Ceramic steel? Nature 258,703–704. https://doi.org/10.1038/258703a0.

Goiogana, M., Sarasua, J. A., Ramos, J. M., 2018. Ultrasonic assisted electrical discharge machining for high aspect ratio blind holes. Procedia CIRP 68, 81–85. https://doi.org/10.1016/j.procir.2 017.12.026.

Guazzato, M., Quach, L., Albakry, M., Swain, M. V., 2005. Influence of surface and heat treatments on the flexural strength of Y-TZP dental ceramic. J. Dent. 33, 9–18. https://doi.org/10.1016/j.jdent.2004.07.001.

Hallmann, L., Ulmer, P., Reusser, E., Louvel, M., Hämmerle, C. H., 2012. Effect of dopants and sintering temperature on microstructure and low temperature degradation of dental Y-TZP-zirconia. J. Eur. Ceram. Soc. 32, 4091–4104. https://doi.org/10.1016/j.jeurceramsoc.2012.07.032.

Jiao, Y., Liu, W. J., Pei, Z. J., Xin, X. J., & Treadwell, C. (2005). Study on edge chipping in rotary ultrasonic machining of ceramics: an integration of designed experiments

and finite element method analysis. Trans. ASME J. Manuf. Sci. Eng. 127, 752–758. https://doi.org/10.1115/1.2034511.

Inokoshi, M., Zhang, F., De Munck, J., Minakuchi, S., Naert, I., Vleugels, J., Meerbeek, B. V., Vanmeensel, K., 2014. Influence of sintering conditions on low-temperature degradation of dental zirconia. Dent. Mater. 30, 669–678. https://doi.org/10.1016/j.ental.2014.03.005.

Kim, M. J., Ahn, J. S., Kim, J. H., Kim, H. Y., Kim, W. C., 2013. Effects of the sintering conditions of dental zirconia ceramics on the grain size and translucency. J. Adv. Prosthodont. 5, 161–166. https://doi.org/10.4047/jap.2013.5.2.161.

Kuruc, M., Necpal, M., Vopát, T., Šimna, V., & Peterka, J. (2017, June). Influence of ultrasonic assistance on delamination during machining of CFRP composite. In Majstorovic V, Jakovljevic Z (eds.) Proceedings of 5th International Conference on Advanced Manufacturing Engineering and Technologies. 443–450, Springer, Switzerland. https://link.springer.com/chapter/10.1007/978-3-319-56430-2_33.

Kosmač, T., Oblak, C., Jevnikar, P., Funduk, N., Marion, L., 1999. The effect of surface grinding and sandblasting on flexural strength and reliability of Y-TZP zirconia ceramic. Dent. Mater. 15, 426–433. https://doi.org/10.1016/S0109564199000706.

Lambert, H., Durand, J. C., Jacquot, B., Fages, M., 2017. Dental biomaterials for chairside CAD/CAM: State of the art. J. Adv. Prosthodont. 9, 486–495. https://doi.org/10.4047/jap.2017.9.6.486.

Li, Z. C., Cai, L. W., Pei, Z. J., Treadwell, C., 2006. Edge-chipping reduction in rotary ultrasonic machining of ceramics: finite element analysis and experimental verification. Int. J. Mach. Tool Manuf. 46, 1469–1477. https://doi.org/10.1016/j.ijmachtools.2005.09.002.

Li, C., Zhang, F., Meng, B., Liu, L., Rao, X., 2017. Material removal mechanism and grinding force modelling of ultrasonic vibration assisted grinding for SiC ceramics. Ceram. Int. 43, 2981–2993. https://doi.org/10.1016/j.ceramint.2016.11.066.

Liu, D., Cong, W. L., Pei, Z. J., Tang, Y., 2012. A cutting force model for rotary ultrasonic machining of brittle materials. Int. J. Mach. Tool Manufact. 52, 77–84. https://doi.org/10.1016/j.ijmachtools.2011.09.006.

Lotfi, M., Sajjady, S. A., Amini, S., 2019. Wettability analysis of titanium alloy in 3D elliptical ultrasonic assisted turning. Int. J. Light Mater. Manuf. 2, 235–240. https://doi.org/10.1016/j.ijlmm.2019.05.001.

Luthardt, R. G., Holzhüter, M. S., Rudolph, H., Herold, V., Walter, M. H., 2004. CAD/CAM-machining effects on Y-TZP zirconia. Dent. Mater. 20, 655–662. https://doi.org/10.1016/j.dental.2003. 08.007.

Malkin, S., Hwang, T. W., 1996. Grinding mechanisms for ceramics. CIRP Ann. 45, 569–580. https://doi.org/10.1016/S0007-8506(07)60511-3.

Manicone, P. F., Iommetti, P. R., Raffaelli, L., 2007. An overview of zirconia ceramics: basic properties and clinical applications. J. Dent. 35, 819–826. https://doi.org/10.1016/j.jdent.2007.07.008.

Meirowitz, A., Bitterman, Y., Levy, S., Mijiritsky, E., Dolev, E., 2019. An in vitro evaluation of marginal fit zirconia crowns fabricated by a CAD-CAM dental laboratory and a milling center. BMC Oral Health 19, 1–6. https://doi.org/10.1186/s12903-019-0810-9.

Mitov, G., Heintze, S. D., Walz, S., Woll, K., Muecklich, F., Pospiech, P., 2012. Wear behavior of dental Y-TZP ceramic against natural enamel after different finishing procedures. Dent. Mater. 28, 909–918. https://doi.org/10.1016/j.dental.2012.04.010.

Miyazaki, T., Nakamura, T., Matsumura, H., Ban, S., Kobayashi, T., 2013. Current status of zirconia restoration. J. Prosthodont. Res. 57, 236–261. https://doi.org/10.1016/j.jpor.2013.09.001.

Monaco, C., Tucci, A., Esposito, L., Scotti, R., 2013. Microstructural changes produced by abrading Y-TZP in presintered and sintered conditions. J. Dent. 41, 121–126. https://doi.org/10.1016/j.jdent.2012.06.009.

Passos, S. P., Linke, B., Major, P. W., Nychka, J. A., 2015. The effect of air-abrasion and heat treatment on the fracture behavior of Y-TZP. Dent. Mater. 31, 1011–1021. https://doi.org/10.1016/j.dental.2015.05.008.

Piconi, C., Maccauro, G., 1999. Zirconia as a ceramic biomaterial. Biomater. 20, 1–25. https://doi.org/10.1016/S0142-9612(98)00010-6.

Quinn, J., Su, L., Flanders, L., Lloyd, I., 2000. “Edge toughness” and material properties related to the machining of dental ceramics. Mach. Sci. Technol. 4, 291–304. https://doi.org/10.1080/10940340008945711.

Quinn, J. B., Quinn, G. D., 1997. Indentation brittleness of ceramics: a fresh approach. J. Mater. Sci. 32, 4331–4346. https://doi.org/10.1023/A:1018671823059.

Rao, R. V., Pawar, P. J., Davim, J. P., 2010. Parameter optimization of ultrasonic machining process using nontraditional optimization algorithms. Mater. Manuf. Process. 25, 1120–1130. https://doi.org/10.1080/10426914.2010.489788.

Reich, S., Wichmann, M., Nkenke, E., Proeschel, P., 2005. Clinical fit of all-ceramic three-unit fixed partial dentures, generated with three different CAD/CAM systems. Eur. J. Oral Sci. 113, 174–179. https://doi.org/10.1111/j.1600722.2004.00197.x.

Ritzberger, C., Apel, E., Höland, W., Peschke, A., Rheinberger, V. M., 2010. Properties and clinical application of three types of dental glass-ceramics and ceramics for CAD-CAM technologies. Mater. 3, 3700–3713. https://doi.org/10.3390/ma3063700.

Ruiz, L., Readey, M. J., 1996. Effect of heat treatment on grain size, phase assemblage, and mechanical properties of 3 mol% Y-TZP. J. Am. Ceram. Soc. 79, 2331–2340. https://doi.org/10.1111/j.1151-2916.1996.tb08980.x.

Sailer, I., Fehér, A., Filser, F., Gauckler, L. J., Lüthy, H., Hämmerle, C. H. F., 2007. Five-year clinical results of zirconia frameworks for posterior fixed partial dentures. Int. J. Prosthodont. 20. https://pubmed.ncbi.nlm.nih.gov/17695869/.

Sakoda, S., Nakao, N., Watanabe, I., 2018. The effect of abrading and cutting instruments on machinability of dental ceramics. J. Mater. Sci. Mater. Med. 29, 1–8. https://doi.org/10.1007/s10856-018-6031-y.

Schmitter, M., Mueller, D., Rues, S., 2012. Chipping behaviour of all-ceramic crowns with zirconia framework and CAD/CAM manufactured veneer. J. Dent. 40, 154–162. https://doi.org/10.1016/j.jdent.2011.12.007.

Schünemann, F. H., Galárraga-Vinueza, M. E., Magini, R., Fredel, M., Silva, F., Souza, J. C., Zhang, Y., Henriques, B., 2019. Zirconia surface modifications for implant dentistry. Mater. Sci. Eng. C 98, 1294–1305. https://doi.org/10.1016/j.msec.2019.01.062.

Schriwer, C., Skjold, A., Gjerdet, N. R., Øilo, M., 2017. Monolithic zirconia dental crowns. Internal fit, margin quality, fracture mode and load at fracture. Dent. Mater. 33, 1012–1020. https://doi.org/10.1016/j.dental.2017.06.009.

Song, X. F., Yang, J. J., Ren, H. T., Lin, B., Nakanishi, Y., Yin, L., 2018. Ultrasonic assisted high rotational speed diamond machining of dental glass ceramics. Int. J. Adv. Manuf. Technol. 96, 387–399. https://doi.org/10.1007/s00170-017-1571-8.

Song, X. F., Ren, H. T., Yin, L., 2016. Machinability of lithium disilicate glass ceramic in in vitro dental diamond bur adjusting process. J. Mech. Behav. Biomed. Mater. 53, 78–92. https://doi.org/10.1016/j.jmbbm.2015.08.003.

Tesfay, H. D., Xu, Z., Li, Z. C., 2016. Ultrasonic vibration assisted grinding of bio-ceramic materials: an experimental study on edge chippings with Hertzian indentation tests. Int. J. Adv. Manuf. Technol. 86, 3483–3494. https://doi.org/10.1007/s00170-015-8326-1.

Triwatana, P., Nagaviroj, N., Tulapornchai, C., 2012. Clinical performance and failures of zirconia-based fixed partial dentures: a review literature. J. Adv. Prosthodont. 4, 76–83. https://doi.org/10.4047/jap.2012.4.2.76.

Tsai, M. Y., Chang, C. T., Ho, J. K., 2016. The machining of hard mold steel by ultrasonic assisted end milling. Appl. Sci. 6, 373. https://doi.org/10.3390/app6110373.

Wendler, M., Belli, R., Petschelt, A., Mevec, D., Harrer, W., Lube, T., Danzer, R., Lohbauer, U., 2017. Chairside CAD/CAM materials. Part 2: Flexural strength testing. Dent. Mater. 33, 99–109. https://doi.org/10.1016/j.dental.2016.10.008.

Whitney, J. M., Nuismer, R. J., 1974. Stress fracture criteria for laminated composites containing stress concentrations. J. Compos. Mater. 8, 253–265.https://journals.sagepub.com/doi/abs/10.1177/002199837400800303.

Xiao, X., Zheng, K., Liao, W., Meng, H., 2016. Study on cutting force model in ultrasonic vibration assisted side grinding of zirconia ceramics. Int. J. Mach. Tool Manufact. 104, 58–67. https://doi.org/10.1016/j.ijmachtools.2016.01.004.

Xu, H. H., Jahanmir, S., Ives, L. K., 1997. Effect of grinding on strength of tetragonal zirconia and zirconia-toughened alumina. Mach. Sci. Technol. 1, 49–66. https://doi.org/10.1080/10940349708945637.

Xu, W. X., Zhang, L. C., 2015. Ultrasonic vibration-assisted machining: principle, design and application. Adv. Manuf. 3, 173–192. https://doi.org/10.1007/s40436-015-0115-4.

Yang, Z., Zhu, L., Lin, B., Zhang, G., Ni, C., Sui, T., 2019a. The grinding force modeling and experimental study of ZrO_2 ceramic materials in ultrasonic vibration assisted grinding. Ceram. Int. 45, 8873–8889. https://doi.org/10.116/j.ceramint.2019.01.216.

Yang, Z., Zhu, L., Ni, C., Ning, J., 2019b. Investigation of surface topography formation mechanism based on abrasive-workpiece contact rate model in tangential ultrasonic vibration-assisted CBN grinding of ZrO_2 ceramics. Int. J. Mech. Sci. 155, 66–82. https://doi.org/10.1016/j.ijmecsci.2019.02.031.

Yang, Z., Zhu, L., Zhang, G., Ni, C., Lin, B., 2020. Review of ultrasonic vibration-assisted machining in advanced materials. Int. J. Mach. Tool Manufact. 156, 103594. https://doi.org/10.1016/j.ijmachtools.2020.103594.

Zhang, Y., Lawn, B. R., 2019. Evaluating dental zirconia. Dent. Mater. 35, 15–23. https://doi.org/10.1016/j.dental.2018.08.291.

Zeng, W. M., Li, Z. C., Pei, Z. J., Treadwell, C., 2005. Experimental observation of tool wear in rotary ultrasonic machining of advanced ceramics. Int. J. Mach. Tool Manufact. 45, 1468–1473. https://doi.org/10.1016/j.ijmachtools.2005.01.031.

Chapter 7 Surface Asperities in Conventional and Ultrasonic Milling

This chapter consists of the published journal article detailed below:

Juri, A. Z., Nakanishi, Y., Yin, L., 2021. Microstructural influence on damage-induced zirconia surface asperities produced by conventional and ultrasonic vibration-assisted diamond machining. Ceram. Int. 47, 25744–25754. https://doi.org/10.1016/j.ceramint.2021.05.301.

Statement of Authorship

Title of Paper	Microstructural influence on damage-induced zirconia surface asperities produced by conventional and ultrasonic vibration-assisted diamond machining.
Publication status	■ Published ☐ Accepted for publication ☐ Submitted for publication ☐ Unpublished and unsuited work written in manuscript style
Publication details	*Juri, A. Z., Nakanishi, Y., Yin, L., 2021. Microstructural influence on damage-induced zirconia surface asperities produced by conventional and ultrasonic vibration-assisted diamond machining. Ceram. Int. 47, 25744–25754. https://doi.org/10.1016/j.ceramint.2021.05.301.*

Principal Author

Name of Principal Author (Candidate)	Afifah Zakiyyah Juri		
Contribution to the Paper	Conceptualization, Methodology, Investigation, Formal analysis, Validation, Data curation, Writing - original draft, Funding acquisition (PhD scholarship).		
Overall percentage (%)	70		
Certification:	This paper reports on original research I conducted during the period of my Higher Degree by Research candidature and is not subject to any obligations or contractual agreements with a third party that would constrain its inclusion in this thesis. I am the primary author of this paper.		
Signature		Date	21/07/2022

By signing the Statement of Authorship, each author certifies that:

i. the candidate's stated contribution to the publication is accurate (as detailed above);

ii. permission is granted for the candidate in include the publication in the thesis; and

iii. the sum of all co-author contributions is equal to 100% less the candidate's stated contribution.

Name of Co-Author	Yoshitaka Nakanishi		
Contribution to the Paper	Writing – review and editing, Validation, Investigation, Data curation.		
Signature		Date	22/07/2022

Name of Co-Author	Ling Yin		
Contribution to the Paper	Writing – review and editing, Validation, Supervision, Project administration, Methodology, Investigation, Funding acquisition, Formal analysis, Conceptualization.		
Signature		Date	22/07/2022

Microstructural influence on damage-induced zirconia surface asperities produced by conventional and ultrasonic vibration-assisted diamond machining

Afifah Z. Juri[1], Yoshitaka Nakanishi[2], Ling Yin[1]*

[1]School of Mechanical Engineering, The University of Adelaide, Adelaide, SA 5005, Australia

[2] Faculty of Advanced Science and Technology, Kumamoto University, Kumamoto 860-8555, Japan

*Corresponding Author: ling.yin@adelaide.edu.au

Abstract Zirconia surface asperities associated with machining-induced damage and deformation jeopardize the quality of zirconia products. Conventional and emerging ultrasonic vibration-assisted machining processes are used to shape zirconia materials. However, a deep understanding of how zirconia microstructures and ultrasonic vibration amplitudes affect material removal mechanisms and surface quality in these processes is missing, rendering the proper mechanical process selection challenging. This paper reports on the 3D characterization of damage-induced surface asperities and the investigation of material removal mechanisms of pre-sintered porous and sintered dense zirconia materials in conventional and ultrasonic vibration-assisted diamond machining processes. 3D white light profilometry was used to measure surface asperities in terms of texture parameters, together with scanning electron microscopy (SEM) for imaging damage and deformation morphologies. The results show that removal mechanisms and damage-induced zirconia surface asperities depended on material microstructures and ultrasonic vibration amplitudes. Both porous and dense zirconia materials had a brittle-ductile mixed removal mode in conventional and ultrasonic vibration-assisted diamond machining processes. However, brittle fracture was dominant for the porous state and ductile deformation was presiding for the dense state. Thus, there were significantly higher fracture damage area ratios with much higher average and maximum roughness values, and maximum peak and valley heights on machined porous surfaces than dense ones. Ultrasonic assistance at an optimal vibration amplitude promoted brittle-ductile transitions on both porous and dense zirconia surfaces, resulting in reduced brittle fracture

damage areas with reduced surface asperities. This microstructure-process-surface quality relation provides insights into manufacturing processes for zirconia products.

7.1 Introduction

Zirconia is a popular structural engineering material due to its attractive mechanical properties, such as high flexural strength and fracture toughness (Piconi and Maccauro, 1999). It also has good biocompatibility and low affinity against bacterial plaque, and thus can function as a biomaterial for bone repair and replacement, dental implants, and crown and bridge core structures (Denry and Kelly, 2008; Manicone et al., 2007; Miyazaki et al., 2013). Newly developed translucent zirconia has the aesthetic appearance of natural teeth, making it ideal for use as monolithic crowns and bridges to avoid interface fractures in veneer-core structures, widening zirconia applications in dentistry (Zhang, 2014; Zhang and Lawn, 2018). Moreover, zirconia is well known for its phase transformation toughening mechanism, which constrains crack propagations to achieve enhanced mechanical properties (Denry and Kelly, 2014; Guazzato et al., 2004; Piconi and Maccauro, 1999).

Zirconia structures are generally shaped by soft machining of its pre-sintered state with the mechanical strength of 70 ± 20 MPa or hard machining of its sintered state with the mechanical strength of 1100 ± 200 MPa using abrasive tools (Wendler et al., 2017). Although soft machining can economically and rapidly shape zirconia workpieces, post sintering is required to strengthen the workpieces, which unavoidably causes shrinkage, deteriorating workpiece accuracies (Denry and Kelly, 2008). Meanwhile, very rough surfaces with extensive brittle fractures and cracks were observed on machined pre-sintered zirconia surfaces, assessed in two dimensions (2D) in terms of the average (R_a) and the maximum roughness (R_z) (Alao et al., 2017). Particularly, dry milling produces the roughest pre-sintered surfaces in comparison with wet and minimum lubrication milling conditions (Anand et al., 2018). Hard machining with high-stiffness machining systems can precisely make zirconia parts, which also induces surface flaws and asperities on zirconia surfaces, and causes severe diamond tool wear, leading to high costs of zirconia products (Denkena et al., 2017; Kosmač et al., 1999; Wang et al., 2018; Yin et al., 2003).

Machining induced surface defects (asperities and damage) in zirconia have a significant impact on the mechanical functions of its products, such as wear (Mitov et al., 2012), fatigue (Denry, 2013; Rekow et al., 2011) and bacterial adhesion (Morgan, 2004). Although polishing is used as a final process for zirconia products, it cannot fully remove deep machining-induced defects (Denry and Kelly, 2014). These defects act as stress concentrators, causing crack propagations and even catastrophic fractures in zirconia products in loading conditions, e.g., chewing forces in zirconia crowns and bridges (Rekow et al., 2011; Zhang and Lawn, 2019). Therefore, machining-induced surface damage and roughness in pre-sintered and sintered zirconia materials are technical challenges in zirconia applications.

To advance conventional abrasive machining, ultrasonic vibrations with small amplitudes are added to a cutting tool or a workpiece to assist the machining (Brehl and Dow, 2008; Yang et al., 2020). This emerging process has been used to machine alumina at a higher spindle speed, resulting in more ductile removal with decreased brittle facture on the machined surface than conventional machining (Abdo et al., 2019). Ultrasonic vibration-assisted grinding of sintered zirconia using a cubic boron nitride (CBN) wheel has produced better surface quality with reduced average 2D roughness R_a value by 25%, than conventional machining (Jia et al., 2019). In dry conditions, ultrasonic vibration-assisted CBN grinding of sintered zirconia has also reduced 3D average roughness S_a (i.e., the arithmetical mean height of the surface) by 32% compared with conventional grinding (Yang et al., 2019a).

Although ultrasonic vibration-assisted machining appears to outperform conventional machining (Jia et al., 2019; Yang et al., 2019a), there are several important issues to be addressed for its application potential. First, most milling processes for dentistry and medicine apply diamond or tungsten carbide tools (Alao et al., 2017; Yin et al., 2003). Thus, the understanding of ultrasonic vibration-assisted machining with diamond tools is more relevant to mechanical processing of zirconia materials for medical and dental applications. Secondly, little work on responses of pre-sintered zirconia to ultrasonic vibration-assisted milling has been reported, which may impede the improvement of widely used chairside dental CAD/CAM milling systems for machinable ceramics. Thirdly, most machined zirconia surfaces were assessed using 2D characterization in terms of the average R_a or the maximum R_z roughness, which does not represent the nature

of three dimensional surfaces. Although 3D surface characterization has been recently used to quantify machined zirconia surfaces (Yang et al., 2019a), only the average roughness S_a was measured, which does not reflect machining-induced peaks and valleys where stresses are concentrated and bacteria/contaminations are adhered. Fourthly, comparative studies of responses of two important zirconia microstructures, i.e., pre-sintered porous versus sintered dense, to material removal mechanisms and surface quality in both conventional and ultrasonic vibration-assisted diamond machining are missing. This renders selecting the proper mechanical processes for high quality zirconia surfaces challenging.

Therefore, this paper aims to investigate the influences of zirconia microstructures (pre-sintered porous versus sintered dense) on material removal mechanisms and surface quality by conventional and ultrasonic vibration-assisted diamond machining at different vibration amplitudes. 3D characterization of damage-induced surface asperities was performed using white light profilometry in terms of texture parameters. The selected texture parameters featuring machining-induced surface damage included the average roughness S_a and the maximum roughness S_z, as well as the maximum peak height S_p and the maximum valley height S_v. Surface damage morphology were also examined using scanning electron microscopy (SEM) to understand material removal mechanisms. This work demonstrates that zirconia microstructures profoundly control their machining behavior and material removal mechanisms, which in turn determine surface quality. Despite a brittle-ductile mixed removal mode for both porous and dense zirconia materials in all machining processes, brittle fracture dominated for the former and ductile deformation dictated for the latter. Consequently, machined pre-sintered zirconia surfaces had significantly higher fracture damage area ratios with higher average and maximum roughness values, and maximum peak and valley heights than sintered ones. The results also demonstrate that ultrasonic vibration significantly benefited diamond machining at an optimal amplitude, by promoting brittle-ductile transitions on both porous and dense zirconia surfaces.

7.2 Experimental Procedure

7.2.1 Materials

Translucent pre-sintered zirconia (ZENOSTAR Zr Translucent, Wieland Dental+Technik GmbH & Co. KG, Pforzheim, Germany) was selected. The material consisted of 87–95 wt% ZrO_2, 4–6 wt% Y_2O_3 as a stabilizer for tetragonal grains, 1–5 wt% HfO_2 as a binder for ZrO_2 powders and 0.1–1 wt% Al_2O_3 for increasing the ageing resistance of zirconia (Denry and Kelly, 2008; Hallmann et al., 2012; Ritzberger et al., 2010). Sintered zirconia was obtained by sintering the pre-sintered material in a digital furnace (Programat S1, Ivoclar Vivadent, Liechtenstein) following the material manufacturer's recommendation. From room temperature of 20 °C, the material was heated to 900 °C at 600 °C/h heating rate and held at the temperature for 30 min. After that it was continuously heated to 1530 °C at 200 °C/h heating rate and held at the temperature for 2 h. Next, the material was cooled to 900 °C at 600 °C/h cooling rate and continuously cooled to 300 °C at 500 °C/h cooling rate. Finally, it was slowly cooled in the furnace to room temperature. The density and porosity of pre-sintered zirconia were 3.0–3.21 g/cm^3 and 47.3–49.3 vol%, respectively (Ritzberger et al., 2010). Sintered zirconia achieved the density and porosity of more than 99% of the theoretical values.

Reported mechanical properties of pre-sintered zirconia included the hardness H = 1.6 GPa (Alao and Yin, 2014a), the modulus of elasticity E = 34.27 GPa (Alao and Yin, 2014a), the fracture toughness K_{IC} = 0.8 MPa m$^{1/2}$ (Alao and Yin, 2016), and the flexural strength σ = 50–90 MPa (Ritzberger et al., 2010). Reported mechanical properties of sintered zirconia included the hardness H = 9.33 GPa (Alao and Yin, 2014b), the modulus of elasticity E = 168.19 GPa (Alao and Yin, 2014b), the fracture toughness K_{IC} = 6 MPa m$^{1/2}$ (Sakoda et al., 2018), and the flexural strength σ = 1300 MPa (Sakoda et al., 2018). Both pre-sintered and sintered zirconia samples of 10 mm × 10 mm × 2 mm were obtained via cutting with a diamond saw machine (Struers Minitom, Denmark), polishing using a polishing machine (Struers, Denmark), and final cleaning with acetone.

7.2.2 Conventional and Ultrasonic Vibration-Assisted Diamond Machining

An ultrasonic milling machine (Ultrasonic 20 linear, DMG Mori Seiki CO., Ltd, Japan) was employed for conventional and ultrasonic vibration-assisted machining of

pre-sintered and sintered zirconia samples. As shown in Fig. 7.1(a), the machine consists of a high speed ultrasonic spindle system with an ultrasonic transducer, an ultrasonic tool holder inserted with a diamond tool, a cooling nozzle in a coolant system, an integrated numerical-control swivel rotary table with a sample holder, and a PC control panel. It enables high-speed (up to 60,000 rpm), high-precision and high-efficiency machining with assisted ultrasonic vibration amplitudes up to 10 μm and frequencies of 20–50 kHz. Fig. 7.1(b) shows details of a zirconia sample in the sample holder, the diamond tool, and machining movements including a depth of cut a, a feed rate v_w, a diamond tool rotational speed v_s and an axial ultrasonic vibration at an amplitude A and a frequency f.

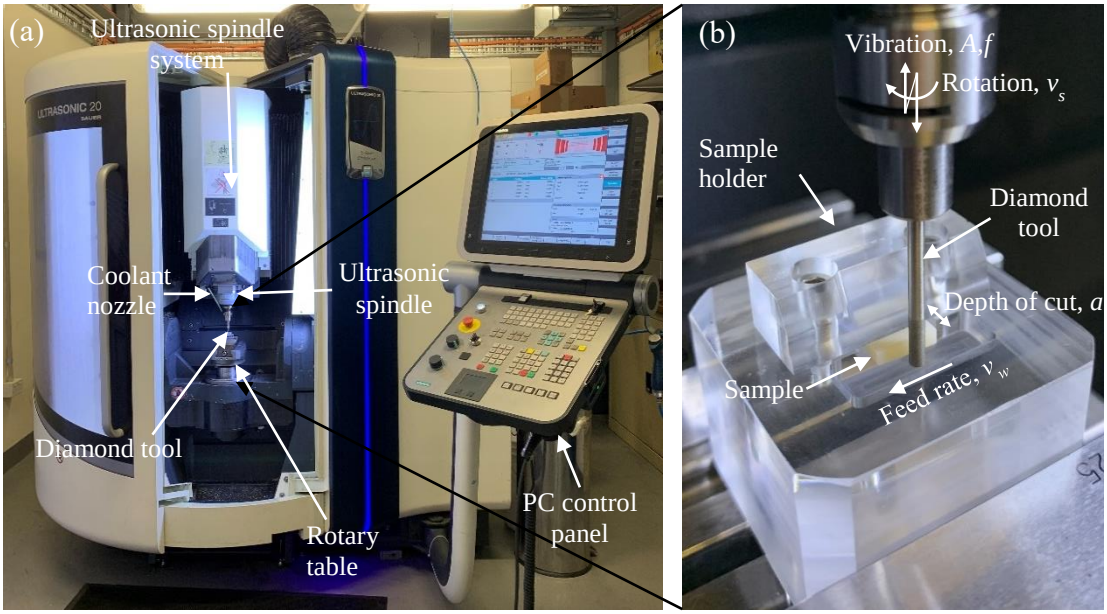

Fig. 7.1. (a) Experimental setup for diamond machining with ultrasonic vibration assistance and (b) details of machining movements in diamond tool-zirconia sample contact.

The diamond tool was metal-bonded with diamond grit size of 53 μm and had a machining portion of 2 mm in diameter and 4 mm in length (Scott, Diamantwerkzeuge GmbH, Germany). In conventional machining, the diamond tool rotated at a cutting speed v_s of 25,000 rpm, moved along a 10 mm × 2 mm sample surface at a feed rate v_w of 500 mm/min, and perpendicularly cut the surface at a depth of cut a of 50 μm to remove a layer of material. In ultrasonic machining, the diamond tool was axially vibrating at a harmonic frequency f of 25 kHz and vibration amplitudes A of 3–9 μm in addition to all movements involved in conventional machining (i.e., vibration amplitude $A = 0$). A

cutting fluid (ECOCOOL 700 NBF (M), Fuchs Lubricants (Australasia) Pty Ltd, Australia) was delivered to the diamond tool-sample contact area at a pressure of 4 bar to reduce cutting temperatures and flush away debris. A new machined surface was obtained after 100 machining passes at each machining condition. After machining, all samples were cleaned using acetone for surface characterization.

7.2.3 Characterization Methodology

All machined surfaces were characterized using a 3D non-contact chromatic white light optical profilometer (Bruker Contour GT-K, UK). Following ISO 25178, the selected 3D surface texture parameters included the average roughness S_a, the maximum peak height S_p, the maximum valley height S_v and the maximum roughness S_z (ISO 25178). In 3D roughness measurement of deterministically digitally manufactured surfaces at each processing condition, the independent sampling number ranges from 1–4 and each sampling area covers from 0.77 mm × 0.77 mm to 4.25 mm × 4.25 mm (Khellaf et al., 2017; Nemoto et al., 2009). Accordingly, three independent sampling areas of 1.20 mm × 1.20 mm at each machining condition were obtained to determine the mean and standard deviations of the selected surface texture parameters.

Based on the 3D surface assessment, ultrasonic machining at 3 μm vibration amplitude produced least surface roughness values of the selected parameters for both materials. Hence, pre-sintered and sintered zirconia surfaces produced by conventional and ultrasonic machining at 3 μm vibration amplitude were carbon-coated and examined using SEM (FEI Quanta 450 FEG ESEM, Thermo Fisher Scientific, USA) to understand material removal and surface damage mechanisms. Each surface was viewed and imaged at random locations with 500–5000× magnifications. A java-based image processing program (ImageJ, NIH Image, USA) was applied to measure fractured damage areas on viewed areas at 1000× magnification, at which the damages were visible and adequately representative. A fracture damage area ratio, i.e., a ratio of the measured fractured areas and the viewed area, was used to quantify the damage degree of the viewed surface area. Three random areas were viewed and image-processed on each machined surface to obtain the mean and standard deviation of the ratio.

A single factor analysis of variance (ANOVA) was performed at 5% significance level to examine the influence of ultrasonic vibration amplitudes on the selected surface texture

parameters. A paired *t*-test was performed at 5% significance level to compare the influence of each amplitude on the selected surface parameters and to examine the material effect on these parameters. Finally, a two-way ANOVA was conducted at 5% significance level to compare fracture damage area ratios in pre-sintered and sintered zirconia surfaces produced by conventional and ultrasonic machining at 3 μm vibration amplitude.

7.3 Results

7.3.1 Surface Asperities

Fig. 7.2 shows 2D and 3D surface topographies of pre-sintered and sintered zirconia surfaces produced by conventional and ultrasonic machining at 3 μm vibration amplitude. Conventional machining produced much wider and deeper cutting grooves and discrete cavities with a peak-valley height of 63.6 μm (16.6 μm + 47.0 μm) for pre-sintered zirconia (Fig. 7.2(a)) and continuing grooves with a peak-valley height of 22.5 μm (10.4 μm + 12.1 μm) for sintered state (Fig. 7.2(b)). Ultrasonic machining generated much less discrete deep cavities with a peak-valley height of 35.7 μm (14.9 μm + 20.8 μm) for pre-sintered zirconia (Fig. 7.2(c)) and evenly distributed machining grooves with a peak-valley height of 16.4 μm (8.2 μm + 8.2 μm) for sintered state (Fig. 7.2(d)).

Fig. 7.3 shows the average roughness S_a values of pre-sintered and sintered zirconia surfaces produced by conventional and ultrasonic machining at different vibration amplitudes. For pre-sintered zirconia (Fig. 7.3(a)), conventional machining produced the largest S_a values of 3.95 ± 0.08 μm. It was followed by ultrasonic machining at 9 μm and 6 μm vibration amplitudes with S_a values of 3.90 ± 0.07 μm and 3.78 ± 0.04 μm, respectively. Ultrasonic machining at 3 μm vibration amplitude yielded the smallest S_a values of 3.60 ± 0.09 μm, 9% reduction in comparison with conventional machining. For sintered zirconia (Fig. 7.3(b)), conventional machining also produced the largest S_a values of 3.07 ± 0.10 μm. Ultrasonic machining at 9 μm and 6 μm vibration amplitudes slightly improved S_a values to 3.06 ± 0.09 μm and 2.91 ± 0.07 μm, respectively. Ultrasonic machining at 3 μm vibration amplitude yielded the smallest S_a values of 2.68 ± 0.08 μm, 13% reduction in comparison with conventional machining. In addition, all S_a values for

pre-sintered zirconia were higher than those for sintered zirconia at any machining conditions.

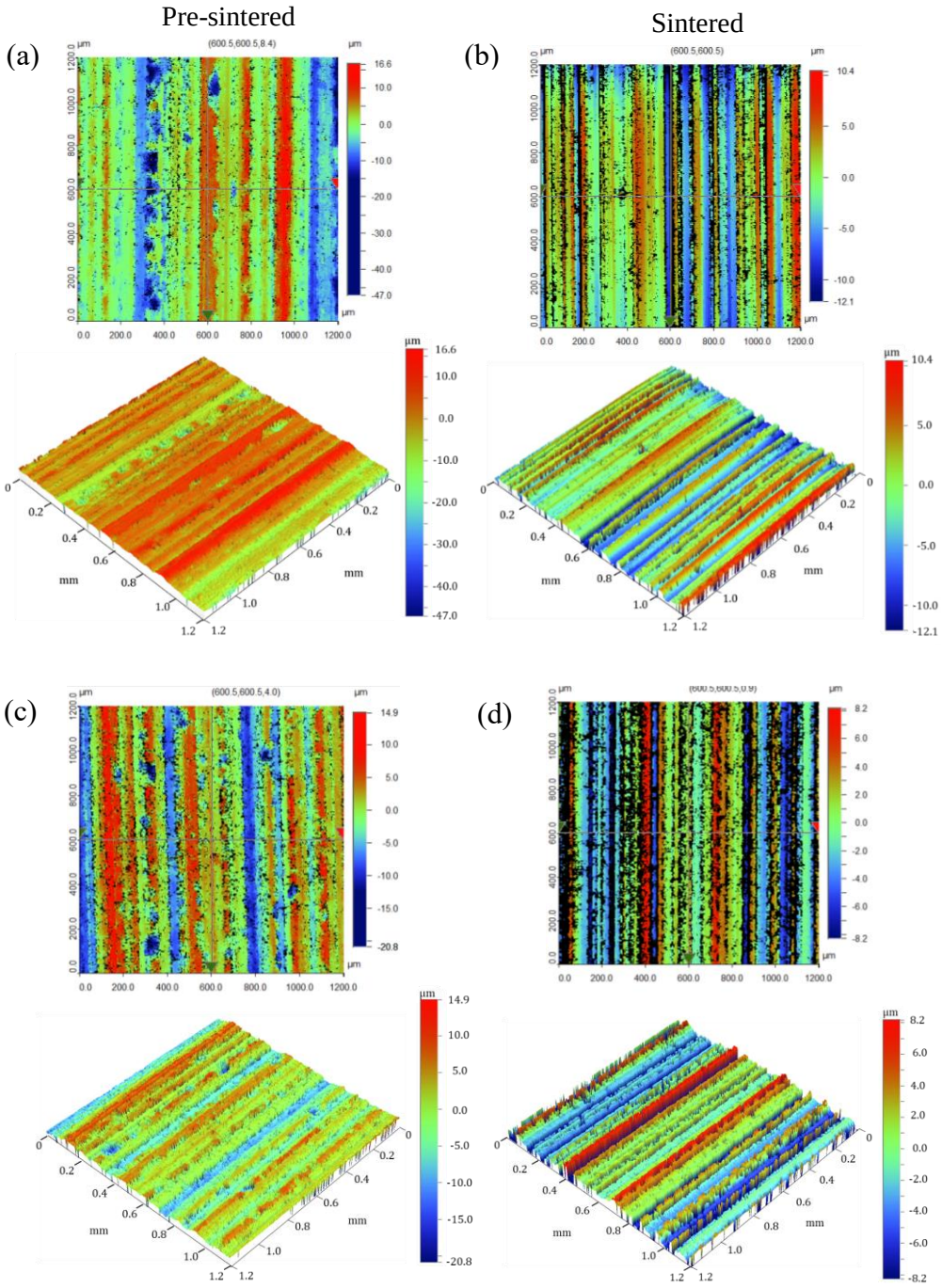

Fig. 7.2. 2D and 3D topographies of (a) pre-sintered and (b) sintered zirconia surfaces produced by conventional machining; (c) pre-sintered and (d) sintered zirconia surfaces produced by ultrasonic machining at 3 µm vibration amplitude.

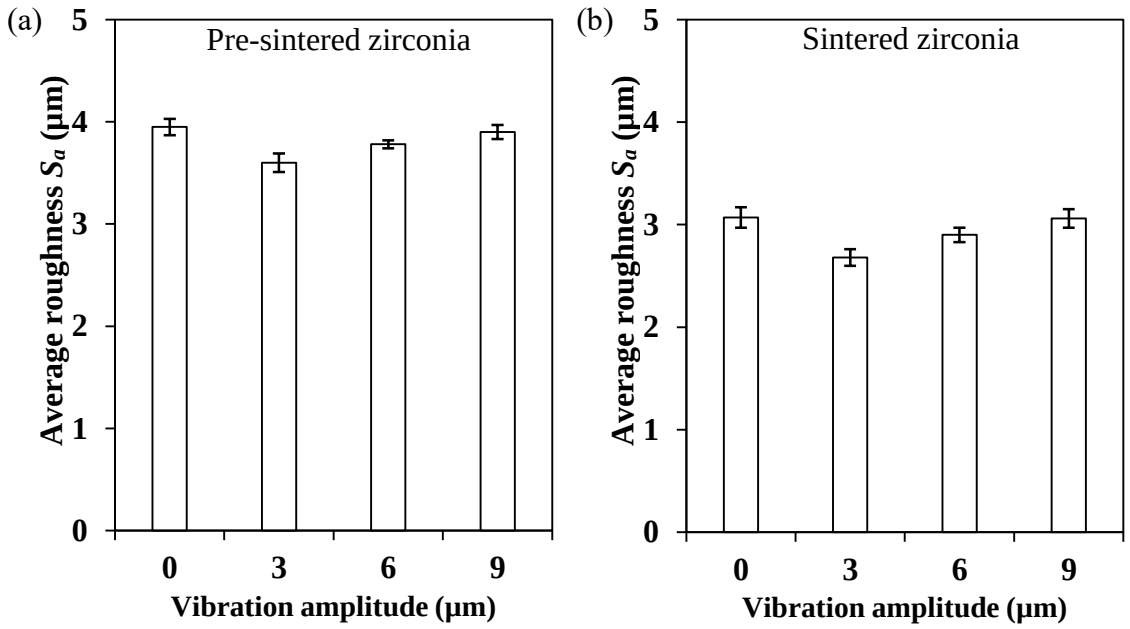

Fig. 7.3. 3D average roughness S_a values for (a) pre-sintered and (b) sintered zirconia surfaces produced by conventional (i.e., vibration amplitude = 0) and ultrasonic machining at different vibration amplitudes.

Fig. 7.4 shows the maximum peak heights S_p, the maximum valley heights S_v, and the maximum roughness S_z values of pre-sintered and sintered zirconia surfaces produced by conventional and ultrasonic machining at different vibration amplitudes. For pre-sintered zirconia (Fig. 7.4(a)), ultrasonic machining at 9 µm vibration amplitude produced the maximum S_p values of 19.10 ± 2.89 µm. Improved S_p values of 15.63 ± 1.13 µm and 13.50 ± 0.64 µm were made by conventional machining and ultrasonic machining at 6 µm vibration amplitude, respectively. Ultrasonic machining at 3 µm vibration amplitude produced the lowest S_p values of 12.36 ± 2.20 µm, 21% decrease compared with conventional machining. Further, the largest S_v values of 43.50 ± 10.25 µm and S_z values of 59.80 ± 10.06 µm were produced by conventional machining. These values were reduced to S_v values of 27.98 ± 6.74 µm and S_z values of 46.70 ± 10.08 µm, respectively, by ultrasonic machining at 9 µm vibration amplitude. Ultrasonic machining at 3 µm and 6 µm vibration amplitudes produced the lowest S_v values of 23.92 ± 4.87 µm and 22.17 ± 4.76 µm and S_z values of 36.30 ± 4.00 µm and 35.60 ± 5.31 µm, respectively, approximately 40% reductions for both parameters compared with conventional machining. For sintered zirconia (Fig. 7.4(b)), conventional machining produced the maximum S_p values of 10.23 ± 0.53 µm, S_v values of 11.69 ± 1.59 µm and S_z values of

22.01 ± 1.93 µm. It was followed by ultrasonic machining at 9 µm vibration amplitude with S_p values of 10.16 ± 0.81 µm, S_v values of 11.02 ± 0.78 µm and S_z values of 21.18 ± 1.25. Ultrasonic machining at 3 µm and 6 µm vibration amplitudes produced relatively smaller S_p values of 9.15 ± 1.57 µm and 8.62 ± 0.64 µm, S_v values of 9.12 ± 1.21 µm and 10.99 ± 0.91 µm, and S_z values of 18.11 ± 3.01 µm and 19.64 ± 1.54 µm, respectively. Meanwhile, all S_p, S_v, and S_z values for pre-sintered zirconia are larger than those for sintered zirconia at any machining conditions.

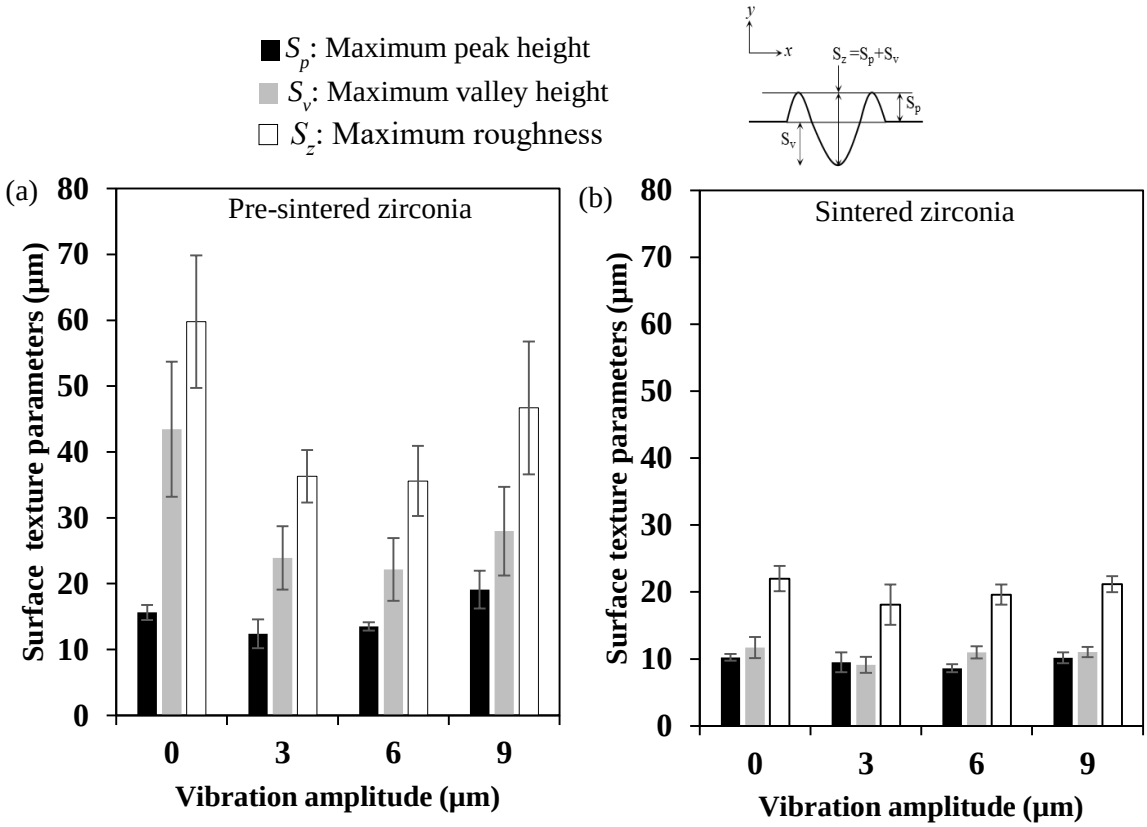

Fig. 7.4. 3D maximum peak heights S_p, maximum valley heights S_v, and maximum roughness S_z values for (a) pre-sintered and (b) sintered zirconia surfaces produced by conventional (i.e., vibration amplitude = 0) and ultrasonic machining at different vibration amplitudes.

7.3.2 Statistical Analysis of Surface Asperities

Table 7.1 shows an example of the one-way ANOVA result for S_a values of pre-sintered zirconia with respect to different vibration amplitudes. Table 7.2 summarizes the *p* values of all the one-way ANOVA for S_a, S_p, S_v, and S_z values of pre-sintered and sintered zirconia materials with respect to different vibration amplitudes. It shows that vibration

amplitudes significantly affected all selected surface texture parameters for pre-sintered zirconia (ANOVA, $p < 0.05$) but only significantly influenced S_a values for sintered zirconia (ANOVA, $p < 0.05$).

Table 7.1. Result of the one-way ANOVA with replication for the average roughness S_a values of pre-sintered zirconia with respect to different vibration amplitudes.

Source of variation	Sum of square (SS)	DF	Mean sum of square (MS)	*F* test	*p* value	*F* crit
Between amplitudes	0.22	3	0.07	14	0.00	4.07
Within amplitudes	0.04	8	0.01			
Total	0.26	11				

Table 7.2. Summary of the *p* values of all the one-way ANOVA with replications for the average roughness S_a values, the maximum peak heights S_p, the maximum valley heights S_v, and the maximum roughness S_z values of pre-sintered and sintered zirconia materials with respect to different vibration amplitudes.

Surface texture parameters (μm)	*p* value	
	Pre-sintered zirconia	Sintered zirconia
S_a	$p < 0.05$	$p < 0.05$
S_p	$p < 0.05$	$p > 0.05$
S_v	$p < 0.05$	$p > 0.05$
S_z	$p < 0.05$	$p > 0.05$

Table 7.3 demonstrates an example of the paired *t*-test for S_a values for pre-sintered zirconia surfaces produced by conventional and ultrasonic machining at 3 μm vibration amplitude. Table 7.4 summarizes the *p* values of all paired *t*-tests for S_a, S_p, S_v, and S_z values produced in conventional and ultrasonic machining at different vibration amplitudes for the two zirconia materials. For pre-sintered zirconia, ultrasonic machining at 3 μm and 6 μm vibration amplitudes yielded significantly smaller S_a, S_p, S_v, and S_z values than conventional machining (*t*-test, $p < 0.05$). A further comparison between ultrasonic machining processes at 3 μm and 6 μm vibration amplitudes indicate that the former also produced significantly lower S_a values than the latter (*t*-test, $p < 0.05$) but made insignificant changes to S_p, S_v, and S_z values (*t*-test, $p > 0.05$). Further, all S_a, S_p, S_v,

and S_z values produced by ultrasonic machining at 9 µm vibration amplitude had insignificant difference from those produced by conventional machining. For sintered zirconia, ultrasonic machining at 3 µm vibration amplitude yielded significantly smaller S_a values than conventional machining (t-test, $p < 0.05$) but made insignificant differences to S_p, S_v, and S_z values (t-test, $p > 0.05$). Ultrasonic machining at 6 µm vibration amplitude produced significantly smaller S_p values than conventional machining (t-test, $p < 0.05$) but made insignificant differences to S_a, S_v, and S_z values (t-test, $p > 0.05$). At 9 µm vibration amplitude, ultrasonic machining showed no significantly different from conventional machining with respect to the generation of all S_a, S_p, S_v, and S_z values (t-test, $p > 0.05$).

Table 7.5 reveals an example of the paired t-test of S_a values for pre-sintered and sintered zirconia materials obtained in all machining conditions. Table 7.6 provides a summary of the p values of all paired t-test of S_a, S_p, S_v, and S_z values for the two materials produced in all machining conditions, indicating that machined pre-sintered zirconia surfaces were significantly rougher than sintered ones (t-test, $p < 0.05$).

Table 7.3. Result of the paired t-test for the average roughness S_a values of pre-sintered zirconia surfaces produced by conventional and ultrasonic machining at 3 µm vibration amplitude.

	Conventional machining	Ultrasonic machining
Mean	3.91	3.60
Variance	0.01	0.01
Observations	3.00	3.00
Pooled Variance	0.01	
Hypothesized Mean Difference	0.00	
Degree of Freedom	4.00	
t Statistics	5.16	
P(T<=t) one-tail	0.00	
t Critical one-tail	2.13	
P(T<=t) two-tail	0.01	
t Critical two-tail	2.78	

Table 7.4. Summary of the *p* values of the paired *t*-tests for the average roughness S_a values, the maximum peak heights S_p, the maximum valley heights S_v, and the maximum roughness S_z values produced in conventional (i.e., vibration amplitude = 0) and ultrasonic machining at different vibration amplitudes for pre-sintered and sintered zirconia materials.

Vibration amplitude (μm)	*Pre-sintered* *p value*				*Sintered* *p value*			
	S_a	S_p	S_v	S_z	S_a	S_p	S_v	S_z
0 versus 3	*p < 0.05*	*p < 0.05*	*p < 0.05*	*p < 0.05*	*p < 0.05*	*p > 0.05*	*p > 0.05*	*p > 0.05*
0 versus 6	*p < 0.05*	*p < 0.05*	*p < 0.05*	*p < 0.05*	*p > 0.05*	*p < 0.05*	*p > 0.05*	*p > 0.05*
0 versus 9	*p > 0.05*	*p > 0.05*	*p > 0.05*	*p > 0.05*	*p > 0.05*	*p > 0.05*	*p > 0.05*	*p > 0.05*
3 versus 6	*p < 0.05*	*p > 0.05*	*p > 0.05*	*p > 0.05*	*p < 0.05*	*p > 0.05*	*p > 0.05*	*p > 0.05*

Table 7.5. Result of the paired *t*-test for the roughness S_a values for pre-sintered and sintered zirconia surfaces produced in all machining conditions

	Pre-sintered zirconia	Sintered zirconia
Mean	3.91	2.92
Variance	0.04	0.03
Observations	12	12
Pooled Variance	0.04	
Hypothesized Mean Difference	0	
Degree of Freedom	22	
t Statistics	12.84	
P(T<=t) one-tail	0.00	
t Critical one-tail	1.72	
P(T<=t) two-tail	0.00	
t Critical two-tail	2.07	

Table 7.6. Summary of the *p* values of all the paired *t*-tests for the average roughness S_a values, the maximum peak heights S_p, the maximum valley heights S_v, and the maximum roughness S_z values of pre-sintered and sintered zirconia materials produced in all machining conditions.

Surface texture roughness parameters (μm)	*p*-value
	Pre-sintered versus sintered zirconia
S_a	$p < 0.05$
S_p	$p < 0.05$
S_v	$p < 0.05$
S_z	$p < 0.05$

7.3.3 Surface Damage Morphology and Material Removal Mechanisms

Fig. 7.5 shows 500× magnification SEM micrographs of pre-sintered and sintered zirconia machined surfaces produced by conventional and ultrasonic machining at 3 μm vibration amplitude. All machined surfaces revealed brittle fracture and ductile flow deformation-induced ploughing striations. For pre-sintered zirconia, conventional machining resulted in wider cutting marks and larger micro cracking areas with arrest lines and convex-shell-like fractures (Fig. 7.5(a)) while ultrasonic machining produced narrower and smaller cracking and fracture regions with arrest lines but without convex-shell-like fractures (Fig. 7.5(b)). For sintered zirconia, although both machining produced similar surfaces, conventional machining induced more fractures (Fig. 7.5(c)) and ultrasonic machining yielded more ductile deformation (Fig. 7.5(d)). Further, there were more fractures on pre-sintered zirconia surfaces (Figs. 7.5(a) and 7.5(b)) and much less damage and more smoothly ductile flow striations on sintered zirconia surfaces (Figs. 7.5(c) and 7.5(d)). In ductile removal areas on both pre-sintered and sintered surfaces, conventional machining produced straight scratches (Figs. 7.5(a) and 7.5(c)) and ultrasonic machining made waved scratches (Figs. 7.5(b) and 7.5(d)). Fig. 7.6(a) details a large and deep cavity with fragmented areas, pulverised powders, and microcracks on conventionally machined pre-sintered zirconia surface. Fig. 7.6(b) features shallower scars with ductile flow, smears, fractures and pulverised powders on conventionally machined sintered zirconia surface.

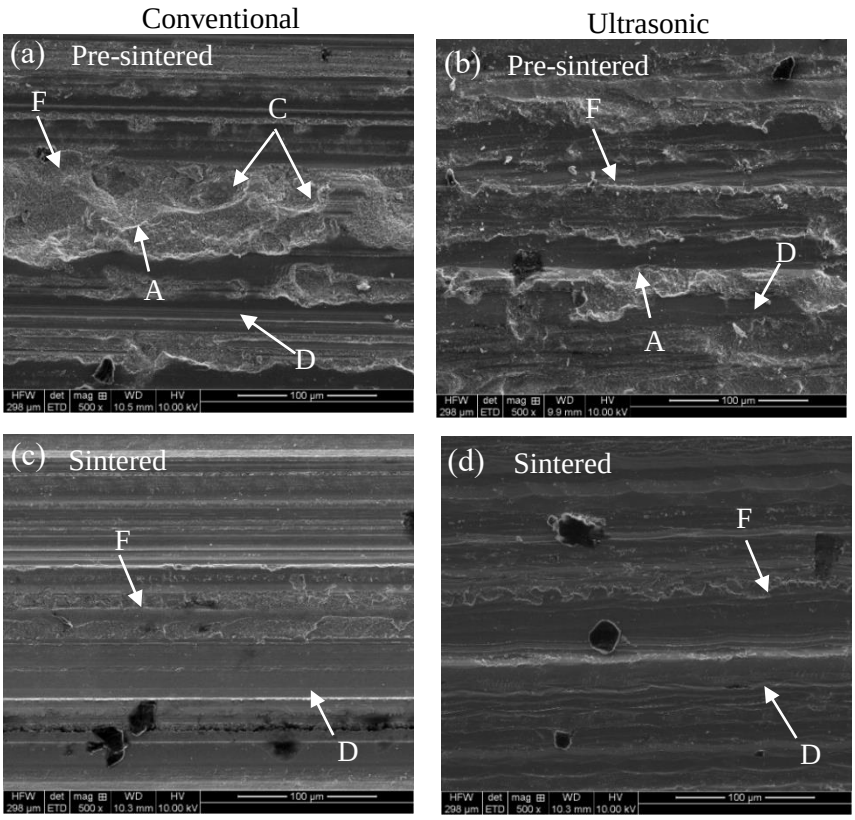

Fig. 7.5. 500× magnification of SEM micrographs of (a) and (b) pre-sintered zirconia surfaces produced by conventional machining and ultrasonic machining at 3 μm vibration amplitude, respectively; and (c) and (d) sintered surfaces produced by conventional and ultrasonic machining at 3 μm vibration amplitude, respectively. Note that fracture is designated by "F", ductile flow by "D", arrest lines by "A", and convex-shell-like fracture by "C".

Fig. 7.7 shows the measurement of fracture damage areas for pre-sintered and sintered zirconia surfaces produced in conventional and ultrasonic machining at 3 μm vibration amplitude based on 1,000× SEM micrographs using the Java-based image processing program. Fig. 7.8 shows fracture damage area ratios for pre-sintered and sintered zirconia materials produced by conventional and ultrasonic machining at 3 μm vibration amplitude. For pre-sintered zirconia, ultrasonic machining reduced fracture damage area ratios from 0.60 ± 0.05 $\mu m^2/\mu m^2$ to 0.45 ± 0.07 $\mu m^2/\mu m^2$, by 25%. For sintered dense zirconia, the corresponding ratios were reduced from 0.19 ± 0.01 $\mu m^2/\mu m^2$ to 0.16 ± 0.01 $\mu m^2/\mu m^2$, by 16%. Table 7.7 shows the two-way ANOVA with replication for comparison of fracture damage area ratios for the two materials produced by the two processes, indicating significant material and process effects on the ratios (ANOVA, $p < 0.05$).

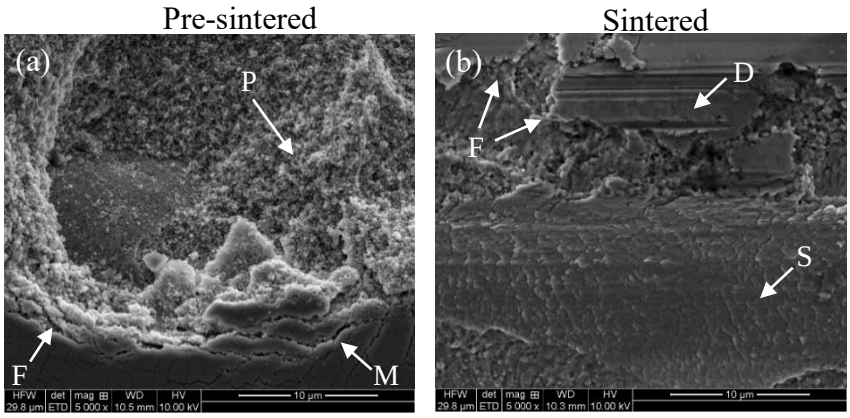

Fig. 7.6. 5000× SEM micrographs of (a) a severe cavity on pre-sintered zirconia surface and (b) a shallower scar on sintered zirconia surface produced by conventional machining. Note that pulverization is designated by "P", ductile flow by "D", microcracks by "M", and smears by "S".

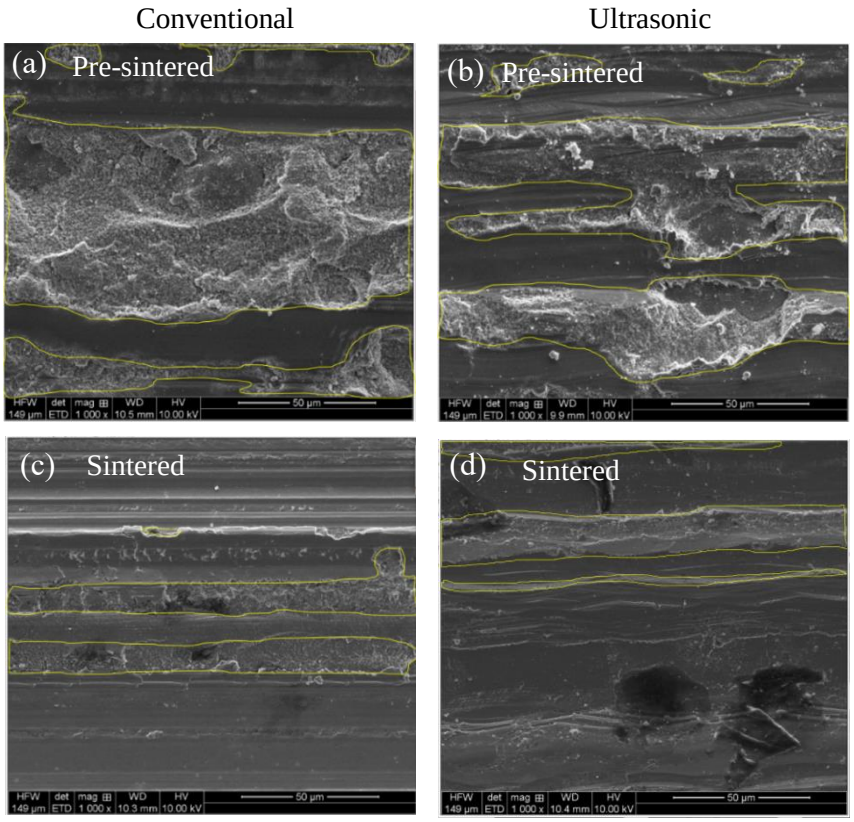

Fig. 7.7. Java-based image measurement of fracture damage areas based on 1,000× SEM micrographs for (a) and (b) pre-sintered zirconia surfaces produced by conventional and ultrasonic machining at 3 μm vibration amplitude, respectively; and (c) and (d) sintered zirconia surfaces produced by conventional and ultrasonic machining at 3 μm vibration amplitude, respectively.

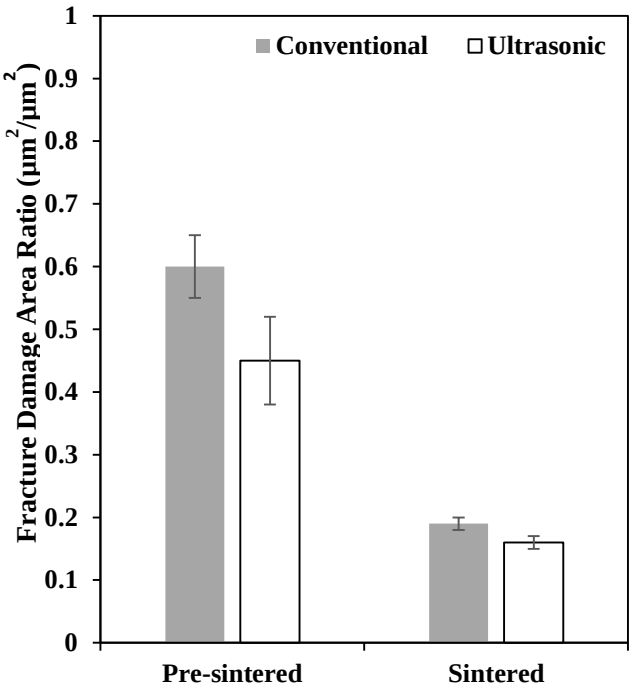

Fig. 7.8. Fracture damage area ratios for pre-sintered and sintered zirconia surfaces produced by conventional and ultrasonic machining at 3 µm vibration amplitude.

Table 7.7. Result of two-way with replication for comparison of fracture damage ratios for pre-sintered and sintered zirconia surfaces produced in conventional and 3-µm vibration amplitude ultrasonic machining.

Source of variation	Sum of square (SS)	DF	Mean sum of square (MS)	*F*-test	*p*-value	*F* crit
Material	0.38	1	0.38	186.70	0.00	5.32
Process	0.02	1	0.02	11.56	0.01	5.32
Interaction	0.01	1	0.01	5.04	0.05	5.32
Within	0.02	8	0.00			
Total	0.42	11				

7.4 Discussion

This work studied effects of microstructures and ultrasonic vibration amplitudes on surface quality of conventionally and ultrasonically machined zirconia materials in terms of 3D surface texture parameters reflecting damage morphologies.

Much lower S_a, S_p, S_v and S_z values for machined sintered zirconia surfaces than those for pre-sintered state (Figs. 7.2–7.4) indicates a significant material-dependent nature of machining-induced surface asperities (Table 7.6). This characteristic could be attributed to their different microstructures to lead to different removal mechanisms in machining. In machining of pre-sintered zirconia, diamond abrasives easily broke weak pore networks to result in grain boundary microcracking. In contrast, sintered zirconia with closely packed crystal microstructure tented to resist fractures invaded by diamond abrasive, and thus its machining yielded much less fractures. Thus, pre-sintered porous microstructure led to large and deep fracture-induced cavities in machining while sintered dense state promoted shallow ductile flows and smears, and small-scale fractures (Figs. 7.5–7.7). The revealing fractures and ductile flows on all machined surfaces (Figs. 7.5–7.7) proves the mixed brittle and ductile removal mode for the two materials. The significantly higher fracture damage area ratios on machined pre-sintered zirconia surfaces than sintered ones (Figs. 7.7 and 7.8) also demonstrate the fracture-dominant removal for the former and the ductile-regime ruling mode for the latter. This can be further analysed using an index of brittleness associated with the mechanical properties (Lawn and Marshall, 1979):

$$B = \frac{H}{K_{IC}} \tag{7.1}$$

where B is the brittleness index, H is the hardness and $K_{IC}$is the fracture toughness. A higher index of brittleness indicates that the material is more brittle and susceptible to fracture. The indices of brittleness for pre-sintered and sintered zirconia materials are 2.0 $\mu m^{-1/2}$ and 1.6 $\mu m^{-1/2}$, respectively. This means that the former is more prone to fracture damage than the latter, and consequently has more severe machining-induced fracture damage (Figs. 7.5–7.8) with significantly higher surface asperities (Figs. 7.2–7.4). This is consistent with the grinding of optical glass in which brittle material removal induces cracks and damage, leading to higher peak-valley heights on machined glass surfaces (Jiang et al., 2017). In addition, fractured-induced deep cavities on conventionally machining pre-sintered zirconia surfaces (Figs. 7.2(a), 7.5(a) and 7.6(a)) are very difficult to remove in post polishing, jeopardising the functional quality of zirconia products.

Further, the degrees of the ultrasonic vibration amplitude effect on machined surface asperities also depended on zirconia microstructures (Figs. 7.3 and 7.4). The ultrasonic vibration amplitude significantly affected all S_a, S_p, S_v and S_z parameters for pre-sintered state but only influenced S_a values for sintered state (Figs. 7.3 and 7.4, Table 7.2). Hence, it is important to understand the role of ultrasonic vibration in ultrasonic machining of these two materials.

Fig. 7.9(a) reveals an illustration of surface grinding in which a diamond tool moves across a sample for material removal at a rotational speed v_s, a feed rate v_w and a depth of cut a. In ultrasonic machining, an assisted vibration was added to conventional machining at an amplitude A and a frequency f, which alters diamond abrasive trajectories. This is proven by ultrasonic vibration-induced sinusoidal oscillation waved scratches (Figs. 7.5(b) and 7.5(d)) and conventional machining-induced straight cutting marks (Figs. 7.5(a) and 7.5(c)) in ductile removal areas on both materials. These sinusoidal oscillation cutting trajectories may have changed diamond-tool sample interactions from a continuous mode in conventional machining to non-continuous because of the reciprocating separations between diamond abrasives and the sample surface (Yang et al., 2020). This phenomenon was also confirmed in ultrasonic grinding of sintered zirconia using a CBN grinding wheel (Yang et al., 2019b). As illustrated in Fig. 7.9(b), conventional machining does not have the separating movements between diamond abrasives and the sample surface, resulting in straight line cutting marks and continuous cutting pathways (Figs. 7.5(a) and 7.5(c)). Fig. 7.9(c) demonstrates that in ultrasonic machining there are two processing stages, i.e., a periodic separation stage for several diamond grains to separate from the sample surface for non-continuous actions, and a cutting stage to lead to waved cutting scratches (Figs. 7.5(b) and 7.5(d)).

This discontinuous tool-sample surface interaction in ultrasonic machining may have enabled diamond abrasives to have longer cutting trajectory lengths than those in conventional machining, resulting in more interactive cutting overlaps with shallower depths of cut (Liang et al., 2019). Therefore, ultrasonic machining produced lower peaks and valleys, and overall maximum and average roughness on machined surfaces, as shown in Figs. 7.2–7.4, particularly for pre-sintered zirconia. Further, it may have promoted more ductile deformation for both materials, evidenced by lower fracture damage area ratios in Figs. 7.7 and 7.8, although the vibration assistance could not

entirely diminish brittle fractures in ceramic removal. In addition, the discontinuous interactions in ultrasonic machining may have also reduced pulverised debris accumulation on the tool surface, leading to improved surface quality as shown in Figs. 7.3 and 7.4.

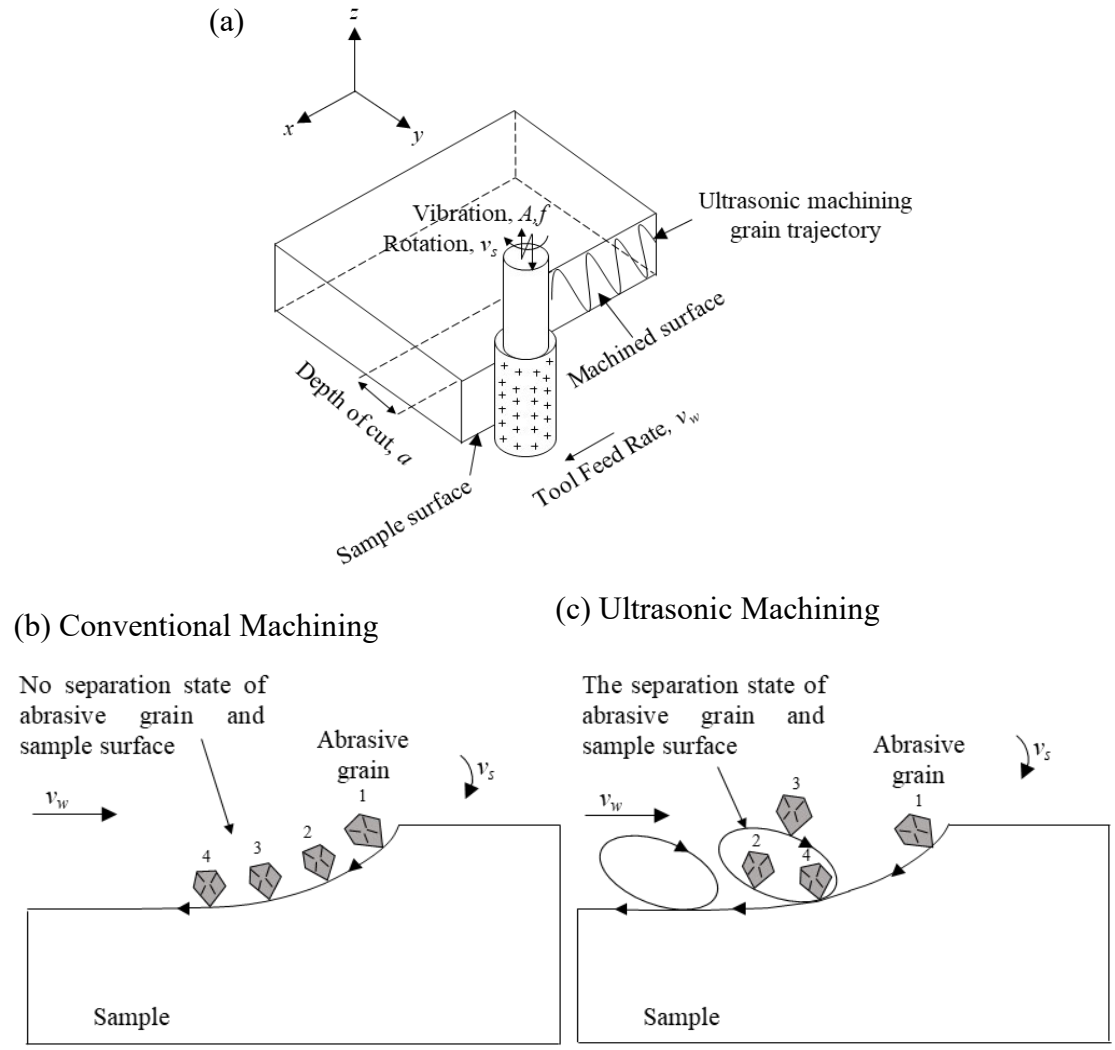

Fig. 7.9. (a) 3D illustration of conventional and ultrasonic machining processes and corresponding diamond abrasive trajectories in (b) conventional and (c) ultrasonic machining.

However, not all vibration amplitudes have provided significant assistance to machining with respect to surface quality (Figs. 7.3 and 7.4, Table 7.4). The statistical analysis (Table 7.4) indicates that ultrasonic milling at 3 μm vibration amplitude yielded the most significant improvement for pre-sintered and sintered zirconia surface quality in comparison with conventional machining. However, the significant reductions in S_a, S_p,

S_v and S_z values were only achieved for pre-sintered state, which may be due to the fracture-dominating removal for the material. For sintered zirconia, only S_a, values were significantly reduced but S_p, S_v and S_z values were insignificantly different from those produced by conventional machining. This may be due to that the ductile-regime leading removal mode resulted in smoother sintered zirconia surfaces (Figs. 7.5 and 7.7) and ultrasonic vibration only significantly reduced the facture damage area ratios (Figs. 7.7 and 7.8) but caused insignificant changes for S_p, S_v and S_z values (Table 7.2). Further, increased vibration amplitude of 9 μm did not yielded significant assistance to conventional machining of both materials (*t*-test, $p > 0.05$). This may be attributed to increased cutting forces with increased vibration amplitudes might have increased hammering actions of diamond abrasives against ceramic surfaces, resulting in increased cracking on machined surfaces to jeopardize surface quality (Li et al., 2017). This is in agreement with the ultrasonic grinding of silicon carbide (Tsai et al., 2016).

This study may provide technical fundamentals to improve current CAD/CAM milling of pre-sintered zirconia for dental crowns and bridges by adding ultrasonic vibration with an optimized amplitude, achieving much better surface quality to reduce manual polishing. It should be noted that the current research focused on flat surface generation, which is easier than shaping of curved surfaces. Given the wide applications of zirconia materials in engineering, medicine and dentistry, continuing efforts will be made to understand the ultrasonic machining of complex shapes.

7.5 Conclusions

Damaged induced surface asperities of pre-sintered porous and sintered dense zirconia materials produced by conventional and ultrasonic machining demonstrate essential roles of microstructures and ultrasonic vibration amplitudes in removal mechanisms and surface quality. While both materials had a brittle-ductile mixed removal mode in all machining processes, porous zirconia responded to machining with dominant fracture-induced microcracking, fragmentation and pulverization while dense surfaces were generated with more ductile deformation. These distinct removal mechanisms resulted in machined porous zirconia surfaces with significantly higher fracture damage area ratios and damage-induced surface asperities than dense surfaces. The selection of an optimized vibration amplitude (3 μm in this study) was crucial for ultrasonic machining. At such an amplitude, ultrasonic machining enabled the promotion of brittle-ductile transitions on

both porous and dense zirconia surfaces to yield reduced fracture damage and average roughness. It also significantly flattened damage-induced maximum peak and valley heights to lead to reduced maximum roughness for pre-sintered zirconia. This research provides useful scientific fundamentals for advancing machining processes with ultrasonic vibration assistance to produce high quality and reliable zirconia products.

Declaration of Competing Interests

The authors declare that they have no known competing financial personal interests that could have appeared to influence the work reported in this paper.

Acknowledgments

The authors would like to thank Dr Animesh Basak of Adelaide Microscopy, and Mr Evan Johnson and Mr Alson Ng of the Institute for Photonics & Advanced Sensing at the University of Adelaide (UoA) for experimental assistance. This work was supported by a PhD scholarship and a seed grant from UoA, and Grants-in-Aid for Scientific Research, Promotion of Joint International Research (Fostering Joint International Research B) from the Japan Society for the Promotion of Science (Grant ID 17401).

References

Abdo, B. M., Anwar, S., El-Tamimi, A., 2019. Machinability study of biolox forte ceramic by milling microchannels using rotary ultrasonic machining. J. Manuf. Process. 43, 175–191. https://doi.org/10.1016/j.jmapro.2019.05.031.

Alao, A. R., Yin, L., 2014a. Nano-scale mechanical properties and behavior of pre-sintered zirconia. J. Mech. Behav. Biomed. Mater. 36, 21–31. https://doi.org/10.1016/j.jmbbm.2014.03.019.

Alao, A. R., Yin, L., 2014b. Loading rate effect on the mechanical behavior of zirconia in nanoindentation. Mater. Sci. Eng. A. 619, 247–255. https://doi.org/10.1016/j.msea.2014.09.101.

Alao, A. R., Yin, L., 2016. Assessment of elasticity, plasticity and resistance to machining-induced damage of porous pre-sintered zirconia using nanoindentation techniques. J. Mater. Sci. Technol. 32, 402–410. https://doi.org/10.1016/j.jmst.2016.02.009.

Alao, A. R., Stoll, R., Song, X. F., Miyazaki, T., Hotta, Y., Shibata, Y., Yin, L., 2017. Surface quality of yttria-stabilized tetragonal zirconia polycrystal in CAD/CAM milling, sintering, polishing and sandblasting processes. J. Mech. Behav. Biomed. Mater. 65, 102–116. https://doi.org/10.1016/j.jmbbm.2016.08.021.

Anand, P. S. P., Arunachalam, N., Vijayaraghavan, L., 2018. Study on grinding of pre-sintered zirconia using diamond wheel. Mater. Manuf. Process. 33, 634–643. https://doi.org/10.1080/10426914.2017.1364761.

Brehl, D. A., Dow, T. A., 2008. Review of vibration-assisted machining. Precis. Eng. 32, 153–172. https://doi.org/10.1016/j.precisioneng.2007.08.003.

Denkena, B., Breidenstein, B., Busemann, S., Lehr, C. M., 2017. Impact of hard machining on zirconia based ceramics for dental applications. Procedia CIRP 65, 248–252. https://doi.org/10.1016/j.procir.2017.04.055.

Denry, I., Kelly, J. R., 2008. State of the art of zirconia for dental applications. Dent. Mater. 24, 299–307. https://doi.org/10.1016/j.dental.2007.05.007.

Denry, I., Kelly, J. R., 2014. Emerging ceramic-based materials for dentistry. J. Dent. Res. 93, 1235–1242. https://doi.org/10.1177/0022034514553627.

Denry, I., 2013. How and when does fabrication damage adversely affect the clinical performance of ceramic restorations?. Dent. Mater. 29, 85–96. https://doi.org/10.1016/j.dental.2012.07.001.

Guazzato, M., Albakry, M., Ringer, S. P., Swain, M. V., 2004. Strength, fracture toughness and microstructure of a selection of all-ceramic materials. Part II. Zirconia-based dental ceramics. Dent. Mater. 20, 449–456. https://doi.org/10.1016/j.dental.2003.05.002.

Hallmann, L., Ulmer, P., Reusser, E., Louvel, M., Hämmerle, C. H., 2012. Effect of dopants and sintering temperature on microstructure and low temperature degradation of dental Y-TZP-zirconia. J. Eur. Ceram. Soc. 32, 4091–4104. https://doi.org/10.1016/j.jeurceramsoc.2012.07.032.

ISO 25178-2:2012 (en) Geometric Product Specifications (GPS) — Surface Texture: Areal — Part 2: Terms, Definitions and Surface Texture Parameters, The International Organization for Standardization, Geneva, Switzerland (2012). https://www.iso.org/obp/ui/#iso:std:iso:25178:-2:ed-1:v1:en.

Jia, D., Li, C., Zhang, Y., Yang, M., Zhang, X., Li, R., Ji, H., 2019. Experimental evaluation of surface topographies of NMQL grinding ZrO2 ceramics combining

multiangle ultrasonic vibration. Int. J. Adv. Manuf. Technol. 100, 457–473. https://doi.org/10.1007/s00170-018-2718y.

Jiang, C., Cheng, J., Wu, T., 2017. Theoretical model of brittle material removal fraction related to surface roughness and subsurface damage depth of optical glass during precision grinding. Precis. Eng. 49, 421–427. https://doi.org/10.1016/j.precisioneng.2017.04.004.

Khellaf, A., Aouici, H., Smaiah, S., Boutabba, S., Yallese, M. A., Elbah, M., 2017. Comparative assessment of two ceramic cutting tools on surface roughness in hard turning of AISI H11 steel: including 2D and 3D surface topography. Int. J. Adv. Manufact. Technol. 89, 333–354. https://doi.org/10.1007/s00170-016-9077-3.

Kosmač, T., Oblak, C., Jevnikar, P., Funduk, N., Marion, L., 1999. The effect of surface grinding and sandblasting on flexural strength and reliability of Y-TZP zirconia ceramic. Dent. Mater. 15, 426–433. https://doi.org/10.1016/S0109-5641(99)00070-6.

Lawn, B. R., Marshall, D. B., 1979. Hardness, toughness, and brittleness: an indentation analysis. J. Am. Ceram. Soc. 62, 347–350. https://doi.org/10.1111/j.1151-2916.1979.tb19075.xManicone, P. F., Iommetti, P. R., Raffaelli, L., 2007. An overview of zirconia ceramics: basic properties and clinical applications. J. Dent. 35, 819–826. https://doi.org/10.1016/j.jdent.2007.07.008.

Liang, Y., Chen, Y., Chen, B., Fan, B., Yan, C., & Fu, Y. (2019). Feasibility of ultrasonic vibration assisted grinding for carbon fiber reinforced polymer with monolayer brazed grinding tools. Int. J. Precis. Eng. Manuf. 20, 1083–1094. https://doi.org/10.1007/s12541-019-00135-8.

Li, C., Zhang, F., Meng, B., Liu, L., Rao, X., 2017. Material removal mechanism and grinding force modelling of ultrasonic vibration assisted grinding for SiC ceramics. Ceram. Int. 43, 2981–2993. https://doi.org/10.1016/j.ceramint.2016.11.066.

Mitov, G., Heintze, S. D., Walz, S., Woll, K., Muecklich, F., Pospiech, P., 2012. Wear behavior of dental Y-TZP ceramic against natural enamel after different finishing procedures. Dent. Mater. 28, 909–918. https://doi.org/10.1016/j.dental.2012.04.010.

Miyazaki, T., Nakamura, T., Matsumura, H., Ban, S., Kobayashi, T., 2013. Current status of zirconia restoration. J. Prosthodont. Res. 57, 236–261. https://doi.org/10.1016/j.jpor.2013.09.001.

Morgan, M., 2004. Finishing and polishing of direct posterior resin restorations. Pract. Proced. Aesthet. Dent. 3, 211–216. https://pubmed.ncbi.nlm.nih.gov/15199696/.

Nemoto, K., Yanagi, K., Aketagawa, M., Yoshida, I., Uchidate, M., Miyaguchi, T., Maruyama, H., 2009. Development of a roughness measurement standard with irregular surface topography for improving 3D surface texture measurement. Meas. Sci. Technol. 20, 84023. https://doi.org/10.1088/09570233/20/8/084023.

Piconi, C., Maccauro, G., 1999. Zirconia as a ceramic biomaterial. Biomaterials 20, 1–25. https://doi.org/10.1016/S0142-9612(98)00010-6.

Rekow, E. D., Silva, N. R. F. A., Coelho, P. G., Zhang, Y., Guess, P., Thompson, V. P., 2011. Performance of dental ceramics: challenges for improvements. J. Dent. Res. 90, 937–952. https://doi.org/10.1177/0022034510391795.

Ritzberger, C., Apel, E., Höland, W., Peschke, A., Rheinberger, V. M., 2010. Properties and clinical application of three types of dental glass-ceramics and ceramics for CAD-CAM technologies. Materials 3, 3700–3713. https://doi.org/10.3390/ma3063700.

Sakoda, S., Nakao, N., Watanabe, I., 2018. The effect of abrading and cutting instruments on machinability of dental ceramics. J. Mater. Sci. Mater. Med. 29, 1–8. https://doi.org/10.1007/s10856-018-6031-y.

Tsai, M. Y., Chang, C. T., Ho, J. K., 2016. The machining of hard mold steel by ultrasonic assisted end milling. Appl. Sci. 6, 373. https://doi.org/10.3390/app6110373.

Wang, C., Wang, X., Sun, F., 2018. Tribological behavior and cutting performance of monolayer, bilayer and multilayer diamond coated milling tools in machining of zirconia ceramics. Surf. Coat. Technol. 353, 49–57. https://doi.org/10.1016/j.surfcoat.2018.08.074.

Wendler, M., Belli, R., Petschelt, A., Mevec, D., Harrer, W., Lube, T., Danzer, R., Lohbauer, U., 2017. Chairside CAD/CAM materials. Part 2: Flexural strength testing. Dent. Mater. 33, 99–109. https://doi.org/10.1016/j.dental.2016.10.008.

Yang, Z., Zhu, L., Lin, B., Zhang, G., Ni, C., Sui, T., 2019a. The grinding force modeling and experimental study of ZrO2 ceramic materials in ultrasonic vibration assisted grinding. Ceram. Int. 45, 8873–8889. https://doi.org/10.1016/j.ceramint.2019.01.216.

Yang, Z., Zhu, L., Ni, C., Ning, J., 2019b. Investigation of surface topography formation mechanism based on abrasive-workpiece contact rate model in tangential ultrasonic vibration-assisted CBN grinding of ZrO2 ceramics. Int. J. Mech. Sci. 155, 66–82. https://doi.org/10.1016/j.ijmecsci.2019.02.031.

Yang, Z., Zhu, L., Zhang, G., Ni, C., Lin, B., 2020. Review of ultrasonic vibration-assisted machining in advanced materials. Int. J. Mach. Tools. Manuf. 156, 103594. https://doi.org/10.1016/j.ijmachtools.2020.103594.

Yin, L., Jahanmir, S., Ives, L. K., 2003. Abrasive machining of porcelain and zirconia with a dental handpiece. Wear 255,975–989. https://doi.org/10.1016/S0043-1648(03)00195-9.

Zhang, Y., 2014. Making yttria-stabilized tetragonal zirconia translucent. Dent. Mater. 30, 1195–1203. https://doi.org/10.1016/j.dental.2014.08.375.

Zhang, Y., Lawn, B. R., 2018. Novel zirconia materials in dentistry. J. Dent. Res. 97, 140–147. https://doi.org/10.1177/0022034517737483.

Zhang, Y., Lawn, B. R., 2019. Evaluating dental zirconia. Dent. Mater. 35, 15–23. https://doi.org/10.1016/j.dental.2018.08.291.

Chapter 8 Conclusions and Recommendation

The research work presented in this thesis is devoted to the study of the micro and nanomechanical behavior and ultrasonic machining responses of zirconia materials. This thesis has explored the influence of zirconia microstructures in structure-property-processing relations. Detailed conclusions are summarized below.

8.1 Conclusions

8.1.1 Micromechanical Properties and Behaviour

This thesis characterized the micromechanical properties and behavior of pre-sintered and sintered zirconia materials. *In-situ* micropillar compression tests were conducted on the materials to understand the deformation and damage mechanisms of zirconia materials at small-scale. Their micromechanical properties were determined from the stress-strain curves. Their deformation and failure modes were observed using scanning electron microscopy throughout the compression process and also after post-deformation. Pre-sintered and sintered zirconia revealed micropillar compression induced plastic deformation but more severe buckling was observed in the former than in the latter. Pre-sintered zirconia revealed a significantly lower yield strength of 285 ± 65 MPa, a fracture strength of 329 ± 64 MPa, a compression strength of 351 ± 46 MPa, a resilience of 2.5 ± 1.1 J/m^3, and a toughness of 30.1 ± 10.1 J/m^3 but higher ductility of 10.8 ± 0.6%. Sintered zirconia revealed a much higher lower yield strength of 5383 ± 855 MPa, a fracture strength of 6330 ± 833 MPa, a compression strength of 6737 ± 902 MPa, a resilience of 200.3 ± 69.5 J/m^3, and a toughness of 525.4 ± 90.8 J/m^3 but lower ductility of 4.7 ± 0.7%.

Distinct deformation and failure modes were observed for the two zirconia materials. The quasi-brittle failure mechanisms for pre-sintered zirconia were mushroom buckling damage with cracking and delamination. The discovery of buckling of the micropillar structure is a new discovery on these brittle ceramic materials. This highlights the length scale influence on brittle materials. Furthermore, the quasi-brittle failure mechanisms of sintered zirconia were plastic crushing with microfractures and delamination. In addition, a compression mechanics model of the two zirconia materials in compression was

developed to provide fundamental insight into the evolution deformation, and damage of the materials under external load.

8.1.2 Single Loading Indentation Mechanics

The thesis investigated the microstructural responses of pre-sintered and sintered zirconia materials to nanoindentation associated with diamond machining processing of zirconia restoration. The indentation technique mimics contact formed on the material during the machining process, hence it represents the mechanics of the diamond machining process. *In-situ* nanoindentation tests were conducted to provide the fundamental understanding of the deformation and damage mechanisms of these ceramics under small-scale contact with diamond tools. Pre-sintered zirconia showed a lower contact hardness of 1.92 ± 0.22 GPa and Young's moduli of 32.6 ± 5.3 GPa. Sintered zirconia showed a higher contact hardness of 21.09 ± 4.20 GPa and Young's moduli of 111.6 ± 10.9 GPa.

Nanoindentation-induced quasi-plastic behavior was observed. The quasi-plastic deformation mechanisms for pre-sintered zirconia were due to shear faults resulting in compression, fragmentation, pulverization of zirconia crystals, and severe microstructural cracking. Based on this observation, it was advisable to develop a new microstructure design for this material by sintering at low temperatures, to obtain balanced machining damage and efficiency. Furthermore, the quasi-plastic deformation mechanism for sintered zirconia was the shear band-plastic mode with localized microfractures. Based on this observation, it is predicted that sintered zirconia with a closely packed microstructure can provide much resistance to machining damage. In addition, the nanoindentation-induced damage reported in this study could be a concern, as this damage may act as a stress concentrator to the ceramic during service.

8.1.3 Cyclic Loading Indentation and Advanced Analysis

The thesis further investigated the cyclic loading indentation mechanics and provided advanced analysis of the mechanical behavior and deformation using Sakai and Sakai-Nowak models. Their cyclic nanomechanical characterization delivers technical insights into the machinability aspects of the ceramic during processing due to the similarities in indentation to abrasive machining in the function of microfractures and deformation events. The cyclic nanoindentation mechanical behaviors were controlled by zirconia

microstructures. Pre-sintered zirconia revealed lower ranges of resistance to plasticity of 15.12 ± 5.30 GPa to 19.11 ± 11.26 GPa and ranges of resistance to machining-induced cracking of 136.77 ± 7.58 GPa to 155.33 ± 21.80 GPa, across 10 cyclic indentations. Sintered zirconia revealed much higher ranges of resistance to plasticity of 244.34 ± 53.73 GPa to 341.34 ± 118.68 GPa and ranges of resistance to machining-induced cracking of 441.54 ± 73.27 GPa to 488.16 ± 57.95 GPa, across 10 cyclic indentations.

Cyclic nanoindentation induced quasi-plasticity in pre-sintered zirconia, revealing compressed and pulverized layers of zirconia crystals with microfractures and large imprint edge cracking. In addition, quasi-plastic deformation in sintered zirconia revealed shear band deformation with microfractures and edge pile-ups. Based on these deformations, damage mechanisms, and mechanical properties, pre-sintered zirconia is predicted to be easier to machine but may suffer extensive machining damage than sintered zirconia.

8.1.4 Machining-Induced Edge Chipping Damage

The thesis also investigated the machining-induced edge chipping damage in conventional and ultrasonic diamond machining of zirconia materials. The edge chipping produced in both machining processes for the two zirconia materials involved brittle fracture material removal and largely depended on zirconia microstructures and ultrasonic vibration amplitudes. In addition, under both machining processes, pre-sintered zirconia with a porous microstructure yielded much larger edge chipping damage depths than sintered zirconia with a closely packed microstructure. In pre-sintered zirconia, ultrasonic machining at 3 µm vibration amplitude significantly reduced the edge chipping damage by 45% and by 40%, on both the top and bottom surfaces, in comparison with conventionally machined zirconia. Similarly in sintered zirconia, the ultrasonic machined zirconia at 3 µm vibration amplitude significantly reduced the edge chipping damage by 33% and by 19%, on both the top and bottom surfaces, in comparison with conventional machined zirconia. In both zirconia materials, ultrasonic machining at an optimal vibration amplitude minimized the brittle fracture scale at the micro-level, hence yielding significantly improved edge chipping damage in the two zirconia materials.

8.1.5 Surface Quality

The thesis investigated the surface quality of pre-sintered and sintered zirconia materials produced in conventional and ultrasonic diamond machining processes, in the function of surface asperities and damage morphology, and material removal mechanisms. Zirconia microstructures and ultrasonic vibration amplitudes control their material removal mechanism and surface asperities. The two zirconia materials revealed a mixed brittle fracture and ductile mode of removal under both conventional and ultrasonic machining processes. The dominant mode in pre-sintered zirconia was brittle fracture and in sintered zirconia the ductile mode was dominant. This lead to much higher fracture damage area ratios ranging from 0.38 to 0.60 $\mu m^2/ \mu m^2$ in pre-sintered zirconia and with much lower ranges of 0.15 to 0.20 $\mu m^2/ \mu m^2$ for sintered zirconia. In addition, pre-sintered zirconia had higher average and maximum values, and maximum peak and valley heights, compared with sintered zirconia. Ultrasonic vibration at 3 µm vibration amplitude minimizes the brittle fracture damages area ratios by 25% for pre-sintered zirconia and by 16% for sintered zirconia, in comparison with conventional machining. Ultrasonic vibration assistance at an optimum vibration amplitude promotes brittle to ductile transition during machining hence resulting in improved brittle fracture damage area ratios with reduced surface asperities.

8.1.6 Overall Summary

The overall findings of Chapters 3–7 indicate that zirconia microstructures control their micromechanical properties and machining responses. This suggests that by microstructure optimization of zirconia materials through controlling sintering conditions of zirconia blanks, different damage degrees and machining responses of zirconia materials may be obtained. Hence, microstructural optimization of zirconia materials is very necessary in CAD/CAM processing of zirconia dental crowns.

Further, ultrasonic machining at optimised vibration conditions produces micro-scale fractures, which enable the reduction of edge chipping damage and surface roughness. Therefore, vibration assistance in diamond machining may be used to improve the quality of current CAD/CAM processing of ceramic restorations.

8.2 Recommendation for Future Studies

Micropillar compression studies should be conducted on pre-sintered and sintered zirconia at different micropillar sizes. This is necessary to understand the influence of the size effect on zirconia materials, providing extra information on their observed micropillar-induced deformation and damage mechanisms and micromechanical properties reported in Chapter 3.

In-situ SEM single and cyclic nanoindentation tests using different shapes of diamond indenters, peak loads, and loading rates should be conducted on pre-sintered and sintered zirconia materials. This is necessary to investigate the responses of zirconia materials during abrasive machining when different diamond abrasives are subjected to the zirconia surface. Hence, it will contribute additional scientific knowledge to the indentation mechanics and deformation mechanisms in Chapters 4 and 5.

Further, scratch test on zirconia materials should be conducted under different scratch depths and speeds. Cross-section scratched samples should be prepared to investigate microstructural changes, such as material damage and deformation, and shear band formation induced. In addition, wear analysis such as coefficients of friction and wear resistance should be investigated. The scratch test is necessary to provide the further understanding of machining processes and machinability of zirconia materials, enriching micro/nanomechanics and machining science of brittle solids.

The practicality of the proposed ultrasonic vibration-assisted technology in Chapters 6 and 7 should be conducted under different removal rates and different diamond tool grit sizes. This is necessary for identifying optimized machining parameters with a suitable diamond tool for a minimized tool wear effect with superior surface quality. Furthermore, a thorough analysis of the machining forces and temperature during the conventional and ultrasonic machining processes will provide additional, valuable knowledge of their observed removal mechanisms and damage morphology.